Sustainable Synthesis of Metal–Organic Frameworks for Applications in Ophthalmic Drug Delivery

Paola Marino

A Thesis

In

The Department

Of

Chemistry and Biochemistry

Presented in Partial Fulfillment of the Requirements

For the Degree of Master of Science (Chemistry) at

Concordia University

Montreal, Quebec, Canada

December 2021

CONCORDIA UNIVERSITY

SCHOOL OF GRADUATE STUDIES

This is to certify that the thesis prepared

By: Paola Marino

Entitled: Sustainable Synthesis of Metal–Organic Frameworks for Applications in Ophthalmic Drug Delivery

and submitted in partial fulfilment of the requirements for the degree of

Master of Science (Chemistry)

complies with the regulations of the University and meets the accepted standards with respect to originality and quality.

Signed by the final examining committee:

Dr. Rafik Naccache_____Chair

Dr. Louis A. Cuccia_____Examiner

Dr. Marek B. Majewski_____Examiner

Dr. Ashlee J. Howarth_____Supervisor

Approved by _____

Dr. Yves Gélinas, Graduate Program Director, Chemistry and Biochemistry

_____20__ _____

Dr. Pascale Sicotte, Dean, Faculty of Arts and Science

Abstract

Sustainable Synthesis of Metal–Organic Frameworks for Applications in Ophthalmic Drug Delivery

Paola Marino

The work described herein explores an emerging class of hybrid porous materials known as metal–organic frameworks (MOFs), comprised of metal nodes bridged by organic linkers. This thesis explores the (i) sustainable synthesis and characterization of a series of structurally diverse MOFs, which include MOF-808, NU-1000, HKUST-1, and ZIF-8 using a green solvent alternative, STEPOSOL® MET-10U, (ii) the design, synthesis, and characterization of thiol-functionalized Zr_6-based MOFs, Zr-UiO-66-$(SH)_2$ and Zr-UiO-67-$(SH)_2$, and (iii) the investigation of thiol-functionalized MOFs as an alternative platform for use in ophthalmic drug delivery applications, through assessing their mucoadhesive properties and drug loading capacity of flurbiprofen.

Chapter 2 explores the use of a plant-derived solvent, STEPOSOL® MET-10U, otherwise known as *N,N*-dimethyl-9-decenamide, for the synthesis and characterization of a diverse series of MOFs, MOF-808, NU-1000, HKUST-1 and ZIF-8, which are MOFs with different metal valency, varying metals nodes and organic linkers. The physical properties of the MOFs are assessed to verify that the materials are similar to those synthesized using the petroleum derived solvent *N,N*-dimethylformamide (DMF), and to verify the viability of the green solvent. Furthermore, synthesis of HKUST-1 on the gram-scale was performed using STEPOSOL® MET-10U to confirm that the method is scalable.

Chapter 3 delves into the synthesis and characterization of thiol-functionalized MOFs or thiolated MOFs, Zr-UiO-66-$(SH)_2$ and Zr-UiO-67-$(SH)_2$. These MOFs were chosen for this study as thiols are known to enhance mucoadhesive properties in drug delivery materials for biomedical applications. The mucoadhesive properties of Zr-UiO-66-$(SH)_2$ and Zr-UiO-67-$(SH)_2$ are presented with the goal of understanding their potential in ophthalmic drug delivery, in addition to verifying the drug loading capacity of these MOFs using a non-steroidal anti-inflammatory drug, flurbiprofen.

Acknowledgements

First and foremost, I would like to thank my supervisor Dr. Ashlee J. Howarth, who is knowledgeable, patient, kind, helpful, and the best mentor anyone could ask for. There aren't enough words to express how grateful and thankful I am for her encouragement, motivation, and relentless support over the years. Her guidance and input have made all the difference in the projects I worked on, and her positivity radiates through everyone in the group. Thank you for introducing me to the world of MOFs in 2018 and thank you for helping me grow!

To my research committee members, Dr. Louis Cuccia – for his guidance, and helpful discussions, and Dr. Marek Majewski – for his advice, mentorship and overall insights in this field since my years as an undergraduate student have made this an inspiring experience for me. Thank you both for supporting me.

To all my lab colleagues and friends, thank you for making my years in the Howarth group truly enjoyable. Zvart – for her enthusiasm, support and friendship – beginning from our journey as undergraduate students, to Italy, and as graduate students – I will be forever grateful. Rafa – for always being helpful and supportive, for teaching me so much about visualizing crystal structures, and for discussing our research together, grazie mille. Victor – for always being genuine and kind, giving me advice, for helping me run over 40 nitrogen sorption experiments in such a short time period, and for his overall willingness to help me. Hudson – for his cheerful personality, for patiently answering all of my questions especially about encapsulation and release experiments, and for always being helpful. Chris – for being a great team player, a tidy fumehood neighbour, for always sharing his baked goods and for always helping me out. Felix – for always being helpful and supportive. Lars – whom I have had the pleasure of mentoring, thank you for being optimistic and motivating, and for sharing similar interests in good food and coffee spots around the city. Amna – for always being helpful, for her unwavering support, and for always encouraging me. Samantha – whom I have had the pleasure of mentoring, for always being supportive and understanding, and for being curious about MOFs for ophthalmic drug delivery applications. Ximena – for always being thoughtful and supportive, and Paria –for always being friendly and believing in me.

Thank you to all the Howarth and Majewski (HOMA) research group members for providing a dynamic and supportive research environment, for which my lab experience would

not be the same without. Thanks to Sabine, whom I have had the pleasure to work with and supervise during her undergraduate degree.

To Hatem, our greatest friend from McGill University. Thank you for all of your help over the years, and for always believing in me and encouraging me.

To my collaborators, Dr. Élodie Boisselier and Gabrielle Raîche-Marcoux, I am very grateful for all your help.

Thank you to the graduate student community at Concordia University, and thanks to everyone I have crossed path with during my Master's degree, and made grad school a memorable experience.

A special thank you to Michael for always encouraging me, for being the shoulder I can always depend on, and for being a ray of sunshine on a rainy day. Thank you for always making me smile and reminding me that I can achieve anything I set my mind to. I could not have done it without you.

To my Mom, thank you for being so supportive, and for all your love and care – I owe it all to you. To my Dad, thank you for making me the person that I am today – I know you would be proud. To my sisters, Mary and Erica, thank you for always encouraging me to reach for the stars and for being the best big sisters. To Erik and Auntie Mariella, and the rest of my friends and family, I am grateful for all of your support and I could not have done it without you.

Dedication

To my family – Mom, Dad and Sisters

Contribution of Authors

In all chapters, Dr. Ashlee J. Howarth acted in a supervisory role. Chapter 2 involved a collaboration with Dr. Hatem M. Titi from the Department of Chemistry at McGill University in Montreal, Canada. Chapter 3 involved a collaboration with Dr. Élodie Boisselier and Gabrielle Raîche-Marcoux from the Department of Ophthalmology at Université Laval in Quebec City, Canada.

Sections of Chapter 1 have been published as a review: Ajoyan, Z.; Marino, P.; Howarth, A. J. *CrystEngComm*, **2018**, *20*, 5899-5912. I am a primary author of this work.

A version of Chapter 2 has been published in the form of a research article: Marino, P.; Donnarumma, P. R.; Bicalho, H. A.; Quezada-Novoa, V.; Titi, H. M.; Howarth, A. J. *ACS Sustain. Chem. Eng.* **2021**, *9*, 16356-16362. I am the primary author of this work. P. Rafael Donnarumma helped in the characterization of the MOFs by PXRD. Hudson A. Bicalho performed SEM imaging. Victor Quezada-Novoa helped in the characterization of the proposed MOFs by N_2 sorption studies and provided the organic linker for NU-1000. Dr. Hatem M. Titi performed SCXRD of the single crystals of ZIF-8 (DMF) and ZIF-8 (STEPOSOL), and TGA analysis.

Chapter 3 is an advanced project which will soon be made into a manuscript for submission to a peer-reviewed journal. I am the primary author of this work. Gabrielle Raîche-Marcoux has performed the mucoadhesion experiments for the thiolated MOFs and controls. Hudson A. Bicalho has helped in the drug loading and release experiments by HPLC analysis, and SEM imaging.

Table of Contents

List of Figures ..... **xi**

List of Tables ..... **xx**

List of Abbreviations ..... **xxi**

Chapter 1 ..... **1**

Introduction **1**

1.1. Brief History and Definition of Metal–Organic Frameworks (MOFs) **1**

1.2. Fundamental Principles and Properties of MOFs **2**

1.2.1. Reticular Chemistry 3

1.2.2. Topology 3

1.2.3. Characteristics and Properties of MOFs 3

1.3. UiO-66, UiO-67, and Isostructural MOFs **4**

1.3.1. Zr-UiO-66 4

1.3.2. Zr-UiO-67 6

1.3.3. Isostructural MOFs 8

1.3.4. Thiol-Functionalized MOFs 8

1.4. Overview of Methods in MOF Synthesis **8**

1.4.1. MOF Synthesis 8

1.4.2. Green Chemistry 10

1.4.2.1. Principles of Green Chemistry 11

1.4.2.2. Green MOF Synthesis 12

1.4.2.3. Green Solvent: STEPOSOL® MET-10U 12

1.4.3. MOF Activation 13

1.4.3.1. Solvent-Exchange Activation 14

1.5. Potential Applications of MOFs **15**

1.5.1. MOFs for Drug Delivery 16

1.6. Characterization of MOFs **17**

1.6.1. Powder X-ray Diffraction (PXRD) 18

1.6.2. Single Crystal X-ray Diffraction (SCXRD) 19

1.6.3. Nitrogen (N_2) Adsorption and Desorption Isotherms 20
1.6.4. Thermogravimetric Analysis (TGA) 22
1.6.5. Scanning Electron Microscopy (SEM) 23
1.6.6. Nuclear Magnetic Resonance (NMR) Spectroscopy 24
1.6.7. Diffuse Reflectance Infrared Fourier Transform Spectroscopy (DRIFTS) 24
1.6.8. Inductively Coupled Plasma–Mass Spectrometry (ICP-MS) 26
1.6.9. Ultraviolet-Visible (UV-Vis) Spectroscopy 26
1.6.10. High Performance Liquid Chromatography (HPLC) 26

1.7. Thiol Quantification Protocol 27

1.8. Mucoadhesion and Periodic Acid–Schiff (PAS) Coloration Protocol 27
1.8.1. Mucins and Mucoadhesion 27
1.8.2. Periodic Acid–Schiff (PAS) Coloration Protocol 29

1.9. Scope of Thesis 30

Chapter 2 31

A Step Toward Change: A Green Alternative for the Synthesis of Metal–Organic Frameworks 31

2.1. Introduction 31

2.2. Experimental Procedures 33
2.2.1. General Materials and Methods 33
2.2.2. Synthesis and Activation of MOF-808, NU-1000, HKUST-1, and ZIF-8 36

2.3. Results and Discussion 39

2.4. Conclusions 59

Chapter 3 60

Thiol-Functionalized Metal–Organic Frameworks as Drug Delivery Platforms for Ophthalmic Therapeutics 60

3.1. Introduction to Ophthalmic Drug Delivery and MOFs 60

3.2. Experimental Procedures 67
3.2.1. General Materials and Methods 67

3.2.2. Synthesis and Activation of Zr-UiO-66-$(SH)_2$, Zr-UiO-67-$(SH)_2$, Zr-UiO-66 and Zr-UiO-67 (Thiolated and Control MOFs) 70

3.3. Results and Discussion 72

3.3.1. Characterization of Thiolated and Control MOFs 72

3.3.2. MOFs and Mucins Mucoadhesion Study 80

3.3.2.1. Periodic Acid–Schiff (PAS) Protocol 80

3.3.3. Thiol Quantification Study 82

3.3.4. Inorganic Metal Precursor and Organic Linker Leaching Study 85

3.3.5. Drug Encapsulation and Release of Flurbiprofen 86

3.4. Conclusions 90

Chapter 4 91

Conclusions and Future Work 91

4.1. General Conclusions 91

4.2. Future Work 92

References 93

Appendix 109

List of Figures

Figure 1.1. Schematic representation of assembling a metal–organic framework (MOF)…….2

Figure 1.2. Structure of Zr-UiO-66. (a) Zr-based hexanuclear cluster, (b) linear ditopic 1,4-benzenedicarboxylic acid (H_2BDC) organic linkers, and (c) Zr-UiO-66 with **fcu** topology. Two types of cages exist in the net, (d) the octahedral cage (yellow sphere), and (e) the tetrahedral cages (purple spheres)……5

Figure 1.3. Connectivity of Zr_6 clusters. (a) 12-connected metal node, and (b) 8-connected metal node due to missing organic linkers, arising from defects in the structure. Zr = teal, C = black, O = red……..……..…….6

Figure 1.4. Structure of Zr-UiO-67. (a) Zr-based hexanuclear cluster, (b) linear ditopic biphenyl-4,4′-dicarboxylic acid (H_2BPDC) organic linkers, and (c) Zr-UiO-67 with **fcu** topology. Two types of cages exist in the net, (d) the octahedral cage (yellow sphere), and (e) the tetrahedral cages (purple spheres)..……..……..……..7

Figure 1.5. Chemical structures of different modulators used in MOF synthesis……...…10

Figure 1.6. The twelve principles of green chemistry as a guide for sustainable chemistry, to design and improve materials, processes, synthesis and systems……...11

Figure 1.7. Chemical structures of a toxic solvent, *N,N*-dimethylformamide (DMF), and an environmentally friendly solvent, *N,N*-dimethyl-9-decenamide (STEPOSOL® MET-10U)…..….13

Figure 1.8. Solvent-exchange activation combined with conventional heating and vacuum drying for a MOF. As-synthesized MOF (left), and an activated MOF (right). The orange shading represents solvent and the green spheres represent leftover molecules post-synthesis……...15

Figure 1.9. Representation of encapsulated drug molecules in the MOF……...…17

Figure 1.10. Stacked PXRD diffractograms exemplifying a comparison between an experimentally obtained one (top), and a simulated one (bottom). The black tick marks are the allowed reflections…….....……..…18

Figure 1.11. Representation of physisorption isotherms (Type I-VI) given by porous and nonporous materials. Figure obtained from Thommes *et al.*[167]……...21

Figure 1.12. SEM micrograph of Zr-UiO-66 exhibiting octahedral crystallites……23

Figure 1.13. ^{1}H-NMR spectrum of Zr-UiO-66 displaying the BDC aromatic proton (purple), NMR solvent (blue), and acid for MOF digestion (green)……24

Figure 1.14. DRIFTS spectra of isostructural MOFs, Zr-UiO-66 and Zr-UiO-67……..25

Figure 1.15. Reaction scheme involved in quantifying the surface accessible thiol groups on MOFs using Ellman's reagent……...27
Figure 1.16. Gel-forming mucins (a) MUC2 and (b) MUC5AC, in the mucous layer. The pink spheres represent cysteine residues……28
Figure 1.17. Periodic Acid–Schiff (PAS) reaction scheme, where (a) alcohol oxidation to form aldehyde groups and (b) Schiff dye reacts with aldehyde groups to form a pink-purple compound……...29
Figure 2.1. A bioderived solvent, STEPOSOL® MET-10U, is used to synthesize a series of structurally diverse metal–organic frameworks……..33
Figure 2.2. MOFs successfully synthesized solvothermally with STEPOSOL® MET-10U, including MOF-808, NU-1000, HKUST-1, and ZIF-8……...40
Figure 2.3. Simulated and experimental PXRD patterns of (a) MOF-808 synthesized by STEPOSOL® MET-10U, (b) NU-1000 synthesized by STEPOSOL® MET-10U (simulated pattern of NU-1000 (FIFFUX) was recorded at 100 K), (c) HKUST-1 synthesized by STEPOSOL® MET-10U, and (d) ZIF-8 synthesized by STEPOSOL® MET-10U using solvothermal and room temperature synthetic procedures……...41
Figure 2.4. Nitrogen adsorption-desorption isotherms of MOF-808 (Type I(b)) synthesized by STEPOSOL® MET-10U and washed with isopropanol, NU-1000 (Type IV(b)) synthesized by STEPOSOL® MET-10U and washed with DMF, HKUST-1 (Type I(a)) synthesized by STEPOSOL® MET-10U and washed with methanol, ZIF-8 (Type I(a)) synthesized by STEPOSOL® MET-10U (solvothermal) and washed with ethanol 95%, and ZIF-8 (Type I(a)) synthesized by STEPOSOL® MET-10U (room temperature) and washed with methanol……..44
Figure 2.5. TGA curves of (a) MOF-808 synthesized by STEPOSOL® MET-10U and by DMF, (b) NU-1000 synthesized by STEPOSOL® MET-10U and by DMF, (c) HKUST-1 synthesized by STEPOSOL® MET-10U and by DMF, and (d) ZIF-8 synthesized by STEPOSOL® MET-10U and by DMF……..….46
Figure 2.6. TGA curve of ZIF-8 synthesized by STEPOSOL® MET-10U at room temperature....47
Figure 2.7. DRIFTS spectra of (a) MOF-808, (b) NU-1000, (c) HKUST-1, and (d) ZIF-8 synthesized by STEPOSOL® MET-10U……48
Figure 2.8. DRIFTS spectrum of ZIF-8 synthesized by STEPOSOL® MET-10U at room temperature……48

Figure 2.9. ^{1}H-NMR spectrum of a digested sample of MOF-808 synthesized by STEPOSOL® MET-10U, in D_2SO_4 and DMSO-d_6……...49
Figure 2.10. ^{1}H-NMR spectrum of a digested sample of NU-1000 synthesized by STEPOSOL® MET-10U, in D_2SO_4 and DMSO-d_6……...49
Figure 2.11. ^{1}H-NMR spectrum of a digested sample of HKUST-1 synthesized by STEPOSOL® MET-10U, in D_2SO_4 and DMSO-d_6……...50
Figure 2.12. ^{1}H-NMR spectrum of a digested sample of ZIF-8 synthesized by STEPOSOL® MET-10U, in D_2O acidified with DCl and DMSO-d_6……..50
Figure 2.13. ^{1}H-NMR spectra of STEPOSOL® MET-10U in D_2SO_4 and DMSO-d_6, a digested sample of MOF-808 (STEPOSOL) in D_2SO_4 and DMSO-d_6, a digested sample of NU-1000 (STEPOSOL) in D_2SO_4 and DMSO-d_6, a digested sample of HKUST-1 (STEPOSOL) in D_2SO_4 and DMSO-d_6, and a digested sample of ZIF-8 (STEPOSOL) in D_2O acidified with DCl and DMSO-d_6……...51
Figure 2.14. ^{1}H-NMR spectrum of a digested sample of ZIF-8 synthesized by STEPOSOL® MET-10U at room temperature, in D_2O acidified with DCl and DMSO-d_6……52
Figure 2.15. ^{1}H-NMR spectra of STEPOSOL® MET-10U in D_2SO_4 and DMSO-d_6, and of a digested sample of ZIF-8 synthesized by STEPOSOL® MET-10U at room temperature, in D_2O acidified with DCl and DMSO-d_6……...52
Figure 2.16. SEM micrographs of (a) MOF-808 synthesized by DMF and (b) MOF-808 synthesized by STEPOSOL® MET-10U, showing octahedral microcrystallites……53
Figure 2.17. SEM micrographs of (a) NU-1000 synthesized by DMF, (b) NU-1000 synthesized by STEPOSOL® MET-10U, (c) NU-1000 synthesized by DMF and captured using a greater magnification, and (d) NU-1000 synthesized by STEPOSOL® MET-10U and captured using a greater magnification, showing smooth hexagonal rods……54
Figure 2.18. SEM micrographs of (a) HKUST-1 synthesized by DMF, (b) HKUST-1 synthesized by STEPOSOL® MET-10U, (c) HKUST-1 synthesized by DMF and captured using a greater magnification, and (d) HKUST-1 synthesized by STEPOSOL® MET-10U and captured using a greater magnification, showing octahedral microcrystallites……55
Figure 2.19. SEM micrographs of (a) ZIF-8 synthesized by DMF showing a mixture of cubic crystals and rhombic dodecahedrons, and (b) ZIF-8 synthesized by STEPOSOL® MET-10U

showing a mixture of hexagonal-faceted crystals, rhombic dodecahedrons and truncated rhombic dodecahedrons..……..56
Figure 2.20. SEM micrographs of (a) ZIF-8 synthesized by STEPOSOL® MET-10U at room temperature, and (b) ZIF-8 synthesized by STEPOSOL® MET-10U at room temperature and captured using a greater magnification……...56
Figure 2.21. Optical micrograph of bulk microcrystalline ZIF-8 synthesized by STEPOSOL® MET-10U……...57
Figure 2.22. Optical micrograph of bulk microcrystalline ZIF-8 synthesized by DMF…….57
Figure 2.23. Photographs detailing the gram-scale synthesis of HKUST-1 in STEPOSOL® MET-10U……..58
Figure 2.24. Large scale synthesis of HKUST-1. (a) PXRD pattern of HKUST-1 synthesized by STEPOSOL® MET-10U, at the gram-scale and (b) N_2 adsorption-desorption isotherm and BET surface area value of HKUST-1 (Type I(a)) synthesized by STEPOSOL® MET-10U and washed with methanol and acetone (S_{BET} = 1895 m^2 g^{-1})…….59
Figure 3.1. Illustration showing the anatomy of the eye.[228]……61
Figure 3.2. Representation of a normal eye (left) and eye with cataract (right).[229]…….61
Figure 3.3. Two barriers to topical ocular drug delivery, tear film barrier (top) and corneal barrier (bottom). Figure obtained from Li *et al.*[241]…….62
Figure 3.4. Representation of drug delivery systems. (a) Thiol-functionalized gold nanoparticles,[186] (b) liposomes comprised of lipid bilayers, and (c) simplified MOF structure……..……64
Figure 3.5. Tear film of the eye comprised of three distinct layers.[253]……65
Figure 3.6. Chemical structures of different non-steroidal anti-inflammatory drugs (NSAIDs)…65
Figure 3.7. Solvothermal synthesis of Zr-UiO-66-$(SH)_2$ (top) and Zr-UiO-67-$(SH)_2$ (bottom)….66
Figure 3.8. PXRD diffractograms of (a) Zr-UiO-66-$(SH)_2$ AA and HCl, and (b) Zr-UiO-67-$(SH)_2$ AA and HCl……73
Figure 3.9. Nitrogen adsorption-desorption isotherms of (a) Zr-UiO-66-$(SH)_2$ AA and HCl (Type I(a)), (b) Zr-UiO-67-$(SH)_2$ AA and HCl (Type I(a)), and pore size distribution analysis of (c) Zr-UiO-66-$(SH)_2$ AA and HCl, and (d) Zr-UiO-67-$(SH)_2$ AA and HCl……74
Figure 3.10. TGA curves of (a) Zr-UiO-66-$(SH)_2$, and (b) Zr-UiO-67-$(SH)_2$……75
Figure 3.11. DRIFTS spectra of (a) Zr-UiO-66-$(SH)_2$, and (b) Zr-UiO-67-$(SH)_2$……..75

Figure 3.12. ^{1}H-NMR spectra of (a) Zr-UiO-66-$(SH)_2$, and (b) Zr-UiO-67-$(SH)_2$……76
Figure 3.13. SEM micrographs of (a) Zr-UiO-66-$(SH)_2$-AA, and (b) Zr-UiO-67-$(SH)_2$-AA…..76
Figure 3.14. DLS measurements of (a) Zr-UiO-66-$(SH)_2$-AA, and (b) Zr-UiO-67-$(SH)_2$-AA…77
Figure 3.15. PXRD diffractograms of (a) Zr-UiO-66 AA and HCl, and (b) Zr-UiO-67 AA and HCl…….77
Figure 3.16. Nitrogen adsorption-desorption isotherms of (a) Zr-UiO-66 AA and HCl (Type I(a)), (b) Zr-UiO-67 AA and HCl (Type I(a)), and pore size distribution analysis of (c) Zr-UiO-66 AA and HCl, and (d) Zr-UiO-67 AA and HCl……...78
Figure 3.17. DLS measurements of (a) Zr-UiO-66-AA, and (b) Zr-UiO-67-AA……..79
Figure 3.18. PXRD diffractogram of Zr-UiO-66 (STEPOSOL)……79
Figure 3.19. Representation of the topical application of a drug loaded MOF to the eye for the mucoadhesion between mucins and the thiolated MOF, followed by drug release…….80
Figure 3.20. Periodic Acid–Schiff (PAS) colorimetric quantification results displaying the amount of mucins adhered to the MOFs……..81
Figure 3.21. Thiol quantification results for N-acetyl-L-cysteine standard, (a) UV-Vis spectra, (b) standard calibration curve, and (c) increasing concentration of N-acetyl-L-cysteine (from 10 to 60 μM) mixed with 5,5′-dithiobis-(2-nitrobenzoic acid) (DTNB) generates increasing concentrations of the yellow-coloured 2-nitro-5-thiobenzoic acid (TNB)……..83
Figure 3.22. UV-Vis spectra for Zr-UiO-66-$(SH)_2$-AA when using increasing concentrations of MOF, for thiol quantification……..……...83
Figure 3.23. UV-Vis spectra for Zr-UiO-67-$(SH)_2$-AA when using increasing concentrations of MOF, for thiol quantification……..……...84
Figure 3.24. Thiolated organic linkers of (a) Zr-UiO-66-$(SH)_2$, (b) Zr-UiO-67-$(SH)_2$, and (c) hexanuclear zirconium node of both MOFs……86
Figure 3.25. Representation of channels found in (a) Zr-UiO-66-$(SH)_2$, and (b) Zr-UiO-67-$(SH)_2$.....86
Figure 3.26. Representation of flurbiprofen drug loading and release from Zr-UiO-66-$(SH)_2$…88
Figure 3.27. PXRD diffractograms of (a) Zr-UiO-66-$(SH)_2$ AA and HCl prior to flurbiprofen (FBP) loading and after drug loading (FBP@MOF), (b) Zr-UiO-67-$(SH)_2$ AA and HCl prior to FBP loading and after drug loading, (c) Zr-UiO-66 AA and HCl prior to FBP loading and after drug loading, and (d) Zr-UiO-67 AA and HCl prior to FBP loading and after drug loading……...89

Figure A.1. PXRD patterns of (a) MOF-808 synthesized by STEPOSOL® MET-10U and washed with different organic solvents including butanol, isopropanol, ethanol 99%, DMF and toluene, (b) HKUST-1 synthesized by STEPOSOL® MET-10U and washed with different organic solvents including butanol, isopropanol, ethanol 99%, DMF and methanol, and (c) ZIF-8 synthesized by STEPOSOL® MET-10U and washed with different organic solvents including methanol, ethanol 95%, ethanol 99%, ethyl acetate and ethyl lactate……109
Figure A.2. PXRD patterns of (a) MOF-808 synthesized by STEPOSOL® MET-10U and by DMF, (b) NU-1000 synthesized by STEPOSOL® MET-10U and by DMF, (c) HKUST-1 synthesized by STEPOSOL® MET-10U and by DMF, and (d) ZIF-8 synthesized by STEPOSOL® MET-10U and by DMF……110
Figure A.3. N_2 adsorption-desorption isotherms and BET surface area values of (a) MOF-808 (Type I(b)) synthesized by STEPOSOL® MET-10U and washed with STEPOSOL® MET-10U and isopropanol (S_{BET} = 1720 m^2 g^{-1}) and by DMF and washed with DMF and isopropanol (S_{BET} = 1835 m^2 g^{-1}), (b) NU-1000 (Type IV(b)) synthesized by STEPOSOL® MET-10U and washed with DMF (S_{BET} = 1635 m^2 g^{-1}) and by DMF and washed with DMF (S_{BET} = 1865 m^2 g^{-1}), (c) HKUST-1 (Type I(a)) synthesized by STEPOSOL® MET-10U and washed with methanol (S_{BET} = 1860 m^2 g^{-1}) and by DMF and washed with methanol (S_{BET} = 1815 m^2 g^{-1}), and (d) ZIF-8 (Type I(a)) synthesized by STEPOSOL® MET-10U (solvothermal) and washed with ethanol 95% (S_{BET} = 670 m^2 g^{-1}), by DMF and washed with DMF (S_{BET} = 1435 m^2 g^{-1}) and by STEPOSOL® MET-10U (room temperature) and washed with methanol (S_{BET} = 1155 m^2 g^{-1})……...111
Figure A.4. N_2 adsorption-desorption isotherms and BET surface area values of MOF-808 (Type I(b)) (a) series 1 synthesized by DMF and washed with DMF and different organic solvents including butanol, isopropanol, ethanol 99%, DMF and toluene, (b) series 2 synthesized by DMF and washed directly with different organic solvents, (c) series 3 synthesized by STEPOSOL® MET-10U and washed with STEPOSOL® MET-10U and different organic solvents including butanol, isopropanol, ethanol 99%, DMF and toluene, and (d) series 4 synthesized by STEPOSOL® MET-10U and washed directly with different organic solvents……113
Figure A.5. N_2 adsorption-desorption isotherms and BET surface area values of HKUST-1 (Type I(a)) (a) series 1 synthesized by DMF and washed with DMF and different organic solvents including butanol, isopropanol, ethanol 99%, DMF and toluene, (b) series 2 synthesized by DMF and washed directly with different organic solvents, (c) series 3 synthesized by STEPOSOL®

MET-10U and washed with STEPOSOL® MET-10U and different organic solvents including butanol, isopropanol, ethanol 99%, DMF and toluene, and (d) series 4 synthesized by STEPOSOL® MET-10U and washed directly with different organic solvents……115
Figure A.6. N_2 adsorption-desorption isotherms and BET surface area values of ZIF-8 (Type I(a)) synthesized by STEPOSOL® MET-10U and washed with different organic solvents including methanol, ethanol 95%, ethanol 99%, and ethyl acetate……...116
Figure A.7. BET linear surface area plot of **(**a) MOF-808 synthesized by STEPOSOL® MET-10U and washed with STEPOSOL® MET-10U and isopropanol (BET plot taken from P/P_0 = 0.0048−0.050) and by DMF and washed with DMF and isopropanol (BET plot taken from P/P_0 = 0.0048−0.052), (b) NU-1000 synthesized by STEPOSOL® MET-10U and washed with DMF (BET plot taken from P/P_0 = 0.0048−0.049) and by DMF and washed with DMF (BET plot taken from P/P_0 = 0.0045−0.048), (c) HKUST-1 synthesized by STEPOSOL® MET-10U and washed with methanol (BET plot taken from P/P_0 = 0.0048−0.049) and by DMF and washed with methanol (BET plot taken from P/P_0 = 0.0045−0.048), and (d) ZIF-8 synthesized by STEPOSOL® MET-10U and washed with ethanol 95% (BET plot taken from P/P_0 = 0.0049−0.056) and by DMF and washed with DMF (BET plot taken from P/P_0 = 0.0049−0.055)……...117
Figure A.8. BET linear surface area plot of ZIF-8 synthesized by STEPOSOL® MET-10U at room temperature and washed with methanol (BET plot taken from P/P_0 = 0.0060−0.054)……118
Figure A.9. BET analysis based on the BET consistency criteria for MOF-808 (DMF) and MOF-808 (STEPOSOL), showing the differences in selecting a larger range (less linear) and narrower range (more linear) of relative pressure points. Green box = criteria is met, red box = criteria is not met……119
Figure A.10. Pore size distribution analysis performed by non-local density functional theory (NLDFT) of (a) MOF-808 synthesized by STEPOSOL® MET-10U and washed with STEPOSOL® MET-10U and isopropanol (pore diameter = 18.4 Å), (b) NU-1000 synthesized by STEPOSOL® MET-10U and washed with DMF (pore diameter = 29.5 Å), (c) HKUST-1 synthesized by STEPOSOL® MET-10U and washed with methanol (pore diameter = 12.4 Å), and (d) ZIF-8 synthesized by STEPOSOL® MET-10U and washed with ethanol 95% (pore diameter = 15.2 Å)……120

Figure A.11. Pore size distribution analysis performed by non-local density functional theory (NLDFT) of ZIF-8 synthesized by STEPOSOL® MET-10U at room temperature and washed with methanol (pore diameter = 15.2 Å)……...121
Figure A.12. Structure of ZIF-8 (STEPOSOL), showing one view of the MOF along the *b*-axis. Zn = grey, N = blue, C = black……..124
Figure A.13. Structure of ZIF-8 (STEPOSOL), showing another view of the MOF through the plane (101). Zn = grey, N = blue, C = black……..124
Figure A.14. Structure of ZIF-8 (DMF), showing an alternative view of the MOF. Zn = grey, N = blue, C = black……..125
Figure A.15. Reaction scheme for the synthesis of 2,5-dimercapto-1,4-benzenedicarboxylic acid (H_2DMBD)……...126
Figure A.16. ^{1}H-NMR spectrum of 2,5-bis(dimethylthiocarbamoyloxy)terephthalic acid diethyl ester……..126
Figure A.17. ^{1}H-NMR spectrum of 2,5-bis(dimethylthiocarbamoylsulfanyl)terephthalic acid diethyl ester……..127
Figure A.18. ^{1}H-NMR spectrum of 2,5-dimercapto-1,4-benzenedicarboxylic acid (H_2DMBD)……...127
Figure A.19. Mucoadhesion of the thiolated and control Zr-UiO-66 assessed by fluorescence spectroscopy…….128
Figure A.20. Mucoadhesion of the thiolated and control Zr-UiO-67 assessed by fluorescence spectroscopy…….128
Figure A.21. ICP-MS calibration curve for the concentration of zirconium……129
Figure A.22. ICP-MS calibration curve for the concentration of sulfur……..129
Figure A.23. HPLC chromatograms for flurbiprofen drug loading, (a) Zr-UiO-66-$(SH)_2$-AA, and (b) Zr-UiO-67-$(SH)_2$-AA, and release experiments, (c) Zr-UiO-66-$(SH)_2$-AA, and (d) Zr-UiO-67-$(SH)_2$-AA…….130
Figure A.24. HPLC chromatograms for flurbiprofen drug loading, (a) Zr-UiO-66-$(SH)_2$-HCl, and (b) Zr-UiO-67-$(SH)_2$-HCl, and release experiments, (c) Zr-UiO-66-$(SH)_2$-HCl and Zr-UiO-67-$(SH)_2$-HCl……131
Figure A.25. HPLC chromatograms for flurbiprofen drug loading of (a) Zr-UiO-66-AA, and (b) Zr-UiO-66-HCl, and release experiments, (c) Zr-UiO-66-AA and Zr-UiO-66-HCl, and for drug

loading of (d) Zr-UiO-67-AA, and (e) Zr-UiO-67-HCl, and release experiments, (f) Zr-UiO-67-AA and Zr-UiO-67-HCl...……132
Figure A.26. HPLC chromatograms to generate a calibration curve for the release of flurbiprofen……..133

List of Tables

Table 2.1. Percent yield of MOFs post-activation……..43

Table 2.2. BET surface areas, pore volumes and percent yield (post-activation) for MOFs synthesized using DMF and STEPOSOL® MET-10U……45

Table 2.3. TGA $\%_{\text{Metal Oxide}}$ and $\%_{\text{Metal}}$ for MOF samples prepared by STEPOSOL® MET-10U and DMF (in the presence of dehydration, TGA $\%_{\text{Metal Oxide}}$ and $\%_{\text{Metal}}$ residues have been corrected)……...46

Table 2.4. TGA $\%_{\text{Metal Oxide}}$ and $\%_{\text{Metal}}$ for ZIF-8 prepared by STEPOSOL® MET-10U at room temperature……47

Table 3.1. Expected and experimental moles of thiol for Zr-UiO-66-$(SH)_2$-AA calculated using the absorbance of TNB at 412 nm……...……84

Table 3.2. Expected and experimental moles of thiol for Zr-UiO-67-$(SH)_2$-AA calculated using the absorbance of TNB at 412 nm……..84

Table 3.3. Zirconium leaching concentrations from the metal node of the thiolated MOFs…….85

Table 3.4. Sulfur leaching concentrations from the organic linkers of the thiolated MOFs……85

Table 3.5. Flurbiprofen drug loading and release results in control and thiolated MOFs, with associated BET surface areas…..……...88

Table A.1. Costs of the solvents used for the reactions and washings of various MOFs……...121

Table A.2. Cost analysis of MOF-808 samples synthesized using DMF and STEPOSOL® MET-10U……...121

Table A.3. Cost analysis of NU-1000 samples synthesized using DMF and STEPOSOL® MET-10U.……..122

Table A.4. Cost analysis of HKUST-1 samples synthesized using DMF and STEPOSOL® MET-10U.……...……122

Table A.5. Cost analysis of ZIF-8 samples synthesized using DMF and STEPOSOL® MET-10U……...122

Table A.6. Crystallographic data for two single crystals of ZIF-8 (STEPOSOL) and one single crystal of ZIF-8 (DMF)……123

Table A.7. Concentrations of flurbiprofen and areas obtained by HPLC chromatograms…….....133

List of Abbreviations

1-MCP	1-methylcyclopropene
2-mIm	2-methylimidazole
BET	Brunauer-Emmett-Teller
CCDC	Cambridge Crystallographic Data Centre
$CDCl_3$	deuterated chloroform
CIF	crystallographic information file
CO_2	carbon dioxide
COX	cyclooxygenase
csq	MOF topology
DCl	deuterium chloride
DEF	*N,N*-diethylformamide
DLS	dynamic light scattering
DMA	*N,N*-dimethylacetamide
DMF	*N,N*-dimethylformamide
DMSO	dimethyl sulfoxide
DMSO-d_6	deuterated dimethyl sulfoxide
D_2O	deuterium oxide
DRIFTS	diffuse reflectance infrared Fourier transform spectroscopy
D_2SO_4	deuterated sulfuric acid
DTNB	5,5′-dithiobis-(2-nitrobenzoic acid)
EDS	energy dispersive X-ray spectroscopy
FBP	flurbiprofen
fcu	face-centered cubic topology
GalNAc	*N*-acetylgalactosamine
H_2BDC	1,4-benzenedicarboxylic acid
H_2BPDC	biphenyl-4,4′-dicarboxylic acid
H_3BTC	1,3,5-benzenetricarboxylic acid
HCl	hydrochloric acid
H_2DMBD	2,5-dimercapto-1,4-benzenedicarboxylic acid
H_2DMBPD	3,3′-dimercaptobiphenyl-4,4′-dicarboxylic acid
HNO_3	nitric acid
HPLC	high performance liquid chromatography
H_2SO_4	sulfuric acid
H_4TBAPy	1,3,6,8-tetrakis(*p*-benzoic acid)pyrene
ICP-MS	inductively coupled plasma–mass spectrometry
IUPAC	International Union of Pure and Applied Chemistry
KBr	potassium bromide
LD	lethal dose
LVP	low vapor pressure

MOF	metal–organic framework
N_2	nitrogen gas
NLDFT	non-local density functional theory
NMR	nuclear magnetic resonance spectroscopy
NSAID	non-steroidal anti-inflammatory drug
PAS	Periodic Acid–Schiff
PG	prostaglandin
PPE	personal protective equipment
PSM	post-synthetic modification
PTFE	polytetrafluoroethylene
PXRD	powder X-ray diffraction
RCSR	Reticular Chemistry Structure Resource
REACH	Registration, Evaluation, Authorisation and Restriction of Chemicals
SALE	solvent-assisted linker exchange
SALI	solvent-assisted ligand incorporation
SAXS	small angle X-ray scattering
SBU	secondary building unit
$scCO_2$	supercritical carbon dioxide
SCXRD	single crystal X-ray diffraction
SEM	scanning electron microscopy
sod	sodalite topology
spn	spinel topology
tbo	twisted boracite topology
TGA	thermogravimetric analysis
TMS	tetramethylsilane
TNB	2-nitro-5-thiobenzoic acid
UV	ultraviolet
UV-Vis	ultraviolet-visible spectroscopy
VOC	volatile organic compound
VT-PXRD	variable temperature powder X-ray diffraction

Chapter 1

Introduction

1.1. Brief History and Definition of Metal–Organic Frameworks (MOFs)

The field of coordination chemistry, coordination polymers and metal–organic frameworks (MOFs) has evolved during the past 30 years to be one of the most explored areas of materials science. The first MOF-like materials were reported in Japan in 1959, however initial publications did not mention porosity.[1] Shortly after, Tomic reported the synthesis of coordination polymers using di- and tetratopic carboxylic acid linkers coordinated to metals with differing valency (di-, tri-, or tetravalent).[2] The field began to grow following fundamental contributions by Hoskins and Robson in the early 1990s, who reported scaffolding-like materials, and discussed the potential for porosity, and potential applications they could be useful for – predicting a great amount of the future of the field of MOFs before they were even called MOFs.[3] Following significant developments from Yaghi,[4-6] Kitagawa,[7] and Férey,[8] Yaghi coined the term metal–organic frameworks to describe these network structures, and specifically to describe a copper-4,4′-bipyridyl complex.[4] Moreover, the first example of a MOF, MOF-5, with permanent porosity post-drying and activation was then reported and continues to be one of the most studied structures.[6] Since the first reports of these materials comprised of inorganic and organic building blocks (secondary building units (SBUs)), MOFs have garnered significant interest in areas of materials chemistry.

As specified by the International Union of Pure and Applied Chemistry (IUPAC), the definition of a MOF states that the material can be two-dimensional or three-dimensional, can be crystalline (long range order) or amorphous (short range order) – the former being more common – and most importantly, that the coordination network must be open and have potential for voids or pores, hereby differing from coordination polymers.[9, 10] MOFs are hybrid porous materials comprising highly versatile functional inorganic and organic building units (Figure 1.1). The inorganic building units, otherwise known as metal nodes, encompass metal ions, chains or clusters, from the *s*-,[11, 12] *p*-,[13, 14] *d*-,[15-18] and *f*-block[19, 20] in the periodic table. On the other hand, the organic building units, also known as organic ligands or linkers, are multidentate/multitopic (di-, tri-, tetratopic) molecules that can bond the inorganic building units together. In fact, the

organic linkers come in many different shapes and sizes, and most often involve carboxylic acid containing linkers, or nitrogen containing linkers, amongst others. Through the combination of metal cations and organic linkers, MOFs are highly tunable in the sense of their geometry, connectivity and functionality allowing for the construction of materials with different structures and functionalities. The key features in addition to their modular and versatile nature include well-defined pore apertures, and the possibility to tailor the chemical identity and functionality of the metal nodes and organic linkers. Other properties which can be fine-tuned include pore size,[21] pore shape,[22] node connectivity[23-25] (i.e., the presence or absence of open metal sites), surface area, density, and stability.[26] The remarkable designability of MOFs has enabled their study in areas such as gas capture and storage,[27, 28] catalysis,[29-32] wastewater remediation,[33-35] chemical separations,[36-38] solar fuels generation,[39, 40] and drug delivery,[41, 42] amongst others.

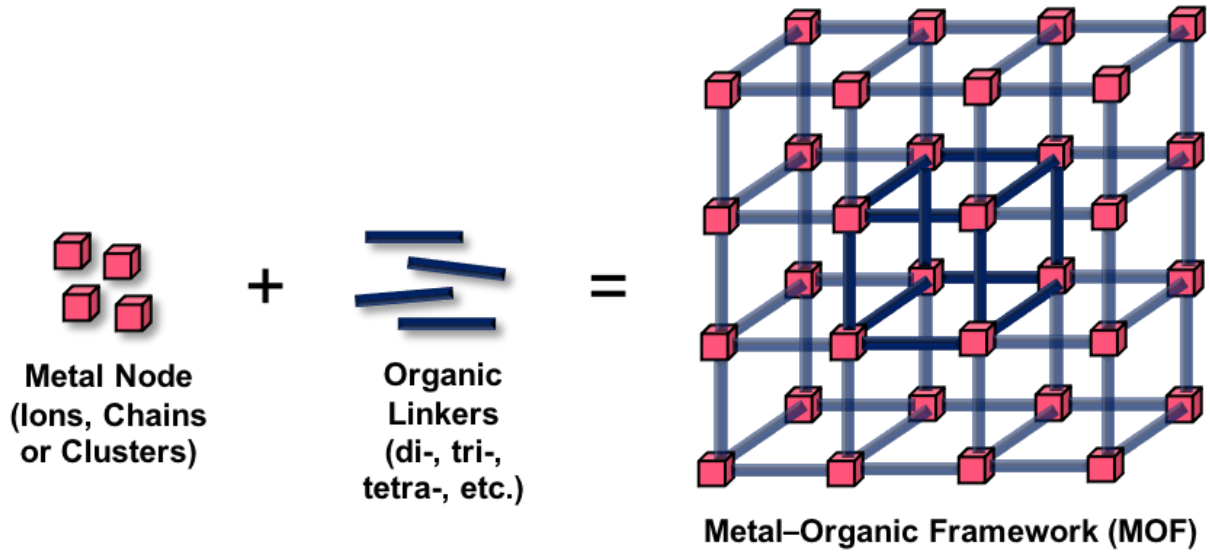

Figure 1.1. Schematic representation of assembling a metal–organic framework (MOF).

1.2. Fundamental Principles and Properties of MOFs

In synthesis, researchers are constantly looking for new building blocks and to make new materials with intricate topologies. The beauty of MOFs lies in the possibility of designing the desired network structure, hereby considering the topology, the vertices and edges of the topology, and how coordination chemistry can be used to design the network. As there are many ways to assemble a MOF, it is crucial to select metals with the correct coordination geometry, and the correct organic linkers with the right connectivity and geometry, when designing MOFs.[43]

1.2.1. Reticular Chemistry

Introduced by renowned MOF chemists, Yaghi and O'Keeffe, reticular chemistry is the foundation of MOF synthesis guided by the design and assembly of building blocks into ordered network materials, through predetermined net structures.[44-46] In principle, reticular chemistry is a useful approach to create an array of MOFs with desirable properties including, but not limited to, high surface area, tailorable composition and structure, and stability. As such, coordination chemistry plays a key role in the careful selection of inorganic and organic building blocks when generating predesigned network structures. Moreover, as the geometrical characteristics and connectivity of building blocks are the main contributors to the overall net, it is also possible to create the same net with a variety of building blocks.[47]

1.2.2. Topology

The underlying connectivity, encompassing the arrangement of vertices and edges of structures, is best represented by a branch of mathematics known as topology. In the field of MOF chemistry, polyatomic groups (metal nodes and linkers) are the vertices (points) and edges (links) of the net, and the representative periodic net of structures is identified and classified with a nomenclature-like descriptor denoted by a bolded three-letter code (i.e., **fcu** (face-centered cubic)), and collected in the Reticular Chemistry Structure Resource (RCSR) database.[47] Moreover, a topology is unaffected by bond deformations including stretching, bending and squeezing. Therefore, the net topology which is mainly affected by the connectivity and site symmetry of the metal node, provides insight into the structural features of the MOF and enables the design of MOF structures with new topologies.[23]

1.2.3. Characteristics and Properties of MOFs

As the field of MOFs continues to grow, MOFs continuously offer unique structural properties and possess attractive characteristics in contrast to other porous materials. Beginning with their permanent porosity, structural tunability and stability, MOFs have demonstrated promising properties including ultrahigh porosity with up to 90% free volume,[48] high surface areas reaching up to 7800 $m^2 g^{-1}$,[49, 50] and densities reaching as low as 0.124 g cm^{-3},[51] hereby making them distinguishable from related materials including zeolites and one-dimensional coordination polymers.[52, 53]

1.3. UiO-66, UiO-67, and Isostructural MOFs

Great emphasis is placed upon tetravalent zirconium (Zr(IV)) MOFs, due to their high surface areas, and high mechanical, thermal and chemical stability that is attributed to their high metal-ligand bond strengths.[54-58] One of the most well studied Zr-based MOF was first discovered and reported in 2008, at the University of Oslo (UiO), with the name UiO-66.[59] Later, an analogue of UiO-66, reported as UiO-67, was prepared by changing the length of the organic linker.[60] Over the years and to this day, the abovementioned MOFs generate exceptional interest in the field of MOF chemistry, due to their promising characteristics and potential applications.

1.3.1. Zr-UiO-66

The porous and crystalline UiO-66 (Figure 1.2) is a prototypical MOF that has displayed notable stability, making it useful for an array of applications. With its ease of being synthesized reproducibly in the laboratory most commonly by *de novo* solvothermal synthesis, it is produced from mixing Zr(IV) salts and 1,4-benzenedicarboxylic acid (H_2BDC), mainly in DMF.[61, 62] Comprised of cationic hexanuclear zirconium oxide clusters ($[Zr_6O_4(OH)_4]^{12+}$) and linear ditopic linkers, the MOF has an **fcu** topology in accordance with the RCSR classification system. As with the **fcu** topology, UiO-66 is described as having a connectivity of 12, which entails that the 12-connected metal node arising from the hexanuclear cluster is bridged to 12 other clusters through BDC linkers.[44] In the metal cluster, the bridging hydroxide (μ_3-OH) or oxide (μ_3-O_2) is bonded to three Zr(IV) ions, and it is Zr(IV)-O bonds between the cluster and organic linkers that is the foundation of the increased stability of the material. Determined by the crystal structure, UiO-66 has a face-centered cubic unit cell system and crystallizes in the $Fm\bar{3}m$ space group.[59, 63] The structure of UiO-66 contains two distinct types of cavities within the structure, specifically, octahedral and tetrahedral cavities. The octahedral cavities have an internal diameter of 12 Å, whereas the tetrahedral cavities have an internal diameter of 7.5 Å, and both cavities have pore apertures of 6 Å.[64] Due to its high stability in combination with its porosity, UiO-66 has a theoretical pore volume of 0.77 $cm^3\ g^{-1}$, and a surface area of 1160 $m^2\ g^{-1}$.[65]

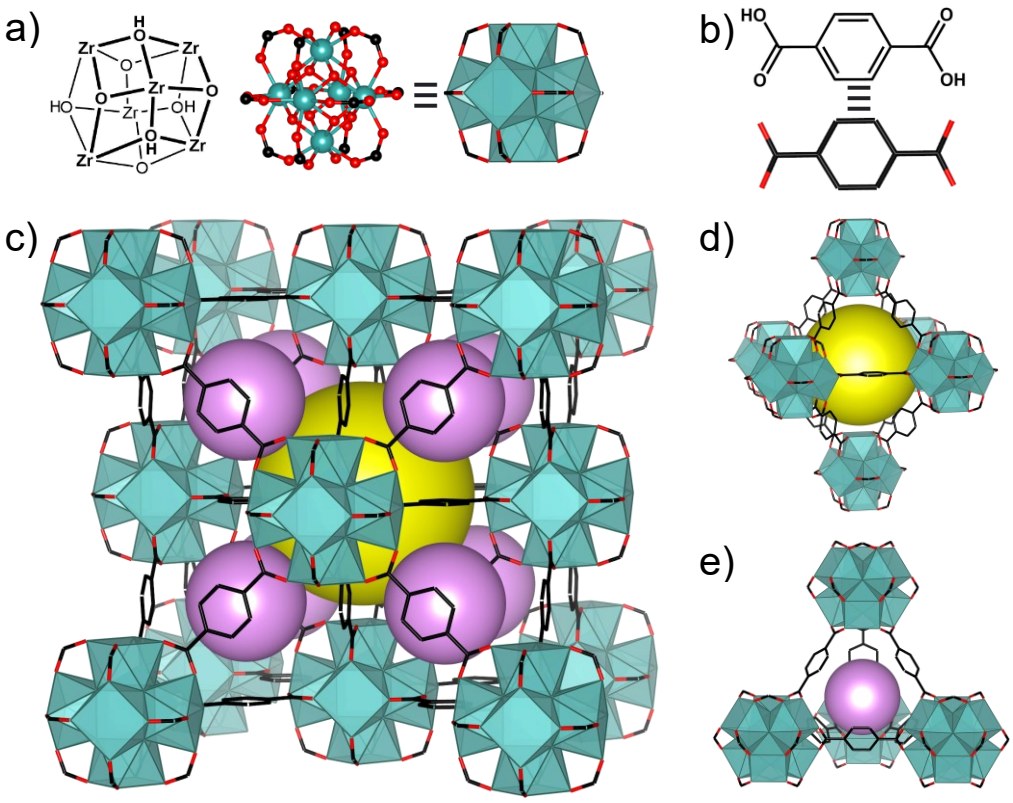

Figure 1.2. Structure of Zr-UiO-66. (a) Zr-based hexanuclear cluster, (b) linear ditopic 1,4-benzenedicarboxylic acid (H_2BDC) organic linkers, and (c) Zr-UiO-66 with **fcu** topology. Two types of cages exist in the net, (d) the octahedral cage (yellow sphere), and (e) the tetrahedral cages (purple spheres).

As for the MOF synthesis, the solvothermal procedure to obtain UiO-66 involves the usage of a modulator in the reaction mixture that can affect the structural properties of the material, relating to the presence of defects, the crystallinity, and the crystal size.[66, 67] Modulators, which direct the crystallinity and slow the growth process allow for a more perfect MOF material, and have been studied extensively for UiO-66.[68] Particularly, hydrochloric acid (HCl) is a modulator used for the synthesis of UiO-66 that acts by protonating carboxylates that get deprotonated by the reaction solvent, hereby making the organic linker less available for coordination. Due to this, HCl behaves differently than other modulators that have –COOH functional groups (i.e., acetic acid) and that compete with the organic linker. In this instance, HCl protonates the linker to slow down the growth, and not by competing with ligand, giving rise to more defective structures and higher hydrophilicity of the MOF,[69] with up to four missing linkers per node (Figure 1.3), which increases the average size of the tetrahedral cavity to 11.5 Å, enabling larger surface areas.[61]

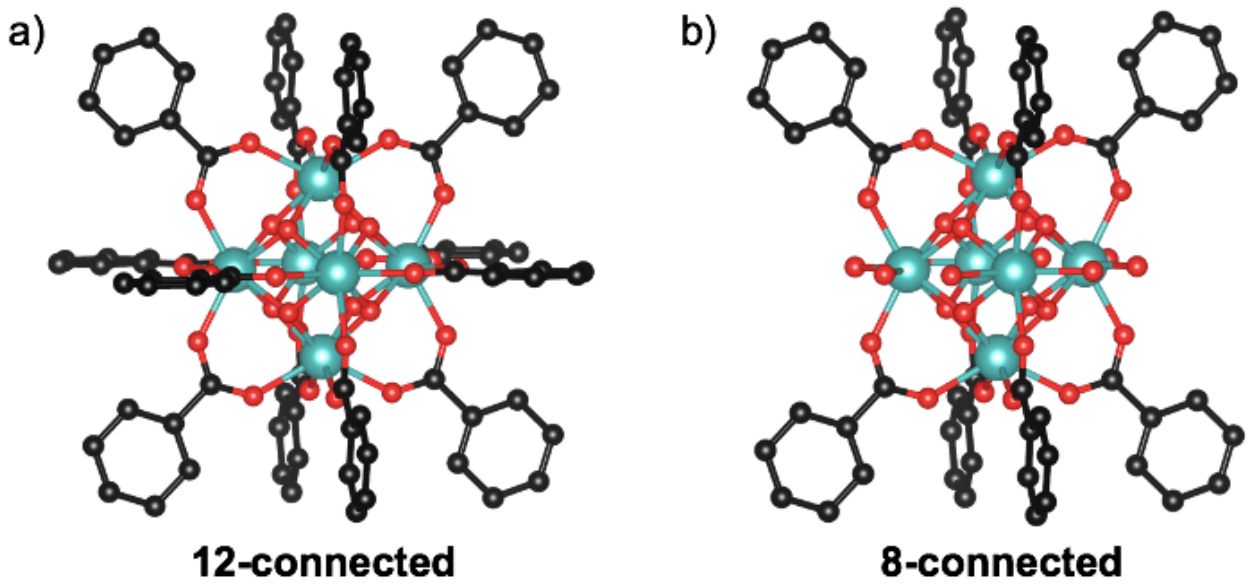

Figure 1.3. Connectivity of Zr_6 clusters. (a) 12-connected metal node, and (b) 8-connected metal node due to missing organic linkers, arising from defects in the structure. Zr = teal, C = black, O = red.

Owing to its promising characteristics, UiO-66 has been studied extensively.[56, 61, 68] In the realm of reticular chemistry, functionalized UiO-66 analogues have been synthesized using a variety of functional groups on the organic linkers, including, but not limited to, $–NH_2$, –Br, $–NO_2$, and –SH, which give rise to isoreticular structures.[70, 71] These structures exhibit the same topology, however the building units (metal node or organic linkers) can change. As such, UiO-66 has also been synthesized with various tetravalent metals other than Zr(IV),[61] including Hf(IV)[72] and Ce(IV),[73, 74] with H_2BDC linkers, and more recently with trivalent metals such as lanthanoids.[75]

1.3.2. Zr-UiO-67

UiO-67 (Figure 1.4) is another well-recognized MOF in the field of materials chemistry. Also having a scalable and reproducible synthesis like UiO-66 using solvothermal conditions, it is comprised of Zr_6-clusters, yet bridged by a longer linear ditopic organic linker, biphenyl-4,4′-dicarboxylic acid (H_2BPDC).[60] Due to its construction using a longer organic linker, UiO-67 features larger pores and higher surface area. The octahedral cavities have an internal diameter of 23 Å, while the tetrahedral cavities have an internal diameter of 11.5 Å, and both cavities have pore apertures of 8 Å.[61] The larger pore size distribution and pore volume (0.94 $cm^3\ g^{-1}$)[76] in UiO-67 affords a higher surface area of 2500 $m^2\ g^{-1}$.[61] The MOF also exhibits **fcu** topology with the

face-centered cubic unit cell system and crystallizes in the cubic $Fm\bar{3}m$ space group.[63] As a result of its **fcu** topology, UiO-67 also has a 12-connected metal node, and therefore has the same coordination chemistry as UiO-66.

This zirconium-based MOF, UiO-67, has been established as highly stable with remarkable thermal stability and chemical resistance in the presence of different acidic or basic solvents.[64] Similarly to UiO-66, UiO-67 also has a series of isoreticular structures, either by changing the metal node or organic linker, such as tetravalent metals including Hf(IV)[77] or trivalent metals[78] with H_2BPDC, and by using organic linkers with different functional groups such as $–NH_2$, $–NO_2$, and –SH.[61, 79]

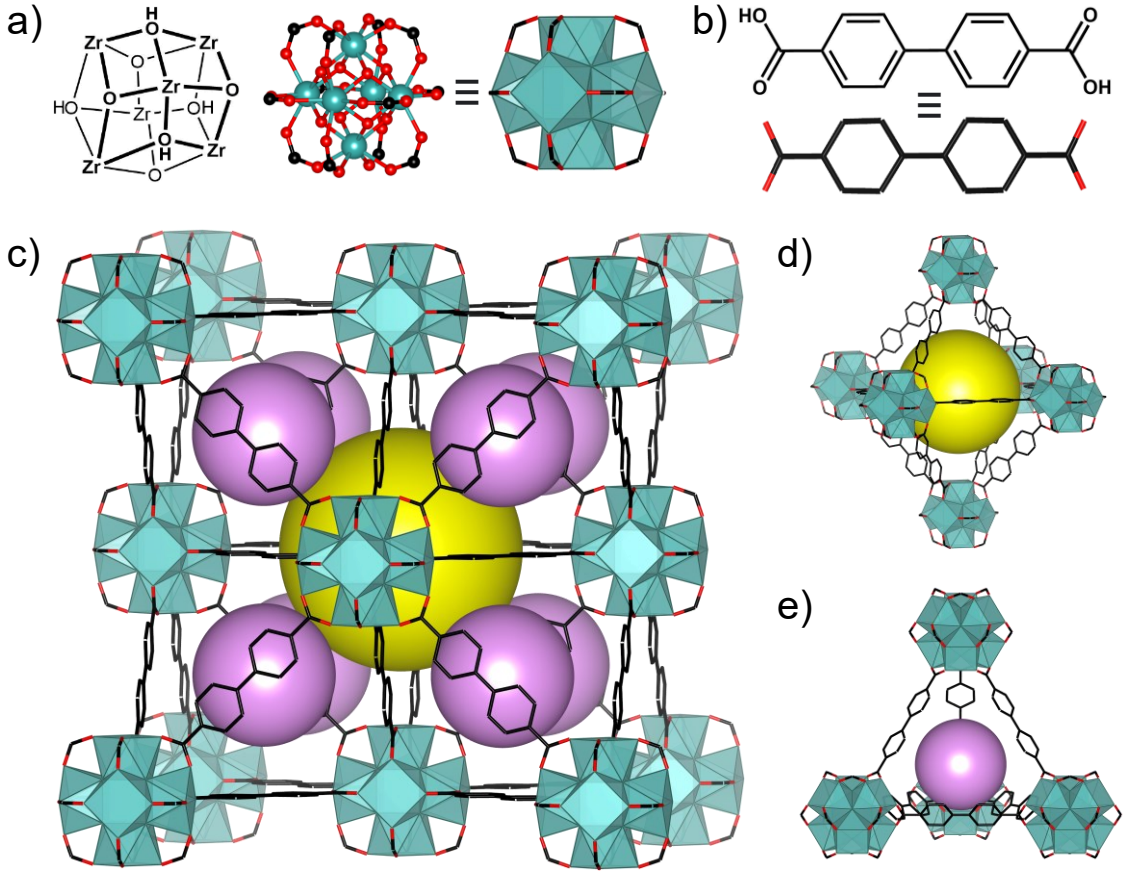

Figure 1.4. Structure of Zr-UiO-67. (a) Zr-based hexanuclear cluster, (b) linear ditopic biphenyl-4,4′-dicarboxylic acid (H_2BPDC) organic linkers, and (c) Zr-UiO-67 with **fcu** topology. Two types of cages exist in the net, (d) the octahedral cage (yellow sphere), and (e) the tetrahedral cages (purple spheres).

1.3.3. Isostructural MOFs

Two MOFs are said to be isostructural when they have a similar crystal structure, however their unit cell dimensions are different, due to differences in chemical composition. As such, Zr-UiO-66 and Zr-UiO-67 are an isostructural pair of MOFs, where the unit cell for Zr-UiO-67 is larger than Zr-UiO-66, in correspondence to the different organic linker building unit involved in its structure.[80]

1.3.4. Thiol-Functionalized MOFs

Thiol (–SH) groups offer intriguing reactivity and properties for functionalizing MOFs, particularly when they are accessible within the network material.[81] The functionalization of MOFs with thiol groups and utilization of these MOFs has been of growing interest in the literature.[81, 82] Within the UiO platform, both Zr-UiO-66 and Zr-UiO-67 have been synthesized with thiol-functionalized linkers, 2,5-dimercapto-1,4-benzenedicarboxylic acid (H_2DMBD) for Zr-UiO-66-$(SH)_2$[71, 82] and 3,3′-dimercaptobiphenyl-4,4′-dicarboxylic acid (H_2DMBPD) for Zr-UiO-67-$(SH)_2$.[79] In these derivatives and in both thiol-functionalized linkers, there is the presence of hard carboxyl and soft sulfur groups, where the carboxyl groups on the linker preferentially bond to hard metal centers such as Zr(IV).[79] The thiol-functionalized MOFs have been studied for their use in environmental applications including the effective removal and uptake of toxic mercury ions from water,[71, 81, 83] however have not been explored for use in drug delivery applications.

1.4. Overview of Methods in MOF Synthesis

1.4.1. MOF Synthesis

In MOF synthesis, several synthetic techniques can be used to produce MOFs including solvothermal,[84] hydrothermal,[4] electrochemical,[85, 86] mechanochemical,[87, 88] sonochemical,[89] and microwave-assisted synthesis,[90] or layer-by-layer deposition techniques for the fabrication of MOF thin-films,[91] amongst others. Most commonly, *de novo* solvothermal synthetic methods are used, which entails mixing the metal salt and organic linker precursors with a high boiling point solvent, i.e., *N,N*-dimethylformamide (DMF), *N,N* -diethylformamide (DEF) or dimethyl sulfoxide (DMSO), inside a vessel, i.e., jar or screw-top vial. The reaction mixture is then heated on a hot-plate or in an oven at a temperature from 80 to 150 °C, with times ranging from hours to days, to produce the final network structure. Several of the reaction parameters to consider when carrying

out solvothermal synthesis include (i) time, (ii) temperature, (iii) reagent concentration, (iv) solvent polarity, (v) solvent volume, (vi) pH, (vii) presence of stirring, and (viii) the nature of materials used.[84, 92] As a result of the reaction conditions influencing the outcome of the product, the parameters can be optimized in order to obtain the formation of a MOF product with desired network structure and topology, phase purity, particle size and morphology. The role of the solvent in MOF synthesis can also influence the outcome. Reaction solvents have multiple purposes including the formation of a coordination environment for the assembly of the structure and behaviour of the metal and linker precursors. Solvents can also play a role as structure directing agents or for templating, in addition to providing a medium for crystal growth as well as solubilizing the starting materials and increasing the basicity for deprotonation of carboxylic acid linkers.[93]

In general, the purpose of heating the reaction mixture is multifold. Firstly, the reaction mixture is heated to dissolve the metal salt and organic linker, and secondly, the mixture is heated to provide enough thermodynamic energy for the metal and linker bonds to form. Overall, the synthesis of MOFs must be a dynamic process. Since MOFs are large three-dimensional and ordered crystalline materials, dynamic bonds are essential for the assembly of the network structure. In this dynamic process, the metal node and organic linker must be able to form a bond, but also subsequently break a bond, and reform, to achieve three-dimensional and ordered structural propagation.[94] In some cases, non-structural monotopic ligands, otherwise known as modulators, are utilized to aid in this dynamic process, and to help prevent rapid precipitation of amorphous material.[66, 95] A modulator (i.e., benzoic acid, acetic acid, hydrochloric acid, and formic acid) (Figure 1.5) is known to compete with the structural organic linker for bonding to the metal node, hereby facilitating a slower formation of structural bonds. Metal-ligand bonds dictate the stability of the MOF thus, if bonding errors occur, they can lead to an amorphous or disordered material (premature precipitation/structure termination), therefore it is necessary to be able to break those bonds and for new ones to fix the errors.

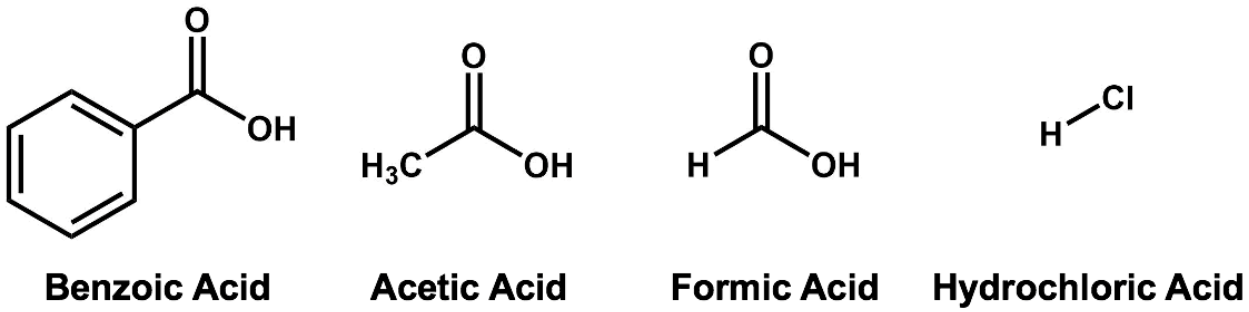

Figure 1.5. Chemical structures of different modulators used in MOF synthesis.

Challenges can arise in MOF synthesis since the mixture of metal node and organic linker precursors have the potential to make multiple network structures, which then require controlling the kinetics and thermodynamics of the reaction to generate the desired network structure. Other than synthesizing a MOF *de novo* to obtain complex structures, another useful approach is to use post-synthetic modification (PSM).[96, 97] In this strategy, it involves synthesizing a MOF with the desired network structure, and then utilizing post-synthetic methodologies to convert the MOF to different forms. For example, transmetallation can be used to exchange the metal nodes in the material for different nodes with different properties, i.e., redox properties or luminescence.[98] As well, the organic linker can be exchanged in the MOF using solvent-assisted linker exchange (SALE)[99] to give new organic linkers with new and different functionalities. Then, it is also possible to perform various and different node and linker based post-synthesis modifications, to decorate the node of a MOF (instead of replacing the node), either with metal ions or atomically precise metal clusters, or organic linkers at open metal sites with solvent-assisted ligand incorporation (SALI).[100] Modifying the organic linker post-synthetically is also possible by performing organic chemistry on the linker in the presence of active functional groups that can be modified, or if the organic linker itself has moieties that can coordinate metals, PSM can be done to the linker to incorporate additional metals, in addition to the metal nodes.

1.4.2. Green Chemistry

The world is faced with significant global environmental issues including, but not limited to, overpopulation, climate change, waste disposal, natural resource depletion, and air, water and soil pollution.[101-104] Our environment has been subjected to years of urbanization[105] and industrialization[106] presenting long term, and in some cases irreversible, effects that need to be addressed.[107] Towards the abatement of some of these critical issues, a relatively new field of

chemistry, green chemistry, has gained tremendous momentum as it embraces and implements the invention and design of chemical products and processes that mitigate and/or eliminate the use and generation of hazardous substances.[108]

1.4.2.1. Principles of Green Chemistry

The field of green chemistry, governed by twelve principles, seeks to provide guidelines for developing materials, processes and systems that mitigate or eliminate the use and generation of hazardous substances.[109, 110] Among the various materials that have been studied in the field of green chemistry are MOFs, including green synthesis and applications. The practice of green chemistry or sustainability at the molecular level follows twelve principles (Figure 1.6), including (1) waste prevention, (2) atom economy, (3) less hazardous chemical synthesis, (4) designing safer chemicals, (5) safer solvents and auxiliaries, (6) design for energy efficiency, (7) use of renewable feedstocks, (8) reduce derivatives, (9) catalysis, (10) design for degradation, (11) real-time pollution prevention, and (12) safer chemistry for accident prevention.

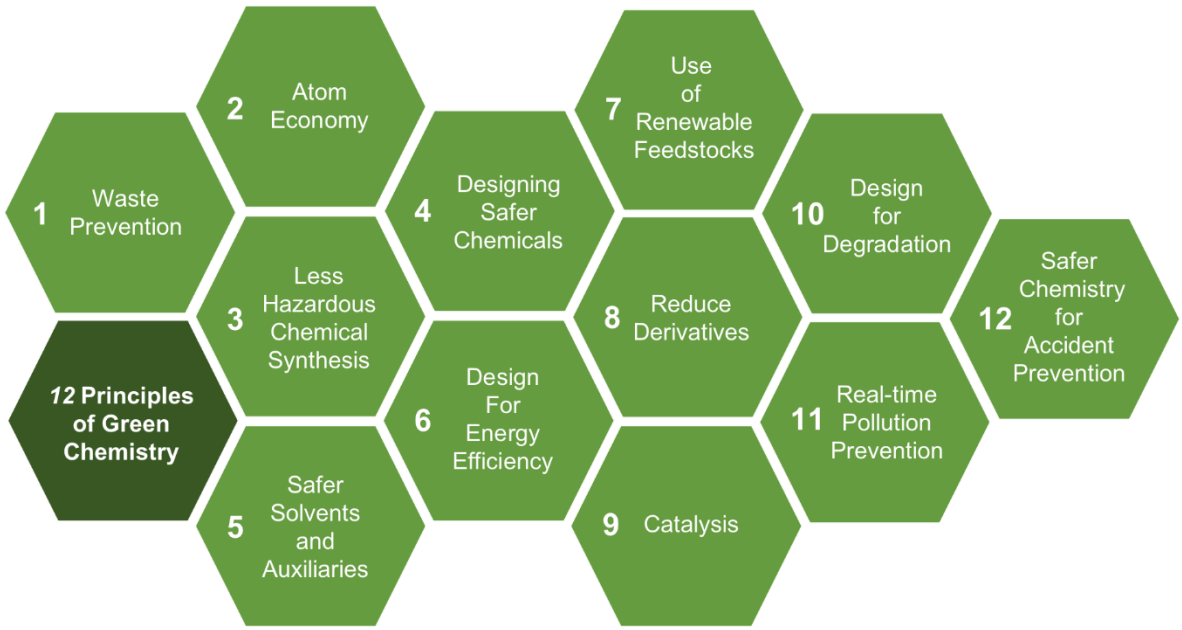

Figure 1.6. The twelve principles of green chemistry as a guide for sustainable chemistry, to design and improve materials, processes, synthesis and systems.

1.4.2.2. Green MOF Synthesis

Green synthetic procedures have recently been a prominent theme in materials research, and mitigating impact to the environment is ideal for the current state of our society. In addition to minimizing our carbon footprint and being conscientious about waste generation in our daily lives, as scientists, we can work towards implementing the twelve principles of green chemistry in both research and industrial laboratories. The synthesis of MOFs is largely performed under solvothermal conditions in high boiling point, polar solvents such as *N,N*-dimethylformamide and *N,N*-diethylformamide.[84, 92] Although recycling and the reuse of these solvents is possible in some cases,[111] there is still a push to reduce or eliminate the use of these hazardous organic compounds in both research and industrial laboratories.[112, 113] This push towards the reduction or elimination of *N,N*-dimethylformamide in particular can be seen by its inclusion on hazardous/priority substances lists created by the United States Clean Air Act,[114] the European Chemicals Agency,[115] and the Canadian Environmental Protection Act.[116] The need to reduce or eliminate the use of these hazardous solvents is also reflected in the twelve principles of green chemistry.[108] As such, there are significant research efforts dedicated to finding suitable replacement solvents for the synthesis of MOFs.[117-119] In addition to replacing hazardous solvents, green synthesis methods including thermochemical,[120] mechanochemical,[121] and aging[122] processes have been developed to eliminate or significantly reduce the amount of solvent required for MOF synthesis, whereas other methods such as electrochemical,[123] sonochemical[124] and microwave-assisted heating[125] seek to lower the energy input required for MOF synthesis. While the development of greener synthetic methods and processes is important to the field of MOF chemistry (as well as many other fields of chemistry),[126] so too is the implementation of MOFs in green applications. The unique and tunable properties of MOFs make them potential candidates for a wide range of environmentally conscious or "green" applications such as hydrogen storage,[127] carbon capture,[128] air pollution remediation,[129] and water pollution remediation,[130] and the ultimate goal should be to bridge green MOF synthesis with green applications to achieve the greatest positive environmental impact of these materials.

1.4.2.3. Green Solvent: STEPOSOL® MET-10U

STEPOSOL® MET-10U by Stepan®, otherwise known as *N,N*-dimethyl-9-decenamide, is a biodegradable (bioderived) solvent. Synthesized in collaboration with Elevance Renewable

Sciences®, STEPOSOL® MET-10U is derived from biorenewable resources and feedstocks such as plant oils and palm kernel oils and it is produced by olefin metathesis.[131, 132] The industrial process required for this metathesis technology involves low-pressure and low-temperature parameters along with a selective catalyst - thus requiring less energy consumption, source pollution and producing a smaller carbon footprint overall. The environmentally friendly solvent has structural similarity to DMF (Figure 1.7). STEPOSOL® MET-10U is a disubstituted amide composed of an unsaturated (10 carbon chain length methyl ester) hydrocarbon chain with a terminal alkene functionality. In addition to having a boiling point of 297 °C, the Hansen solubility parameter space of STEPOSOL® MET-10U encompasses that of hydrocarbons, esters, glycol ethers, and alcohols.[133] Herein, STEPOSOL® MET-10U plays a vital role as a potential green solvent in the synthesis of MOFs.[134]

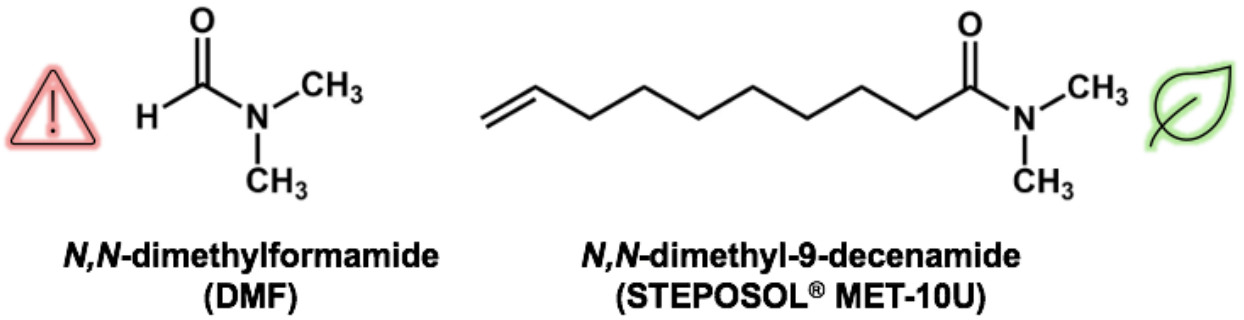

Figure 1.7. Chemical structures of a toxic solvent, *N,N*-dimethylformamide (DMF), and an environmentally friendly solvent, *N,N*-dimethyl-9-decenamide (STEPOSOL® MET-10U).

1.4.3. MOF Activation

After MOF synthesis and the formation of the targeted structure, the next step involves a process known as activation, which is essential for accessing the void space of MOFs. Generally, when MOFs are synthesized, the pores of the materials are filled with different guest molecules, which include leftover metal precursors, leftover solvents, leftover organic linkers, as well as other impurities or by-products.[135] Herein, in order to use the materials for applications, it is required to access the pores and attain the maximum potential porosity of the materials. Several activation methods exist for removing guest molecules including (i) conventional heating and vacuum, (ii) solvent-exchange, (iii) supercritical carbon dioxide ($scCO_2$) drying,[136, 137] (iv) freeze drying,[138, 139] and (v) chemical treatment.[140]

1.4.3.1. Solvent-Exchange Activation

An effective strategy for accessing the highest surface area and porosity of MOFs, while maintaining the structural integrity, is called solvent-exchange activation (Figure 1.8).[84] Considered as the most common way to activate MOFs, solvent-exchange involves the exchange of a high boiling point and high surface tension solvent (i.e., DMF and water) for a low boiling point and low surface tension solvent (i.e., acetone, ethanol, and methanol) that also has higher volatility. Following solvent-exchange, conventional activation combining heat and vacuum can be utilized to dry the framework.[139, 141-143] Herein, the activation procedure must be carried out carefully because if the activation procedures are too harsh, then there is a risk of collapsing the framework, and losing the porosity and surface area.[144-146] Specifically, when MOF synthesis is carried out using high boiling point and high surface tension solvents, strong capillary forces can be generated under heat when solvent molecules undergo a liquid-to-gas phase transition, and the framework can collapse.[145] However, if solvent-exchange and vacuum drying are too harsh, an alternative activation method can be implemented.

In a typical solvent-exchange procedure, the MOF sample is washed numerous times with the reaction solvent, while allowing the MOF sample to soak in between washes, to remove guest molecules including leftover metal precursors, non-coordinated organic likers, modulator, or other impurities. The MOF sample can then be left in fresh reaction solvent for an overnight wash. Then, the high boiling point reaction solvent is replaced for a low boiling point solvent, where the same procedure can be repeated, and the MOF pores will be filled with the new solvent rather than the reaction solvent. To ensure the removal of as many guest molecules as possible, longer soaking times can be employed, prior to heating the sample under vacuum.

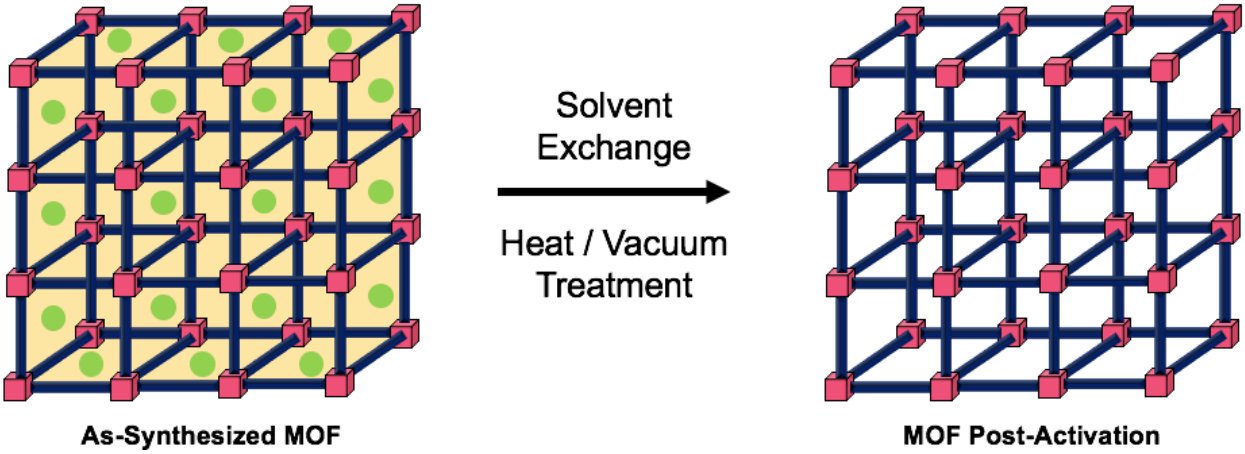

Figure 1.8. Solvent-exchange activation combined with conventional heating and vacuum drying for a MOF. As-synthesized MOF (left), and an activated MOF (right). The orange shading represents solvent and the green spheres represent leftover molecules post-synthesis.

1.5. Potential Applications of MOFs

The infinite variety of inorganic nodes and organic linkers, foundation of reticular chemistry, and different synthetic methods permit an endless number of MOF structures to be synthesized. Due to their high degree of structural tunability and their interesting properties related to high porosity and surface area, MOFs have been studied for many different potential applications in gas capture and storage,[27, 28] catalysis,[29-32] wastewater remediation,[33-35] chemical separations,[36-38] bioimaging,[147, 148] chemical sensing,[149, 150] and drug delivery,[41, 42] amongst others. To highlight the commercial applications of MOFs, there are currently two commercially available MOF materials. NuMat Technologies launched a product known as ION-X, which is a gas cylinder filled with a MOF, that is used to store and deliver hazardous gases used in the semiconductor industry at room temperature and atmospheric pressure. This cylinder is much safer than typical pressurized cylinders that are normally used to deliver gases requiring high pressures and temperatures for loading and delivery.[151] The other commercial MOF application is from MOF Technologies who developed a product known as TruPick, which utilizes a MOF to store and slowly deliver a chemical compound known as 1-methylcyclopropene (1-MCP), which slows down the ripening process of fruits and vegetables – keeping them fresh for storage and transportation purposes.[152] There are also many start-up companies that are working towards commercializing MOFs for different applications including, but not limited to, carbon dioxide capture and conversion, chemical sensing, and drug delivery.

1.5.1. MOFs for Drug Delivery

Over the years, MOFs have become promising candidates as drug carriers for potential biomedical applications in drug delivery (Figure 1.9).[153, 154] Owing to their tunable chemical functionality, surface area and porous structure - microporous (up to 2 nm) or mesoporous (2 to 50 nm), MOFs and nanoscale MOFs (nanoMOFs) have been studied as drug delivery systems to enhance therapeutic efficacy.[155] For successful drug incorporation in a MOF, the pore size aperture and window dimensions, and pore type (cage or channel), are key parameters for drug diffusion in the framework.[156] Moreover, the various interactions that can exist between MOFs and drug molecules include van der Waals forces, π–π stacking, and hydrogen bonding.[156] In the realm of drug delivery, the MOFs (host) used for encapsulating therapeutic agents (guest) must have key properties including the possibility to be synthesized in a range of sizes and specifically in the nanoscale size regime, high loading or storage capacity, and suitable biocompatibility and stability.[157] The size of the MOFs plays a crucial role as they must be appropriately sized for *in vivo* experiments, and the particle size impacts cellular uptake and the circulation throughout the body.[157] As well, MOFs have highly accessible internal and external surface areas making it possible to store and deliver a larger amount of therapeutic drug than traditional drug delivery agents (i.e., nanoparticles and polymers), hereby making treatment at the target more effective. As with any material used for biological applications, the MOF material must exhibit good biocompatibility and stability under biological conditions – two factors that are governed by the inorganic and organic building blocks of the MOF – in order to present minimal or no toxicity to the organism, and to reach a target without degrading.[158] In regard to the host-guest performance and controlled or sustained and triggered drug release, the drug cargo can be delivered by (i) diffusion of the drug through the MOF pores by a concentration gradient,[157] (ii) biodegradable release by collapse of the MOF,[159] (iii) competitive binding through external surface functionalization of the MOF,[160] and (iv) physiological change (stimuli such as pH and temperature).[160] In recent examples, MOFs were demonstrated as promising materials for the encapsulation of insulin,[161] for the delivery of anticancer therapeutic agents,[162] as well as for reducing the amount of active therapeutic required in cancer treatments.[163]

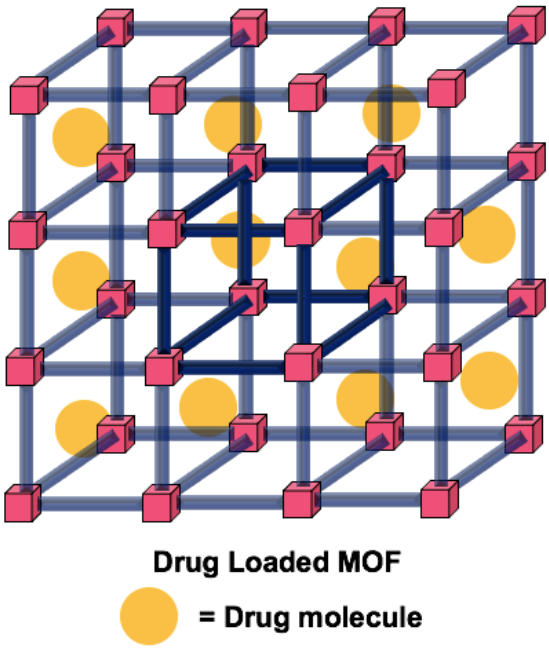

Figure 1.9. Representation of encapsulated drug molecules in the MOF.

1.6. Characterization of MOFs

As MOFs are unique materials with diverse structural and chemical properties, various characterization techniques are used to better understand their features.[84] The characterization techniques used in this thesis include (i) powder X-ray diffraction (PXRD) to gain information regarding the phase purity and crystallinity of a MOF, (ii) single crystal X-ray diffraction (SCXRD) to obtain the absolute MOF crystal structure, (iii) nitrogen (N_2) adsorption and desorption isotherms to measure the surface area and porosity, (iv) thermogravimetric analysis (TGA) to determine the thermal stability, (v) scanning electron microscopy (SEM) to obtain the particle size and morphology, (vi) nuclear magnetic resonance (NMR) spectroscopy to study the linker purity and incorporation of the linker, modulator, or other guest molecules in the pores, (vii) diffuse reflectance infrared Fourier transform spectroscopy (DRIFTS) to measure the presence or absence of IR active functional groups, and (viii) inductively coupled plasma–mass spectrometry (ICP-MS) to determine the percentage of metal in a MOF. Other techniques used for analytical testing in this thesis include (i) ultraviolet-visible (UV-Vis) spectroscopy for colorimetric detection of thiols, and (ii) high performance liquid chromatography (HPLC) to separate, identify and quantify drug molecules being loaded into MOFs. As for the MOF characterization techniques, a discussion of each is described below.

1.6.1. Powder X-ray Diffraction (PXRD)

Powder X-ray diffraction is a powerful, non-destructive and fundamental tool in MOF chemistry to obtain information regarding the bulk crystallinity of a crystalline sample.[164] Upon collecting a diffractogram, it provides evidence of a crystalline material, along with other useful information that can be extracted concerning phase composition, crystallite size, and unit cell dimensions. Moreover, when examining a diffractogram: (i) the reflection positions allow for an understanding of the unit cell symmetry and dimension and phase identification, (ii) the reflection intensities relate to the atoms distribution in the unit cell and the relative strength of the diffraction, (iii) the reflection shapes and width can relate to the presence of defects or presence of small crystallites, and (iv) the background can show if there is diffuse scattering from the sample, scattering from the sample holder, or even if there is the presence of amorphous phases. As for confirming the phase purity, a comparison can be done between the experimentally obtained diffractogram and the simulated diffractogram that is available in the Cambridge Crystallographic Data Centre (CCDC) from reported single crystal or structure refinement data (Figure 1.10).

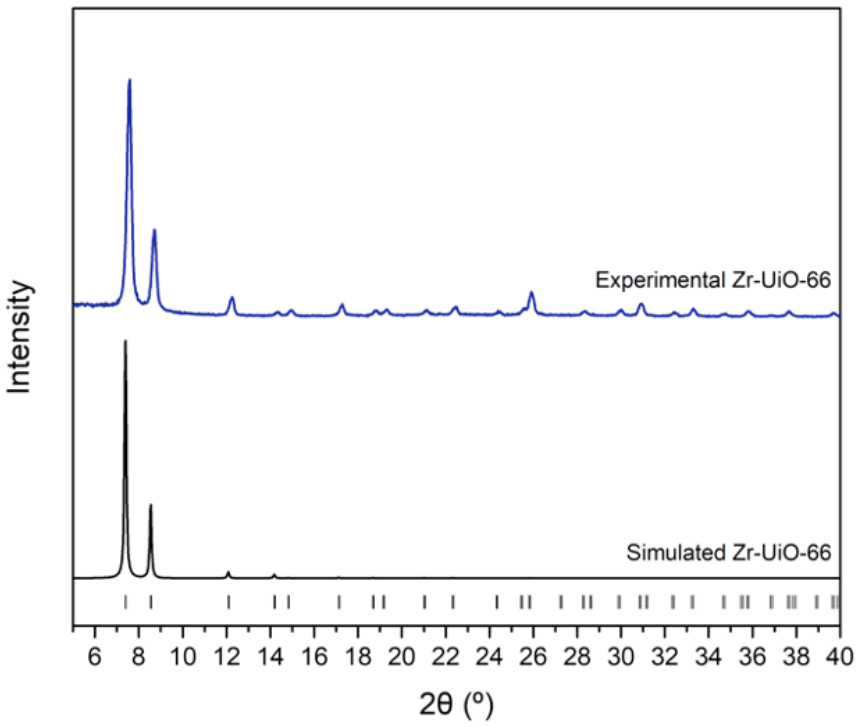

Figure 1.10. Stacked PXRD diffractograms exemplifying a comparison between an experimentally obtained one (top), and a simulated one (bottom). The black tick marks are the allowed reflections.

In a typical PXRD experiment, a powdered sample can be loaded onto a sample holder that contains a plate of material, often a zero-background plate made of silicon, either as a dry sample or loaded using a volatile solvent or oil. When a powdered sample of a crystalline material is deposited and flattened on the plate, the crystallites have the possibility to pack in a preferred orientation, particularly true for needle or plate-shaped crystals, rather than a random order, which may lead to differences between the reflections and reflection intensities in the experimental and stimulated patterns. Therefore, to prevent this, variable rotation can be used to ensure the crystallite orientation will be nearly random to the incoming X-rays and the detector. In X-ray diffraction, the X-rays are generated by a cathode ray tube, and the electrons are accelerated by an anode (i.e., often copper due to its short wavelength, wavelength of the emitted photon, Cu K-alpha (Kα) source is 1.5406 Å). When the conditions satisfy Bragg's Law ($n\lambda = 2d \sin\theta$), the interaction between the incident rays and the sample produce constructive interference and a diffracted ray. In the case of isostructural MOFs such as UiO-66 and UiO-67, shifting of the diffractogram occurs due to the differences in the unit cell size, where larger unit cells give larger d-spacing with lower angles on PXRD.

1.6.2. Single Crystal X-ray Diffraction (SCXRD)

When a single crystal of a MOF is obtained and is of sufficient size (≥ 100 μm in at least one dimension) and suitable quality, single crystal X-ray diffraction (SCXRD) is an elemental characterization technique that can be utilized to determine the absolute structure of the crystal.[165, 166] Similar to PXRD, SCXRD is a non-destructive technique, yet the X-ray radiation is directed towards a single crystal to obtain information regarding the crystalline phase and internal lattice of the crystalline material including the unit cell dimension, coupled with a diffractogram that can then undergo refinement. SCXRD is an effective technique to determine the position of the atoms that assemble the framework, it can provide evidence of post-synthetic modifications (i.e., transmetallation and SALE), and it can also confirm the presence of pore-occupying species (i.e., guest molecules). To prepare a sample for measurement, a single crystal, usually solvated, is mounted on the goniometer of the instrument, which enables the crystal to be positioned at different orientations. Therefore, as the geometry of the incident X-rays are varied, along with the crystal orientation, all of the various diffraction directions of the crystal lattice should be obtained. The temperature at which the experiment is being carried out can also play a role in the collected

diffraction data. Based on the temperature, solvent molecules have the ability to move freely creating disorder in the crystal structure.

1.6.3. Nitrogen (N_2) Adsorption and Desorption Isotherms

To establish the porosity, pore size, pore volume and surface area of a MOF, nitrogen gas sorption (adsorption-desorption) isotherms can be used. Prior to collecting the sorption isotherms, the MOF samples must be thoroughly activated, often with heat and under vacuum to ensure the maximum porosity is achieved.[84] When measuring the porosity and surface area of MOFs, nitrogen gas at the cryogenic temperature of 77 K is the standard adsorbate, which is the temperature of liquid nitrogen (boiling point of N_2), and the measurements are done at this low temperature as this is the temperature at which nitrogen gas condenses. At this low temperature where the nitrogen gas condenses, the nitrogen gas can easily stick to the surface of the MOF, and when the nitrogen gas interacts with the surface, it can form a well-defined and uniform monolayer on the surface of the MOF. Depending on the number of molecules of nitrogen gas that are required to form the monolayer, the surface area and porosity of the material can be determined. In an experiment, the activated and weighed MOF sample is placed in a tube with a filler rod and seal frit and mounted onto the instrument with an isothermal jacket. The tube on the instrument is evacuated at room temperature under vacuum, and then backfilled with an inert gas such as helium gas, to measure the free space in the tube. Following this, the sample gets evacuated with vacuum once more, and then the liquid nitrogen can cool the samples and the nitrogen gas gets slowly infiltrated into the tube in a controlled fashion and at different pressures. During this process, the instrument measures how much nitrogen gas is taken up by the sample as a function of pressure, and each pressure point is collected at equilibrium, with at least 30 adsorption points on an isotherm, followed by nitrogen gas desorption, and as a result, the data collection can take between 8 to 10 hours to complete. Therefore, by infiltrating nitrogen gas molecules into the sample tube and from low to high pressure, a monolayer of nitrogen molecules (adsorbate) is created through physisorption (reversible adsorption) on the adsorbent (MOF) forming weak interactions. The adsorbate monolayer provides information about the surface area, and after the monolayer forms, the pressure in the tube increases and the pores get filled with nitrogen gas molecules, filling the smaller pores before the larger pores, giving information about the pore size distribution. Moreover, if MOF particles aggregate, they form macropores and so those macropores are filled

at high pressures, which is why a large increase in nitrogen gas uptake sometimes occurs at higher pressure.

Porous materials have pore sizes that are classified as (i) micropores (pore width not exceeding 2 nm), (ii) mesopores (pore width between 2 and 50 nm), and (iii) macropores (pore width exceeding 50 nm) – which all fall into the category of nanopores (not exceeding 100 nm in diameter). An isotherm provides information based on the shape and can be classified under 6 different types (Figure 1.11) including (i) Type I – given by microporous solids, and further subcategorized as Type I(a) – given by materials with mainly narrow micropores (less than 1 nm), and Type I(b) – given by materials with larger micropores or small mesopores, (ii) Type II – given by materials with macropores or those which are nonporous, (iii) Type III – given by materials with macropores or those which are nonporous, and do no present an identifiable monolayer formation due to weak adsorbent-adsorbate interactions, (iv) Type IV – given by mesoporous materials that undergo capillary condensation (gas condenses to a liquid-like phase), and further subcategorized as Type IV(a) – given by mesoporous materials with cylindrical pores greater than 4 nm, and Type IV(b) – given for mesoporous materials with pores less than 4 nm, (v) Type V – similar to Type III, however pore filling occurs at higher relative pressures, and (vi) Type VI – given by nonporous materials that have uniform layer-by-layer adsorption.[167]

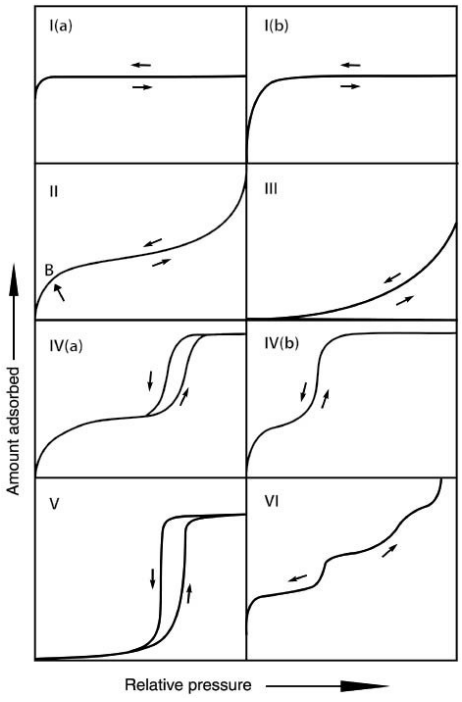

Figure 1.11. Representation of physisorption isotherms (Type I-VI) given by porous and nonporous materials. Figure obtained from Thommes *et al.*[167]

To calculate the surface area ($m^2 g^{-1}$) of a MOF from the gas sorption isotherm, the Brunauer-Emmett-Teller (BET) theory is the most widely accepted method.[168] In BET theory, it allows for the prediction of the number of adsorbate molecules required to form a monolayer on the surface of the adsorbent, even though one perfect monolayer may never form during gas adsorption. This is preferred for analysis of MOF isotherms in comparison to the Langmuir theory because the Langmuir theory is limited to fitting only Type I isotherms, and assumes adsorption is limited to a monolayer, where in reality it is rare for a perfect monolayer to form.[169] In addition to surface area information, the pore size distribution and pore volume of the MOF material can also be extracted from gas sorption isotherm data. There are numerous models that enable the determination of these properties, however the non-local density functional theory (NLDFT) method, is the most used and accepted model.[170] NLDFT is a pore size fitting model containing a kernel or series of theoretical isotherms generated for materials with different isotherms and pore sizes, and the experimental isotherm of a MOF can be fine-tuned and fitted to a theoretical isotherm.[171]

1.6.4. Thermogravimetric Analysis (TGA)

In the field of porous materials including MOFs, thermogravimetric analysis (TGA) is used most commonly to assess the thermal stability of a MOF, to determine the weight percent loss of guest molecules and linkers, and to help with determining the molecular formula of a MOF.[172] In general, the sample is placed on a sample pan and thermogravimetry measures the change in sample weight as a function of increasing temperature at a constant rate under a carrier gas, most commonly air, N_2, or O_2. Prior to TGA analysis, it is best to activate the MOF sample to ensure the removal of any trapped molecules, however based on the activation of the material the thermogram can show evidence of different molecules in the sample starting with solvent or volatile substances, followed by the removal of organic materials in the pores of the MOF, then degradation of the organic linkers of the MOF, and finally left with a metal oxide. An alternative technique such as variable temperature (VT-PXRD) also functions to determine the thermal stability of a MOF, as well as if the MOF undergoes any phase transitions when exposed to increasing temperature.[173]

1.6.5. Scanning Electron Microscopy (SEM)

In terms of MOF characterization, scanning electron microscopy (SEM) is commonly used to analyze a sample surface and to determine crystallite size and morphology (Figure 1.12), and elemental composition when coupled with energy dispersive X-ray spectroscopy (EDS).[84] In SEM, a beam of electrons is used to obtain high resolution micrographs with magnification up to 150,000X. SEM is performed in a vacuum; therefore, samples must be dry, and can be mounted on metal holders or stubs primarily made from vacuum grade aluminum, first coated with double-sided carbon tape. Since the acceleration voltage of the electron beam can damage the MOF crystallite, an ultra-thin layer of a conducting material (i.e., gold) can be applied by sputter coating to the MOF sample, to decrease the charge build up or charging effects in the MOF generated from the electrons.[174] Hence, the MOF material itself is not conductive, and the addition of a layer of a conducting material circumvents issues with electrons being trapped in the surface layer of the MOF, and allows for the electrons to easily flow through the MOF structure or bounce back.

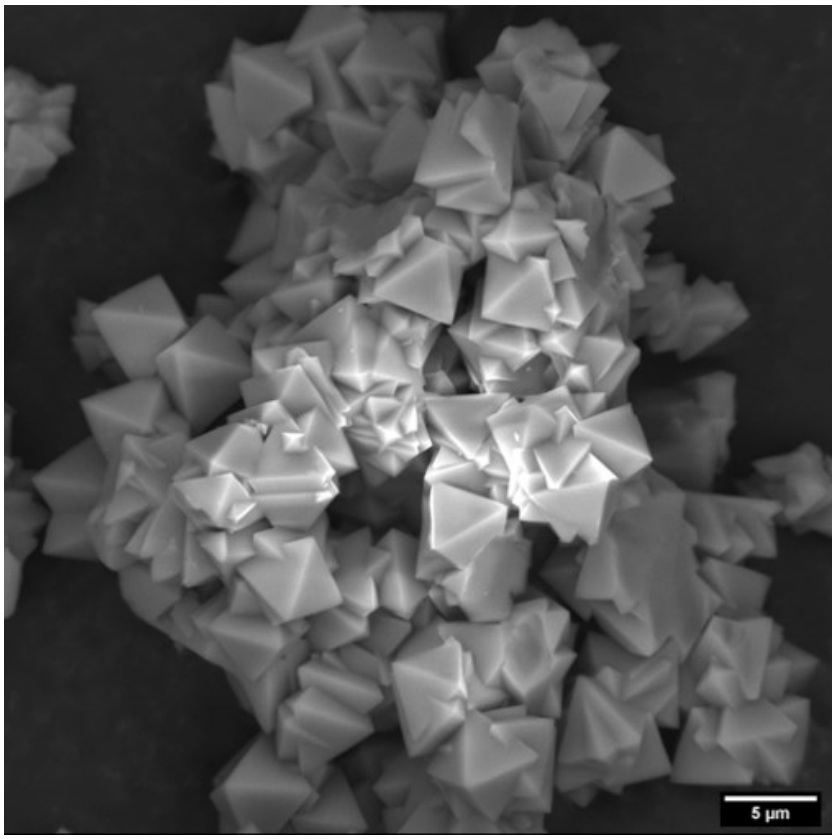

Figure 1.12. SEM micrograph of Zr-UiO-66 exhibiting octahedral crystallites.

1.6.6. Nuclear Magnetic Resonance (NMR) Spectroscopy

Nuclear magnetic resonance (NMR) spectroscopy can be used to determine the linker purity and incorporation, the linker ratio in the case of mixed linker MOFs, and leftover modulator, impurities, and solvent presence in the MOF material (Figure 1.13). Due to the insolubility of MOFs in conventional NMR solvents (i.e., deuterated chloroform ($CDCl_3$) or deuterated dimethyl sulfoxide (DMSO-d_6)), solution-state NMR is performed, where the MOF sample (~1-2 mg) is first digested in a deuterated acid (~7-10 drops) (i.e., deuterated sulfuric acid (D_2SO_4) or deuterium chloride (DCl)), and sonicated, prior to adding a solvent (i.e., DMSO-d_6) that is capable to dissolve the components of the digested mixture, which include metals, organic linkers, and in some cases, modulators and solvent.[175] If the acid digestion is not effective, a basic digestion of the MOF can be used as an alternative, or solid-state NMR spectroscopy.

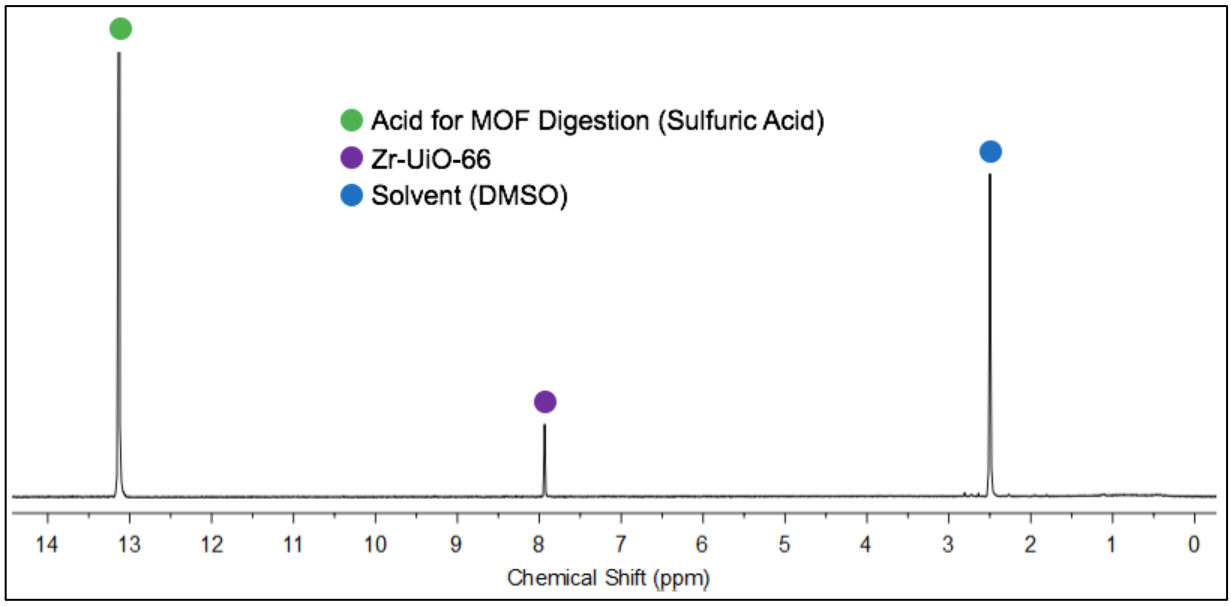

Figure 1.13. ^{1}H-NMR spectrum of Zr-UiO-66 displaying the BDC aromatic proton (purple), NMR solvent (blue), and acid for MOF digestion (green).

1.6.7. Diffuse Reflectance Infrared Fourier Transform Spectroscopy (DRIFTS)

The most common type of infrared spectroscopy technique used for MOFs and powder samples is diffuse reflectance infrared Fourier transform spectroscopy (DRIFTS), which is used to confirm the presence or absence of IR active functional groups, as well as determining the MOF purity and if there is the presence of guest molecules in the framework.[84] As the IR beam is focused

onto a particulate material, the radiation is reflected off the top surface of the particles or can penetrate deeper into the sample. Specifically, with DRIFTS, the infrared radiation can go into the crevices of the material and reflect, hereby seeing the IR active functional groups of organic linkers on internal and external surfaces of the MOF. In other IR spectroscopy techniques, pressure is applied to the sample, but applying pressure to porous MOFs can collapse the network structure, therefore DRIFTS meets the accommodations for the pores and empty spaces. In a DRIFTS experiment, a non-absorbent matrix such as potassium bromide (KBr) must be prepared using a mortar and pestle and placed into a sample holder, in order to collect the background which can be subtracted from the sample mixture spectrum. The MOF powder can then be diluted with the IR transparent matrix, KBr, gently mixed to ensure homogeneity, and loaded into the sample holder to obtain the DRIFTS spectrum of the MOF.

For a MOF sample, there are several characteristic IR stretches observed in a DRIFTS spectrum, which include the –OH stretching from the bridging and terminal hydroxyl ligands in the metal node, and C–H stretching and C=O stretching from the organic linker (Figure 1.14). Moreover, it is best to activate the MOF sample prior to running DRIFTS and to keep the KBr dry, since the presence of water in the sample can produce a broad peak and hydroxyl stretches from 3500 to 3800 cm^{-1}, which can obstruct the peaks of IR active functional groups in this region.

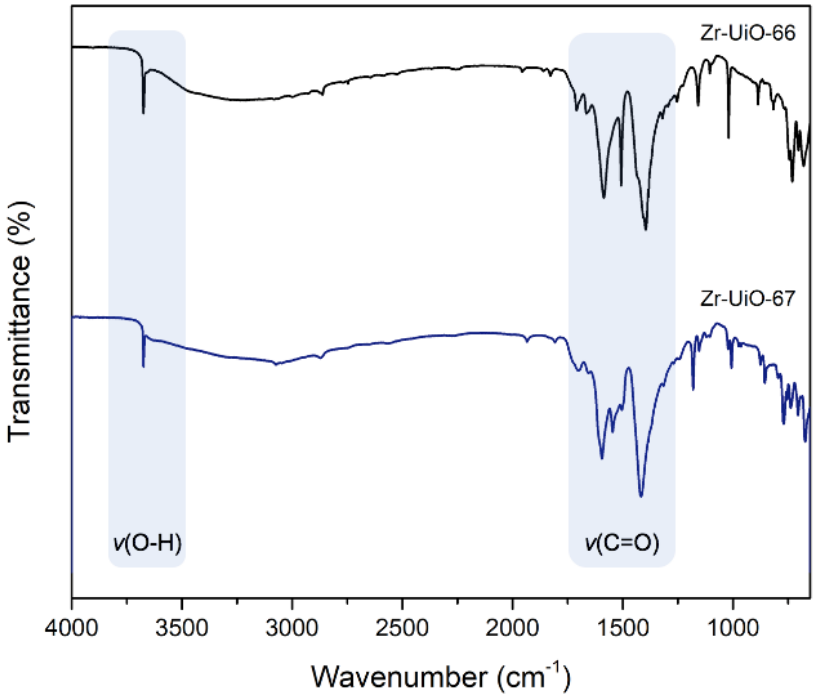

Figure 1.14. DRIFTS spectra of isostructural MOFs, Zr-UiO-66 and Zr-UiO-67.

1.6.8. Inductively Coupled Plasma–Mass Spectrometry (ICP-MS)

Inductively coupled plasma–mass spectrometry (ICP-MS) is a sensitive technique that can be used to determine the percentage of metal in a MOF, to confirm the purity, or elemental ratios in a MOF.[84] Prior to collecting ICP-MS data, the MOF sample must be carefully digested using an acid (i.e., nitric acid (HNO_3) or sulfuric acid (H_2SO_4)), as well as hydrogen peroxide (H_2O_2) to mineralize the organic component, and heated at an elevated temperature (i.e., 100 °C). The sample can then be diluted to an appropriate concentration suitable for the ICP-MS instrument.

1.6.9. Ultraviolet-Visible (UV-Vis) Spectroscopy

Ultraviolet-Visible (UV-Vis) spectroscopy is used to measure the amount of light that is absorbed by a solution at a specified wavelength.[176] Therefore, this allows for a quantitative analysis between concentration and absorbance. Herein, it is important to prepare a cuvette with a blank solution which does not include the analyte of interest, in order to calibrate the apparatus and set it to zero prior to measuring the absorbance of samples. Beer's Law ($A = \varepsilon c l$) establishes a relationship between the value of absorbance determined by the spectrophotometer to the concentration of the sample and comprises of the use of the molar extinction coefficient, which explains how strongly a sample absorbs light at a specified wavelength and the path length, otherwise known as the distance the light will pass through in the sample. In addition, a standard calibration curve with a linear response, can be generated with known concentrations of a sample against their respective absorbance values to be able to determine the concentration of the unknown sample. In this thesis, UV-Vis spectroscopy is useful for the thiol quantification protocol (Section 1.7).

1.6.10. High Performance Liquid Chromatography (HPLC)

High performance liquid chromatography (HPLC) is a valuable tool for identifying and quantitating analytes in a given sample, in addition to separating the components through the utilization of their affinity towards the stationary phase.[177] The principle of separation in HPLC relies on the notion that upon injecting a sample comprised of a mixture of species into the HPLC column, the different species will move along the column according to their relative affinities towards the chosen stationary phase. Moreover, the greater the affinity a component has towards the adsorbing stationary phase, the slower it will move through the column, and therefore, the

species with less affinity towards the stationary phase can move through the column more quickly. Herein, in the context of MOFs and in this thesis, HPLC is useful for drug loading and release kinetics experiments.

1.7. Thiol Quantification Protocol

First reported in 1959, Ellman's test can be used for the colorimetric determination of thiol groups.[178] The Ellman's reagent, or 5,5′-dithiobis-(2-nitrobenzoic acid) (DTNB) reacts with a free and reduced thiol group to yield a mixed disulfide and yellow-coloured 2-nitro-5-thiobenzoic acid (TNB) molecule, in accordance with the reaction scheme (Figure 1.15). This procedure can be translated for MOFs, where the thiol groups found on the external surface of thiol-functionalized MOFs can be quantified using UV-Vis spectroscopy, due to the production of the yellow-coloured product.

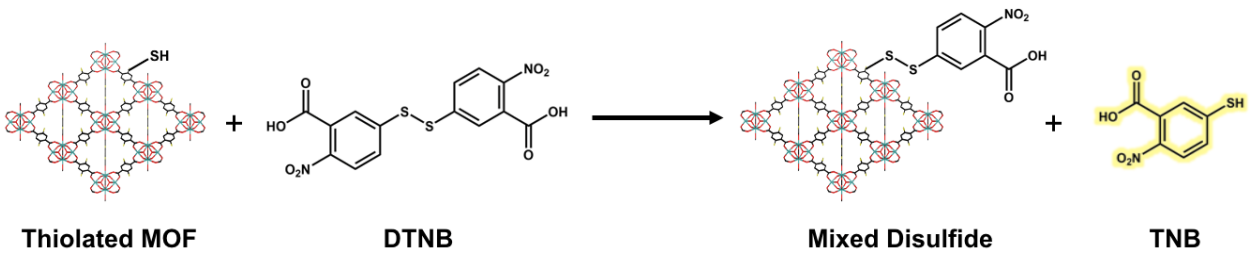

Figure 1.15. Reaction scheme involved in quantifying the surface accessible thiol groups on MOFs using Ellman's reagent.

1.8. Mucoadhesion and Periodic Acid–Schiff (PAS) Coloration Protocol

1.8.1. Mucins and Mucoadhesion

The ocular surface is naturally protected with a layer of mucous over the cornea and conjunctiva or ocular surface membrane, which functions to trap and eliminate allergens, debris and pathogens.[179] The mucous is comprised of several components which include water (~95%), lipids, salts, mucins (~1-5%), and non-mucin proteins such as enzymes, growth factors, and antibodies.[179] Mucins are glycosylated proteins known as glycoprotein macromolecules, which are the major component responsible for the structure and functions of mucous. These proteins assist in the maintenance of lacrimal fluid, in the lubrication of the ocular surface to allow smooth blinking and the formation of a smooth spherical surface for good vision, and as a barrier for the

ocular surface. Mucins are characterized by several features including (i) high molecular weight of 0.5 to 40 MDa (1 Da = 1 g mol^{-1}, and 1 MDa = 1000000 Da), (ii) a polypeptide backbone with repeat domains rich in proline, threonine and serine amino acids, and (iii) a high degree of glycosylation.[179] In mucins, *N*-acetylgalactosamine (GalNAc), a sugar molecule, is covalently bonded to the hydroxyl (–OH) groups of serine or threonine residues in the protein, which is referred to as an O-glycosidic bond.[180] Mucins can be classified as (i) secreted mucins, further subcategorized into gel-forming mucins and soluble mucins, and (ii) membrane-associated mucins.[179] Gel-forming mucins can be further classified into the following subtypes with the nomenclature MUC2, MUC5AC, MUC5B, MUC6, and MUC19, whereas soluble mucins are classified into subtypes MUC7 and MUC9, where the assigned number related to the order of discovery (Figure 1.16).[179] From the gel-forming mucins, MUC5AC is known to be expressed at higher levels at the ocular surface.[179]

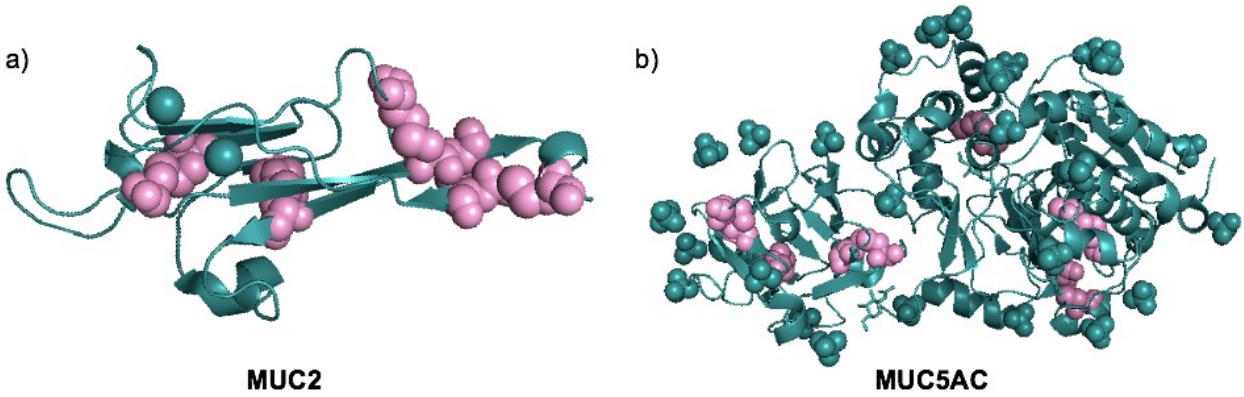

Figure 1.16. Gel-forming mucins (a) MUC2 and (b) MUC5AC, in the mucous layer. The pink spheres represent cysteine residues.

Mucoadhesion is defined by the ability to adhere to mucosal tissues, including, but not limited to, oral, nasal and ocular mucous. For drug delivery, mucoadhesive drug delivery systems[181] have the capacity to interact with the mucous layer comprised of mucin molecules. Due to the inefficient drug delivery of current medications as a result of poor corneal permeability, reflex blinking, tear secretion, dose spillage and nasolacrimal drainage,[179] mucoadhesive systems or mucin-penetrating particles have the potential to improve the bioavailability and therapeutic performance of drugs by increasing the retention time of drugs near the mucous. The mucoadhesion is strongly directed by mucin proteins, which are the main family of proteins found in mucous. Furthermore, mucins are negatively charged molecules that can form electrostatic

interactions to positively-charged systems, and some regions of mucins are rich in cysteine amino acids, which contain thiol (–SH) groups,[182] that can form disulfide (–S-S–) bonds.[183] Herein in this thesis, mucoadhesion is established between the free thiol groups from cysteine amino acids, to the thiol groups on the organic linkers of the MOFs.

1.8.2. Periodic Acid–Schiff (PAS) Coloration Protocol

To study and quantify the amount of mucin (protein) that interacts and adheres to the drug vector (MOF), the Periodic Acid–Schiff (PAS) staining technique can be used. First reported in 1978, this coloration method allows for the understanding of mucoadhesive properties of different materials (i.e., gold nanoparticles and MOFs) to mucins.[184-186] In this technique (Figure 1.17), periodate oxidizes vicinal hydroxyl groups of saccharides (sugars) to aldehydes. Subsequently, basic fuchsin (pink-purple coloured) is decoloured upon addition of sodium metabisulfite, where the central carbon of the triarylmethane system of fuchsin gets saturated, and the electrons are no longer highly delocalized. By mixing the oxidized mucins and the decoloured fuchsin, the compounds react and promotes fuchsin to regain a highly delocalized π-system. Through PAS coloration and UV-Vis spectroscopy, the amount of mucins adhered to the MOF can be quantified.

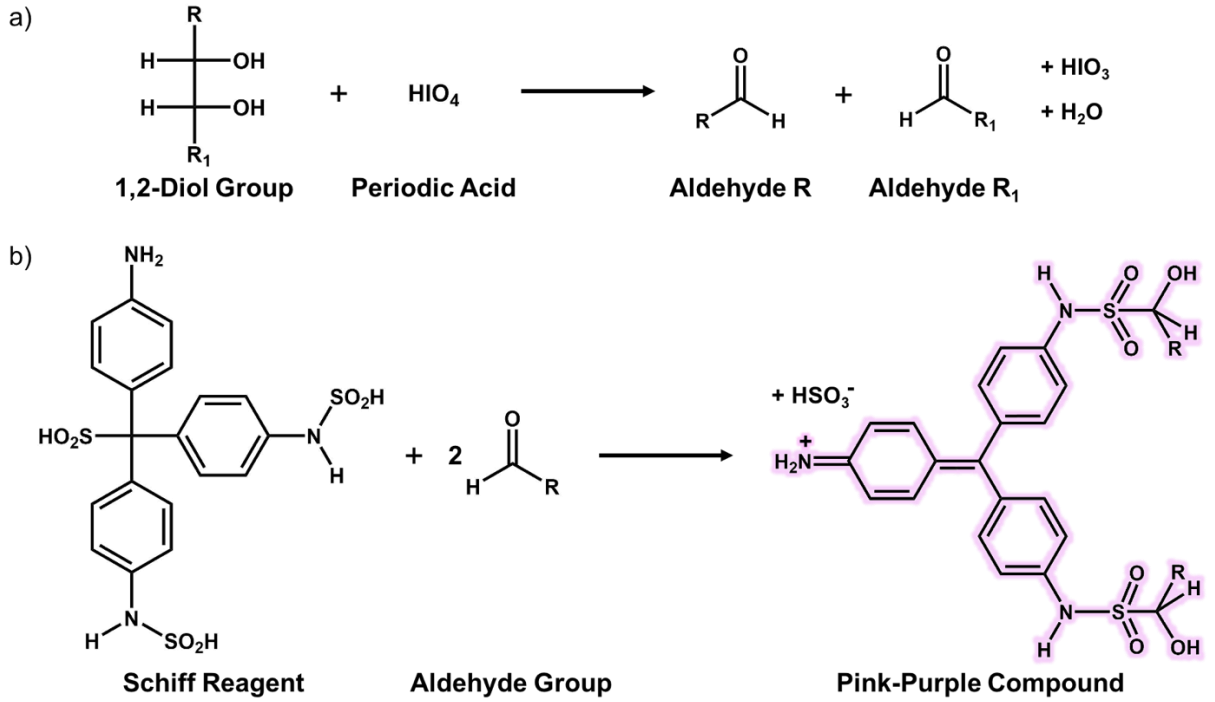

Figure 1.17. Periodic Acid–Schiff (PAS) reaction scheme, where (a) alcohol oxidation to form aldehyde groups and (b) Schiff dye reacts with aldehyde groups to form a pink-purple compound.

1.9. Scope of Thesis

The following two chapters will present studies on the sustainable synthesis of MOFs, and the use of thiolated MOFs for ophthalmic drug delivery applications. The long-term goal of this work is to utilize sustainably synthesized MOFs for drug delivery.

Chapter 2 describes the synthesis of four structurally diverse MOFs, MOF-808, NU-1000, HKUST-1 and ZIF-8, with the use of a green solvent alternative in line with several of the principles of green chemistry, STEPOSOL® MET-10U. The MOFs were successfully characterized using PXRD, N_2 sorption isotherms, TGA, SEM, ^{1}H-NMR spectroscopy, and DRIFTS. In addition to highlighting the importance of green solvents in academic and industry laboratories, HKUST-1 was also synthesized at the gram-scale using STEPOSOL® MET-10U to show its potential in industrial settings.

Chapter 3 explores the design and synthesis of thiol-functionalized analogues of Zr-UiO-66 and Zr-UiO-67. The isostructural MOFs are successfully characterized using PXRD, N_2 sorption isotherms, TGA, SEM, ^{1}H-NMR spectroscopy, and DRIFTS. Furthermore, investigations between the MOF material and mucins were measured by PAS coloration, and UV-Vis spectroscopy, metal leaching studies were carried out using ICP-MS, and the drug encapsulation of an anti-inflammatory drug, flurbiprofen, was quantified using HPLC.

Chapter 2

A Step Toward Change: A Green Alternative for the Synthesis of Metal–Organic Frameworks

2.1. Introduction

The development and implementation of green synthetic procedures is important for minimizing the environmental impact of industrial and academic research in the chemical sciences.[108, 109, 187] Our environment is suffering considerably due to many global issues including, but not limited to, waste disposal, natural resource depletion, and air, water and soil pollution.[188] The comparatively new field of chemistry, green chemistry, embraces and implements the notion of developing chemical products and processes that seek to mitigate and/or eliminate the use/generation of hazardous substances.[108] More specifically, less hazardous chemical synthesis (principle #3), safer solvents and auxiliaries (principle #5), and renewable feedstocks (principle #7) are three principles of green chemistry that encourage the discovery of greener alternatives in synthetic chemistry.[109]

Metal–organic frameworks (MOFs) are an intriguing class of porous, and often crystalline, materials that are comprised of metal nodes bridged by organic linkers, giving rise to network materials.[3, 5-7] The notable designability of MOFs, coupled with high surface area and porosity has enabled their study in various applications such as gas capture and storage,[189, 190] catalysis,[31, 191] chemical sensing,[149, 150] wastewater remediation,[33, 35] drug delivery,[41, 42] and solar fuels generation,[39] amongst others. Demonstrating that these potential applications can become a reality, the first commercial MOF products were released in 2017.[151, 152] MOFs have shown great promise in the field of green chemistry, from synthesis[126, 192] to application.[193, 194] Like most fields of chemistry however, there are still many challenges that lie ahead to ensure the sustainable synthesis and application of MOFs.[126] Several MOFs, including those studied for potential green applications, are still synthesized in, and washed with, petroleum-derived solvents that are hazardous to human health and the environment such as *N,N*-dimethylformamide (DMF), meaning that in some cases, extensive volumes of DMF are used. Risks are therefore twofold – not only to the environment through the extraction of fossil fuels and again through the expulsion of DMF-containing waste, but also to human health, where acute exposure to DMF can cause hepatotoxicity, while chronic exposure can lead to reproductive issues and cancer in humans.[195]

As a result, the Registration, Evaluation, Authorisation and Restriction of Chemicals (REACH) has listed DMF as a "substance of very high concern", while the Pfizer solvent selection guide lists DMF as "undesirable" for use.[196] Although DMF can be used safely with proper personal protective equipment (PPE) in the laboratory, and can also be recycled in some instances, finding greener alternatives to DMF is of interest.

Herein, we explore the use of a plant derived solvent, STEPOSOL® MET-10U,[131] otherwise known as *N,N*-dimethyl-9-decenamide, for the synthesis of a diverse series of MOFs (Figure 1). Produced by Stepan® in collaboration with Elevance Renewable Sciences®, STEPOSOL® MET-10U is synthesized using a biodegradable C10 methyl ester, generated by the cross metathesis of plant oils, such as canola, soybean and palm oil, with olefins.[132, 197] The industrial olefin metathesis process is performed under low-pressure and low-temperature conditions, in the presence of a highly selective proprietary catalyst. The production of this C10 methyl ester by Elevance Renewable Sciences® is thus in line with several of the twelve principles of green chemistry including: prevention (principle #1), less hazardous chemical synthesis (principle #3), safer solvents and auxiliaries (principle #5), design for energy efficiency (principle #6), use of renewable feedstocks (principle #7), catalysis (principle #9), and design for degradation (principle #10). The C10 methyl ester is then converted to *N,N*-dimethyl-9-decenamide (STEPOSOL® MET-10U), a disubstituted amide composed of an unsaturated hydrocarbon chain with a terminal alkene functionality. On the other hand, DMF is industrially synthesized[198] using carbon monoxide, which is petroleum-derived, and ammonia, which is produced from a very energy intensive process (the Haber-Bosch process).[199] STEPOSOL® MET-10U, a solvent that is also recognized as a powerful surfactant, has a boiling point of 297 °C, and has a biorenewable carbon index (BCI) of 75%.[133] In addition, the Hansen solubility parameter space of STEPOSOL® MET-10U encompasses that of hydrocarbons, esters, glycol ethers, and alcohols, demonstrating that it can dissolve materials with a wide range of chemical functionality.[133] Importantly, STEPOSOL® MET-10U demonstrates minimal toxicity, $LD_{50} > 2000$ mg kg^{-1} (OECD No. 402, acute dermal toxicity method),[200] including biotoxicity as it does not accumulate in organisms, and is readily biodegradable (OECD No. 301, ready biodegradability).[201] Moreover, the bioderived solvent exhibits a low volatile organic compound (VOC) content, specifically it is a low vapor pressure (LVP) VOC, and excellent solvency comparable to DMF. From a cost standpoint, the list price of DMF (Fisher Scientific) is \$107CAD L^{-1} whereas the list price of STEPOSOL® MET-10U

(Stepan® company) is $36CAD L^{-1}. Finally, although the thermal decomposition pathway is not well studied, STEPOSOL® MET-10U is likely to undergo hydrolysis, leading to the formation of amine species (dimethylamine, dimethylammonium), and decanoic acid.[92, 202, 203] The generation of low concentrations of dimethylamine is thought to aid in MOF synthesis by deprotonating the organic linker and facilitating slow and dynamic coordination between the metal and linker precursors.[84] Furthermore, the generation of a carboxylic acid (such as decanoic acid, or formic acid in the case of DMF) can aid in MOF synthesis by acting as a modulator and/or stabilizing capping ligand.[204] Given the high boiling point, broad Hansen solubility parameter space, potential to generate fruitful degradation products, and bioderived nature, STEPOSOL® MET-10U is well-poised to replace DMF as a greener alternative for the synthesis of MOFs (Figure 2.1).[205]

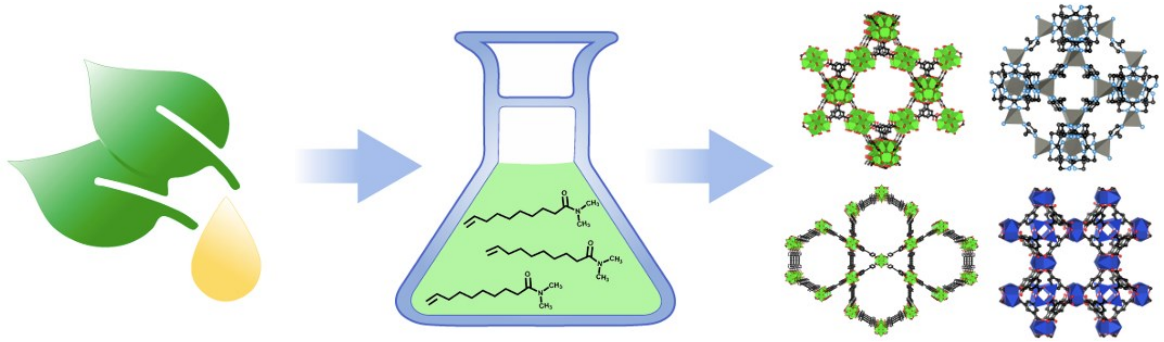

Figure 2.1. A bioderived solvent, STEPOSOL® MET-10U, is used to synthesize a series of structurally diverse metal–organic frameworks.

2.2. Experimental Procedures

2.2.1. General Materials and Methods

All reagents and solvents were used without further purification: zirconium dichloride oxide octahydrate ($ZrOCl_2 \cdot 8H_2O$, Alfa Aesar, 98%), copper(II) nitrate trihydrate ($Cu(NO_3)_2 \cdot 3H_2O$, ACROS Organics, 99%), zinc(II) nitrate hexahydrate ($Zn(NO_3)_2 \cdot 6H_2O$, Alfa Aesar, 99%), 1,3,5-benzenetricarboxylic acid (H_3BTC, Alfa Aesar, 98%), 2-methylimidazole (2-mIm, Sigma Aldrich, 99%), formic acid (Alfa Aesar, 97%), benzoic acid (Alfa Aesar, 99%), nitric acid (HNO_3, Fisher Chemical, 70%), ethanol (Greenfield Global, 95% and 99%), *N,N*-dimethylformamide (DMF; Fisher Chemical Certified ACS, ≥99.8%), STEPOSOL® MET-10U (Stepan® Company), methanol (Fisher Chemical Certified ACS, 99.9%), isopropanol (Sigma-Aldrich, ACS Reagent, ≥99.5%), 1-butanol (Fisher Chemical Certified ACS, 99.9%), acetone (Fisher Chemical Certified ACS,

99.5%), toluene (Fisher Chemical Certified ACS, 99.9%), ethyl acetate (Fisher Chemical Certified ACS, ≥99.5%), ethyl L(-)-lactate (Acros Organics, 97%), deuterated dimethyl sulfoxide (DMSO-d_6; Sigma Aldrich, 99.9 atom % D), deuterated sulfuric acid (D_2SO_4; Sigma Aldrich, 99.5 atom % D), deuterium chloride (DCl; 35 wt.% solution in deuterium oxide, D_2O, 99 atom % D; Sigma Aldrich). 1,3,6,8-tetrakis(*p*-benzoic acid)pyrene (H_4TBAPy) was prepared according to the literature.[175]

Powder X-ray diffraction (PXRD) data were collected on a Bruker D2 Phaser (Bruker AXS, Madison, WI, USA) equipped with Cu*K*α X-ray source (wavelength, λ = 1.54 Å), and a Nickel filter. Neat samples were smeared directly onto the silicon wafer of a proprietary low-zero background sample holder. Data was collected in the 2θ-range of 4-20° in increments of 0.02°.

Single crystal X-ray diffraction (SCXRD) data were measured on a Bruker D8 Venture diffractometer equipped with a Photon 200 area detector, and *IμS* microfocus X-ray source (Bruker AXS, Cu*K*α source). All measurements were carried out at room temperature for all ZIF-8 crystals coated with a thin layer of amorphous oil to decrease crystal deterioration, structural disorder, or any related thermal motion effects and to improve the accuracy of the structural results. Structure solution was carried out using the SHELXTL package from Bruker.[206] The parameters were refined for all data by full-matrix-least-squares or F^2 using SHELXL.[207] The structures exhibit disordered moieties that could not be reliably modeled by discrete atoms was subtracted by the SQUEEZE procedure, using the PLATON software.[208] All of the nonhydrogen atoms were refined with anisotropic thermal parameters. All hydrogen atom thermal parameters were constrained to ride on the carrier atom. Crystallographic data in CIF format have been deposited in the Cambridge Crystallographic Data Centre (CCDC) under deposition numbers CCDC 2067976, 2067977, and 2067978.

Small angle X-ray scattering (SAXS) measurements were conducted on a SAXSpoint 2.0 (Anton Paar, Austria) equipped with a Cu*K*α radiation source (wavelength, λ = 1.54 Å), using an Eiger R 1M (Horizontal) detector at SAXS distance of 568 mm. Powder samples were placed on a sample holder for solids provided by Anton Paar, which was further secured by tape. X-ray exposure times were 30 min per frame for a total of 4 frames for every experiment. The obtained SAXS profiles were corrected and shown as a function of scattering vector ($q = (4\pi/\lambda) \sin\theta$, where θ is the scattering angle in ° and q in nm^{-1}).

Nitrogen adsorption-desorption (sorption) isotherm data were collected at 77 K on a Micromeritics TriStar II Plus surface area and porosity analyzer. All samples were activated (MOF-808, NU-1000, and ZIF-8 at 120 °C for 24 h, HKUST-1 at 150 °C for 24 h) before each isotherm was collected by heating under vacuum using a Micromeritics Smart VacPrep equipped with a hybrid turbo vacuum pump system.

Diffuse reflectance infrared Fourier transform spectroscopy (DRIFTS) spectra were recorded using a Thermo Scientific Nicolet 6700 FT-IR equipped with a MCT detector with a resolution of 1 cm^{-1}.

Proton nuclear magnetic resonance (^{1}H-NMR) spectroscopy spectra were recorded on a 500 MHz Varian spectrometer and the chemical shifts were referenced to the residual solvent peaks. MOF samples were digested using ~7 drops of D_2SO_4 for MOF-808, NU-1000 and HKUST-1, or with 200 μL of D_2O acidified with DCl for ZIF-8, followed by sonication and dissolution of the suspension in DMSO-d_6.

Thermogravimetric analysis (TGA) measurements were carried out in a TGA/DSC 1 from Mettler Toledo, from room temperature to 800 °C at a rate of 5 °C/min under air.

Scanning electron microscopy (SEM) micrographs were collected on a Phenom ProX desktop SEM, at 12 kV. Prior to the analysis, all samples were coated with 5 nm gold (Au) layers by using a Cressington 108 Auto/SE Sputter Coater with MTM-20 high resolution film thickness controller.

Optical microscope images were captured using a Laxco™ LMC-2000 Compound Microscope equipped with a SeBaCam Digital Microscope Camera (with SeBaView Software), with magnification achieved by a 4X objective lens.

The following naming convention is used for several figures:

- STEPOSOL® MET-10U Samples:
    - "1) MOF name, 2) Synthesis solvent (STEPOSOL), 3) Solvent used to wash the sample for activation"
- DMF Samples:
    - "1) MOF name, 2) Synthesis solvent (DMF), 3) Solvent used to wash the sample for activation"
    - In the case where a solvent used to wash the sample for activation is not specified, DMF is the solvent used to wash the sample for activation.

2.2.2. Synthesis and Activation of MOF-808, NU-1000, HKUST-1, and ZIF-8

MOF-808 (DMF),[209] NU-1000 (DMF),[175] HKUST-1 (DMF),[117] and ZIF-8 (DMF)[210] were synthesized using DMF, using literature procedures. The MOFs were also prepared with STEPOSOL® MET-10U as a solvent, directly in place of DMF with identical reaction conditions pertaining to the reaction precursors, concentration, time, and temperature being used. All MOFs were washed with various organic solvents including butanol, isopropanol, ethanol 99%, DMF and toluene (MOF-808), butanol, isopropanol, ethanol 99%, DMF and methanol (HKUST-1), methanol, ethanol 95%, ethanol 99%, ethyl acetate and ethyl lactate (ZIF-8), or DMF (NU-1000) to remove excess reagents, impurities and by-products.

MOF-808 was synthesized solvothermally in an 8-dram vial containing the corresponding $ZrOCl_2 \cdot 8H_2O$ (50.0 mg, 0.154 mmol) and H_3BTC (70.0 mg, 0.333 mmol), with 5 mL of formic acid and 10 mL of DMF. Once the reagents were dissolved by sonication, the sample mixture was heated at 120 °C for 3 days (72 h). In the first series of samples, white precipitate was collected by centrifugation and washed three times with 10 mL of fresh DMF for 4 days, exchanging the DMF every second day. Then, each sample was washed with different organic solvents including butanol, isopropanol, ethanol 99%, DMF and toluene, for 4 to 5 days, exchanging the solvent every second day. The organic solvent was then exchanged with acetone and washed three times with 10 mL of fresh acetone. The as-synthesized MOF-808 was left in 10 mL of fresh acetone for one day. In the second series of samples, white precipitate was collected by centrifugation and washed directly with different organic solvents, followed by acetone, hereby omitting the wash with DMF. For both series, the samples were dried under vacuum at 120 °C for 24 h, yielding a white crystalline solid. This procedure can be repeated by directly replacing the 10 mL of DMF in the synthetic protocol of both series with 10 mL of STEPOSOL® MET-10U. Several batches of MOF-808 were synthesized in STEPOSOL® MET-10U and each washed with different organic solvents in place of DMF prior to activation, including butanol, isopropanol, ethanol 99%, DMF and toluene. The highest surface area was obtained after performing washes with STEPOSOL® MET-10U, followed by isopropanol and acetone.

NU-1000 was synthesized solvothermally in an 8-dram vial containing the corresponding $ZrOCl_2 \cdot 8H_2O$ (97.0 mg, 0.299 mmol) and benzoic acid (2780.0 mg, 22.76 mmol), suspended in 8 mL of DMF. The vial was tightly capped and the mixture was sonicated until an even suspension was obtained. Subsequently, the solution was placed into an 80 °C oven for a few hours to allow

the Zr_6-cluster to form. After cooling the solution, H_4TBAPy (40.0 mg, 0.0647 mmol) was added, and the suspension was sonicated. The suspension was then placed into a 100 °C oven for 3 days (72 h), yielding a yellow solid that was isolated by centrifugation. As-synthesized NU-1000 was washed three times with 10 mL of fresh DMF. Then, the DMF was exchanged with acetone, washed three times with 10 mL of fresh acetone, and soaked in 10 mL of fresh acetone for two days. The sample was dried under vacuum at 120 °C for 24 h, yielding a yellow crystalline solid. This procedure can be repeated by directly replacing the 8 mL of DMF in the synthetic protocol with 8 mL of STEPOSOL® MET-10U. The MOF synthesized in STEPOSOL® MET-10U was still washed with DMF. The highest surface area was obtained after performing washes with DMF and acetone.

HKUST-1 was synthesized solvothermally in an 8-dram vial containing the corresponding $Cu(NO_3)_2{\cdot}3H_2O$ (45.0 mg, 0.186 mmol) and H_3BTC (30.0 mg, 0.143 mmol), with a mixture solvent of 2 mL of DMF, 2 mL of ethanol 99%, and 2 mL of deionized water. After the reagents were dissolved by sonication, the sample was heated in an 80 °C oven for 3 days (72 h). In the first series of samples, blue precipitate was collected by centrifugation and washed three times with 10 mL of fresh DMF for 4 days, exchanging the DMF every second day. Then, each sample was washed with different organic solvents including butanol, isopropanol, ethanol 99%, DMF and methanol, for 4 to 5 days, exchanging the solvent every second day. The organic solvent was then exchanged with acetone and washed three times with 10 mL of fresh acetone. The as-synthesized HKUST-1 was left in 10 mL of fresh acetone for one day. In the second series of samples, blue precipitate was collected by centrifugation and washed directly with different organic solvents, followed by acetone, hereby omitting the wash with DMF. For both series of samples, the as-synthesized HKUST-1 (blue-teal crystalline solid) was dried under vacuum at 150 °C for 24 h, yielding a purple-blue crystalline solid. This procedure can be repeated by directly replacing the 2 mL of DMF in the synthetic protocol of both series with 2 mL of STEPOSOL® MET-10U. Several batches of HKUST-1 were synthesized in STEPOSOL® MET-10U and each washed with different organic solvents including butanol, isopropanol, ethanol 99%, DMF and methanol. The highest surface area was obtained after performing washes with methanol and acetone.

ZIF-8 was synthesized solvothermally in an 8-dram vial containing the corresponding $Zn(NO_3)_2{\cdot}6H_2O$ (350 mg, 1.18 mmol) and 2-mIm (200 mg, 2.44 mmol), with 15 mL of DMF and three drops of HNO_3 were added to the mixture with a Pasteur pipette. After the reagents were

dissolved by sonication, the sample was heated in a 120 °C oven for 1 day (24 h). ZIF-8 crystals were collected by centrifugation and washed three times with 10 mL of fresh DMF and ~2 mL of acetone. The as-synthesized ZIF-8 was dried under vacuum at 120 °C for 24 h, yielding off-white crystals. This procedure can be repeated by directly replacing the 15 mL of DMF in the synthetic protocol with 15 mL of STEPOSOL® MET-10U. Several batches of ZIF-8 were synthesized in STEPOSOL® MET-10U and each washed with different organic solvents including methanol, ethanol 95%, ethanol 99%, ethyl acetate and ethyl lactate, and yielded orange-brown crystals. The highest surface area was obtained after performing solvent exchange with ethanol 95% and acetone.

ZIF-8 was synthesized at room temperature in a 25-mL screw cap reaction jar containing the corresponding $Zn(NO_3)_2 \cdot 6H_2O$ (530 mg, 1.79 mmol) and 2-mIm (1195 mg, 14.58 mmol), with 17 mL of STEPOSOL® MET-10U and three drops of HNO_3 were added to the mixture with a Pasteur pipette. The reagents were stirred at 600 rpm (or medium-high speed) for 1 h and then left undisturbed in a fume hood at room temperature for 7 days. A white microcrystalline powder was collected by vacuum filtration using a Whatman™ grade 602H qualitative filter paper and washed with ~5 mL of methanol. The as-synthesized ZIF-8 was left to dry by vacuum on the filter paper in the Buchner funnel, yielding a white powder.

HKUST-1 was synthesized solvothermally at the gram-scale in a 1-L screw cap reaction jar containing the corresponding $Cu(NO_3)_2 \cdot 3H_2O$ (2254.0 mg, 9.317 mmol) and H_3BTC (1503.0 mg, 7.154 mmol), with a mixture solvent of 100 mL of STEPOSOL® MET-10U, 100 mL of ethanol 99%, and 100 mL of deionized water (Figure 2.23). After the reagents were dissolved by sonication, the sample was heated in an 80 °C oven for 3 days (72 h). Then, the sample was washed three times with 20 mL of methanol for 6 days, exchanging the solvent every second day. The organic solvent was then exchanged with acetone and washed three times with 20 mL of fresh acetone. The as-synthesized HKUST-1 was left in 20 mL of fresh acetone for one day. The as-synthesized HKUST-1 (blue-teal crystalline solid, Figure 2.23) was dried under vacuum at 150 °C for 24 h, yielding a purple-blue crystalline solid Figure 2.23).

2.3. Results and Discussion

To assess the viability of using STEPOSOL® MET-10U as a replacement for DMF in the synthesis of MOFs, we chose a small series of well-known MOFs with varying structural features, including MOF-808,[209] NU-1000,[140] HKUST-1,[211] and ZIF-8.[212] MOF-808 is a Zr_6-based MOF with open metal sites comprised of 6-connected Zr_6-cluster nodes bridged by tritopic 1,3,5-benzenetricarboxylic acid (BTC) linkers giving rise to a framework with **spn** topology (Figure 2.2).[209] NU-1000 is also a Zr_6-based MOF but is comprised of 8-connected Zr_6-cluster nodes bridged by tetratopic pyrene-based linkers, 1,3,6,8-tetrakis(*p*-benzoic acid)pyrene (H_4TBAPy), with an overall **csq** topology (Figure 2.2).[140] HKUST-1 is a Cu_2-based MOF comprised of 4-connected Cu_2-cluster nodes bridged by BTC linkers giving a **tbo** topology (Figure 2.2).[211] Finally, ZIF-8 is a Zn-based MOF comprised of Zn ion metal nodes, bridged by 2-methylimidazole (2-mIm) linkers with **sod** topology (Figure 2.2).[212] This diverse series of MOFs represents frameworks with (i) ditopic, tritopic, and tetratopic organic linkers, (ii) divalent and tetravalent metals, (ii) metal ion and cluster nodes with varying connectivity, and (iv) structures with channel-type and cage-type pore architectures. In all cases, STEPOSOL® MET-10U could be used directly in place of DMF with reaction conditions nearly identical to those of reported solvothermal procedures[117, 175, 209, 210] pertaining to reaction precursors, time, concentration, and temperature, without optimization. It should be noted that these MOFs have been synthesized using other green solvents[213-217] or green techniques,[218] but not yet with STEPOSOL® MET-10U.

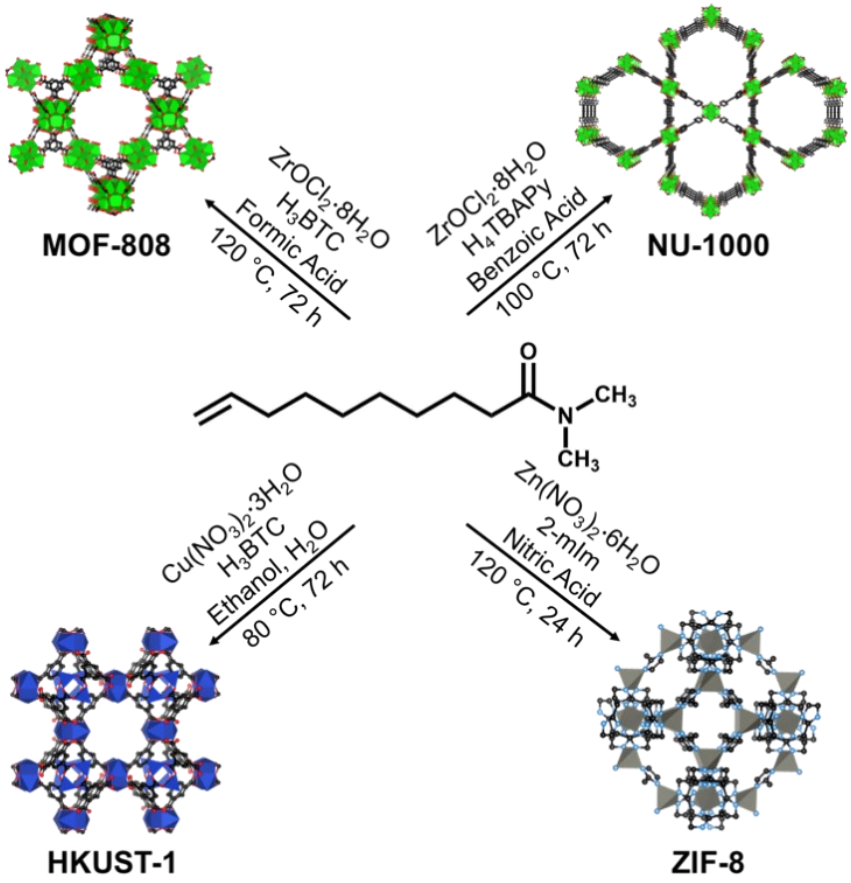

Figure 2.2. MOFs successfully synthesized solvothermally with STEPOSOL® MET-10U, including MOF-808, NU-1000, HKUST-1, and ZIF-8.

The bulk crystallinity and phase purity of the MOFs synthesized in STEPOSOL® MET-10U is confirmed by powder X-ray diffraction (PXRD) (Figure 2.3 and Figures A.1-A.2) showing that each MOF was successfully synthesized. In the case of ZIF-8, single crystals suitable for X-ray diffraction were obtained without any synthetic optimization required, further highlighting the utility of STEPOSOL® MET-10U for obtaining high quality samples.

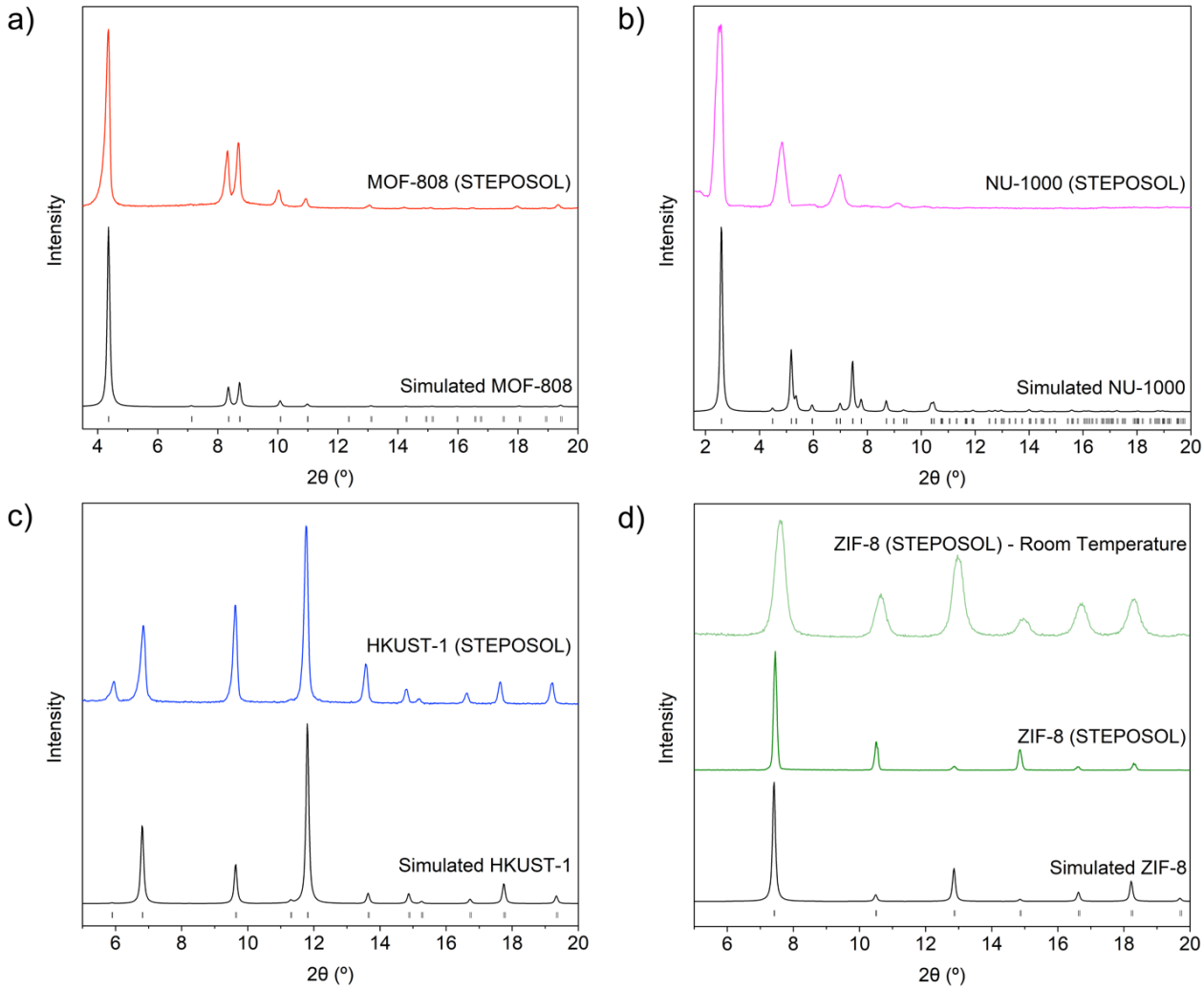

Figure 2.3. Simulated and experimental PXRD patterns of (a) MOF-808 synthesized by STEPOSOL® MET-10U, (b) NU-1000 synthesized by STEPOSOL® MET-10U (simulated pattern of NU-1000 (FIFFUX) was recorded at 100 K), (c) HKUST-1 synthesized by STEPOSOL® MET-10U, and (d) ZIF-8 synthesized by STEPOSOL® MET-10U using solvothermal and room temperature synthetic procedures.

The speed of growth for the various MOFs was monitored, and the observations have been recorded below. For MOF-808 samples, after 2 hours of being placed in an oven at 120 °C, precipitate forms, where there is slightly more present for the sample synthesized using DMF compared to STEPOSOL® MET-10U. Then, after 7 hours of being placed in the oven, the MOF precipitate consistently increases for both samples, where there is more precipitate present for the sample synthesized using DMF. The following day (second day), the samples of MOF-808 synthesized using DMF and STEPOSOL® MET-10U have roughly the same amount of precipitate

produced in their respective vials. The next day (third day), the amount of precipitate produced appears to be the same as the previous day. By using the synthetic procedure described above, the yield of the MOF-808 samples post-activation (synthesized using DMF and STEPOSOL® MET-10U) varies from 50 to 55 mg.

For NU-1000 samples, on the first day after being placed in an oven at 100 °C, there is a small amount of growth of MOF precipitate for the samples synthesized using DMF and STEPOSOL® MET-10U. The following day (second day), the sample of NU-1000 synthesized using DMF has a greater amount of precipitate compared to the sample of NU-1000 synthesized using STEPOSOL® MET-10U. The next day (third day), the amount of precipitate produced appears to be the same as the previous day. By using the synthetic procedure described above, the yield of the NU-1000 samples post-activation varies from 30 to 35 mg when using DMF as the solvent, and 25 to 30 mg when using STEPOSOL® MET-10U as the solvent.

For HKUST-1 samples, after 2 hours of being placed in an oven at 80 °C, precipitate forms, where there is slightly more present for the sample synthesized using DMF compared to STEPOSOL® MET-10U. Then, after 7 hours of being placed in the oven, the MOF precipitate consistently increases for both samples, where there is more precipitate present for the sample synthesized using DMF. The following day (second day), the sample of HKUST-1 synthesized using DMF has a greater amount of MOF growth in the form of precipitate relative to the sample synthesized using STEPOSOL® MET-10U, in their respective vials. The next day (third day), the amount of precipitate produced appears to have increased compared to the second day for the samples of HKUST-1 synthesized using DMF and STEPOSOL® MET-10U. By using the synthetic procedure described above, the yield of the HKUST-1 samples post-activation varies from 35 to 40 mg when using DMF as the solvent, and 20 to 22 mg when using STEPOSOL® MET-10U as the solvent.

For ZIF-8 samples, after 2 hours of being placed in an oven at 120 °C, the colour of the solvent changes, where it becomes yellow for the samples synthesized using DMF and orange-brown for the sample synthesized using STEPOSOL® MET-10U. Then, after 7 hours of being placed in the oven, the colours of the solvents become more prominent, where it becomes slightly darker yellow for the sample synthesized using DMF and darker orange-brown for the samples synthesized using STEPOSOL® MET-10U. The following day, the formation of ZIF-8 crystallites are present on the walls of the vials for the samples synthesized using DMF and STEPOSOL®

MET-10U, and by eye, have roughly the same amount of crystallites produced in their respective vials. By using the synthetic procedure described above, the yield of the MOF-808 samples post-activation (synthesized using DMF and STEPOSOL® MET-10U) varies from 30 to 35 mg.

For the ZIF-8 sample synthesized at room temperature, after stirring the starting materials for 1 hr and leaving the sample undisturbed in a fume hood for a time period of 7 days, the growth of MOF in the form of a precipitate gradually increases. By using the synthetic procedure described above, the yield of the ZIF-8 sample post-activation (synthesized STEPOSOL® MET-10U and at room temperature) varies from 75 to 80 mg.

Table 2.1. Percent yield of MOFs post-activation.

MOF	Percent Yield (%) DMF	Percent Yield (%) STEPOSOL® MET-10U
MOF-808	78 – 86	78 – 86
NU-1000	47 – 55	39 – 47
HKUST-1	72 – 83	41 – 46
ZIF-8	11 – 13	11 – 13
ZIF-8 (Room Temperature)	N/A	4.5 – 4.8

The surface area and porosity of the MOFs synthesized in STEPOSOL® MET-10U was determined and compared to values obtained for materials synthesized using standard solvothermal procedures in DMF. The MOFs were characterized using N_2 adsorption-desorption analysis performed at 77 K, where each activated MOF demonstrates the expected, reversible isotherm. This includes Type I(b) for MOF-808, Type IV(b) for NU-1000, and Type I(a) for both HKUST-1 and ZIF-8 (Figure 2.4). Moreover, the MOFs exhibit Brunauer-Emmett-Teller (BET) areas that are comparable to those obtained for the MOFs synthesized with DMF, in our hands, using identical procedures and reagents [117, 209, 210, 219] with values of 1720 (1835), 1635 (1865), 1860 (1815), 670 (1435), and 1155 $m^2 g^{-1}$ for MOF-808, NU-1000, HKUST-1, ZIF-8 and ZIF-8 (room temperature), synthesized in STEPOSOL® MET-10U and (DMF), respectively (Table 2.2 and Figures A.3-A.9). Pore size distribution analysis calculated using non-local density functional theory (NLDFT) for the MOFs synthesized with STEPOSOL® MET-10U, show the expected pore diameters of 18.4 Å, 29.5 Å, and 12.4 Å, 15.2 Å, and 15.2 Å for MOF-808, NU-1000, HKUST-1, ZIF-8, and ZIF-8 (room temperature) respectively (Figures A.10-A.11). Although synthetic protocols using

STEPOSOL® MET-10U did not need to be modified, the solvent exchange procedure performed prior to MOF activation under heat and vacuum required optimization to obtain surface areas comparable to those previously reported. An array of organic solvents that are miscible with STEPOSOL® MET-10U, and more environmentally friendly than DMF,[220] were tested for solvent exchange, including butanol, isopropanol, methanol, ethanol, ethyl acetate, ethyl lactate, and toluene. The highest surface areas were obtained when washing with isopropanol for MOF-808, methanol for HKUST-1, ethanol 95% for ZIF-8, and methanol for ZIF-8 (room temperature) (Figures A.4-A.6). Therefore, in these examples, DMF was replaced with a greener alternative in both the synthesis and solvent exchange processes. Solvent exchange and activation of NU-1000, however, was most successful using DMF (Figure A.3b), meaning that the amount of DMF used to synthesize and activate NU-1000 was minimized, but could not be eliminated entirely from the process.

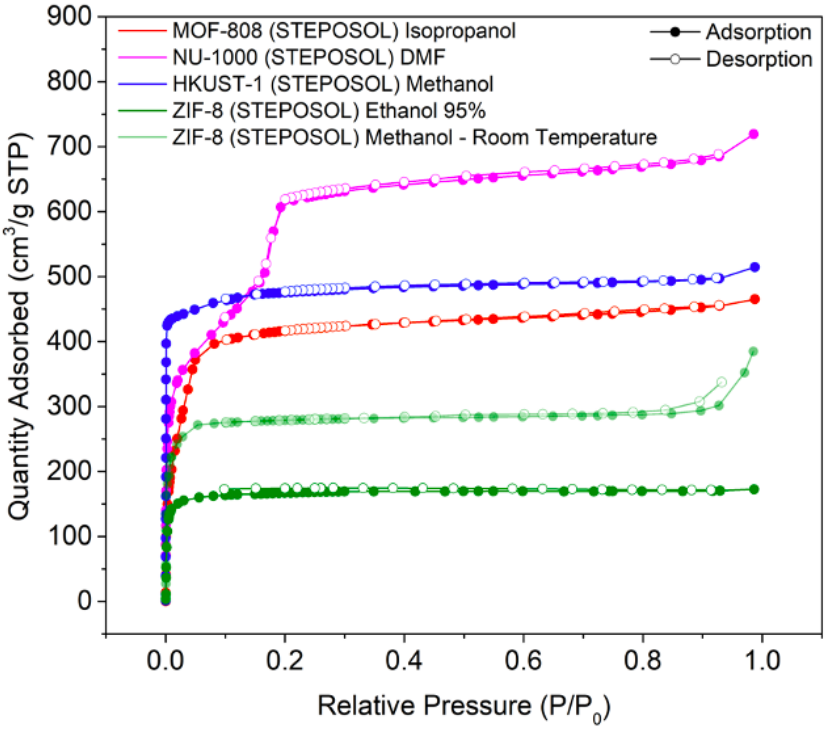

Figure 2.4. Nitrogen adsorption-desorption isotherms of MOF-808 (Type I(b)) synthesized by STEPOSOL® MET-10U and washed with isopropanol, NU-1000 (Type IV(b)) synthesized by STEPOSOL® MET-10U and washed with DMF, HKUST-1 (Type I(a)) synthesized by STEPOSOL® MET-10U and washed with methanol, ZIF-8 (Type I(a)) synthesized by STEPOSOL® MET-10U (solvothermal) and washed with ethanol 95%, and ZIF-8 (Type I(a)) synthesized by STEPOSOL® MET-10U (room temperature) and washed with methanol.

Table 2.2. BET surface areas, pore volumes and percent yield (post-activation) for MOFs synthesized using DMF and STEPOSOL® MET-10U.

MOF	BET Surface Area (m^2 g^{-1})		Measured Pore Volume (cm^3 g^{-1})		Literature Pore Volume (cm^3 g^{-1}) using DMF	Percent Yield (%)	
	DMF	STEPOSOL® MET-10U	DMF	STEPOSOL® MET-10U		DMF	STEPOSOL® MET-10U
MOF-808	1835	1720	1.02	0.70	0.84[209]	78 – 86	78 – 86
NU-1000	1865	1635	1.06	1.07	1.40[140]	47 – 55	39 – 47
HKUST-1	1815	1860	0.79	0.82	0.78[221]	72 – 83	41 – 46
ZIF-8	1435	670	0.44	0.23	0.63[212]	11 – 13	11 – 13
ZIF-8 (Room Temperature)	N/A	1155	N/A	0.43	N/A	N/A	4.5 – 4.8

In order to evaluate the thermal stability of the activated MOFs synthesized with STEPOSOL® MET-10U, and compare to those synthesized in DMF, we performed thermogravimetric analysis (TGA). In all cases, the thermogram was in excellent agreement with those obtained for the MOFs synthesized in DMF (Figures 2.5-2.6 and Tables 2.3-2.4).

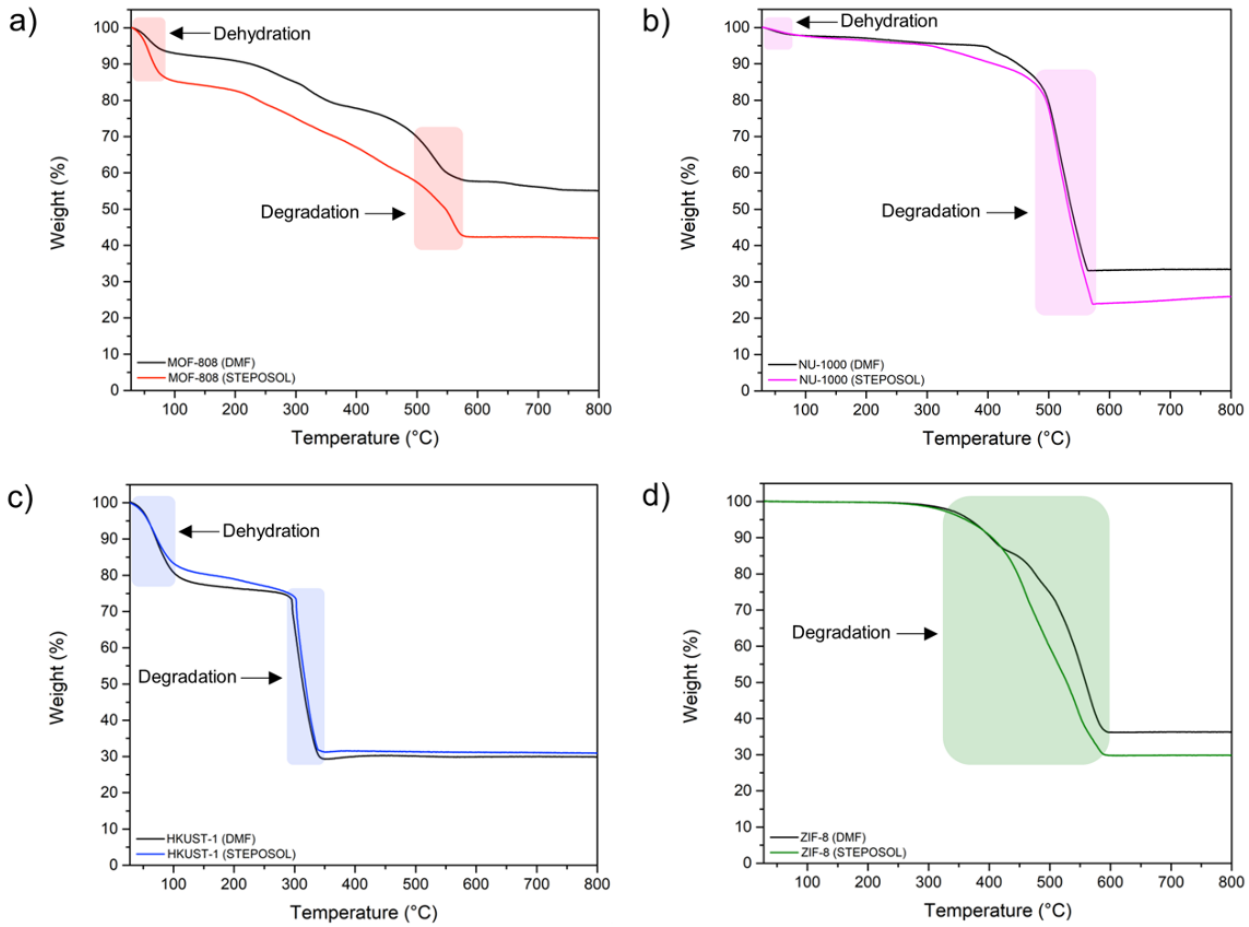

Figure 2.5. TGA curves of (a) MOF-808 synthesized by STEPOSOL® MET-10U and by DMF, (b) NU-1000 synthesized by STEPOSOL® MET-10U and by DMF, (c) HKUST-1 synthesized by STEPOSOL® MET-10U and by DMF, and (d) ZIF-8 synthesized by STEPOSOL® MET-10U and by DMF.

Table 2.3. TGA $\%_{\text{Metal Oxide}}$ and $\%_{\text{Metal}}$ for MOF samples prepared by STEPOSOL® MET-10U and DMF (in the presence of dehydration, TGA $\%_{\text{Metal Oxide}}$ and $\%_{\text{Metal}}$ residues have been corrected).

MOF	Theoretical $\%_{\text{Metal Oxide}}$	Theoretical $\%_{\text{Metal}}$	MOF	TGA $\%_{\text{Metal Oxide}}$	TGA $\%_{\text{Metal}}$
MOF-808	54.0	40.0	MOF-808 (DMF)	59.6	44.1
			MOF-808 (STEPOSOL)	50.6	37.4
NU-1000	34.0	25.1	NU-1000 (DMF)	34.7	25.7
			NU-1000 (STEPOSOL)	25.5	18.9
HKUST-1	39.5	31.5	HKUST-1 (DMF)	37.5	30.0
			HKUST-1 (STEPOSOL)	39.0	31.1
ZIF-8	35.6	28.7	ZIF-8 (DMF)	36.6	29.4
			ZIF-8 (STEPOSOL)	31.0	24.9

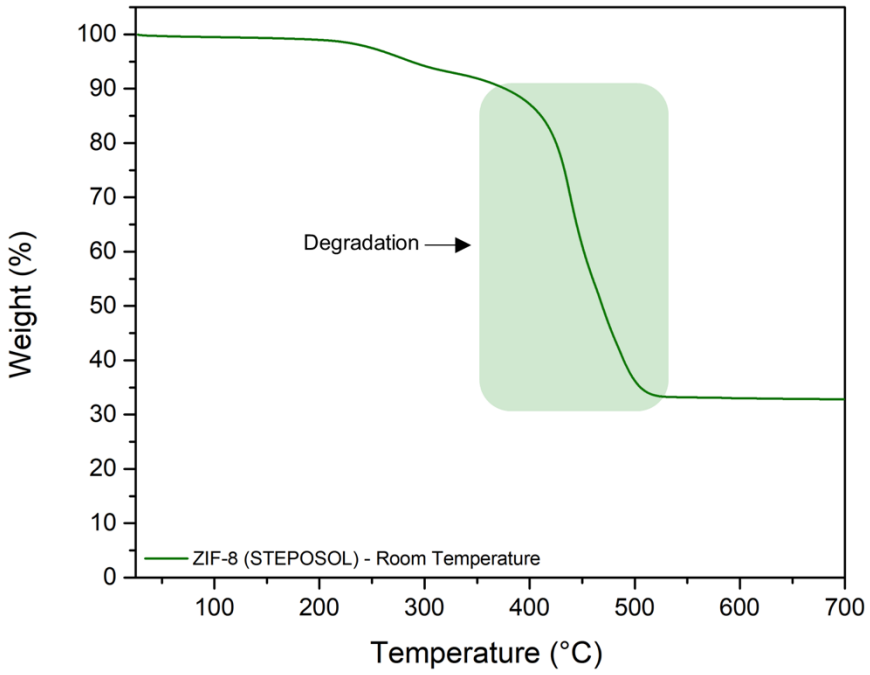

Figure 2.6. TGA curve of ZIF-8 synthesized by STEPOSOL® MET-10U at room temperature.

Table 2.4. TGA $\%_{\text{Metal Oxide}}$ and $\%_{\text{Metal}}$ for ZIF-8 prepared by STEPOSOL® MET-10U at room temperature.

MOF	Theoretical $\%_{\text{Metal Oxide}}$	Theoretical $\%_{\text{Metal}}$	MOF	TGA $\%_{\text{Metal Oxide}}$	TGA $\%_{\text{Metal}}$
ZIF-8	35.6	28.7	ZIF-8 (STEPOSOL) Room Temperature	32.8	26.4

The MOFs were further characterized using diffuse reflectance infrared Fourier transform spectroscopy (DRIFTS) to gain information about the infrared active functional groups in the materials. The DRIFTS data demonstrates the expected absorption bands corresponding to carboxylate (MOF-808, NU-1000, and HKUST-1) and methylimidazolate (ZIF-8) linker stretching (Figures 2.7-2.8), as well as O-H stretching bands corresponding to the terminal –OH ligands in the node of MOF-808 and NU-1000 (Figures 2.7-2.8).

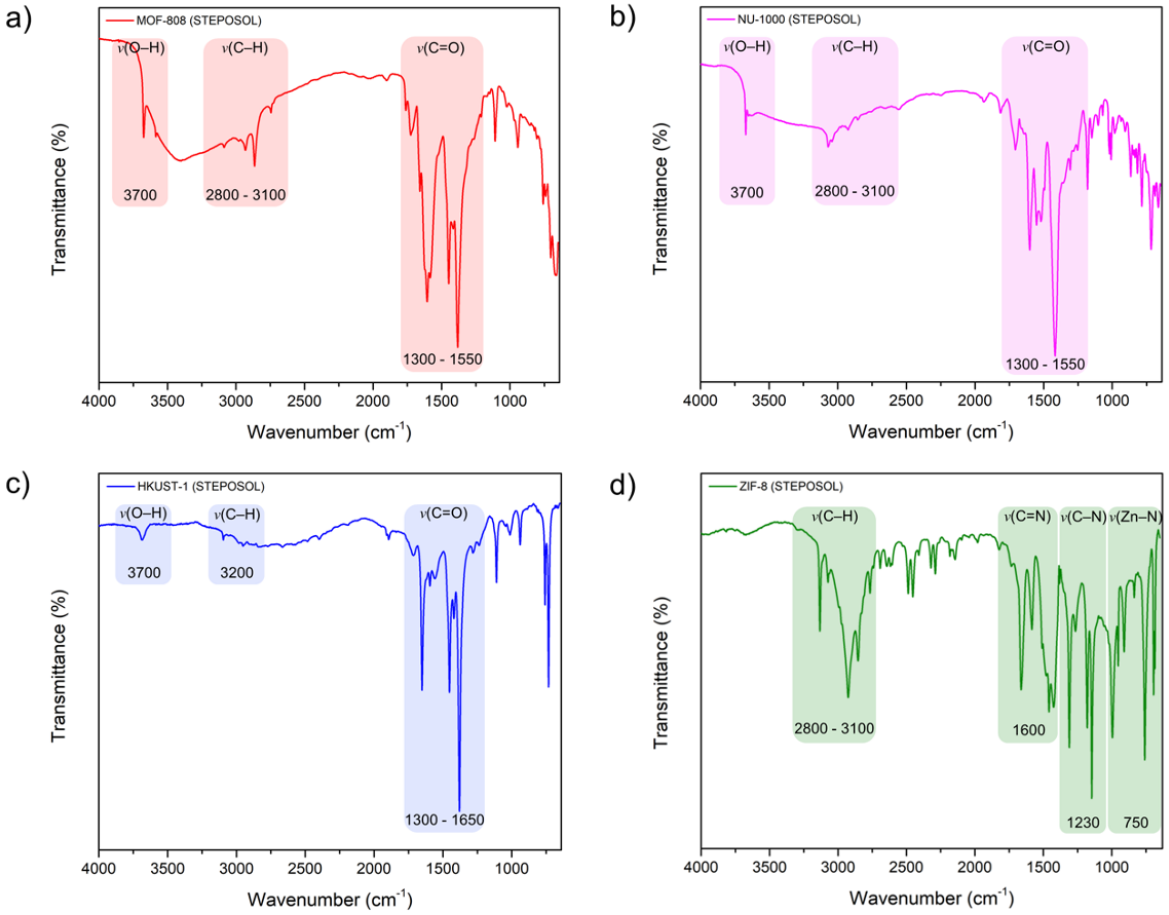

Figure 2.7. DRIFTS spectra of (a) MOF-808, (b) NU-1000, (c) HKUST-1, and (d) ZIF-8 synthesized by STEPOSOL® MET-10U.

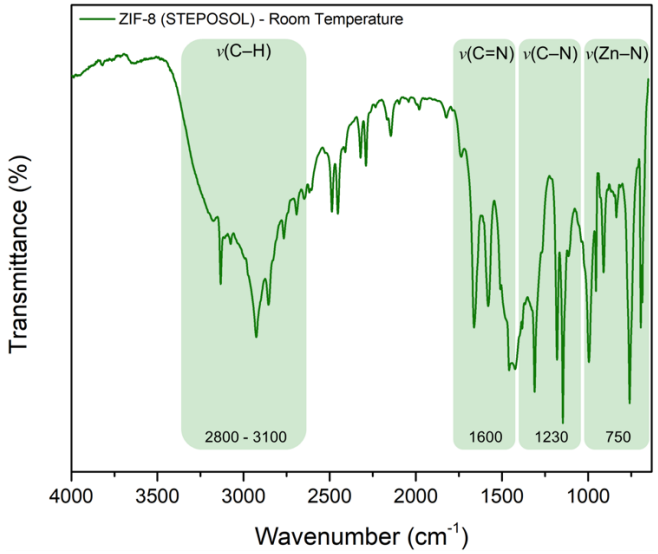

Figure 2.8. DRIFTS spectrum of ZIF-8 synthesized by STEPOSOL® MET-10U at room temperature.

Proton nuclear magnetic resonance (^{1}H-NMR) spectroscopy of the digested MOF samples synthesized in STEPOSOL® MET-10U shows the linker purity and incorporation into the MOF structures, with only trace amounts of STEPOSOL® MET-10U leftover post-activation (Figures 2.9-2.15).

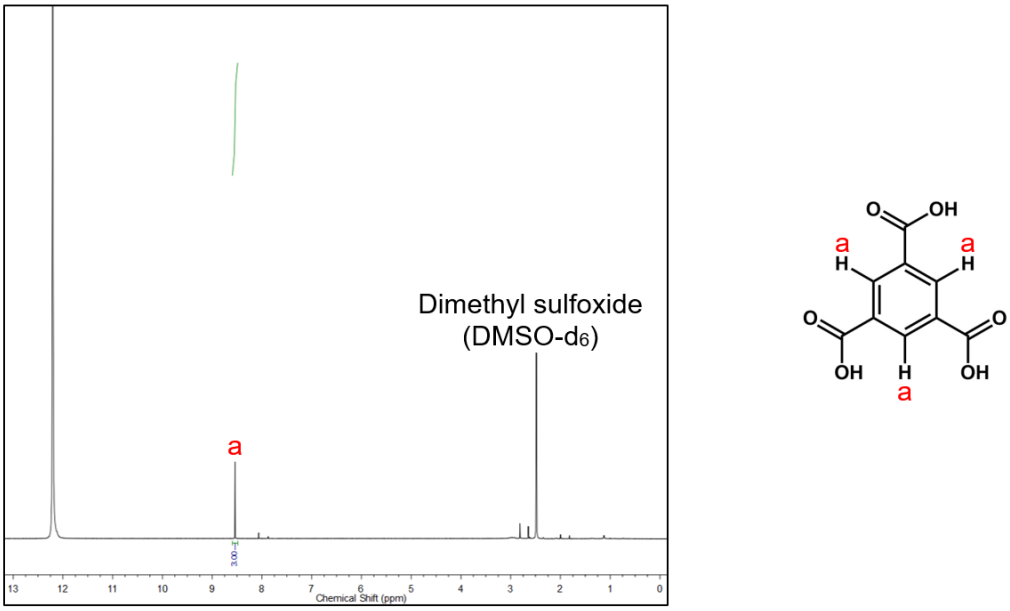

Figure 2.9. ^{1}H-NMR spectrum of a digested sample of MOF-808 synthesized by STEPOSOL® MET-10U, in D_2SO_4 and DMSO-d_6.

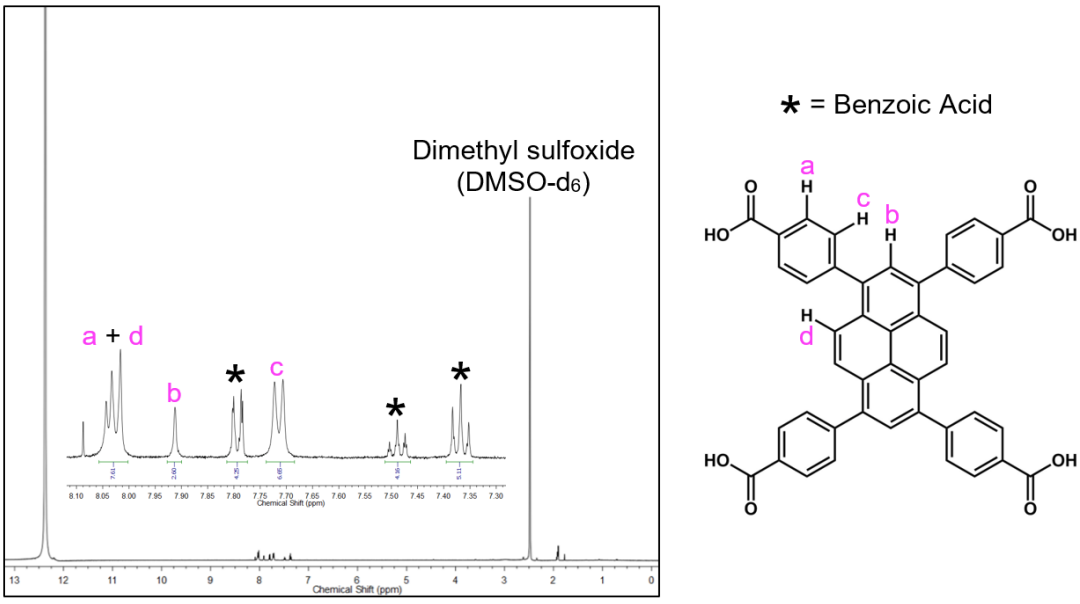

Figure 2.10. ^{1}H-NMR spectrum of a digested sample of NU-1000 synthesized by STEPOSOL® MET-10U, in D_2SO_4 and DMSO-d_6.

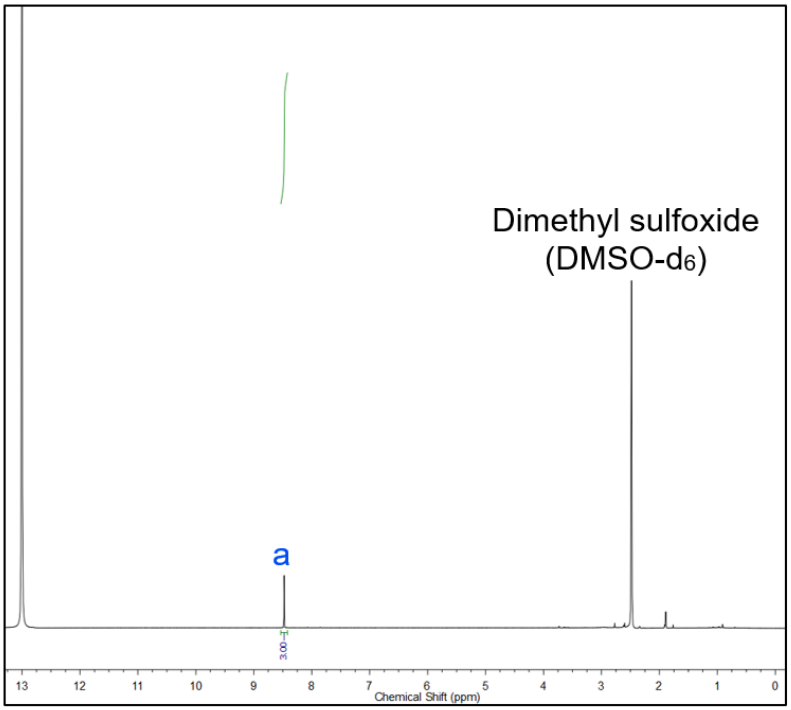

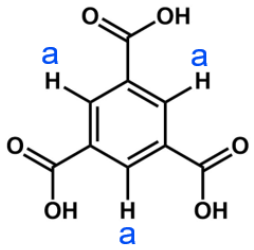

Figure 2.11. ^{1}H-NMR spectrum of a digested sample of HKUST-1 synthesized by STEPOSOL® MET-10U, in D_2SO_4 and DMSO-d_6.

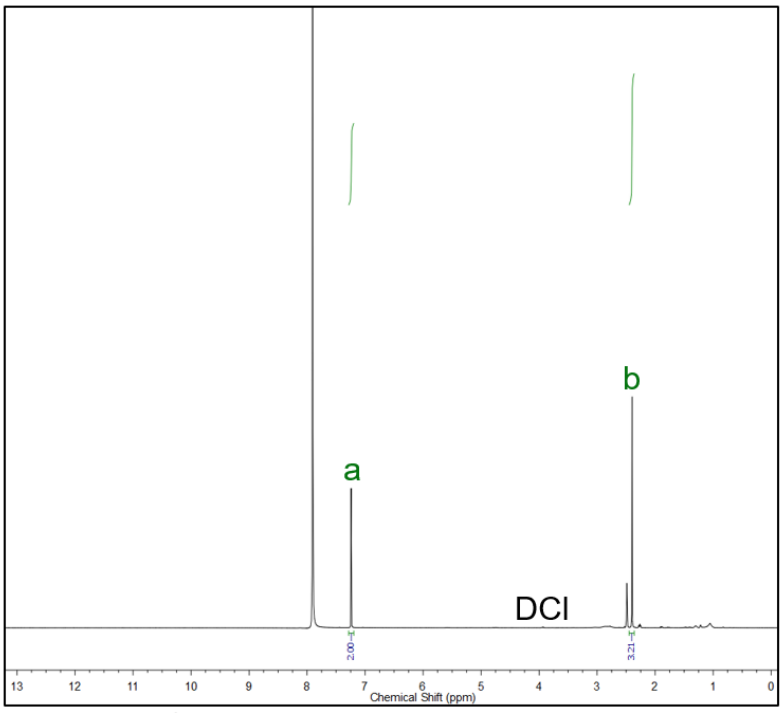

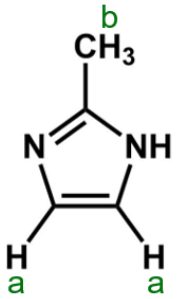

Figure 2.12. ^{1}H-NMR spectrum of a digested sample of ZIF-8 synthesized by STEPOSOL® MET-10U, in D_2O acidified with DCl and DMSO-d_6.

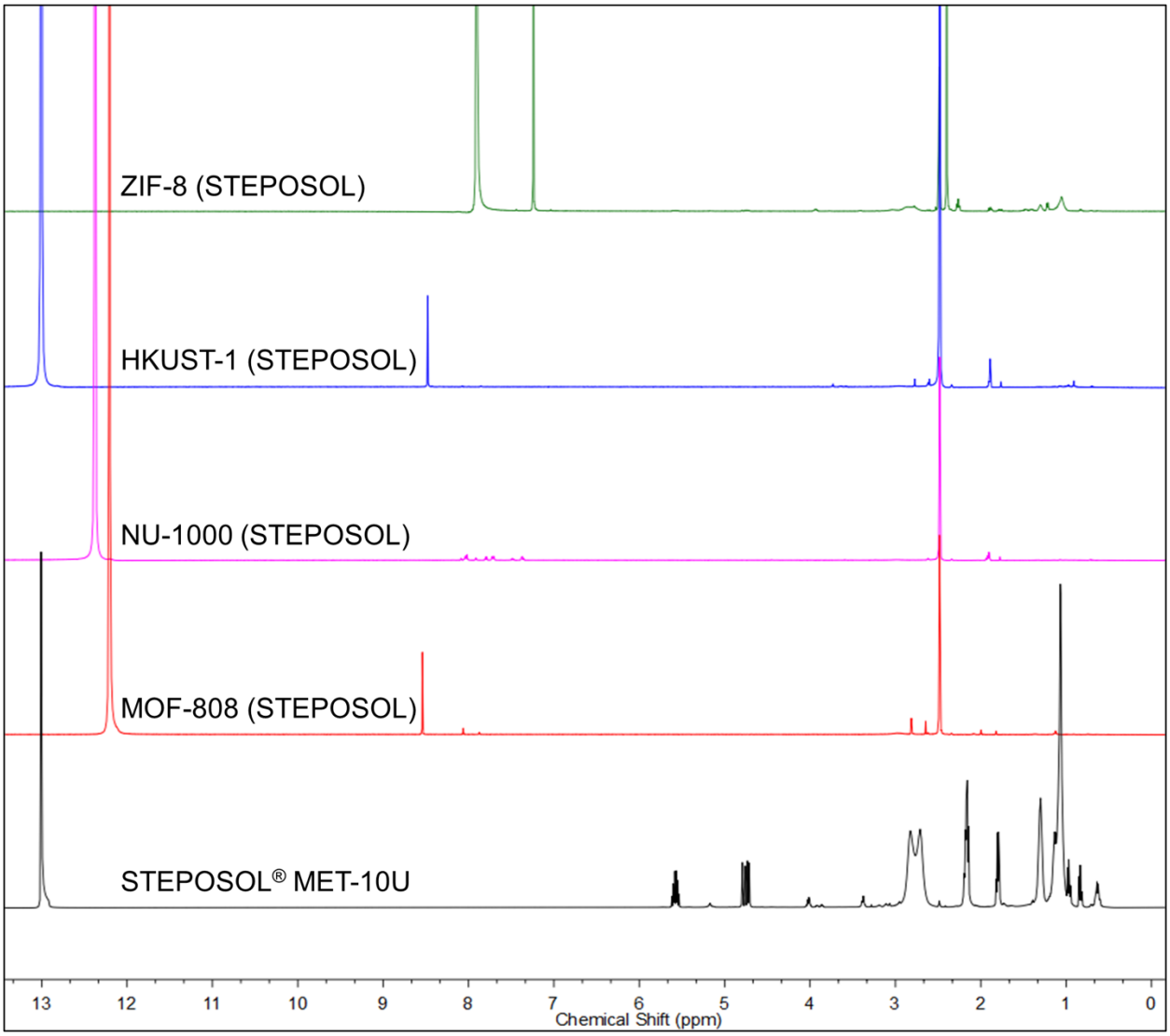

Figure 2.13. ^{1}H-NMR spectra of STEPOSOL® MET-10U in D_2SO_4 and DMSO-d_6, a digested sample of MOF-808 (STEPOSOL) in D_2SO_4 and DMSO-d_6, a digested sample of NU-1000 (STEPOSOL) in D_2SO_4 and DMSO-d_6, a digested sample of HKUST-1 (STEPOSOL) in D_2SO_4 and DMSO-d_6, and a digested sample of ZIF-8 (STEPOSOL) in D_2O acidified with DCl and DMSO-d_6.

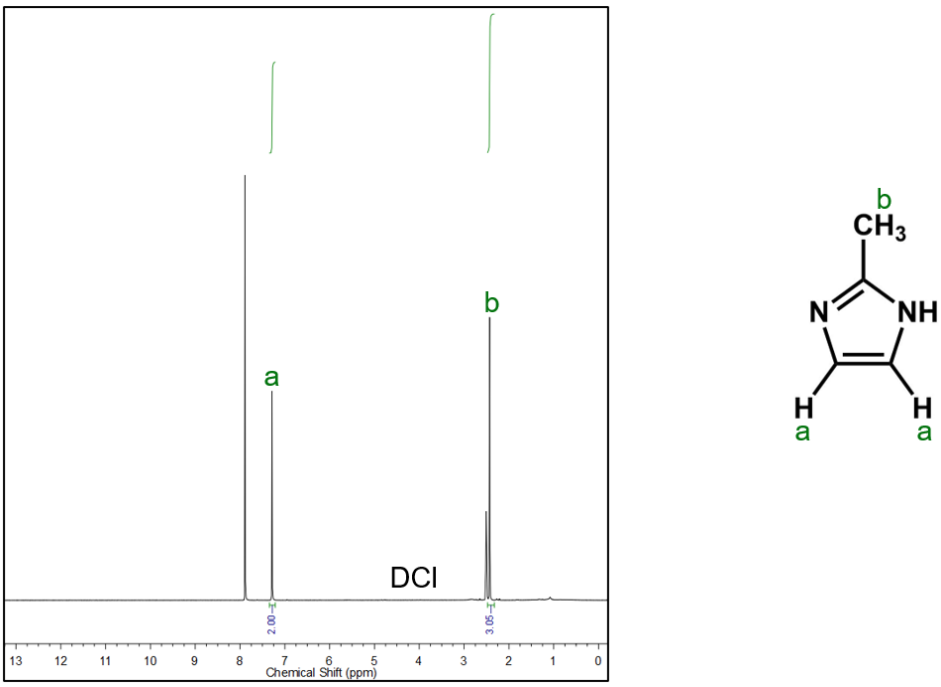

Figure 2.14. ^{1}H-NMR spectrum of a digested sample of ZIF-8 synthesized by STEPOSOL® MET-10U at room temperature, in D_2O acidified with DCl and DMSO-d_6.

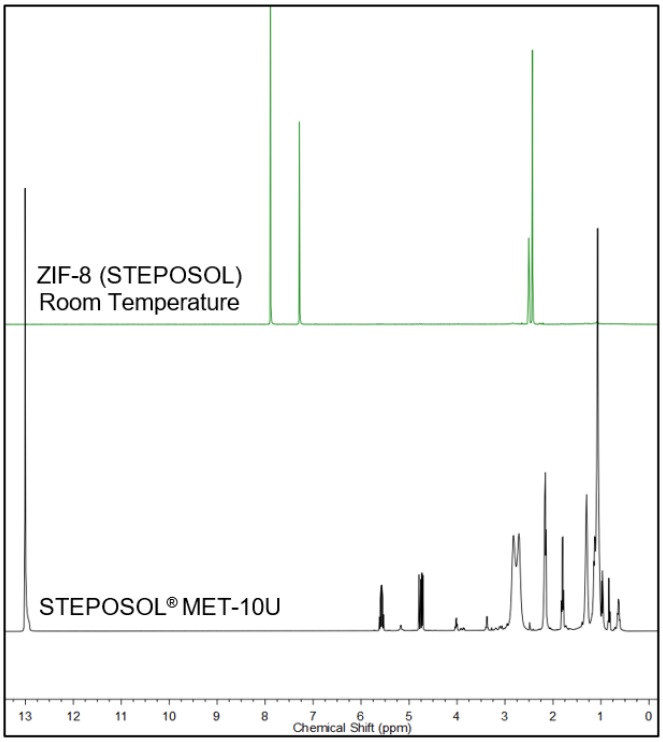

Figure 2.15. ^{1}H-NMR spectra of STEPOSOL® MET-10U in D_2SO_4 and DMSO-d_6, and of a digested sample of ZIF-8 synthesized by STEPOSOL® MET-10U at room temperature, in D_2O acidified with DCl and DMSO-d_6.

Finally, in order to further explore the samples synthesized with STEPOSOL® MET-10U, and compare to those synthesized by DMF, scanning electron microscopy (SEM) images were captured to confirm the morphology of the MOF crystallites. In each case the expected morphology was demonstrated. Specifically, octahedral microcrystallites for MOF-808, hexagonal rods with rectangular facets for NU-1000, octahedral microcrystallites for HKUST-1, and a mixture of hexagonal-faceted crystals, cubic crystals, and rhombic dodecahedrons for ZIF-8 (Figures 2.16-2.20).

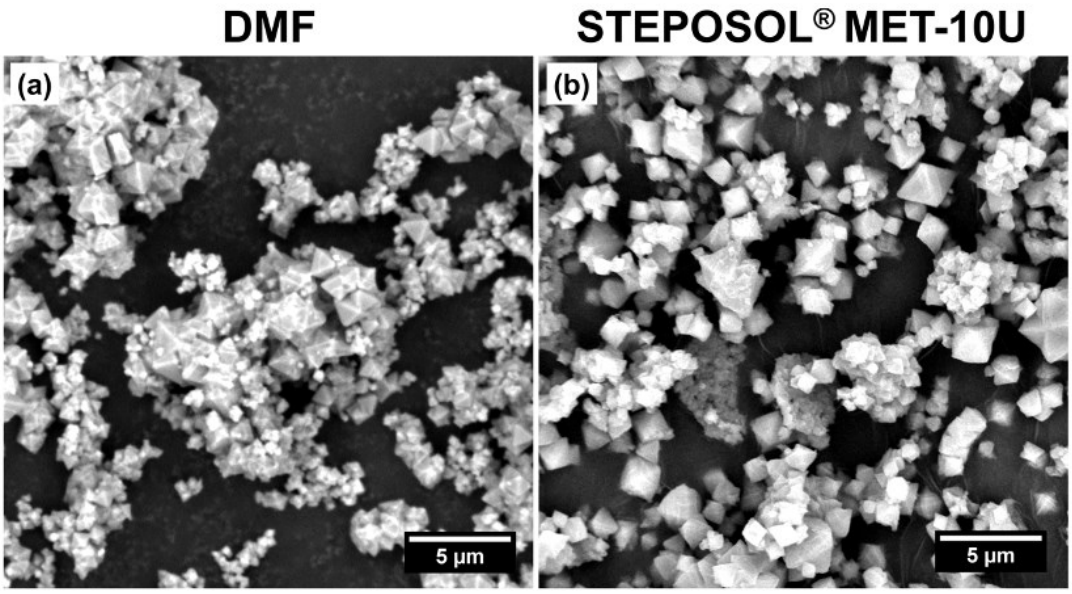

Figure 2.16. SEM micrographs of (a) MOF-808 synthesized by DMF and (b) MOF-808 synthesized by STEPOSOL® MET-10U, showing octahedral microcrystallites.

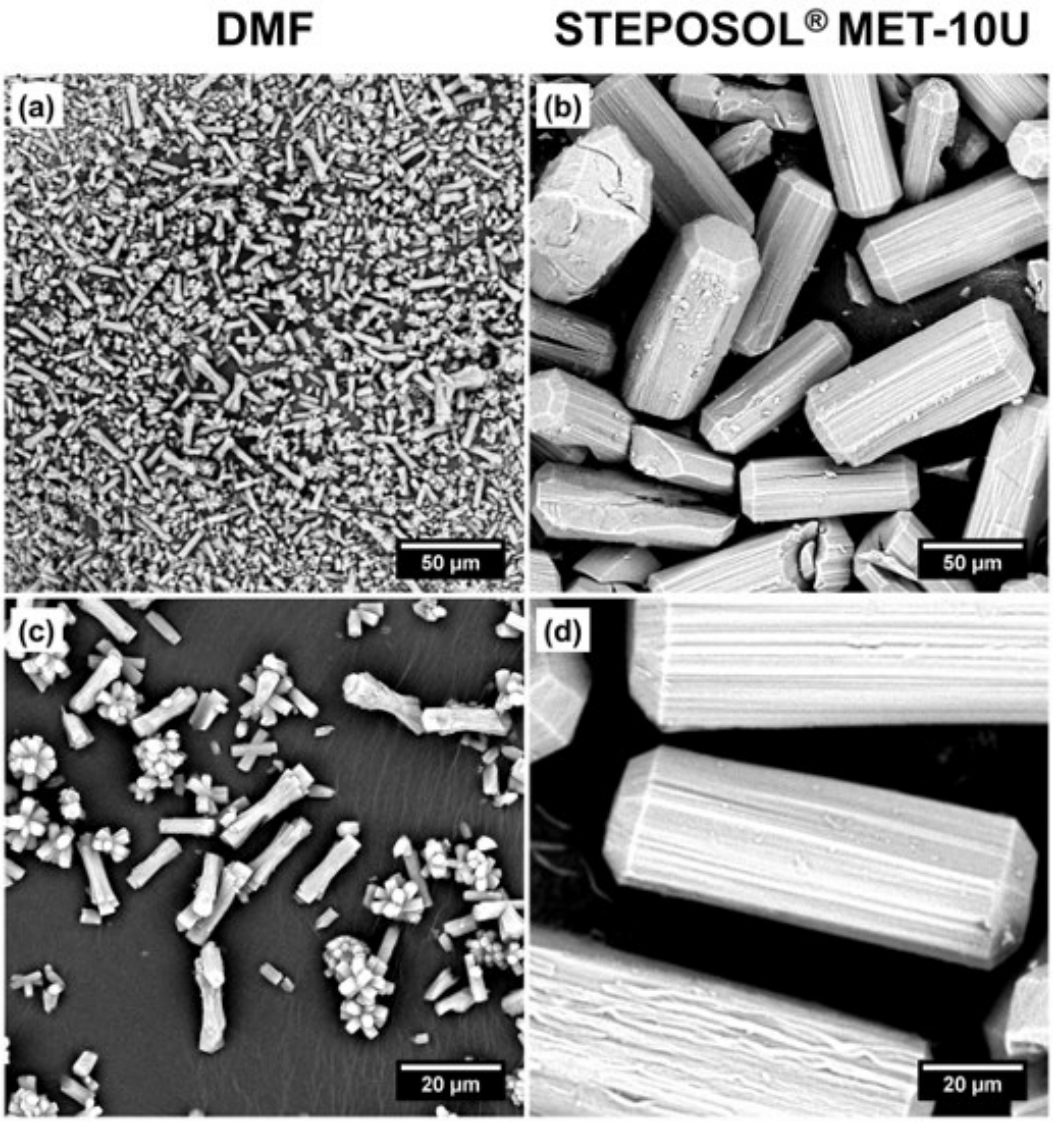

Figure 2.17. SEM micrographs of (a) NU-1000 synthesized by DMF, (b) NU-1000 synthesized by STEPOSOL® MET-10U, (c) NU-1000 synthesized by DMF and captured using a greater magnification, and (d) NU-1000 synthesized by STEPOSOL® MET-10U and captured using a greater magnification, showing smooth hexagonal rods.

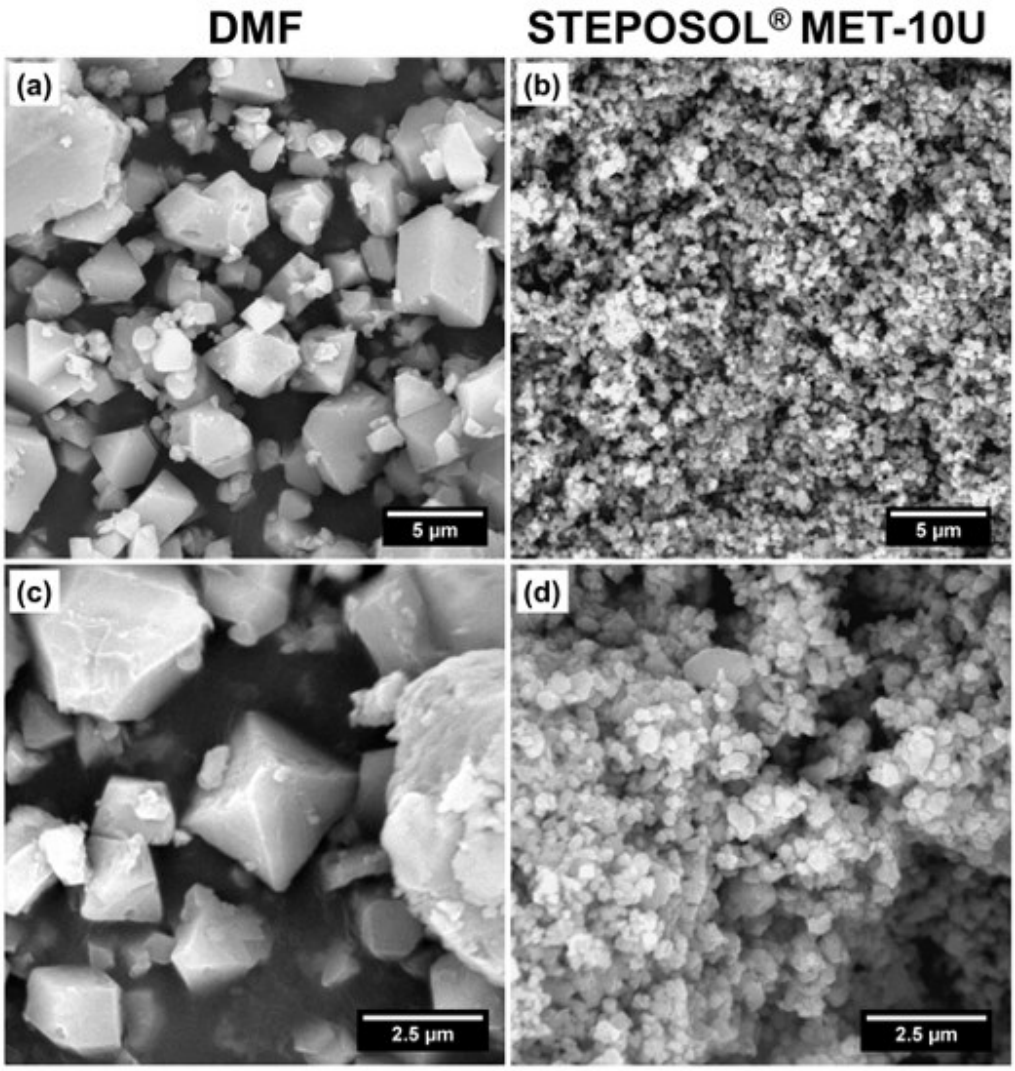

Figure 2.18. SEM micrographs of (a) HKUST-1 synthesized by DMF, (b) HKUST-1 synthesized by STEPOSOL® MET-10U, (c) HKUST-1 synthesized by DMF and captured using a greater magnification, and (d) HKUST-1 synthesized by STEPOSOL® MET-10U and captured using a greater magnification, showing octahedral microcrystallites.

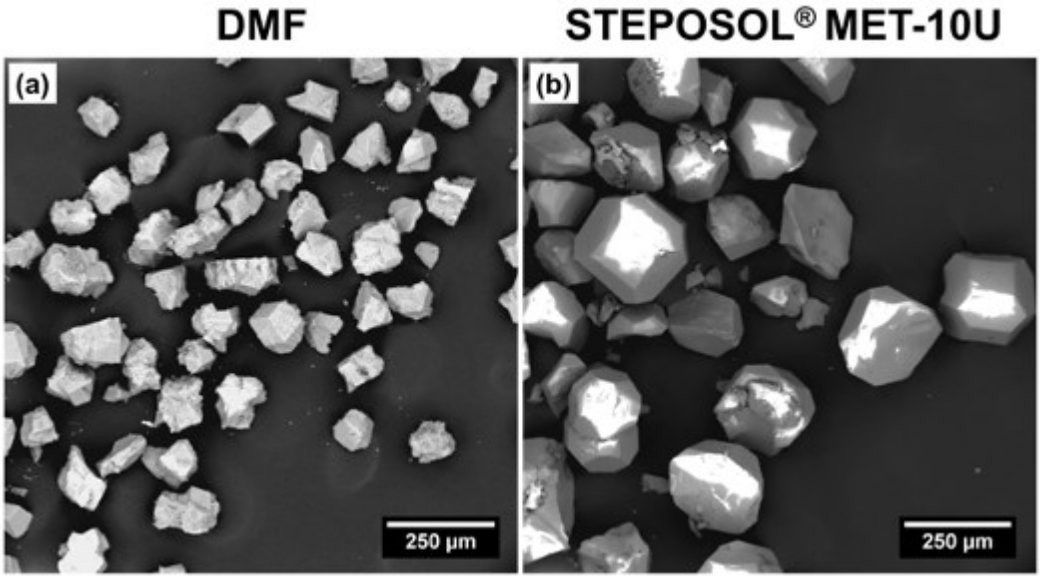

Figure 2.19. SEM micrographs of (a) ZIF-8 synthesized by DMF showing a mixture of cubic crystals and rhombic dodecahedrons, and (b) ZIF-8 synthesized by STEPOSOL® MET-10U showing a mixture of hexagonal-faceted crystals, rhombic dodecahedrons and truncated rhombic dodecahedrons.

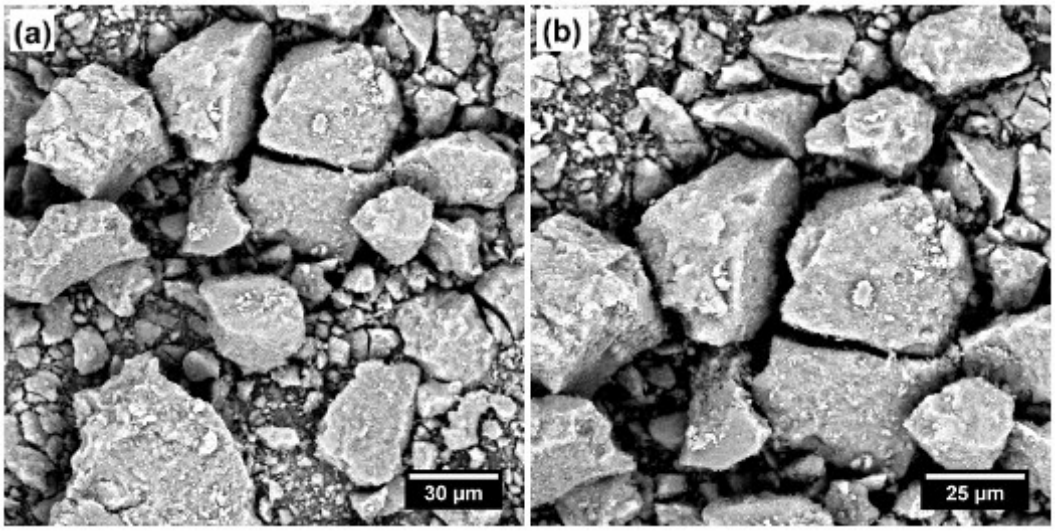

Figure 2.20. SEM micrographs of (a) ZIF-8 synthesized by STEPOSOL® MET-10U at room temperature, and (b) ZIF-8 synthesized by STEPOSOL® MET-10U at room temperature and captured using a greater magnification.

Interestingly, the crystallite size of the MOFs synthesized in DMF varies from those synthesized in STEPOSOL® MET-10U. In particular, the crystallites of MOF-808, NU-1000, and

ZIF-8 synthesized in STEPOSOL® MET-10U are all larger than those synthesized in DMF, suggesting that STEPOSOL® MET-10U has potential to be of interest in MOF synthesis where single crystals suitable for X-ray diffraction are desired (Figures 2.16-2.22).

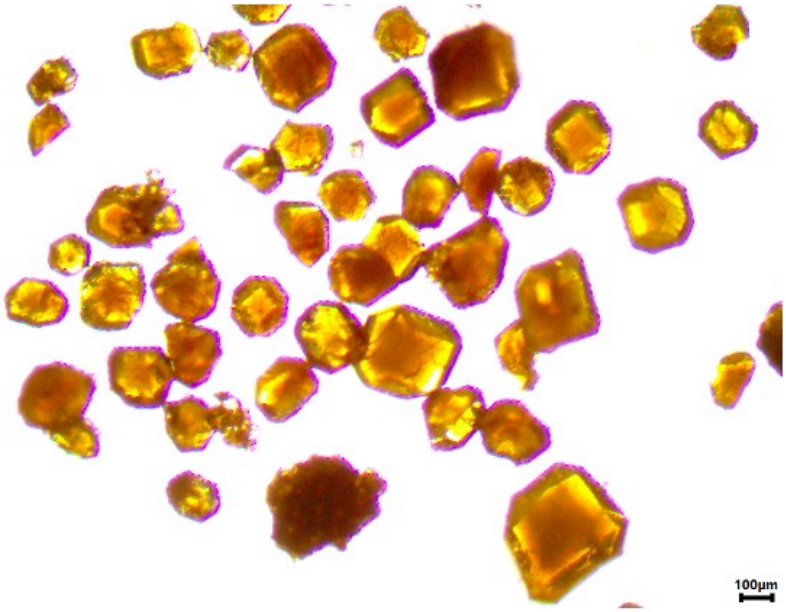

Figure 2.21. Optical micrograph of bulk microcrystalline ZIF-8 synthesized by STEPOSOL® MET-10U.

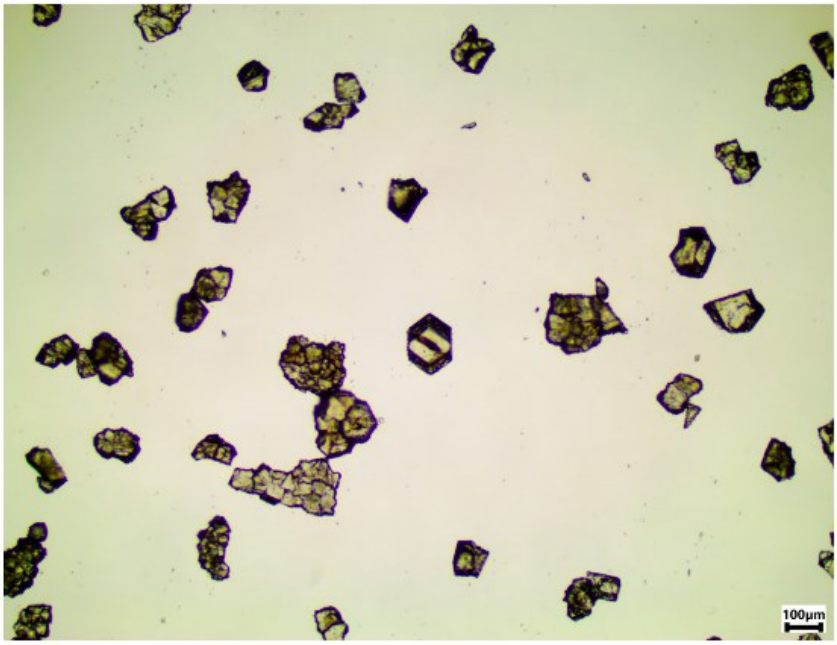

Figure 2.22. Optical micrograph of bulk microcrystalline ZIF-8 synthesized by DMF.

To evaluate the cost and scalability of MOFs synthesized in STEPOSOL® MET-10U, a cost analysis and representative large-scale synthesis was performed. Using solvent list prices in Canadian dollars for comparison (Tables A.1-A.5), we found that the solvent costs for MOF syntheses performed in STEPOSOL® MET-10U are equivalent or less expensive by a factor up to 6 depending on the MOF.

In addition, the synthesis of HKUST-1 in STEPOSOL® MET-10U was performed on the gram-scale (Figure 2.23), yielding 1.2 g of activated MOF with a surface area of 1895 m^2 g^{-1} (Figure 2.24).

Starting Materials:
1. Metal: $Cu(NO_3)_2 \cdot 3H_2O$
2. Linker: H_3BTC

Solvent and Modulator:
1. STEPOSOL® MET-10U
2. Ethanol
3. Deionized Water

HKUST-1 (STEPOSOL)
in 80 °C oven for 3 days

HKUST-1 (STEPOSOL)
reaction after 3 days

HKUST-1 (STEPOSOL)
pre-activation

HKUST-1 (STEPOSOL)
post-activation, 1.2 g
(under vacuum and heat)

Figure 2.23. Photographs detailing the gram-scale synthesis of HKUST-1 in STEPOSOL® MET-10U.

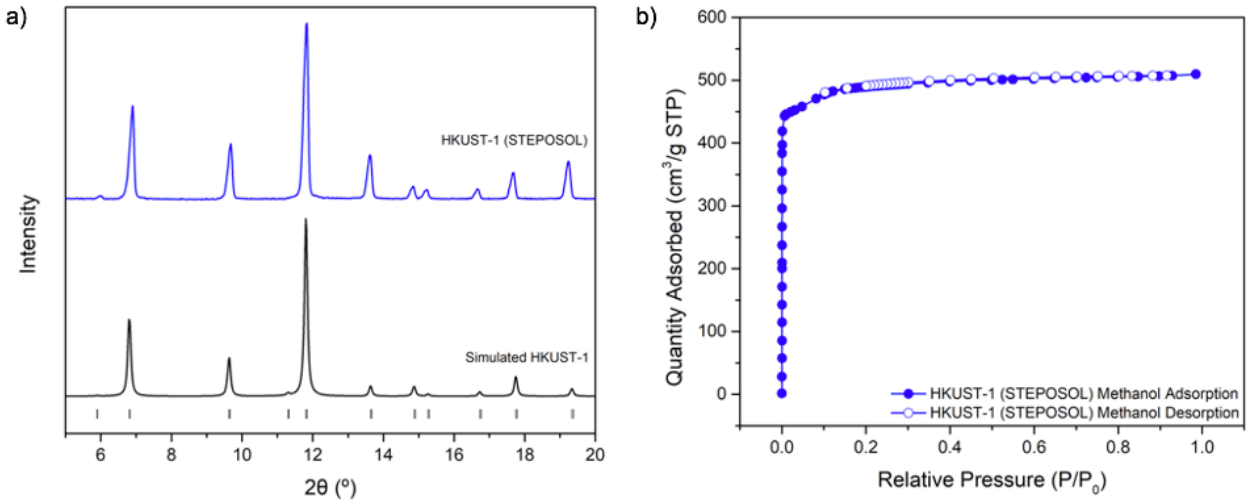

Figure 2.24. Large scale synthesis of HKUST-1. (a) PXRD pattern of HKUST-1 synthesized by STEPOSOL® MET-10U, at the gram-scale and (b) N_2 adsorption-desorption isotherm and BET surface area value of HKUST-1 (Type I(a)) synthesized by STEPOSOL® MET-10U and washed with methanol and acetone (S_{BET} = 1895 m^2 g^{-1}).

2.4. Conclusions

The use of green solvent alternatives to DMF for the synthesis of MOFs, particularly where synthetic conditions do not have to be optimized significantly from those reported in DMF, is highly desired and an integral part of the green chemistry toolbox. The effectiveness of STEPOSOL® MET-10U, a bioderived solvent, was assessed for the synthesis of four structurally diverse MOFs, MOF-808, NU-1000, HKUST-1 and ZIF-8, and proved to be successful in each case. Furthermore, the MOFs synthesized with STEPOSOL® MET-10U demonstrate crystallinity, surface area and porosity, morphology, and thermal stability comparable to those synthesized using standard procedures in DMF. The high boiling point of STEPOSOL® MET-10U is also of interest for exploratory MOF synthesis, where higher reaction temperatures could produce new phases not accessible in standard solvothermal procedures using DMF. The use of STEPOSOL® MET-10U for MOF synthesis holds significant promise, and allows for less hazardous chemical synthesis, as well as the use of renewable feedstocks and safer solvents, which is of utmost importance in both academic and industry settings where the synthesis and study of MOFs is flourishing.

Chapter 3

Thiol-Functionalized Metal–Organic Frameworks as Drug Delivery Platforms for Ophthalmic Therapeutics

3.1. Introduction to Ophthalmic Drug Delivery and MOFs

Ophthalmic diseases – an umbrella term for a vast number of eye conditions – include age-related macular degeneration, diabetic retinopathy, glaucoma, and cataracts, which are the four most common eye conditions.[222] In fact, cataracts are the leading cause of vision loss and blindness in individuals of all ages worldwide.[223] A cataract is the clouding or loss of transparency in the lens of either one or both eyes as a result of tissue breakdown and protein clumping or aggregation.[224] Over a period of time, a cataract can grow larger, clouding a superior amount of the lens, hereby causing a decrease in vision. Although cataracts mostly develop in individuals over the age of 55 years old, they can also occur in infants and young children.[225]

To understand how cataracts can lead to vision impairment, it is important to understand the anatomy of the eye (Figure 3.1).[223] The lens of our eye - made of proteins and water - is located behind the iris, which is the coloured region of the eye.[226, 227] The lens has the primary function to focus the light passing from the cornea onto the retina, which can then send a sharp image through the optic nerve to the brain.[227] However, when the lens of the eye is clouded due to a cataract, light gets scattered and the lens cannot focus it properly, hereby leading to vision issues. The lens is comprised of three distinct layers, notably the outermost layer known as the capsule, the layer in the capsule known as the cortex, and the innermost layer known as the nucleus.[227] A cataract may potentially develop in any of the aforementioned layers, and there are three different cataracts based on the location in the lens.[225] Firstly, a nuclear cataract, located in the center of the lens, involves the darkening of the nucleus with age, often from clear to yellow, and sometimes to brown.[225] Secondly, a cortical cataract is one that occurs in the edges of the lens cortex and has a white appearance with wedge-shaped opacities.[225] Thirdly, a posterior capsular cataract is an opacity that occurs near the back of the lens, directly in the path of light.[225]

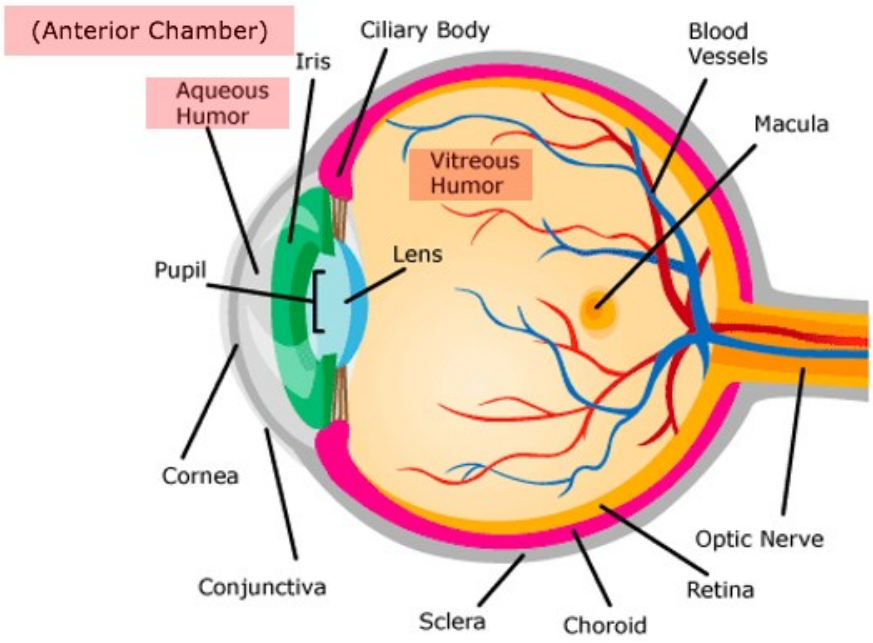

Figure 3.1. Illustration showing the anatomy of the eye.[228]

There are four main risk factors associated with the development of cataracts including (i) age-related, which is most common, (ii) congenital, i.e., abnormality present from birth, (iii) secondary, i.e., due to diabetes or steroid usage, and (iv) traumatic, i.e., due to ocular trauma or eye injury.[225] Currently, the exact cause of cataracts remains uncertain, however some contributing factors that increase the risk of cataracts are age, smoking, diabetes, and ultraviolet (UV) exposure.[222, 225]

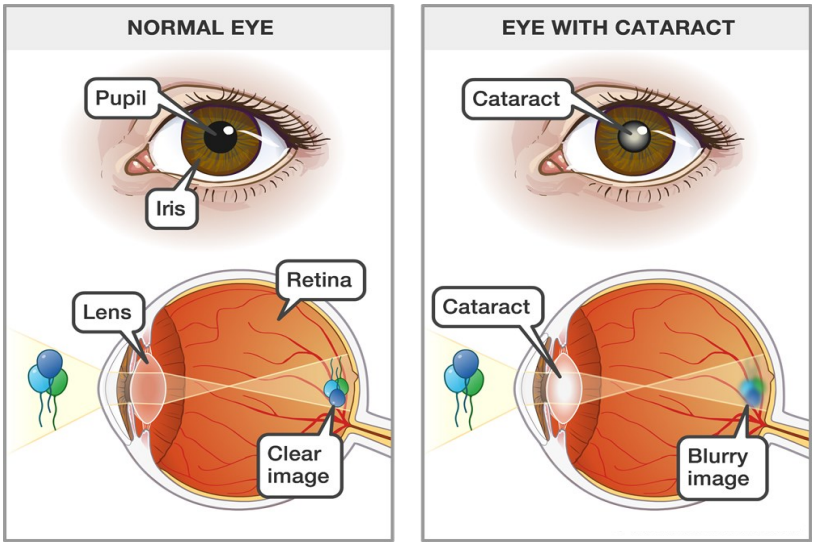

Figure 3.2. Representation of a normal eye (left) and eye with cataract (right).[229]

Several millions of cataract surgeries are performed each year in North America having an effective and successful result.[230] Following cataract surgery where the cloudy natural lens is replaced by an artificial clear lens,[223] patients are generally prescribed a set of three different types of eye drops that are administered with a different frequency, which include an antibiotic, a non-steroidal anti-inflammatory drug (NSAID), and a corticosteroid.[231] In general, NSAIDs in the form of eye drops should be administered three times daily for one month following surgery.[231] Eye drops are considered as a convenient, safe, and non-invasive method of delivering drugs to the anterior segment of the eye.[232] For ocular therapeutics, 90% of the drugs used in ophthalmology are administered by ocular drops, specifically onto the mucosal layer of the cornea of the eye.[233, 234] Though, the bioavailability of ocular drugs is low, as a result of poor mucoadhesion of the current formulations. When considering eye drops for drug delivery, only 0.0006% to 0.02% of the active drug molecules administered onto the cornea can reach the anterior chamber of the eye, which is the location of most intended drug targets (Figure 3.1).[235-238] This penetration depth issue is a result of challenges arising from the precorneal tear clearance mechanism and corneal-epithelial barrier (Figure 3.3).[232] In addition, this mode of administration is associated with low patient compliance and specialists have identified that having a drug vector to reduce the frequency of eye drop administration would be very useful to improve ophthalmic medication.[239] In fact, it was reported that the noncompliance rate for eyedrop treatment is approximately 30%.[240]

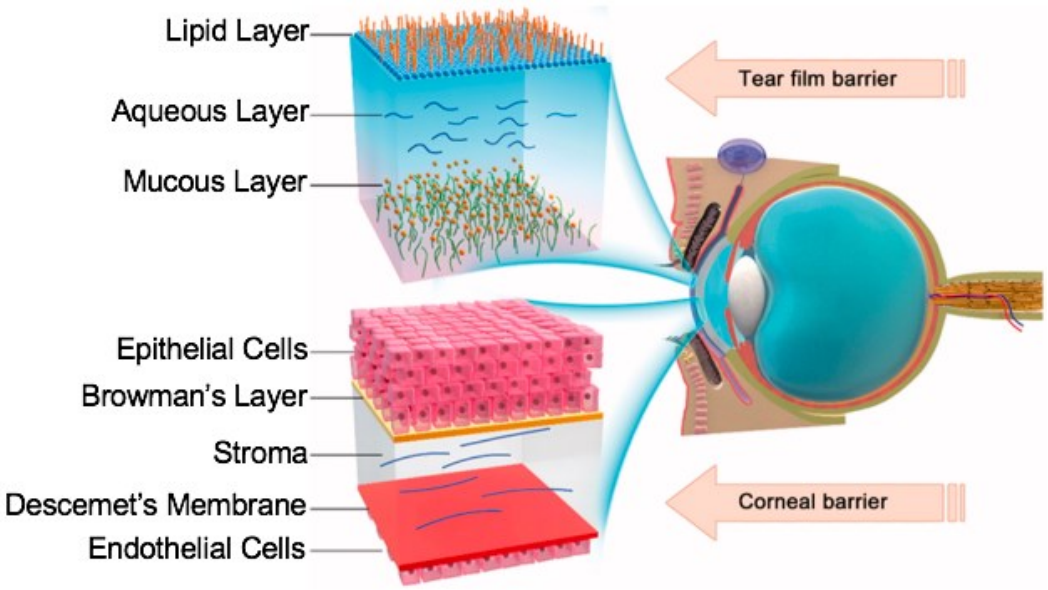

Figure 3.3. Two barriers to topical ocular drug delivery, tear film barrier (top) and corneal barrier (bottom). Figure obtained from Li *et al.*[241]

Mucoadhesive drug vectors can increase the retention time of drugs at the cornea, improving their bioavailability, efficiency, and minimizing the frequency at which eye drops need to be administered. In view of both the limited volume of the ocular cavity (< 3 to 4 cm^3) and allowance of fluid in the human eye (7 to 10 μL), delivery platforms for ocular therapeutics must fulfill additional requirements relative to precorneal devices including (i) large loading capacity (in gravimetric (wt %) and volumetric (w/v %) basis) to avoid interference in vision after a dose; (ii) slow delivery kinetics such as days or weeks to enable long-term therapy; (iii) biocompatibility for retinal cells, and (iv) structural instability once the material achieves the desired effects.[154] Two main strategies exist for improving the mucoadhesion, i.e., the adhesion of molecules on the mucins which are the proteins found at the surface of the cornea. The most recent and promising one consists in the use of thiol groups which will interact with the thiol groups found in the mucins, in their cysteine amino acids, to form disulfide bonds (–S-S–). In fact, some regions of mucin proteins are rich in cysteines, i.e., > 10% of the amino acids,[186] making the usage of thiolated materials a promising platform for ophthalmic drug delivery applications.

In recent years, significant advances have been made in the field of materials chemistry and medicine. Among the variety of proposed systems including lipids,[242] hydrogels,[243] nanovesicles,[244] nanoparticles,[245] and polymers,[246, 247] metal–organic frameworks (MOFs) are being investigated for potential applications as drug delivery systems, since other proposed systems are challenged with low loading capacities and rapid release of drugs (Figure 3.4). In drug delivery systems, MOF carriers are designed to (i) encapsulate a drug, (ii) enhance drug absorption (diffusion through epithelium), (iii) control release of the drug (pharmacokinetics), and (iv) improve intracellular diffusion.[154] MOFs offer an interesting alternative platform for use in drug delivery applications, and specifically as potential mucoadhesive drug vectors. Comprised of metal nodes bridged by organic linkers, MOFs are highly modular, porous, and crystalline materials.[3, 5-7] Using the right combination of metal and organic building units, MOFs can be made to have permanent porosity, ultrahigh surface area, and low density. As a consequence, MOFs have been studied for a large variety of potential applications ranging from gas capture and storage[189, 190] to catalysis.[31, 191] These crystalline and porous materials offer a high degree of structural tunability through variation of the metal node and organic linker building blocks used in their synthesis. Moreover, the chemical identity and functionality of the organic linkers can be tailored to obtain desired properties for applications. It has been reported in the literature that MOFs are promising

for the drug delivery of antitumoral and retroviral drugs, with cytotoxicity assays demonstrating low toxicity and inflammatory activity.[153, 248, 249] Key properties for the use of MOFs in biological applications include biocompatibility, such as to have minimal toxicity to living cells, biodegradability, and the possibility to synthesize them with nanoscale sizes.[25] Hence when designing MOFs for drug delivery applications, and specifically for ophthalmic drug delivery, the various factors to consider include (i) size of the desired crystallites, (ii) properties of the drug to be encapsulated, i.e., aqueous solubility and stability, (iii) surface characteristics and functionality, (iv) degree of biodegradability and biocompatibility, and (v) drug release profile of the final product.[154]

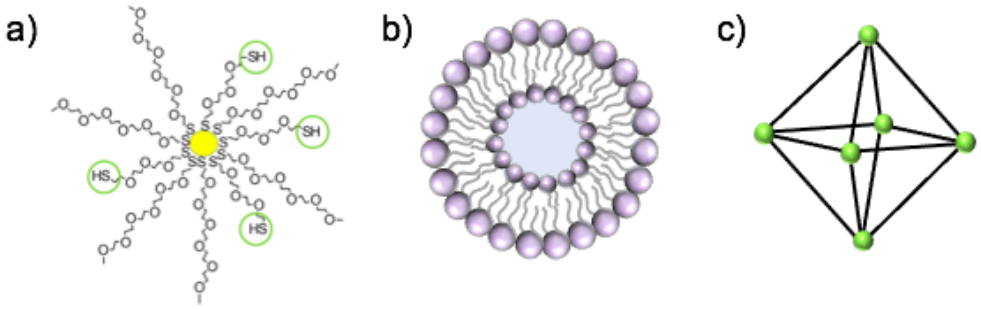

Figure 3.4. Representation of drug delivery systems. (a) Thiol-functionalized gold nanoparticles,[186] (b) liposomes comprised of lipid bilayers, and (c) simplified MOF structure.

Mucoadhesion involving the use of thiolated MOFs is a new approach introduced herein that has not yet been explored in the literature. Previous studies on NH_2-MIL-88(Fe), reported the use of hydrogen bonding and ionic interactions of the positively charged MOF surface to negatively charged mucin, in order to achieve mucoadhesion.[250] While some studies have looked at the potential of hexanuclear zirconium (Zr_6) MOFs for ophthalmic drug delivery applications,[154, 251, 252] the mucoadhesive properties of these materials have not been tuned or extensively explored.

In the tear film[183] of our eye (Figure 3.5), there are three layers that protect the cornea of the eye, and the first layer is the lipid layer, therefore the MOF has to go through lipid layer to reach the second layer, known as the aqueous layer. The aqueous layer is the thickest one, which is used for nutrition, and oxygenation, and there are soluble mucins in that layer – but those small soluble mucins do not contain thiol groups. Then, we arrive at the third layer, which is referred to as the mucin layer which is the interesting one for this drug delivery application. In the mucin layer, there are transmembrane mucins or large glycoproteins and mucins in corneal cells, and the

type of mucins that are targeted for mucoadhesion are gel-forming mucins, therefore small mucins that form a gel on top of eye and they form gels because they have sulfur bonds.[183]

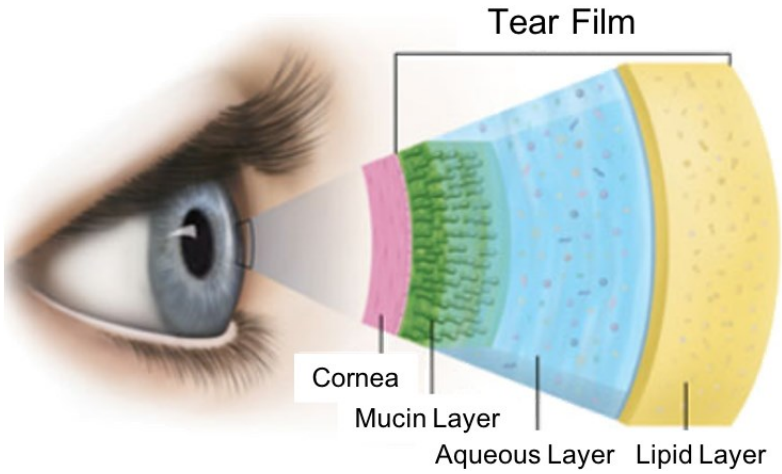

Figure 3.5. Tear film of the eye comprised of three distinct layers.[253]

In general, non-steroidal anti-inflammatory drugs act as inhibitors of cyclooxygenase (COX) enzymes,[254] which allows for the reduction of the biosynthesis of proinflammatory prostaglandins (PGs) from arachidonic acid.[255] One such NSAID is flurbiprofen, which specifically inhibits the two COX enzymes, COX-1 and COX-2.[254] Flurbiprofen, which has analgesic, anti-inflammatory, and anti-pyretic properties, has dimensions of ~12 Å x 5 Å, has a hydrophobic nature, and is similar in structure to other NSAIDs including ibuprofen, naproxen, fenoprofen, and ketoprofen (Figure 3.6).[254] While flurbiprofen is used for treatment of rheumatoid arthritis and osteoarthritis, it is also topically used in the form of eye drops by dissolution in a saline solution[256] to treat ocular surface inflammation after cataract surgery[257] and has been reported to be safe up to a dose of 0.1 mL after intravitreal injection.[258]

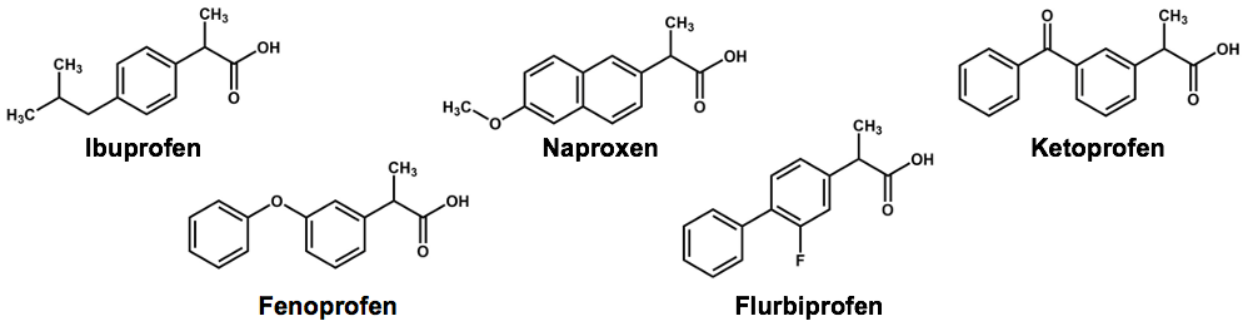

Figure 3.6. Chemical structures of different non-steroidal anti-inflammatory drugs (NSAIDs).

For this study, two isostructural and thiol-functionalized Zr_6-based MOFs, UiO-66-$(SH)_2$ and UiO-67-$(SH)_2$ will be used, where the thiolated linkers are used to enhance mucoadhesive properties. For both of the frameworks, the metal node is zirconium-based and the organic linkers are derivatives of terephthalic acid and biphenyl-4,4′-dicarboxylic acid, which fit well for usage in biological applications. In fact, recent biocompatibility data demonstrated that zirconium is poorly absorbed by the body and is therefore not considered toxic, and polycarboxylate linkers such as terephthalic acid are not considered toxic owing to their high polarity and easy removal under physiological conditions.[158] Moreover, the metal precursors used to synthesize the MOFs selected for this study exhibit low toxicity, specifically for zirconium chloride where the lethal dose (LD_{50}) is approximately 3500 mg kg^{-1}.[154]

Herein, Zr-UiO-66-$(SH)_2$ and Zr-UiO-67-$(SH)_2$ are synthesized (Figure 3.7) and the mucoadhesion of the thiolated MOFs are assessed by fluorescence spectroscopy and colorimetric quantification. In addition, the encapsulation and release of the NSAID, flurbiprofen, in these thiolated MOFs are tested.

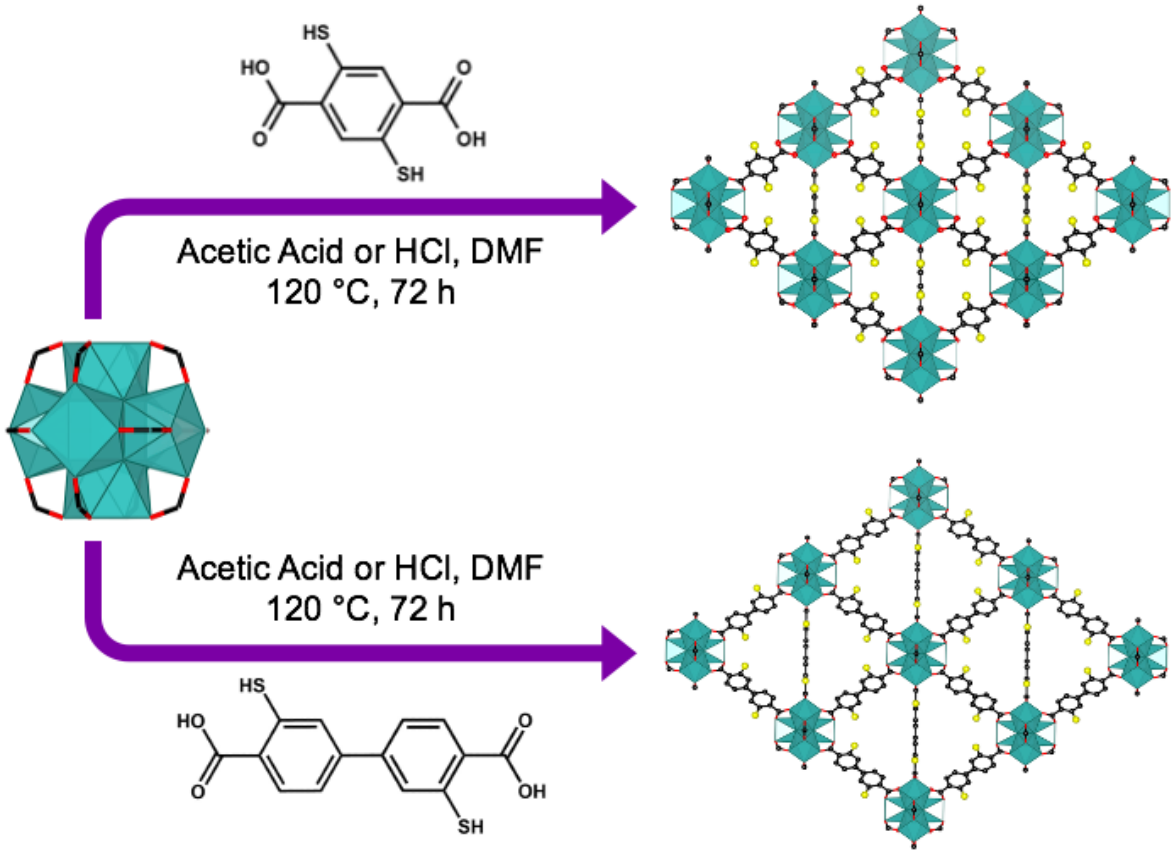

Figure 3.7. Solvothermal synthesis of Zr-UiO-66-$(SH)_2$ (top) and Zr-UiO-67-$(SH)_2$ (bottom).

3.2. Experimental Procedures

3.2.1. General Materials and Methods

All reagents and solvents were used without further purification: zirconium (IV) chloride ($ZrCl_4$; Alfa Aesar, 99.5%), 3,3'-dimercapto-[1,1'-biphenyl]-4,4′-dicarboxylic acid (H_2DMBPD); Ambeed, 95%), terephthalic acid (BDC; Acros Organics, 99+%), biphenyl-4,4′-dicarboxylic acid (BPDC; Acros Organics, 98%), *N,N*-dimethylformamide (DMF; Fisher Chemical Certified ACS, ≥99.8%), glacial acetic acid (Fisher Scientific, 99.7%), hydrochloric acid (HCl; Fisher Scientific, 36.5 – 38.0%), acetone (Fisher Chemical Certified ACS, 99.5%), 1,4-diazabicyclo[2.2.2]octane (Tokyo Chemical Industry (TCI), >98.0%), diethyl 2,5-dihydroxyterephthalate, (Sigma Aldrich, 97%), dimethylthiocarbamoyl chloride (TCI, >97.0%), *N,N*-dimethylacetamide (DMA; Fisher Chemical Reagent Grade), potassium hydroxide (Alfa Aesar, 85%), deuterated chloroform ($CDCl_3$; Cambridge Isotope Laboratories, 99.8 atom % D with 0.05% v/v tetramethylsilane (TMS)), deuterated sulfuric acid (D_2SO_4; Sigma Aldrich, 99.5 atom % D), deuterated dimethyl sulfoxide (DMSO-d_6; Sigma Aldrich, 99.9 atom % D), 2-fluoro-alpha-methyl-4-biphenylacetic acid (Flurbiprofen (FBP) Fisher Scientific, 99%), ethanol (Greenfield Global, 99%), sodium acetate (Sigma Aldrich, ≥99%), Tris (Tris(Hydroxymethyl)aminomethane) (BioShop®, min. 99.9%), N-acetyl-L-cysteine (Alfa Aesar, 98+%), and 5-5′-dithiobis(2-nitrobenzoic acid) (Alfa Aesar, 99%). 2,5-dimercapto-1,4-benzenedicarboxylic acid (H_2DMBD) was prepared according to the literature (Figures A.15-A.18).[259]

Powder X-ray diffraction **(**PXRD) data were collected on a Bruker D2 Phaser (Bruker AXS, Madison, WI, USA) equipped with Cu*K*α X-ray source (wavelength, λ = 1.54 Å), and a Nickel filter. Neat samples were smeared directly onto the silicon wafer of a proprietary low-zero background sample holder. Data was collected in the 2θ-range of 4-40° in increments of 0.02°.

Nitrogen adsorption-desorption (sorption) isotherm data were collected at 77 K on a Micromeritics TriStar II Plus surface area and porosity analyzer. All samples were activated at 120 °*C* for 24 h before each isotherm was collected by heating under vacuum using a Micromeritics Smart VacPrep equipped with a hybrid turbo vacuum pump system.

Diffuse reflectance infrared Fourier transform spectroscopy (DRIFTS) spectra were recorded using a Thermo Scientific Nicolet 6700 FT-IR equipped with a MCT detector with a resolution of 1 cm^{-1} in the range of 4000-450 cm^{-1}. DRIFTS was used to confirm the presence of the carbonyl and carboxylate group from the organic linker, the hydroxyl stretches from the

bridging and terminal hydroxyl ligands in the MOF node, and in some cases the thiol functional group from the organic linker. The samples were run after activation with no further treatment.

Proton nuclear magnetic resonance (^{1}H-NMR) spectroscopy spectra were recorded on a 300 MHz Bruker spectrometer and the chemical shifts were referenced to the residual solvent peaks. MOF samples were digested using ~7 drops of D_2SO_4, followed by sonication and dissolution of the suspension in DMSO-d_6.

Thermogravimetric analysis (TGA) measurements were carried out using a TGA 5500 from TA Instruments, from room temperature to 550 °C at a rate of 5 °C/min under air. For TGA analysis, ~5 mg of the activated MOF sample was weighed with no further treatment.

Scanning electron microscopy (SEM) micrographs were collected on a Phenom ProX desktop SEM, at 12 kV. Prior to the analysis, all samples were coated with 5 nm gold (Au) layers by using a Cressington 108 Auto/SE Sputter Coater with MTM-20 high resolution film thickness controller.

Ultraviolet–visible (UV-Vis) absorption spectra were acquired on a Cary 5000 Series UV-Vis-NIR spectrophotometer from Agilent Technologies, from 200 to 800 nm in single beam mode and with a source wavelength changeover at 350 nm. Solutions were analyzed using a two-sided UV-Vis fused quartz cuvette with 1 cm path length and 3.50 mL capacity from Alpha Nanotech.

High performance liquid chromatography (HPLC) chromatograms were acquired using an Agilent Technologies 1200 Series equipped with a UV-Vis detector and an ACE C18 column (15.0 mm x 4.6 mm, 5 µm). Flurbiprofen (FBP) concentrations were measured by setting the wavelength of the UV-Vis detector to 247 nm and the column's temperature was kept at room temperature (27 °C). To determine the concentration of flurbiprofen, the mobile phase was kept isocratic, which consisted of 50:50 ultrapure water (0.1% trifluoroacetic acid) and acetonitrile (0.1% trifluoroacetic acid) at a flow rate of 1.0 mL min^{-1}.

Inductively coupled plasma–mass spectrometry (ICP-MS) data were measured on an Agilent 7500 Series instrument.

Dynamic light scattering (DLS) measurements were performed using a Zetasizer Nano ZSP system from Malvern Panalytical at 25 °C. MOF samples were sonicated in ethanol 99%, and 500 µL of the MOF suspension was diluted with 1000 µL ethanol 99%, and measured in a standard fluorometer quartz cuvette with 1 cm path length and 3.50 mL capacity.

Thiol quantification using the Ellman's test: A sodium acetate solution with a concentration of 50 mM was prepared in a 100 mL volumetric flask using sodium acetate (277 mg, 3.38 mmol) and acetic acid (93.5 μL), diluted to 100 mL using Millipore water. A Tris buffer solution with a concentration of 1 M was prepared in a 100 mL volumetric flask using Tris (12,220 mg, 101 mmol) and Millipore water, and the pH was adjusted to 8.0 using hydrochloric acid. The 5,5′-dithiobis(2-nitrobenzoic acid) (DTNB) solution was prepared by dissolving DTNB (8.50 mg, 0.0214 mmol) in 10 mL of sodium acetate (50 mM) in a 10 mL volumetric flask, followed by sonication and was kept refrigerated. The Ellman's test was performed according to the reported procedure.[260] A standard thiol calibration curve was prepared using N-acetyl-L-cysteine, starting from 10 μM. Water was used as the solvent blank/background. To the quartz cuvette, 2520 μL of Millipore water, 300 μL of Tris buffer solution, 150 μL of DTNB solution, and 30 μL of N-acetyl-L-cysteine at the desired concentration from 10 μM to 60 μM, was added (for a total of 3000 uL in the cuvette). For the thiol quantification of thiolated MOF samples (Zr-UiO-66-$(SH)_2$ and Zr-UiO-67-$(SH)_2$), increasing amounts of activated MOF were added to the cuvette with the same reagents (Millipore water, Tris solution, DTNB solution), however an additional 30 μL of Millipore water was added in place of the N-acetyl-L-cysteine standard to give a total of 3000 μL in the cuvette. The cuvette was sealed with Parafilm, inverted to mix, and incubated for 5 min at room temperature (produced yellow colour in the cuvette), before being placed into the UV-Vis spectrophotometer.

Flurbiprofen loading and release: To carry out the drug loading experiments, flurbiprofen is loaded into the activated MOFs by soaking 5 mg of each MOF in a 5000 ppm ethanolic solution of the drug in a 0.5-dram vial for 24 h on a rotary shaker, at room temperature. This model exposes the MOF to a 5 mg mL^{-1} solution of FBP, at a molar loading of 10 equivalents. For Zr-UiO-66-$(SH)_2$, a sample of 18.0 mg of FBP is dissolved in 3 mL of ethanol 99%, for Zr-UiO-67-$(SH)_2$, a sample of 14.5 mg of FBP is dissolved in 3 mL of ethanol 99%, for Zr-UiO-66, a sample of 22.0 mg FBP is dissolved in 3 mL of ethanol 99%, and for Zr-UiO-67, a sample of 17.0 mg of FBP is dissolved in 3 mL of ethanol 99%. The FBP is readily dissolved in ethanol 99% with swirling and little sonication, giving a transparent and homogenous FBP solution. A control solution of FBP was prepared without the addition of MOFs, to determine the amount that was encapsulated in the MOF (FBP@MOF) by difference. The loading of FBP in the MOFs is determined by separating the free drug from that which is encapsulated, and the concentration of

the FBP in the supernatant solution is probed using HPLC. Prior to HPLC analysis, 100 µL aliquots were diluted 100 times with ethanol 99% and filtered by a 0.2 µm polytetrafluoroethylene (PTFE) syringe filter. To carry out the drug release experiments, the MOF material loaded with FBP is vacuum filtered using a Whatman grade 602H qualitative filter paper, washed with ~1 mL of ethanol 99%, and air dried in the Buchner funnel under vacuum. In a 1.5-dram vial, the drug loaded MOF material is soaked in 1 mL of ethanol 99% and 1 mL of HCl solution (pH = 3) for at least 24 h and filtered by a 0.2 µm PTFE syringe filter prior to running HPLC analysis. A calibration curve of ethanol 99% and HCl solution (pH =3) was also generated using HPLC.

Quantification of metal/linker leaching: 1.5 mg of the activated thiolated MOF sample was weighed and transferred to a 15 mL centrifuge tube, followed by the addition of 2 mL of Millipore water and the sample was placed on a rotary shaker for 2 h. The MOF sample was then centrifuged at 6250 g (g-force at 7500 rpm, rotor = 9.5 cm) for 5 min, where the MOF was pelleted, and the supernatant was isolated. The supernatant was then transferred to a 25 mL round bottom flask and rotary evaporated to dryness. To the round bottom flask, 800 µL of nitric acid was added to digest any organic content. Then, the contents from the round bottom flask were transferred to a 10 mL volumetric flask and diluted to the 10 mL mark with Millipore water. A blank sample was prepared in a 10 mL volumetric flask by adding 800 µL nitric acid and diluting to the 10 mL mark using Millipore water. The samples for ICP-MS analysis were transparent and homogenous solutions.

3.2.2. Synthesis and Activation of Zr-UiO-66-$(SH)_2$, Zr-UiO-67-$(SH)_2$, Zr-UiO-66 and Zr-UiO-67 (Thiolated and Control MOFs)

Zr-UiO-66-$(SH)_2$ was synthesized solvothermally in an 8-dram vial containing $ZrCl_4$ (31.0 mg, 0.133 mmol) and H_2DMBD (30.0 mg, 0.130 mmol), with 7.5 mL of DMF and 750 µL of acetic acid. Once the reagents were partially dissolved by sonication, the slight yellow and cloudy sample mixture was heated at 120 °C for 3 days (72 h). Light yellow precipitate was collected by centrifugation and washed three times with 10 mL of fresh DMF for 4 days, exchanging the DMF every second day. The organic solvent was then exchanged with acetone and washed three times with 10 mL of fresh acetone. The as-synthesized Zr-UiO-66-$(SH)_2$ was left in 10 mL of fresh acetone for one day. The sample was dried under vacuum at 120 °C for 24 h, yielding a darker yellow crystalline solid. To synthesize Zr-UiO-66-$(SH)_2$ with hydrochloric acid (HCl) as a

modulator, this procedure can be repeated by directly replacing the 750 μL of acetic acid in the synthetic protocol with 500 μL of HCl.

Zr-UiO-67-$(SH)_2$ was synthesized solvothermally in an 8-dram vial containing $ZrCl_4$ (31.0 mg, 0.133 mmol) and H_2DMBPD (40.0 mg, 0.131 mmol), with 7.5 mL of DMF and 750 μL of acetic acid. Once the reagents were partially dissolved by sonication, the slight yellow and cloudy sample mixture was heated at 120 °C for 3 days (72 h). Light yellow precipitate was collected by centrifugation and washed three times with 10 mL of fresh DMF for 4 days, exchanging the DMF every second day. The organic solvent was then exchanged with acetone and washed three times with 10 mL of fresh acetone. The as-synthesized Zr-UiO-67-$(SH)_2$ was left in 10 mL of fresh acetone for one day. The sample was dried under vacuum at 120 °C for 24 h, yielding a darker yellow crystalline solid. To synthesize Zr-UiO-67-$(SH)_2$ with hydrochloric acid (HCl) as a modulator, this procedure can be repeated by directly replacing the 750 μL of acetic acid in the synthetic protocol with 500 μL of HCl.

Zr-UiO-66 was synthesized solvothermally in an 8-dram vial containing $ZrCl_4$ (31.0 mg, 0.133 mmol) and H_2BDC (38.0 mg, 0.229 mmol), with 7.5 mL of DMF and 750 μL of acetic acid. Once the reagents were partially dissolved by sonication, the cloudy and semi-opaque sample mixture was heated at 120 °C for 3 days (72 h). White precipitate was collected by centrifugation and washed three times with 10 mL of fresh DMF for 4 days, exchanging the DMF every second day. The organic solvent was then exchanged with acetone and washed three times with 10 mL of fresh acetone. The as-synthesized Zr-UiO-66 was left in 10 mL of fresh acetone for one day. The sample was dried under vacuum at 120 °C for 24 h, yielding a white crystalline solid. To synthesize Zr-UiO-66 with hydrochloric acid (HCl) as a modulator, this procedure can be repeated by directly replacing the 750 μL of acetic acid in the synthetic protocol with 500 μL of HCl, and after sonication, the sample mixture was transparent and not cloudy.

Zr-UiO-67 was synthesized solvothermally in an 8-dram vial containing $ZrCl_4$ (31.0 mg, 0.133 mmol) and H_2BPDC (30.0 mg, 0.124 mmol), with 7.5 mL of DMF and 750 μL of acetic acid. Once the reagents were partially dissolved by sonication, the white, cloudy and opaque sample mixture was heated at 120 °C for 3 days (72 h). White precipitate was collected by centrifugation and washed three times with 10 mL of fresh DMF for 4 days, exchanging the DMF every second day. The organic solvent was then exchanged with acetone and washed three times with 10 mL of fresh acetone. The as-synthesized Zr-UiO-66 was left in 10 mL of fresh acetone for

one day. The sample was dried under vacuum at 120 °C for 24 h, yielding a white crystalline solid. To synthesize Zr-UiO-67 with hydrochloric acid (HCl) as a modulator, this procedure can be repeated by directly replacing the 750 µL of acetic acid in the synthetic protocol with 500 µL of HCl, and after sonication, the sample mixture was also white, cloudy and opaque.

Zr-UiO-66 (STEPOSOL) was synthesized solvothermally in a 6-dram vial containing $ZrCl_4$ (116.0 mg, 0.498 mmol) and H_2BDC (85.5 mg, 0.515 mmol), with 4 mL of STEPOSOL® MET-10U and 27 µL of deionized water. Once the reagents were partially dissolved by sonication, the cloudy sample mixture was heated at 120 °C for 16 h. White precipitate was collected by centrifugation and washed three times with 10 mL of fresh methanol for 4 days, exchanging the methanol every second day. The organic solvent was then exchanged with acetone and washed three times with 10 mL of fresh acetone. The as-synthesized Zr-UiO-66 (STEPOSOL) was left in 10 mL of fresh acetone for one day. The sample was dried under vacuum at 120 °C for 24 h, yielding a white crystalline solid.

3.3. Results and Discussion

3.3.1. Characterization of Thiolated and Control MOFs

Two MOFs have been judiciously selected for this study, notably Zr-UiO-66-$(SH)_2$ and Zr-UiO-67-$(SH)_2$, that were synthesized using acetic acid (AA) or HCl as modulators. Both MOFs are comprised of 12-connected hexanuclear zirconium-oxo clusters, and ditopic thiolated linkers, giving a structure with **fcu** topology. The bulk crystallinity and phase purity of the selected MOFs is determined through powder X-ray diffraction (PXRD), confirming the successful synthesis of the materials (Figure 3.8).

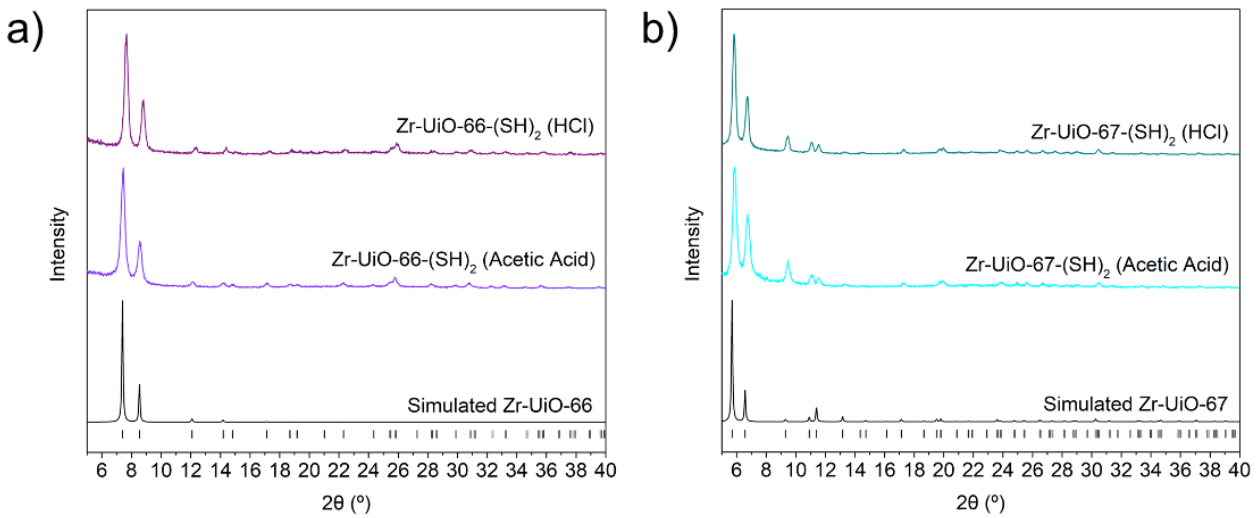

Figure 3.8. PXRD diffractograms of (a) Zr-UiO-66-$(SH)_2$ AA and HCl, and (b) Zr-UiO-67-$(SH)_2$ AA and HCl.

The surface area and porosity of Zr-UiO-66-$(SH)_2$ and Zr-UiO-67-$(SH)_2$ was measured by N_2 adsorption-desorption analysis performed at 77 K. When activated at 120 °C under vacuum for 24 h, N_2 sorption analysis reveals the expected reversible Type I(a) isotherms with Brunauer-Emmett-Teller (BET) surface areas of 650 and 1065 m^2 g^{-1} for Zr-UiO-66-$(SH)_2$-AA and Zr-UiO-67-$(SH)_2$-AA, respectively (Figure 3.9). This demonstrates that the thiolated MOFs have accessible surface areas suitable for the encapsulation of guest molecules, such as drug molecules. Similarly, when activated at 120 °C under vacuum for 24 h, N_2 sorption analysis of the Zr-UiO-66-$(SH)_2$-HCl and Zr-UiO-67-$(SH)_2$-HCl revealed Type I(a) isotherms with BET surface areas of 665 and 1010 m^2 g^{-1}, respectively (Figure 3.9). Owing to the presence of thiol groups, the accessible surface area of Zr-UiO-66-$(SH)_2$ and Zr-UiO-67-$(SH)_2$ is lower than that of Zr-UiO-66 (1580 m^2 g^{-1}).[61] Specifically, the sulfur atom with an ionic radius of 1.84 Å can block the pore aperture (6 Å) and decrease the nitrogen accessible surface area - a notable consideration for drug loading. The pore size distribution calculated using non-local density functional theory (NLDFT) confirms the presence of a pore cavity of 9.5 Å and 12.4 Å for Zr-UiO-66-$(SH)_2$-AA and Zr-UiO-67-$(SH)_2$-AA, respectively, and a pore cavity of 12.0 Å and 12.4 Å for Zr-UiO-66-$(SH)_2$-HCl and Zr-UiO-67-$(SH)_2$-HCl, respectively (Figure 3.9).

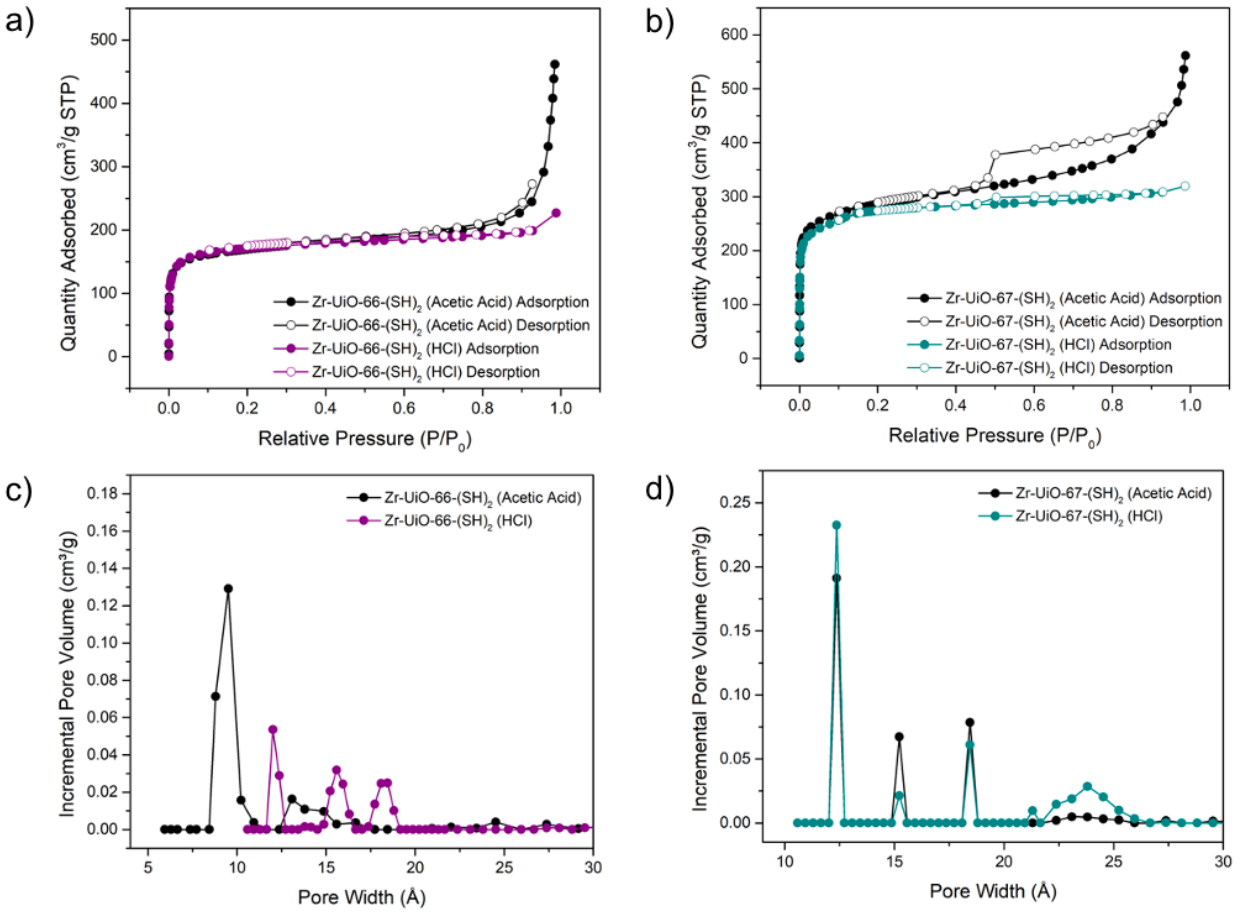

Figure 3.9. Nitrogen adsorption-desorption isotherms of (a) Zr-UiO-66-$(SH)_2$ AA and HCl (Type I(a)), (b) Zr-UiO-67-$(SH)_2$ AA and HCl (Type I(a)), and pore size distribution analysis of (c) Zr-UiO-66-$(SH)_2$ AA and HCl, and (d) Zr-UiO-67-$(SH)_2$ AA and HCl.

The thermal decomposition of the activated MOFs is investigated through thermogravimetric analysis (TGA), and in both cases the thermogram demonstrates the MOFs are stable to approximately 400 °C before the linker degrades and the framework decomposes (Figure 3.10).

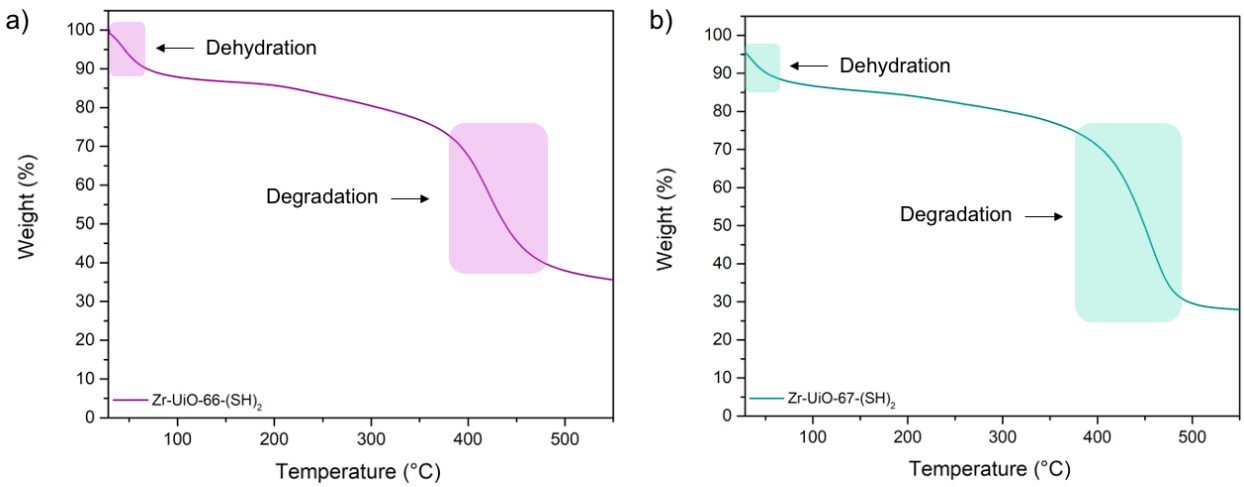

Figure 3.10. TGA curves of (a) Zr-UiO-66-$(SH)_2$, and (b) Zr-UiO-67-$(SH)_2$.

To further characterize the MOFs, diffuse reflectance infrared Fourier transform spectroscopy (DRIFTS) is used to acquire information about the infrared active functional groups in the materials. The DRIFTS data demonstrates the expected absorption bands corresponding to carboxylate and thiol linker stretching as well as O-H stretching bands corresponding to the terminal and bridging –OH ligands in the metal node.

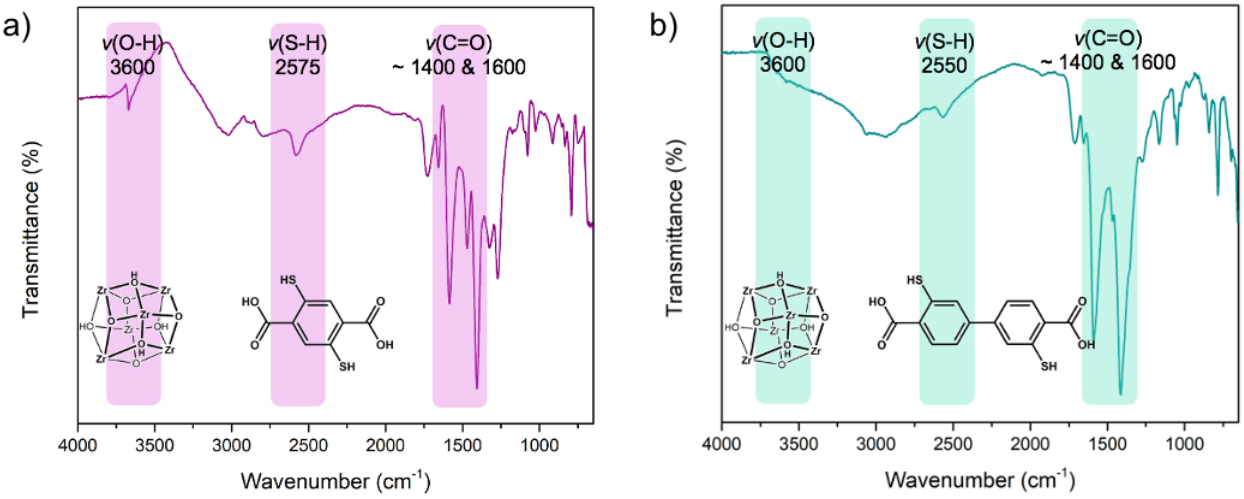

Figure 3.11. DRIFTS spectra of (a) Zr-UiO-66-$(SH)_2$, and (b) Zr-UiO-67-$(SH)_2$.

Proton nuclear magnetic resonance (^{1}H-NMR) spectroscopy of the digested MOF samples shows the linker purity and incorporation into the MOF structures (Figure 3.12).

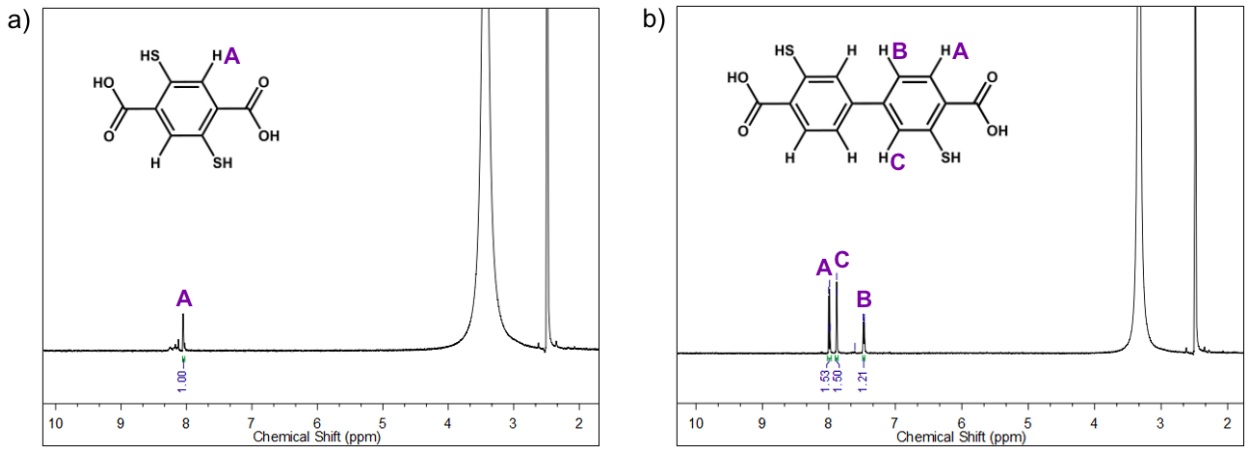

Figure 3.12. ^{1}H-NMR spectra of (a) Zr-UiO-66-$(SH)_2$, and (b) Zr-UiO-67-$(SH)_2$.

Finally, scanning electron microscope micrographs of the thiolated MOFs were also captured to gain information regarding the crystallite sizes, and although not monodisperse, they reveal particle sizes ranging from approximately 100 nm to 1000 nm in the case of aggregated particles (Figure 3.13). The particle sizes were also assessed with dynamic light scattering (DLS) measurements, showing particle sizes of ~142 nm for Zr-UiO-66-$(SH)_2$-AA and ~232 nm for Zr-UiO-67-$(SH)_2$-AA (Figure 3.14).

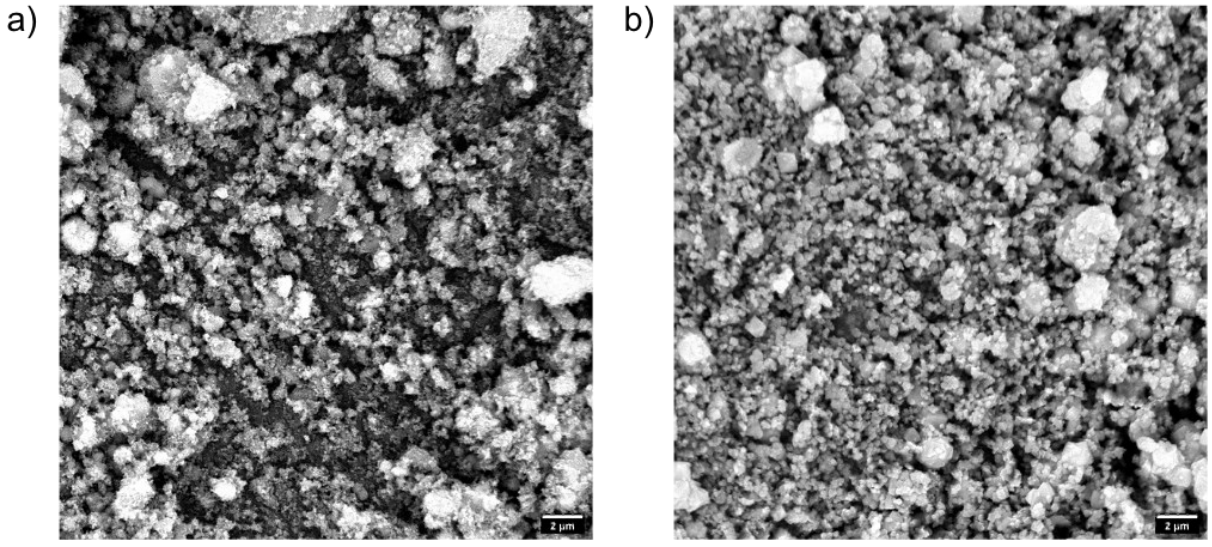

Figure 3.13. SEM micrographs of (a) Zr-UiO-66-$(SH)_2$-AA, and (b) Zr-UiO-67-$(SH)_2$-AA.

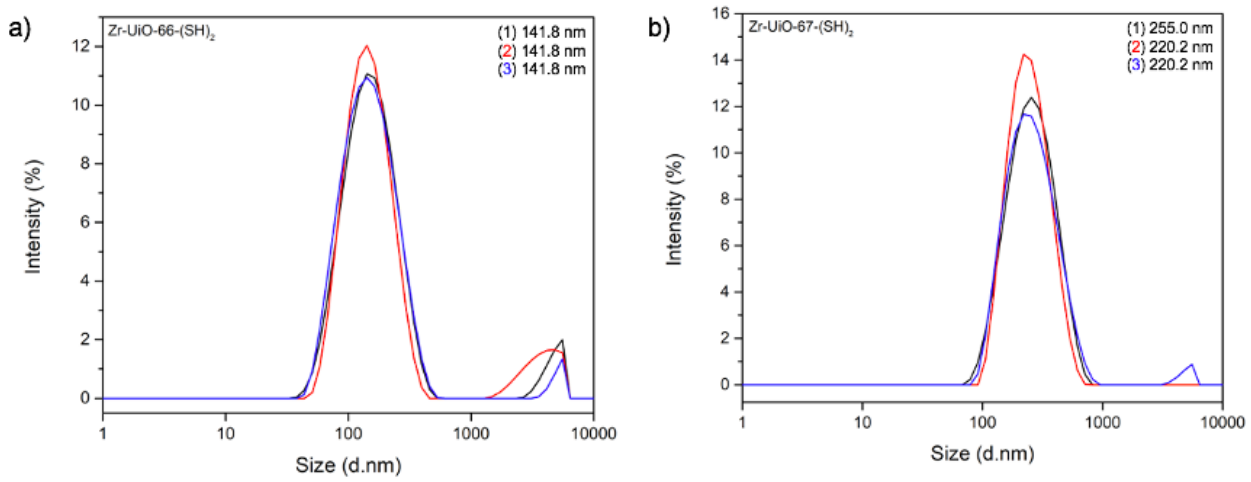

Figure 3.14. DLS measurements of (a) Zr-UiO-66-$(SH)_2$-AA, and (b) Zr-UiO-67-$(SH)_2$-AA.

As with any experiment, proper controls are essential to assess the viability of the thiolated MOFs. The control MOFs, Zr-UiO-66 and Zr-UiO-67 that do not contain thiol groups were also synthesized using both acetic acid and HCl modulators. The MOFs were first characterized by PXRD demonstrating that the materials are crystalline and phase pure (Figure 3.15).

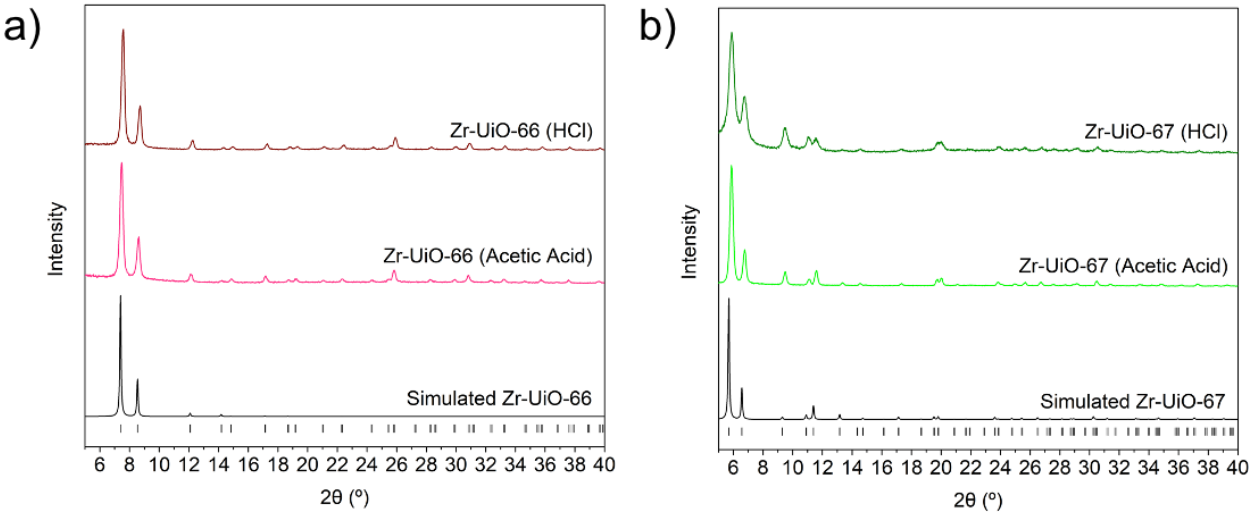

Figure 3.15. PXRD diffractograms of (a) Zr-UiO-66 AA and HCl, and (b) Zr-UiO-67 AA and HCl.

The control MOFs were activated at 120 °C under vacuum for 24 h, and N_2 sorption analysis demonstrated the expected reversible Type I(a) isotherm with BET surface areas of 840 and 1790 m^2 g^{-1} for Zr-UiO-66-AA and Zr-UiO-67-AA, respectively (Figure 3.16). In a similar

manner, the controls MOFs synthesized using HCl as a modulator were activated at 120 °C under vacuum for 24 h, and N_2 sorption analysis revealed BET surface areas of 1550 and 1910 $m^2\ g^{-1}$ for Zr-UiO-66-HCl and Zr-UiO-67-HCl, respectively (Figure 3.16). Due to the use of HCl as a modulator, the BET surface area of the MOFs tends to be higher than those synthesized using acetic acid, which can be attributed to missing linkers or nodes (i.e., defects) in the MOF structure, leading to more accessible space in the network structure. The pore size distribution calculated using NLDFT confirms the presence of a pore cavity of 12.0 Å and 12.7 Å for Zr-UiO-66-AA and Zr-UiO-67-AA, respectively, and pore cavities of 15.6 Å for Zr-UiO-66-HCl and Zr-UiO-67-HCl, respectively (Figure 3.16). The particle sizes were also assessed with DLS measurements, revealing particle sizes of ~378 nm for Zr-UiO-66-AA and ~648 nm for Zr-UiO-67-AA (Figure 3.17).

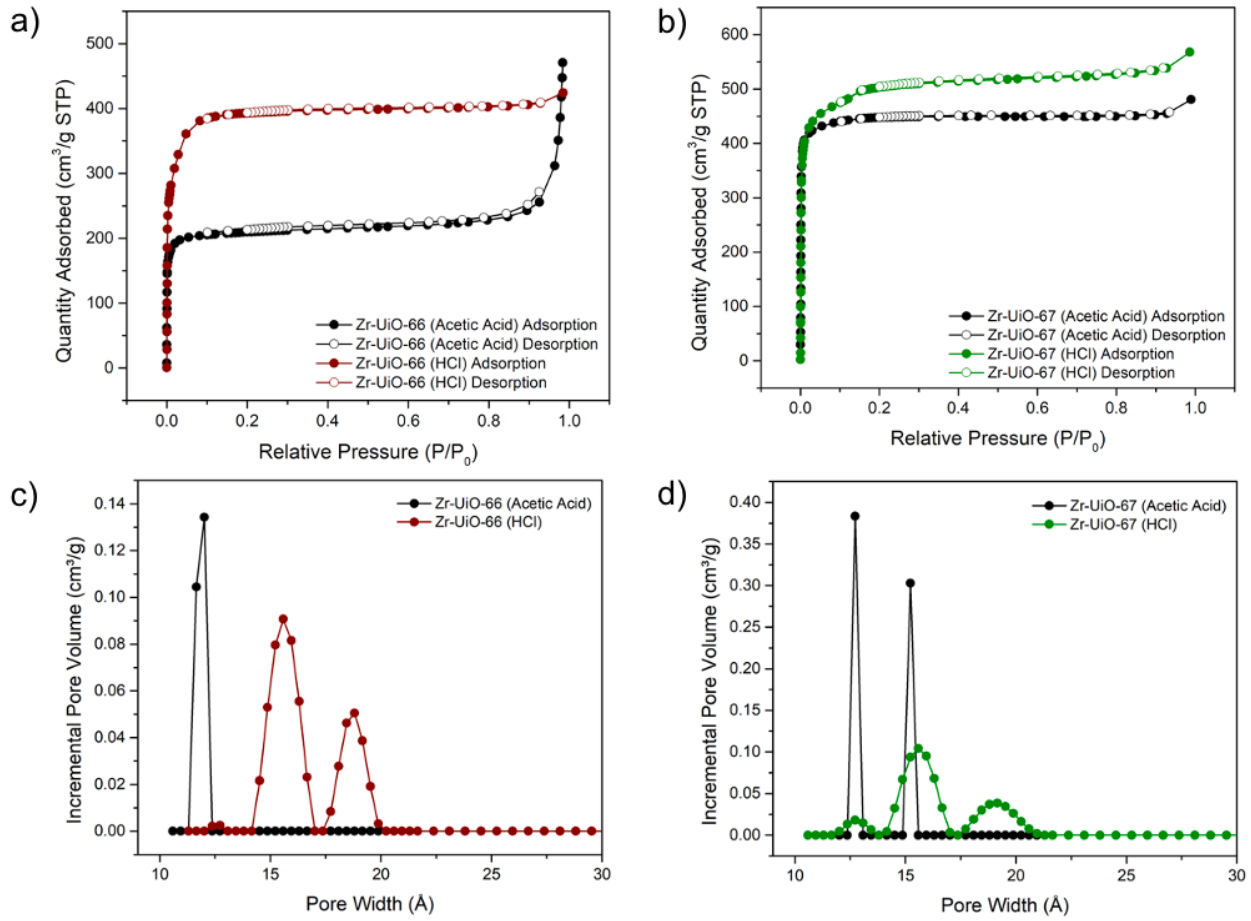

Figure 3.16. Nitrogen adsorption-desorption isotherms of (a) Zr-UiO-66 AA and HCl (Type I(a)), (b) Zr-UiO-67 AA and HCl (Type I(a)), and pore size distribution analysis of (c) Zr-UiO-66 AA and HCl, and (d) Zr-UiO-67 AA and HCl.

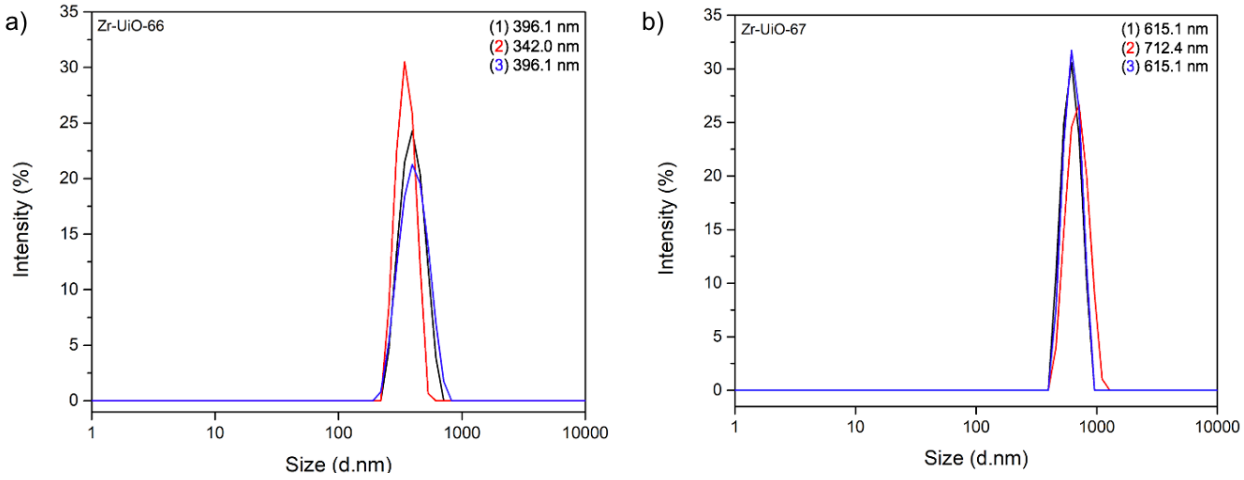

Figure 3.17. DLS measurements of (a) Zr-UiO-66-AA, and (b) Zr-UiO-67-AA.

With the goal of synthesizing the thiolated MOFs using STEPOSOL® MET-10U as a green solvent alternative to DMF, experiments were first carried out with the control MOFs. Zr-UiO-66 was synthesized using STEPOSOL® MET-10U as confirmed by PXRD,[205] (Figure 3.18) although the procedure could not directly be translated for Zr-UiO-67, and the thiolated MOFs, therefore further optimization is required.

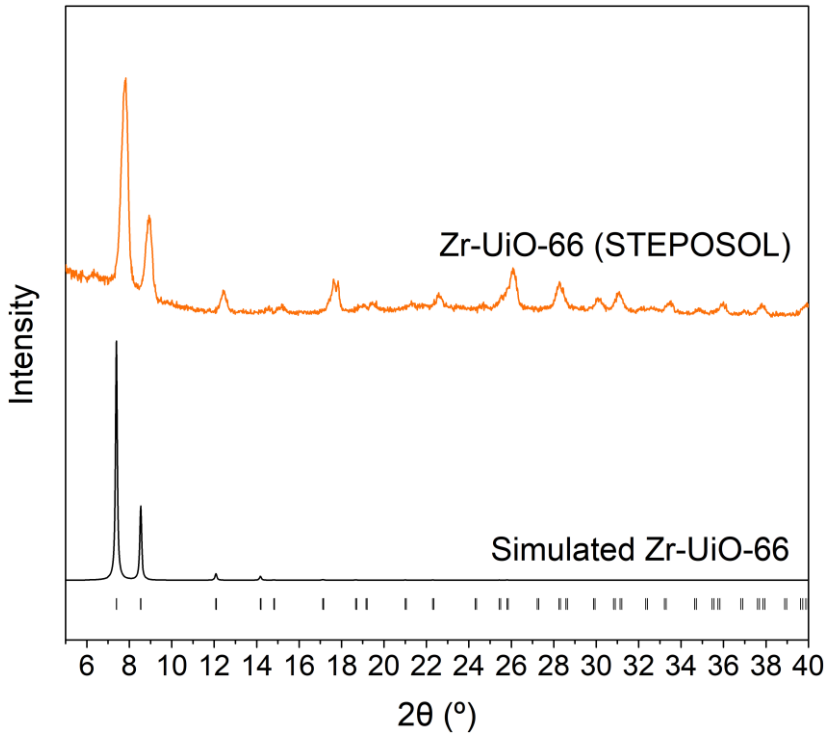

Figure 3.18. PXRD diffractogram of Zr-UiO-66 (STEPOSOL).

3.3.2. MOFs and Mucins Mucoadhesion Study

The thiolated MOFs are mixed with commercial mucins and their mucoadhesive interactions are studied. The mucoadhesion between the MOFs and the mucins can be understood in three steps (Figure 3.19) where (i) a topical application of the flurbiprofen drug loaded MOFs will be administered to the eye(s), (ii) the mucoadhesion interaction between the MOF and mucins occurs at the surface of the cornea, where disulfide bonds will be formed between the thiol groups from the cysteine amino acids and the thiol groups on the surface of the MOF from the organic linkers, and (iii) the flurbiprofen drug release can occur through the cornea cells.

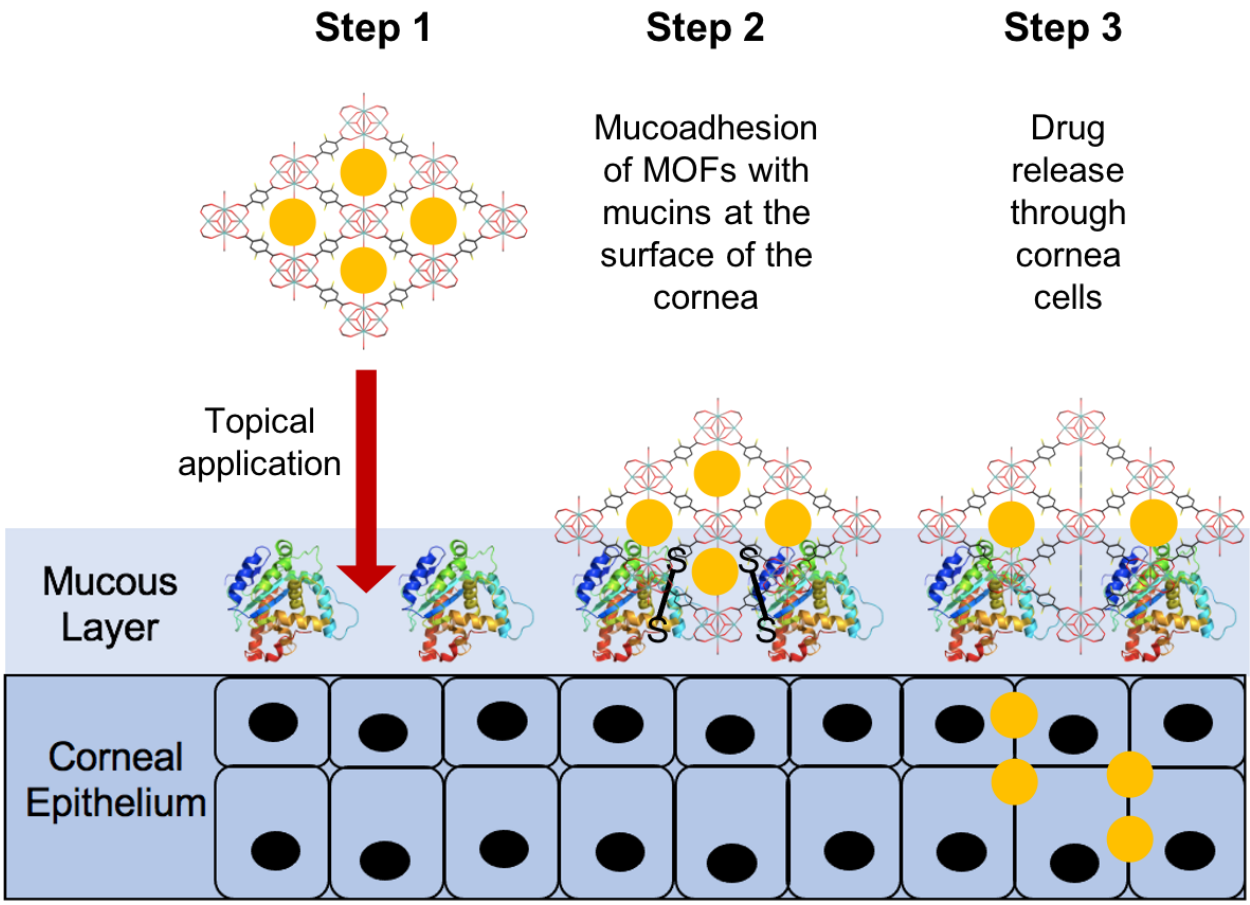

Figure 3.19. Representation of the topical application of a drug loaded MOF to the eye for the mucoadhesion between mucins and the thiolated MOF, followed by drug release.

3.3.2.1. Periodic Acid–Schiff (PAS) Protocol

To assess the potential of the control and thiolated MOFs to act as mucoadhesive drug vectors, Periodic Acid–Schiff (PAS) colorimetric quantification experiments were conducted to

determine the amount of mucins adhered to the MOFs. By mixing the MOFs with a commercial mix of bovine submaxillary mucins in water on a rotary shaker for 2 h at a pH of 7.4, the amount of adhered mucins can be quantified by UV-Vis spectroscopy. The PAS protocol shows that 90.00 ± 0.25% of mucins adhered to Zr-UiO-66-$(SH)_2$-AA, and 99.71 ± 11.21% of mucins adhered to Zr-UiO-67-$(SH)_2$-AA (Figure 3.20). As well, the PAS protocol shows that 99.65 ± 1.17% of mucins adhered to Zr-UiO-66-AA, and -2.67 ± 4.57% mucins adhered to Zr-UiO-67-AA (Figure 3.20). In the case of the control MOF, Zr-UiO-66, significant mucoadhesion was observed, however further studies need to be performed to verify this result. In an ideal case, the mucoadhesion should be exclusive to the thiolated MOFs. Given that the surface of zirconium-based MOFs are slightly negatively charged,[261] there is not expected to be an interaction between the control MOFs with the negatively charged mucins. As for the thiolated MOFs, since thiols have a pKa value of approximately 10, the thiol groups should be protonated during the experiment that is carried out at a neutral pH. As for the disulfide bond formation, which is a covalent bond linkage between two sulfur atoms, it can occur readily in the presence of oxygen and water, but further characterization is required to establish if the thiolated MOF is actually bound to the mucin or just physically adhered to the mucin.

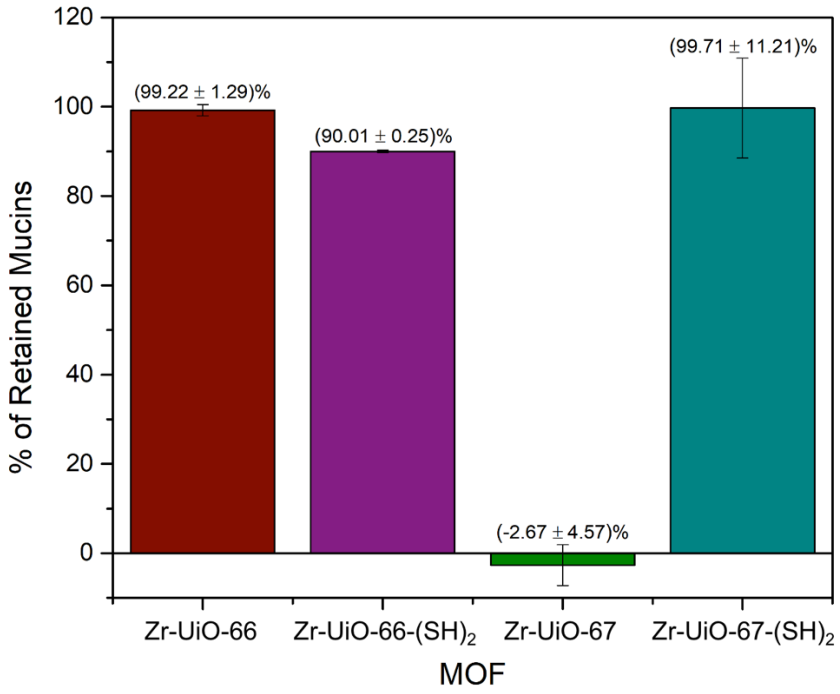

Figure 3.20. Periodic Acid–Schiff (PAS) colorimetric quantification results displaying the amount of mucins adhered to the MOFs.

3.3.3. Thiol Quantification Study

In order to quantify the thiol functional groups present on the external surface of the thiolated MOFs, the colorimetric quantification protocol referred to as the Ellman's test was used. During the thiol quantification tests, the number of thiol groups on the external surface of the MOF are being measured since the reagents are too large to enter the MOF pores. The thiol groups on the external surface are the most relevant to the mucoadhesive drug delivery process, since it's only the external surface of the MOF that would be able to interact with the large mucins. As a result, we expect the experimental moles of thiol determined using the Ellman's test to be much lower than the expected moles of thiol in the entire MOF. To begin, N-acetyl-L-cysteine which has a thiol group, is used as a standard to verify the technique and produce a standard calibration curve (Figure 3.21). The calibration curve shows a linear response, where an increasing concentration of N-acetyl-L-cysteine (from 10 to 60 μM) mixed with 5,5′-dithiobis-(2-nitrobenzoic acid) (DTNB) produces increasing concentrations of 2-nitro-5-thiobenzoic acid (TNB) (Figure 3.21). TNB is a yellow-coloured reagent that can be measured spectrophotometrically and absorbs at 412 nm. As such, for every mole of thiol that reacts with DTNB, one mole of TNB is produced. The procedure was then translated for its use with the thiolated MOFs, also showing that an increase in the concentration of thiolated MOFs produces a darker yellow colour and validates the procedure (Figures 3.22-3.23). For both Zr-UiO-66-$(SH)_2$-AA and Zr-UiO-67-$(SH)_2$-AA, the experimental moles of thiol are shown in Tables 3.1-3.2. These values are lower than the total moles of thiol in the material (Tables 3.1-3.2), since the DTNB reagent (~17 Å x 6 Å) is too large to be encapsulated by the thiolated MOFs.

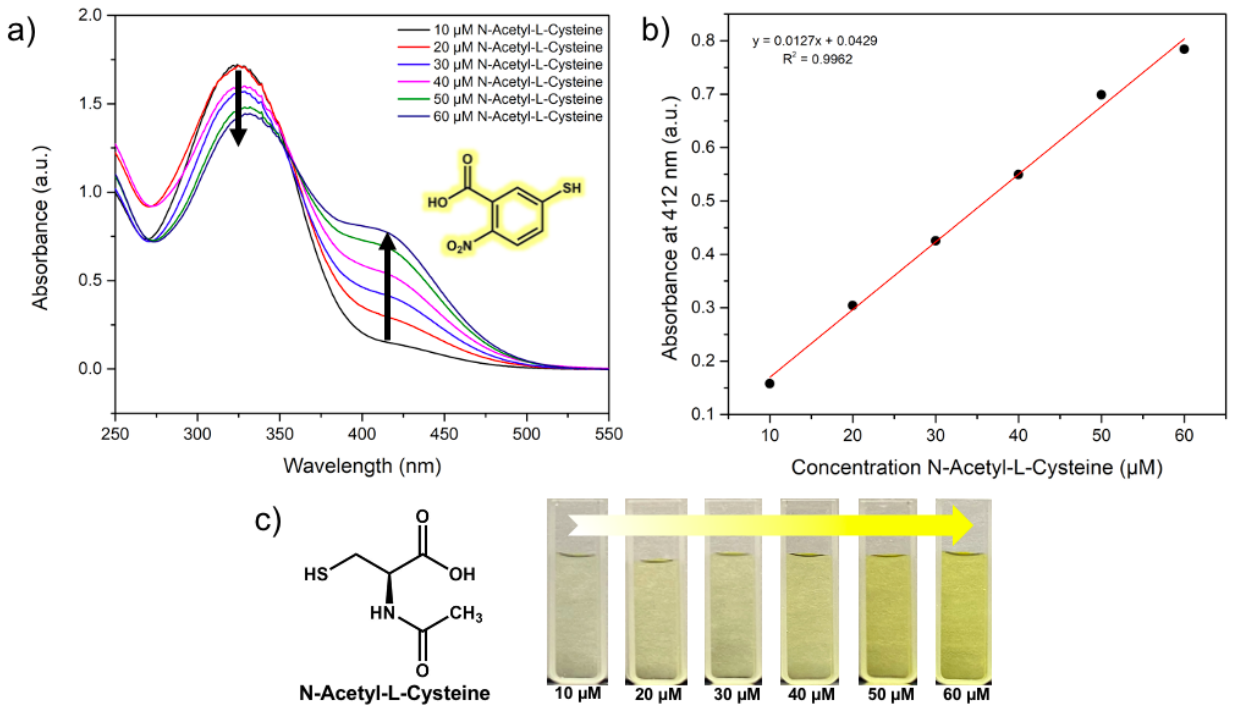

Figure 3.21. Thiol quantification results for N-acetyl-L-cysteine standard, (a) UV-Vis spectra, (b) standard calibration curve, and (c) increasing concentration of N-acetyl-L-cysteine (from 10 to 60 µM) mixed with 5,5′-dithiobis-(2-nitrobenzoic acid) (DTNB) generates increasing concentrations of the yellow-coloured 2-nitro-5-thiobenzoic acid (TNB).

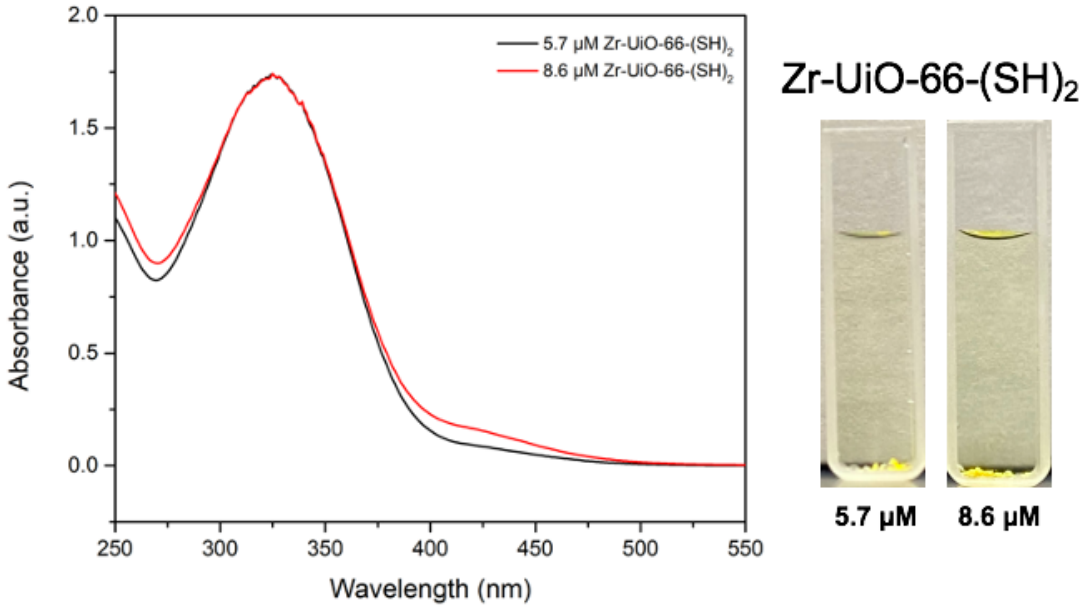

Figure 3.22. UV-Vis spectra for Zr-UiO-66-$(SH)_2$-AA when using increasing concentrations of MOF, for thiol quantification.

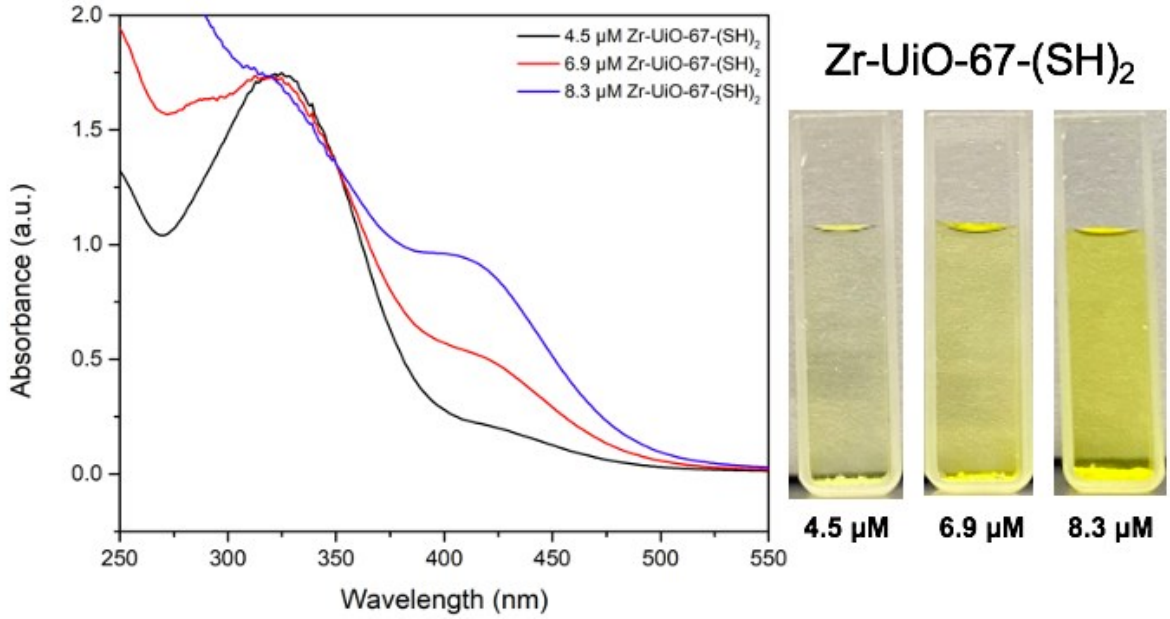

Figure 3.23. UV-Vis spectra for Zr-UiO-67-$(SH)_2$-AA when using increasing concentrations of MOF, for thiol quantification.

Table 3.1. Expected and experimental moles of thiol for Zr-UiO-66-$(SH)_2$-AA calculated using the absorbance of TNB at 412 nm.

Zr-UiO-66-$(SH)_2$	Expected moles thiol	Experimental moles thiol
5.7 μM	2.0×10^{-5}	2.3×10^{-8}
8.6 μM	3.1×10^{-5}	4.0×10^{-8}

Table 3.2. Expected and experimental moles of thiol for Zr-UiO-67-$(SH)_2$-AA calculated using the absorbance of TNB at 412 nm.

Zr-UiO-67-$(SH)_2$	Expected moles thiol	Experimental moles thiol
4.5 μM	1.6×10^{-5}	5.1×10^{-8}
6.9 μM	2.5×10^{-5}	1.2×10^{-7}
8.3 μM	3.0×10^{-5}	2.1×10^{-7}

3.3.4. Inorganic Metal Precursor and Organic Linker Leaching Study

To confirm that the thiolated MOFs remain stable under the conditions used in the PAS protocol, metal and linker leaching studies were carried out by measuring Zr and S concentrations by ICP-MS (Figure 3.24). Trace Zr leaching was observed with values of 6.7 ppb for Zr-UiO-66-$(SH)_2$, and 4.9 ppb for Zr-UiO-67-$(SH)_2$, representing 0.0017% and 0.0015% of the Zr content in the MOF. In addition, trace amounts of S were found, specifically 4.8×10^3 ppb for Zr-UiO-66-$(SH)_2$, and 3.8×10^3 ppb for Zr-UiO-67-$(SH)_2$, representing 1.7% and 1.6% of the S content in the linkers of the MOF. The trace amount of Zr and S leaching can be attributed to metal and linkers on the surface of the MOF, since in general the clusters and linkers terminating the surface of MOFs are not fully connected.

Table 3.3. Zirconium leaching concentrations from the metal node of the thiolated MOFs.

MOF	Zr Leaching Concentration (ppb)	% Zr of MOF
Zr-UiO-66-$(SH)_2$	6.734	0.0017
Zr-UiO-67-$(SH)_2$	4.902	0.0015

Table 3.4. Sulfur leaching concentrations from the organic linkers of the thiolated MOFs.

MOF	S Leaching Concentration (ppb)	% S of MOF
Zr-UiO-66-$(SH)_2$	4789	1.65
Zr-UiO-67-$(SH)_2$	3782	1.60

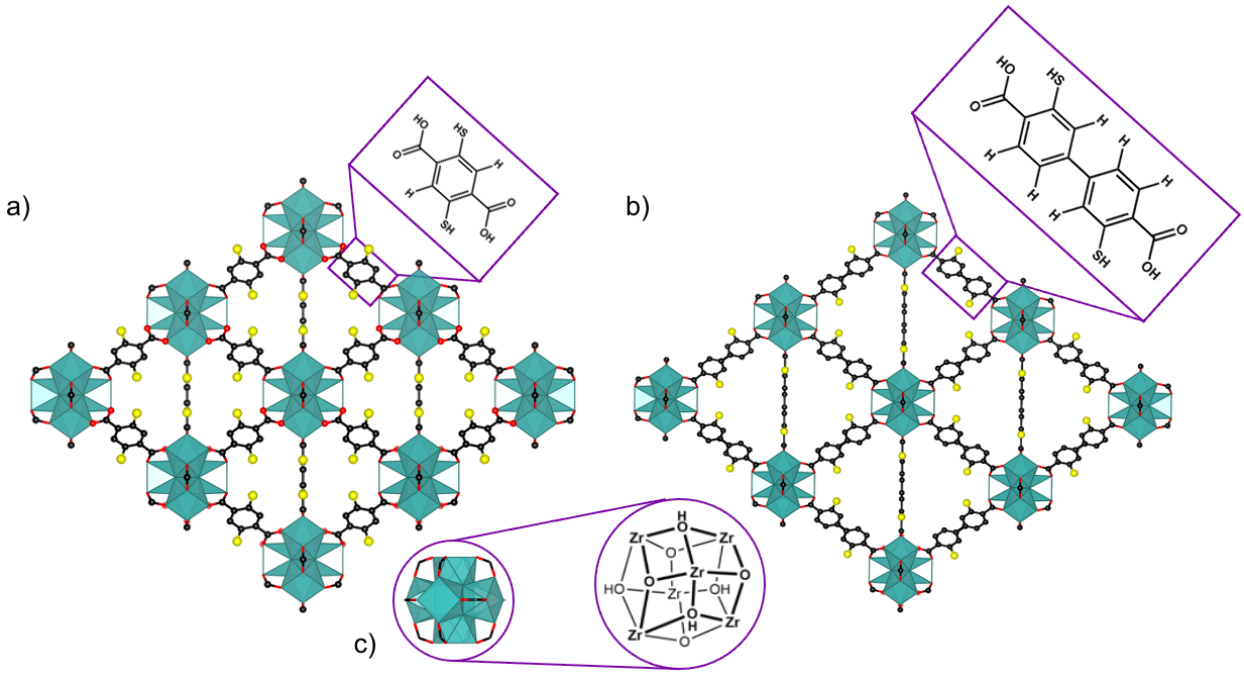

Figure 3.24. Thiolated organic linkers of (a) Zr-UiO-66-$(SH)_2$, (b) Zr-UiO-67-$(SH)_2$, and (c) hexanuclear zirconium node of both MOFs.

3.3.5. Drug Encapsulation and Release of Flurbiprofen

Zr-UiO-66-$(SH)_2$ and Zr-UiO-67-$(SH)_2$ have cage-type and channel-type pores, which is advantageous for drug delivery applications. Since the channels extend infinitely down one axis of the MOF and are connected to the cages (Figure 3.25), FBP can diffuse into the MOF through the infinite channels, and it can be "trapped" in the cages.

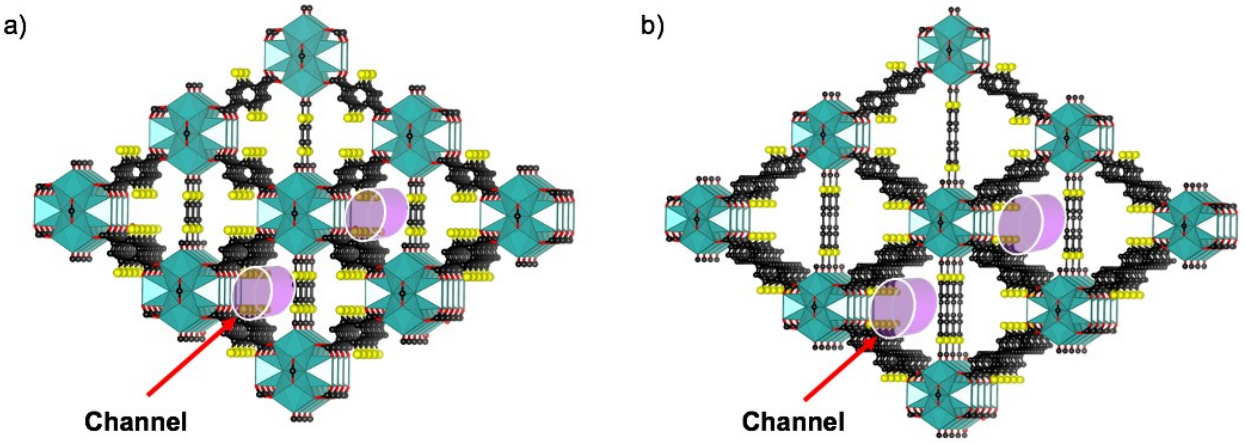

Figure 3.25. Representation of channels found in (a) Zr-UiO-66-$(SH)_2$, and (b) Zr-UiO-67-$(SH)_2$.

The adsorption and desorption of FBP in the control and thiolated MOFs were determined using HPLC and are summarized in Table 3.5. Values of 48.6 mg FBP/g MOF (4.28% of FBP adsorbed by MOF after 24 h or 0.43 mol drug/mol MOF) and 64.5 mg FBP/g MOF (5.70% of FBP adsorbed by MOF after 24 h or 0.57 mol drug/mol MOF) were obtained for for Zr-UiO-66-$(SH)_2$-AA and Zr-UiO-66-$(SH)_2$-HCl, respectively. The adsorption of FBP in Zr-UiO-67-$(SH)_2$-AA and Zr-UiO-67-$(SH)_2$-HCl were found to be 21.5 mg FBP/g MOF (2.35% of FBP adsorbed by MOF after 24 h or 0.24 mol drug/mol MOF) and 117.1 mg FBP/g MOF (13.34% of FBP adsorbed by MOF after 24 h or 1.33 mol drug/mol MOF), respectively. These results demonstrate that the thiolated MOFs synthesized using HCl as a modulator are better candidates for loading FBP, compared to the thiolated MOFs synthesized using acetic acid as a modulator. This is to be expected since it is well-known that UiO-66 analogues synthesized using HCl as a modulator contain more structural defects (i.e., missing nodes and linkers),[61] which can increase the drug loading capacity.

The control MOF samples show FBP adsorption with values of 111.5 mg FBP/g MOF (8.32% of FBP adsorbed by MOF after 24 h or 0.83 mol drug/mol MOF) and 251.0 mg FBP/g MOF (17.95% of FBP adsorbed by MOF after 24 h or 1.79 mol drug/mol MOF) for Zr-UiO-66-AA and Zr-UiO-66-HCl, respectively. On the other hand, the adsorption of FBP in Zr-UiO-67-AA and Zr-UiO-67-HCl gives values of 223.4 mg FBP/g MOF (23.82% of FBP adsorbed by MOF after 24 h or 2.38 mol drug/mol MOF) and 163.7 mg FBP/g MOF (16.91% of FBP adsorbed by MOF after 24 h or 1.69 mol drug/mol MOF), respectively.

The differences in the drug loading capacity between the thiolated and control MOFs can be attributed to the differences in the accessible surface area and porosity, where the BET surface areas are lower for the thiolated MOFs, owing to the sulfur atom which partially blocks the window into the pore of the MOF.

The desorption of FBP from the drug loaded MOFs was found to be 0.95 mg FBP/g MOF and 2.5 mg FBP/g MOF for Zr-UiO-66-$(SH)_2$-AA and Zr-UiO-66-$(SH)_2$-HCl, respectively. Moreover, the desorption values for Zr-UiO-67-$(SH)_2$-AA and Zr-UiO-67-$(SH)_2$-HCl are 1.79 mg FBP/g MOF and 9.5 mg FBP/g MOF, respectively.

The desorption values of FBP in the control MOFs are 11.5 mg FBP/g MOF for Zr-UiO-66-AA, and 10.1 mg FBP/g MOF for Zr-UiO-66-HCl. Moreover, the desorption values of FBP in

the control MOFs are 7.5 mg FBP/g MOF for Zr-UiO-67-AA and 8.5 mg FBP/g MOF for Zr-UiO-67-HCl.

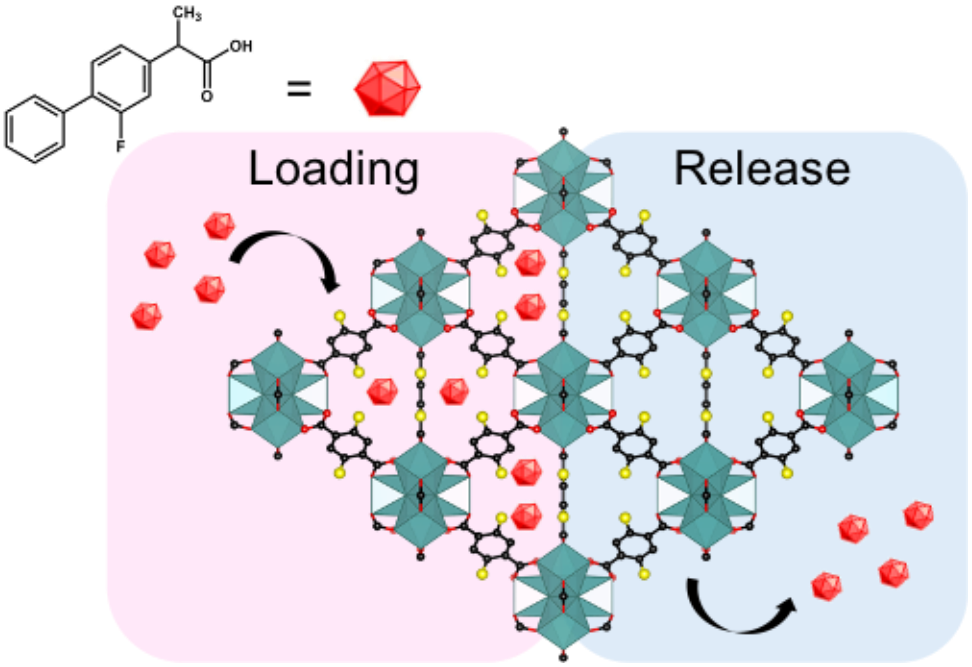

Figure 3.26. Representation of flurbiprofen drug loading and release from Zr-UiO-66-$(SH)_2$.

Table 3.5. Flurbiprofen drug loading and release results in control and thiolated MOFs, with associated BET surface areas.

MOF	BET Surface Area ($m^2 g^{-1}$)	Loading (mg Flurbiprofen / g MOF)	Release (mg Flurbiprofen / g MOF)
CONTROL MOFs			
Zr-UiO-66-AA	840	111.5	11.5
Zr-UiO-67-AA	1790	223.4	7.5
Zr-UiO-66-HCl	1550	251.0	10.1
Zr-UiO-67-HCl	1910	163.7	8.5
THIOLATED MOFs			
Zr-UiO-66-$(SH)_2$-AA	650	48.6	0.95
Zr-UiO-67-$(SH)_2$-AA	1065	21.5	1.79
Zr-UiO-66-$(SH)_2$-HCl	665	64.5	2.5
Zr-UiO-67-$(SH)_2$-HCl	1010	117.1	9.5

The samples of drug loaded MOF (FBP@MOF) were characterized by PXRD to verify if the structural integrity was maintained. PXRD confirms that the network structure is maintained after loading FBP for the thiolated and control Zr-UiO-66, however the thiolated and control Zr-UiO-67 undergo some loss of crystallinity when FBP is loaded into the porous structures (Figure 3.27).

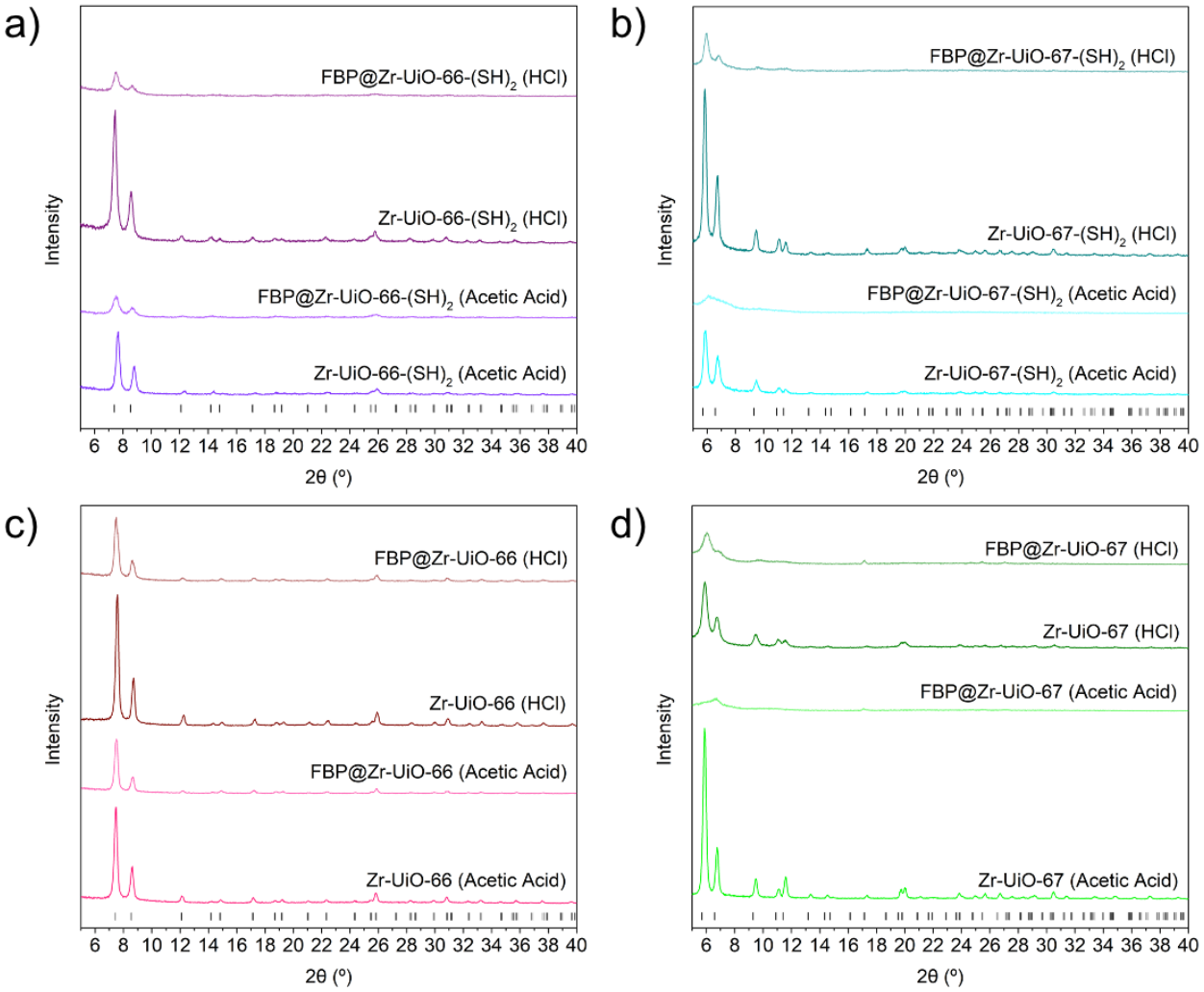

Figure 3.27. PXRD diffractograms of (a) Zr-UiO-66-$(SH)_2$ AA and HCl prior to flurbiprofen (FBP) loading and after drug loading (FBP@MOF), (b) Zr-UiO-67-$(SH)_2$ AA and HCl prior to FBP loading and after drug loading, (c) Zr-UiO-66 AA and HCl prior to FBP loading and after drug loading, and (d) Zr-UiO-67 AA and HCl prior to FBP loading and after drug loading**.**

3.4. Conclusions

In conclusion, thiolated Zr_6-based MOFs offer an interesting alternative platform for use in ophthalmic drug delivery applications. The network structure and phase purity of Zr-UiO-66-$(SH)_2$ and Zr-UiO-67-$(SH)_2$ is confirmed by PXRD, and the surface area and porosity are confirmed with N_2 sorption isotherms, showing suitable surface areas for drug delivery applications. The thiol quantification results demonstrate that there are accessible thiols on the MOF surface, and ICP-MS confirms minimal leaching of Zr and S from the MOF. The mucoadhesive properties of the MOFs were assessed and demonstrate that the thiolated MOFs are mucoadhesive and have significant promise as mucoadhesive drug vectors.

Chapter 4

Conclusions and Future Work

4.1. General Conclusions

In the realm of green chemistry, the use of safer solvents and renewable feedstocks are just two of the twelve principles of green chemistry that chemists strive to implement in their synthetic protocols. STEPOSOL® MET-10U (*N,N*-dimethyl-9-decenamide), a bioderived solvent produced *via* olefin metathesis using renewable feedstocks, such as plant oils, was explored as a solvent for the synthesis of a series of structurally diverse MOFs, including MOF-808, NU-1000, HKUST-1, and ZIF-8, in order to verify the viability of the green solvent. The abovementioned MOFs were successfully synthesized, characterized, and activated, confirming that the MOFs can be synthesized using STEPOSOL® MET-10U, and that the physical properties of the MOFs are analogous to those synthesized in DMF. STEPOSOL® MET-10U, as an alternative to DMF, was used for the sustainable synthesis of two MOFs which are zirconium-based, highlighting the potential to synthesize thiolated Zr_6-based MOFs with this green solvent towards ophthalmic drug delivery applications.

The foundation for the development of a novel thiolated MOF-based ophthalmic drug delivery system capable of mucoadhesion to mucins for biomedical applications has been established. Thiol-functionalized MOFs can be anticipated as promising drug vectors to (i) improve the retention time of therapeutic drugs at the cornea and (ii) improve their bioavailability, hereby improving the efficiency and overall patient health. The isostructural thiol-functionalized Zr_6-based MOFs, UiO-66-$(SH)_2$ and UiO-67-$(SH)_2$, with **fcu** topology were successfully synthesized and characterized, demonstrating crystalline and robust structures with adequate surface areas and porosity. The MOFs exhibited excellent mucoadhesive interactions as determined by the PAS protocol. UiO-66-$(SH)_2$ and UiO-67-$(SH)_2$ were explored for the encapsulation of a non-steroidal anti-inflammatory drug, flurbiprofen – towards establishing a drug vector capable of reducing the frequency of administration. Flurbiprofen uptake was found to be higher in UiO-66-$(SH)_2$ and UiO-67-$(SH)_2$ analogues synthesized using HCl modulator compared to acetic acid, likely due to the presence of defects in the former.

4.2. Future Work

In order to synthesize a larger library of MOFs guided by the twelve principles of green chemistry, additional optimization should be carried out to synthesize Zr-UiO-66-$(SH)_2$ and Zr-UiO-67-$(SH)_2$ using STEPOSOL® MET-10U. This would expand the diversity of MOFs synthesized with the green solvent alternative and promote sustainable MOF synthesis for applications in ophthalmic drug delivery, along with minimizing environmental impacts.

In the interest of constructing efficient and biocompatible MOF-based ophthalmic drug delivery systems for biomedical applications, the thiol-functionalized Zr-UiO-66-$(SH)_2$ and Zr-UiO-67-$(SH)_2$ should be subjected to post-synthetic surface functionalization with a hydrophilic polymer, polyethylene glycol (PEG), to improve or enhance biocompatibility and drug vector uptake. To improve the drug loading capacity and minimize the challenges associated with thiol groups blocking the MOF pores, further research efforts should concentrate on the synthesis of mixed-linker MOFs comprised of both 1,4-benzenedicarboxylic acid and 2,5-dimercapto-1,4-benzenedicarboxylic acid for Zr-UiO-66, and biphenyl-4,4′-dicarboxylic acid and 3,3′-dimercaptobiphenyl-4,4′-dicarboxylic acid for Zr-UiO-67. This should improve the accessible surface areas and porosity of the thiolated MOFs, which is essential for higher drug loading in MOFs.

With the initial success of studying thiol-functionalized MOFs comprised of linear ditopic linkers, the MOFs of interest can be expanded to include MOFs constructed with thiol-functionalized tritopic linkers or post-synthetically modified MOFs to include thiol groups at open metal sites. MOFs with tritopic linkers would also provide larger pore sizes, and potentially lead to a better trade-off between pore size and thiol group functionalization. Through the use of reticular chemistry, we can tune the pore sizes of MOFs to encapsulate and deliver flurbiprofen, and potentially other ophthalmic drugs such as ones used for glaucoma, bimatoprost (~15 Å x 9 Å) and travoprost (~13 Å x 10 Å).

Lastly, due to the high modularity of MOFs, we can tune the metal nodes to include rare-earth metals or lanthanoids such as Eu(III) and Tb(III), to obtain materials with metal-based luminescence properties that will extend the applications of the MOF materials to other areas of ophthalmic therapy such as neurotransmitter detection and imaging.

References

1. Kinoshita, Y.; Matsubara, I.; Higuchi, T.; Saito, Y. *Bull. Chem. Soc. Jpn.* **1959,** *32* (11), 1221-1226.
2. Tomic, E. A. *J. Appl. Polym. Sci.* **1965,** *9* (11), 3745-3752.
3. Hoskins, B. F.; Robson, R. *J. Am. Chem. Soc.* **1989,** *111* (15), 5962-5964.
4. Yaghi, O. M.; Li, H. *J. Am. Chem. Soc.* **1995,** *117* (41), 10401-10402.
5. Yaghi, O. M.; Li, G.; Li, H. *Nature* **1995,** *378* (6558), 703-706.
6. Li, H.; Eddaoudi, M.; O'Keeffe, M.; Yaghi, O. M. *Nature* **1999,** *402*, 276-279.
7. Kondo, M.; Yoshitomi, T.; Matsuzaka, H.; Kitagawa, S.; Seki, K. *Angew. Chem. Int. Ed. Engl.* **1997,** *36* (16), 1725-1727.
8. Cheetham, A. K.; Férey, G.; Loiseau, T. *Angew. Chem. Int. Ed.* **1999,** *38* (22), 3268-3292.
9. Batten, S. R.; Champness, N. R.; Chen, X.-M.; Garcia-Martinez, J.; Kitagawa, S.; Öhrström, L.; O'Keeffe, M.; Suh, M. P.; Reedijk, J. *CrystEngComm* **2012,** *14* (9), 3001-3004.
10. Batten, S. R.; Champness, N. R.; Chen, X.-M.; Garcia-Martinez, J.; Kitagawa, S.; Öhrström, L.; O'Keeffe, M.; Suh, M. P.; Reedijk, J. *Pure Appl. Chem.* **2013,** *85* (8), 1715-1724.
11. Rosi, N. L.; Kim, J.; Eddaoudi, M.; Chen, B.; O'Keeffe, M.; Yaghi, O. M. *J. Am. Chem. Soc.* **2005,** *127* (5), 1504-1518.
12. Joseph, N.; Lawson, H. D.; Overholt, K. J.; Damodaran, K.; Gottardi, R.; Acharya, A. P.; Little, S. R. *Sci. Rep.* **2019,** *9* (1), 13024-13024.
13. Robison, L.; Zhang, L.; Drout, R. J.; Li, P.; Haney, C. R.; Brikha, A.; Noh, H.; Mehdi, B. L.; Browning, N. D.; Dravid, V. P.; Cui, Q.; Islamoglu, T.; Farha, O. K. *ACS Appl. Bio Mater.* **2019,** *2* (3), 1197-1203.
14. Férey, G.; Latroche, M.; Serre, C.; Millange, F.; Loiseau, T.; Percheron-Guégan, A. *Chem. Commun.* **2003,** (24), 2976-2977.
15. Feng, D.; Gu, Z.-Y.; Li, J.-R.; Jiang, H.-L.; Wei, Z.; Zhou, H.-C. *Angew. Chem. Int. Ed.* **2012,** *51* (41), 10307-10310.
16. Feng, D.; Wang, K.; Wei, Z.; Chen, Y.-P.; Simon, C. M.; Arvapally, R. K.; Martin, R. L.; Bosch, M.; Liu, T.-F.; Fordham, S.; Yuan, D.; Omary, M. A.; Haranczyk, M.; Smit, B.; Zhou, H.-C. *Nat. Commun.* **2014,** *5* (1), 5723.

17. Phan, A.; Doonan, C. J.; Uribe-Romo, F. J.; Knobler, C. B.; O'Keeffe, M.; Yaghi, O. M. *Acc. Chem. Res.* **2010,** *43* (1), 58-67.
18. Otake, K.-i.; Cui, Y.; Buru, C. T.; Li, Z.; Hupp, J. T.; Farha, O. K. *J. Am. Chem. Soc.* **2018,** *140* (28), 8652-8656.
19. Xue, D.-X.; Cairns, A. J.; Belmabkhout, Y.; Wojtas, L.; Liu, Y.; Alkordi, M. H.; Eddaoudi, M. *J. Am. Chem. Soc.* **2013,** *135* (20), 7660-7667.
20. Dolgopolova, E. A.; Rice, A. M.; Shustova, N. B. *Chem. Commun.* **2018,** *54* (50), 6472-6483.
21. Furukawa, H.; Go, Y. B.; Ko, N.; Park, Y. K.; Uribe-Romo, F. J.; Kim, J.; O'Keeffe, M.; Yaghi, O. M. *Inorg. Chem.* **2011,** *50* (18), 9147-9152.
22. Ramsahye, N. A.; Trens, P.; Shepherd, C.; Gonzalez, P.; Trung, T. K.; Ragon, F.; Serre, C. *Microporous Mesoporous Mater.* **2014,** *189*, 222-231.
23. Kim, D.; Liu, X.; Lah, M. S. *Inorg. Chem. Front.* **2015,** *2* (4), 336-360.
24. Zhao, D.; Timmons, D. J.; Yuan, D.; Zhou, H.-C. *Acc. Chem. Res.* **2011,** *44* (2), 123-133.
25. O'Keeffe, M.; Yaghi, O. M. *Chem. Rev.* **2012,** *112* (2), 675-702.
26. Furukawa, H.; Cordova, K. E.; O'Keeffe, M.; Yaghi, O. M. *Science* **2013,** *341* (6149), 1230444.
27. Li, H.; Wang, K.; Sun, Y.; Lollar, C. T.; Li, J.; Zhou, H.-C. *Mater. Today* **2018,** *21* (2), 108-121.
28. Li, B.; Wen, H.-M.; Zhou, W.; Chen, B. *J. Phys. Chem. Lett.* **2014,** *5* (20), 3468-3479.
29. Bernales, V.; Ortuño, M. A.; Truhlar, D. G.; Cramer, C. J.; Gagliardi, L. *ACS Cent. Sci.* **2018,** *4* (1), 5-19.
30. Rossin, A.; Tuci, G.; Luconi, L.; Giambastiani, G. *ACS Catal.* **2017,** *7* (8), 5035-5045.
31. Rimoldi, M.; Howarth, A. J.; DeStefano, M. R.; Lin, L.; Goswami, S.; Li, P.; Hupp, J. T.; Farha, O. K. *ACS Catal.* **2017,** *7* (2), 997-1014.
32. Zhang, X.; Wasson, M. C.; Shayan, M.; Berdichevsky, E. K.; Ricardo-Noordberg, J.; Singh, Z.; Papazyan, E. K.; Castro, A. J.; Marino, P.; Ajoyan, Z.; Chen, Z.; Islamoglu, T.; Howarth, A. J.; Liu, Y.; Majewski, M. B.; Katz, M. J.; Mondloch, J. E.; Farha, O. K. *Coord. Chem. Rev.* **2021,** *429*, 213615.
33. Howarth, A. J.; Liu, Y.; Hupp, J. T.; Farha, O. K. *CrystEngComm* **2015,** *17* (38), 7245-7253.

34. Kobielska, P. A.; Howarth, A. J.; Farha, O. K.; Nayak, S. *Coord. Chem. Rev.* **2018,** *358*, 92-107.
35. Mon, M.; Bruno, R.; Ferrando-Soria, J.; Armentano, D.; Pardo, E. *J. Mater. Chem. A* **2018,** *6* (12), 4912-4947.
36. Sadiq, M. M.; Suzuki, K.; Hill, M. R. *Chem. Commun.* **2018,** *54* (23), 2825-2837.
37. Karmakar, A.; Samanta, P.; Desai, A. V.; Ghosh, S. K. *Acc. Chem. Res.* **2017,** *50* (10), 2457-2469.
38. Adil, K.; Belmabkhout, Y.; Pillai, R. S.; Cadiau, A.; Bhatt, P. M.; Assen, A. H.; Maurin, G.; Eddaoudi, M. *Chem. Soc. Rev.* **2017,** *46* (11), 3402-3430.
39. Majewski, M. B.; Peters, A. W.; Wasielewski, M. R.; Hupp, J. T.; Farha, O. K. *ACS Energy Lett.* **2018,** *3* (3), 598-611.
40. Dhakshinamoorthy, A.; Asiri, A. M.; García, H. *Angew. Chem. Int. Ed.* **2016,** *55* (18), 5414-5445.
41. Horcajada, P.; Serre, C.; Maurin, G.; Ramsahye, N. A.; Balas, F.; Vallet-Regí, M.; Sebban, M.; Taulelle, F.; Férey, G. *J. Am. Chem. Soc.* **2008,** *130* (21), 6774-6780.
42. Orellana-Tavra, C.; Marshall, R. J.; Baxter, E. F.; Lázaro, I. A.; Tao, A.; Cheetham, A. K.; Forgan, R. S.; Fairen-Jimenez, D. *J. Mater. Chem. B* **2016,** *4* (47), 7697-7707.
43. Öhrström, L. *Crystals* **2015,** *5*, 154-162.
44. Yaghi, O. M.; O'Keeffe, M.; Ockwig, N. W.; Chae, H. K.; Eddaoudi, M.; Kim, J. *Nature* **2003,** *423* (6941), 705-714.
45. Yaghi, O. M. *J. Am. Chem. Soc.* **2016,** *138* (48), 15507-15509.
46. Yaghi, O. M. *ACS Cent. Sci.* **2019,** *5* (8), 1295-1300.
47. O'Keeffe, M.; Peskov, M. A.; Ramsden, S. J.; Yaghi, O. M. *Acc. Chem. Res.* **2008,** *41* (12), 1782-1789.
48. Furukawa, H.; Ko, N.; Go Yong, B.; Aratani, N.; Choi Sang, B.; Choi, E.; Yazaydin, A. Ö.; Snurr Randall, Q.; O'Keeffe, M.; Kim, J.; Yaghi Omar, M. *Science* **2010,** *329* (5990), 424-428.
49. Hönicke, I. M.; Senkovska, I.; Bon, V.; Baburin, I. A.; Bönisch, N.; Raschke, S.; Evans, J. D.; Kaskel, S. *Angew. Chem. Int. Ed.* **2018,** *57* (42), 13780-13783.

50. Chen, Z.; Li, P.; Anderson, R.; Wang, X.; Zhang, X.; Robison, L.; Redfern, L. R.; Moribe, S.; Islamoglu, T.; Gómez-Gualdrón, D. A.; Yildirim, T.; Stoddart, J. F.; Farha, O. K. *Science* **2020,** *368* (6488), 297-303.

51. Li, P.; Vermeulen, N. A.; Malliakas, C. D.; Gómez-Gualdrón, D. A.; Howarth, A. J.; Mehdi, B. L.; Dohnalkova, A.; Browning, N. D.; O'Keeffe, M.; Farha, O. K. *Science* **2017,** *356* (6338), 624-627.

52. Bai, Y.; Dou, Y.; Xie, L.-H.; Rutledge, W.; Li, J.-R.; Zhou, H.-C. *Chem. Soc. Rev.* **2016,** *45* (8), 2327-2367.

53. Barthel, S.; Alexandrov, E. V.; Proserpio, D. M.; Smit, B. *Crys. Growth Des.* **2018,** *18* (3), 1738-1747.

54. Kandiah, M.; Nilsen, M. H.; Usseglio, S.; Jakobsen, S.; Olsbye, U.; Tilset, M.; Larabi, C.; Quadrelli, E. A.; Bonino, F.; Lillerud, K. P. *Chem. Mater.* **2010,** *22* (24), 6632-6640.

55. Huang, Y.; Qin, W.; Li, Z.; Li, Y. *Dalton Trans.* **2012,** *41* (31), 9283-9285.

56. Wu, H.; Yildirim, T.; Zhou, W. *J. Phys. Chem. Lett.* **2013,** *4* (6), 925-930.

57. DeCoste, J. B.; Peterson, G. W.; Jasuja, H.; Glover, T. G.; Huang, Y.-g.; Walton, K. S. *J. Mater. Chem. A* **2013,** *1* (18), 5642-5650.

58. Jiao, Y.; Liu, Y.; Zhu, G.; Hungerford, J. T.; Bhattacharyya, S.; Lively, R. P.; Sholl, D. S.; Walton, K. S. *J. Phys. Chem. C* **2017,** *121* (42), 23471-23479.

59. Cavka, J. H.; Jakobsen, S.; Olsbye, U.; Guillou, N.; Lamberti, C.; Bordiga, S.; Lillerud, K. P. *J. Am. Chem. Soc.* **2008,** *130* (42), 13850-13851.

60. Guillerm, V.; Ragon, F.; Dan-Hardi, M.; Devic, T.; Vishnuvarthan, M.; Campo, B.; Vimont, A.; Clet, G.; Yang, Q.; Maurin, G.; Férey, G.; Vittadini, A.; Gross, S.; Serre, C. *Angew. Chem. Int. Ed.* **2012,** *51* (37), 9267-9271.

61. Katz, M. J.; Brown, Z. J.; Colón, Y. J.; Siu, P. W.; Scheidt, K. A.; Snurr, R. Q.; Hupp, J. T.; Farha, O. K. *Chem. Commun.* **2013,** *49* (82), 9449-9451.

62. Trickett, C. A.; Gagnon, K. J.; Lee, S.; Gándara, F.; Bürgi, H.-B.; Yaghi, O. M. *Angew. Chem. Int. Ed.* **2015,** *54* (38), 11162-11167.

63. Øien, S.; Wragg, D.; Reinsch, H.; Svelle, S.; Bordiga, S.; Lamberti, C.; Lillerud, K. P. *Crys. Growth Des.* **2014,** *14* (11), 5370-5372.

64. Valenzano, L.; Civalleri, B.; Chavan, S.; Bordiga, S.; Nilsen, M. H.; Jakobsen, S.; Lillerud, K. P.; Lamberti, C. *Chem. Mater.* **2011,** *23* (7), 1700-1718.

65. Schoenecker, P. M.; Carson, C. G.; Jasuja, H.; Flemming, C. J. J.; Walton, K. S. *Ind. Eng. Chem. Res.* **2012,** *51* (18), 6513-6519.
66. Schaate, A.; Roy, P.; Godt, A.; Lippke, J.; Waltz, F.; Wiebcke, M.; Behrens, P. *Chem. Eur. J.* **2011,** *17* (24), 6643-6651.
67. DeStefano, M. R.; Islamoglu, T.; Garibay, S. J.; Hupp, J. T.; Farha, O. K. *Chem. Mater.* **2017,** *29* (3), 1357-1361.
68. Wu, H.; Chua, Y. S.; Krungleviciute, V.; Tyagi, M.; Chen, P.; Yildirim, T.; Zhou, W. *J. Am. Chem. Soc.* **2013,** *135* (28), 10525-10532.
69. Ghosh, P.; Colón, Y. J.; Snurr, R. Q. *Chem. Commun.* **2014,** *50* (77), 11329-11331.
70. Garibay, S. J.; Cohen, S. M. *Chem. Commun.* **2010,** *46* (41), 7700-7702.
71. Yee, K. K.; Reimer, N.; Liu, J.; Cheng, S. Y.; Yiu, S. M.; Weber, J.; Stock, N.; Xu, Z. *J. Am. Chem. Soc.* **2013,** *135* (21), 7795-8.
72. Hu, Z.; Nalaparaju, A.; Peng, Y.; Jiang, J.; Zhao, D. *Inorg. Chem.* **2016,** *55* (3), 1134-1141.
73. Lammert, M.; Wharmby, M. T.; Smolders, S.; Bueken, B.; Lieb, A.; Lomachenko, K. A.; Vos, D. D.; Stock, N. *Chem. Commun.* **2015,** *51* (63), 12578-12581.
74. Wu, X.-P.; Gagliardi, L.; Truhlar, D. G. *J. Am. Chem. Soc.* **2018,** *140* (25), 7904-7912.
75. Donnarumma, P. R.; Frojmovic, S.; Marino, P.; Bicalho, H. A.; Titi, H. M.; Howarth, A. J. *Chem. Commun.* **2021,** *57* (50), 6121-6124.
76. Fisher, D. J., *Carbon-Capture by Metal-Organic Framework Materials*. Materials Research Forum LLC: 2020.
77. Firth, F. C. N.; Cliffe, M. J.; Vulpe, D.; Aragones-Anglada, M.; Moghadam, P. Z.; Fairen-Jimenez, D.; Slater, B.; Grey, C. P. *J. Mater. Chem. A* **2019,** *7* (13), 7459-7469.
78. Liu, C.; Eliseeva, S. V.; Luo, T.-Y.; Muldoon, P. F.; Petoud, S.; Rosi, N. L. *Chem. Sci.* **2018,** *9* (42), 8099-8102.
79. Wong, Y. L.; Diao, Y.; He, J.; Zeller, M.; Xu, Z. *Inorg. Chem.* **2019,** *58* (2), 1462-1468.
80. Chavan, S.; Vitillo, J. G.; Gianolio, D.; Zavorotynska, O.; Civalleri, B.; Jakobsen, S.; Nilsen, M. H.; Valenzano, L.; Lamberti, C.; Lillerud, K. P.; Bordiga, S. *Phys. Chem. Chem. Phys.* **2012,** *14* (5), 1614-1626.
81. Leus, K.; Perez, J. P. H.; Folens, K.; Meledina, M.; Van Tendeloo, G.; Du Laing, G.; Van Der Voort, P. *Faraday Discuss.* **2017,** *201*, 145-161.

82. Chen, T.-F.; Han, S.-Y.; Wang, Z.-P.; Gao, H.; Wang, L.-Y.; Deng, Y.-H.; Wan, C.-Q.; Tian, Y.; Wang, Q.; Wang, G.; Li, G.-S. *Appl. Catal. B: Environ.* **2019,** *259*, 118047.
83. Ding, L.; Luo, X.; Shao, P.; Yang, J.; Sun, D. *ACS Sustain. Chem. Eng.* **2018,** *6* (7), 8494-8502.
84. Howarth, A. J.; Peters, A. W.; Vermeulen, N. A.; Wang, T. C.; Hupp, J. T.; Farha, O. K. *Chem. Mater.* **2016,** *29* (1), 26-39.
85. Li, M.; Dincă, M. *J. Am. Chem. Soc.* **2011,** *133* (33), 12926-12929.
86. Al-Kutubi, H.; Gascon, J.; Sudhölter, E. J. R.; Rassaei, L. *ChemElectroChem* **2015,** *2* (4), 462-474.
87. Friščić, T.; Reid, D. G.; Halasz, I.; Stein, R. S.; Dinnebier, R. E.; Duer, M. J. *Angew. Chem. Int. Ed.* **2010,** *49* (4), 712-715.
88. Friščić, T. *Chem. Soc. Rev.* **2012,** *41* (9), 3493-3510.
89. Khan, N. A.; Jhung, S. H. *Coord. Chem. Rev.* **2015,** *285*, 11-23.
90. Klinowski, J.; Almeida Paz, F. A.; Silva, P.; Rocha, J. *Dalton Trans.* **2011,** *40* (2), 321-330.
91. Zacher, D.; Shekhah, O.; Wöll, C.; Fischer, R. A. *Chem. Soc. Rev.* **2009,** *38* (5), 1418-1429.
92. Stock, N.; Biswas, S. *Chem. Rev.* **2012,** *112* (2), 933-969.
93. Seetharaj, R.; Vandana, P. V.; Arya, P.; Mathew, S. *Arab. J. Chem.* **2019,** *12* (3), 295-315.
94. Yang, D.; Gates, B. C. *ACS Catal.* **2019,** *9* (3), 1779-1798.
95. Vermoortele, F.; Bueken, B.; Le Bars, G.; Van de Voorde, B.; Vandichel, M.; Houthoofd, K.; Vimont, A.; Daturi, M.; Waroquier, M.; Van Speybroeck, V.; Kirschhock, C.; De Vos, D. E. *J. Am. Chem. Soc.* **2013,** *135* (31), 11465-11468.
96. Wang, Z.; Cohen, S. M. *Chem. Soc. Rev.* **2009,** *38* (5), 1315-1329.
97. Mandal, S.; Natarajan, S.; Mani, P.; Pankajakshan, A. *Adv. Funct. Mater.* **2021,** *31* (4), 2006291.
98. Bicalho, H. A.; Donnarumma, P. R.; Quezada-Novoa, V.; Titi, H. M.; Howarth, A. J. *Inorg. Chem.* **2021,** *60* (16), 11795-11802.
99. Karagiaridi, O.; Bury, W.; Sarjeant, A. A.; Hupp, J. T.; Farha, O. K. *J. Vis. Exp.* **2014,** (91), e52094.

100. Deria, P.; Bury, W.; Hod, I.; Kung, C.-W.; Karagiaridi, O.; Hupp, J. T.; Farha, O. K. *Inorg. Chem.* **2015,** *54* (5), 2185-2192.
101. Trevors, J. T. *Water, Air, Soil Pollut.* **2010,** *205* (1), 113-114.
102. de Lorenzo, V.; Marlière, P.; Solé, R. *Microb. Biotechnol.* **2016,** *9* (5), 618-625.
103. Harper, C. L., *Environment and Society: Human Perspectives on Environmental Issues*. Pearson/ Prentice Hall: 2004.
104. Obama, B. *Science* **2017,** *355* (6321), 126-129.
105. Dodman, D., *Environment and Urbanization, in International Encyclopedia of Geography: People, the Earth, Environment and Technology*. ed. D. Richardson, N. Castree, M. F. Goodchild, A. Kobayashi, W. Liu and R. A. Marston: 2017.
106. Wallace, D., *Sustainable Industrialization*. Royal Institute of International Affairs: 1996.
107. Karpudewan, M.; Hj Ismail, Z.; Mohamed, N. *J. Educ. Sustain. Dev.* **2011,** *5* (2), 197-214.
108. Anastas, P. T.; Warner, J. C., *Green Chemistry: Theory and Practice*. Oxford University Press: 1998.
109. Anastas, P.; Eghbali, N. *Chem. Soc. Rev.* **2010,** *39* (1), 301-12.
110. Erythropel, H. C.; Zimmerman, J. B.; de Winter, T. M.; Petitjean, L.; Melnikov, F.; Lam, C. H.; Lounsbury, A. W.; Mellor, K. E.; Janković, N. Z.; Tu, Q.; Pincus, L. N.; Falinski, M. M.; Shi, W.; Coish, P.; Plata, D. L.; Anastas, P. T. *Green Chem.* **2018,** *20* (9), 1929-1961.
111. Torok, B.; Dransfield, T., *Green Chemistry: An Inclusive Approach*. Elsevier Science: 2017.
112. Gaab, M.; Trukhan, N.; Maurer, S.; Gummaraju, R.; Müller, U. *Microporous Mesoporous Mater.* **2012,** *157*, 131-136.
113. Reinsch, H.; Waitschat, S.; Chavan, S. M.; Lillerud, K. P.; Stock, N. *Eur. J. Inorg. Chem.* **2016,** *2016* (27), 4490-4498.
114. Toxics Use Reduction Institute, *Summary of Policy Analysis*, Aug 12, 2014, Higher Hazard Substance Designation Recommendation: Dimethylformamide (CAS 68-12-2).
115. European Chemicals Agency, *Substance Information: N,N-dimethylformamide.* https://echa.europa.eu/de/substance-information/-/substanceinfo/100.000.617 (accessed November 25, 2021.

116. Government of Canada, *ARCHIVED - Priority Substances List Assessment Report for N,N-Dimethylformamide.* https://www.canada.ca/en/health-canada/services/environmental-workplace-health/reports-publications/environmental-contaminants/canadian-environmental-protection-act-1999-priority-substances-list-assessment-report-dimethylformamide.html (accessed November 25, 2021).
117. Zhang, J.; White, G. B.; Ryan, M. D.; Hunt, A. J.; Katz, M. J. *ACS Sustain. Chem. Eng.* **2016,** *4* (12), 7186-7192.
118. Parnham, E. R.; Morris, R. E. *Acc. Chem. Res.* **2007,** *40* (10), 1005-1013.
119. Sánchez-Sánchez, M.; Getachew, N.; Díaz, K.; Díaz-García, M.; Chebude, Y.; Díaz, I. *Green Chem.* **2015,** *17* (3), 1500-1509.
120. Lanchas, M.; Vallejo-Sánchez, D.; Beobide, G.; Castillo, O.; Aguayo, A. T.; Luque, A.; Román, P. *Chem. Commun.* **2012,** *48* (79), 9930-9932.
121. Do, J.-L.; Friščić, T. *ACS Cent. Sci.* **2017,** *3* (1), 13-19.
122. Užarević, K.; Wang, T. C.; Moon, S.-Y.; Fidelli, A. M.; Hupp, J. T.; Farha, O. K.; Friščić, T. *Chem. Commun.* **2016,** *52* (10), 2133-2136.
123. Martinez Joaristi, A.; Juan-Alcañiz, J.; Serra-Crespo, P.; Kapteijn, F.; Gascon, J. *Crys. Growth Des.* **2012,** *12* (7), 3489-3498.
124. Carson, C. G.; Brown, A. J.; Sholl, D. S.; Nair, S. *Crys. Growth Des.* **2011,** *11* (10), 4505-4510.
125. Liang, W.; Babarao, R.; D'Alessandro, D. M. *Inorg. Chem.* **2013,** *52* (22), 12878-12880.
126. Julien, P. A.; Mottillo, C.; Friščić, T. *Green Chem.* **2017,** *19* (12), 2729-2747.
127. Suh, M. P.; Park, H. J.; Prasad, T. K.; Lim, D.-W. *Chem. Rev.* **2012,** *112* (2), 782-835.
128. Sumida, K.; Rogow, D. L.; Mason, J. A.; McDonald, T. M.; Bloch, E. D.; Herm, Z. R.; Bae, T.-H.; Long, J. R. *Chem. Rev.* **2012,** *112* (2), 724-781.
129. Kumar, P.; Kim, K.-H.; Kwon, E. E.; Szulejko, J. E. *J. Mater. Chem. A* **2016,** *4* (2), 345-361.
130. Sun, D. T.; Peng, L.; Reeder, W. S.; Moosavi, S. M.; Tiana, D.; Britt, D. K.; Oveisi, E.; Queen, W. L. *ACS Cent. Sci.* **2018,** *4* (3), 349-356.
131. STEPOSOL® MET-10U, https://www.stepan.com/content/stepan-dot-com/en/products-markets/product/STEPOSOLMET10U.html. (accessed March 22, 2021).

132. Stepan introduces STEPOSOL® MET-10U as part of its joint development agreement with Elevance, https://elevance.com/news/stepan-introduces-steposol-met-10u-as-part-of-its-joint-development-agreement-with-elevance/. (accessed March 22, 2021).
133. Stepan®, STEPOSOL® MET-10U Product Bulletin, 2019.
134. Marino, P.; Donnarumma, P. R.; Bicalho, H. A.; Quezada-Novoa, V.; Titi, H. M.; Howarth, A. J. *ACS Sustain. Chem. Eng.* **2021,** *9* (48), 16356-16362.
135. Mondloch, J. E.; Karagiaridi, O.; Farha, O. K.; Hupp, J. T. *CrystEngComm* **2013,** *15* (45), 9258-9264.
136. Prasad, T. K.; Suh, M. P. *Chem. Eur. J.* **2012,** *18* (28), 8673-8680.
137. Liu, B.; Wong-Foy, A. G.; Matzger, A. J. *Chem. Commun.* **2013,** *49* (14), 1419-1421.
138. Ma, L.; Jin, A.; Xie, Z.; Lin, W. *Angew. Chem. Int. Ed.* **2009,** *48* (52), 9905-9908.
139. Zhang, X.; Chen, Z.; Liu, X.; Hanna, S. L.; Wang, X.; Taheri-Ledari, R.; Maleki, A.; Li, P.; Farha, O. K. *Chem. Soc. Rev.* **2020,** *49* (20), 7406-7427.
140. Mondloch, J. E.; Bury, W.; Fairen-Jimenez, D.; Kwon, S.; DeMarco, E. J.; Weston, M. H.; Sarjeant, A. A.; Nguyen, S. T.; Stair, P. C.; Snurr, R. Q.; Farha, O. K.; Hupp, J. T. *J. Am. Chem. Soc.* **2013,** *135* (28), 10294-10297.
141. Efome, J. E.; Rana, D.; Matsuura, T.; Lan, C. Q. *ACS Appl. Mater. Interfaces* **2018,** *10* (22), 18619-18629.
142. Alezi, D.; Belmabkhout, Y.; Suyetin, M.; Bhatt, P. M.; Weseliński, Ł. J.; Solovyeva, V.; Adil, K.; Spanopoulos, I.; Trikalitis, P. N.; Emwas, A.-H.; Eddaoudi, M. *J. Am. Chem. Soc.* **2015,** *137* (41), 13308-13318.
143. Yuan, S.; Huang, L.; Huang, Z.; Sun, D.; Qin, J.-S.; Feng, L.; Li, J.; Zou, X.; Cagin, T.; Zhou, H.-C. *J. Am. Chem. Soc.* **2020,** *142* (10), 4732-4738.
144. Chung, Y. G.; Camp, J.; Haranczyk, M.; Sikora, B. J.; Bury, W.; Krungleviciute, V.; Yildirim, T.; Farha, O. K.; Sholl, D. S.; Snurr, R. Q. *Chem. Mater.* **2014,** *26* (21), 6185-6192.
145. Mondloch, J. E.; Katz, M. J.; Planas, N.; Semrouni, D.; Gagliardi, L.; Hupp, J. T.; Farha, O. K. *Chem. Commun.* **2014,** *50* (64), 8944-8946.
146. Wilmer, C. E.; Leaf, M.; Lee, C. Y.; Farha, O. K.; Hauser, B. G.; Hupp, J. T.; Snurr, R. Q. *Nat. Chem.* **2012,** *4* (2), 83-89.
147. Cui, Y.; Yue, Y.; Qian, G.; Chen, B. *Chem. Rev.* **2012,** *112* (2), 1126-1162.

148. Cui, Y.; Li, B.; He, H.; Zhou, W.; Chen, B.; Qian, G. *Acc. Chem. Res.* **2016,** *49* (3), 483-493.

149. Bauer, C. A.; Timofeeva, T. V.; Settersten, T. B.; Patterson, B. D.; Liu, V. H.; Simmons, B. A.; Allendorf, M. D. *J. Am. Chem. Soc.* **2007,** *129* (22), 7136-7144.

150. Kreno, L. E.; Leong, K.; Farha, O. K.; Allendorf, M.; Van Duyne, R. P.; Hupp, J. T. *Chem. Rev.* **2012,** *112* (2), 1105-1125.

151. Faust, T. *Nat. Chem.* **2016,** *8* (11), 990-991.

152. *Nat. Chem.* **2016,** *8* (11), 987-987.

153. Horcajada, P.; Chalati, T.; Serre, C.; Gillet, B.; Sebrie, C.; Baati, T.; Eubank, J. F.; Heurtaux, D.; Clayette, P.; Kreuz, C.; Chang, J.-S.; Hwang, Y. K.; Marsaud, V.; Bories, P.-N.; Cynober, L.; Gil, S.; Férey, G.; Couvreur, P.; Gref, R. *Nat. Mater.* **2010,** *9* (2), 172-178.

154. Gandara-Loe, J.; Ortuño-Lizarán, I.; Fernández-Sanchez, L.; Alió, J. L.; Cuenca, N.; Vega-Estrada, A.; Silvestre-Albero, J. *ACS Appl. Mater. Interfaces* **2019,** *11* (2), 1924-1931.

155. Majewski, M. B.; Noh, H.; Islamoglu, T.; Farha, O. K. *J. Mater. Chem. A* **2018,** *6* (17), 7338-7350.

156. He, S.; Wu, L.; Li, X.; Sun, H.; Xiong, T.; Liu, J.; Huang, C.; Xu, H.; Sun, H.; Chen, W.; Gref, R.; Zhang, J. *Acta Pharm. Sin. B.* **2021,** *11* (8), 2362-2395.

157. Sun, Y.; Zheng, L.; Yang, Y.; Qian, X.; Fu, T.; Li, X.; Yang, Z.; Yan, H.; Cui, C.; Tan, W. *Nano-Micro Lett.* **2020,** *12* (1), 103.

158. Singh, N.; Qutub, S.; Khashab, N. M. *J. Mater. Chem. B* **2021,** *9* (30), 5925-5934.

159. Suresh, K.; Matzger, A. J. *Angew. Chem. Int. Ed.* **2019,** *58* (47), 16790-16794.

160. Cai, W.; Wang, J.; Chu, C.; Chen, W.; Wu, C.; Liu, G. *Adv. Sci.* **2019,** *6* (1), 1801526.

161. Chen, Y.; Li, P.; Modica, J. A.; Drout, R. J.; Farha, O. K. *J. Am. Chem. Soc.* **2018,** *140* (17), 5678-5681.

162. Sun, C.-Y.; Qin, C.; Wang, C.-G.; Su, Z.-M.; Wang, S.; Wang, X.-L.; Yang, G.-S.; Shao, K.-Z.; Lan, Y.-Q.; Wang, E.-B. *Adv. Mater.* **2011,** *23* (47), 5629-5632.

163. Teplensky, M. H.; Fantham, M.; Li, P.; Wang, T. C.; Mehta, J. P.; Young, L. J.; Moghadam, P. Z.; Hupp, J. T.; Farha, O. K.; Kaminski, C. F.; Fairen-Jimenez, D. *J. Am. Chem. Soc.* **2017,** *139* (22), 7522-7532.

164. Holder, C. F.; Schaak, R. E. *ACS Nano* **2019,** *13* (7), 7359-7365.
165. Øien-Ødegaard, S.; Shearer, G. C.; Wragg, D. S.; Lillerud, K. P. *Chem. Soc. Rev.* **2017,** *46* (16), 4867-4876.
166. Gándara, F.; Bennett, T. D. *IUCrJ* **2014,** *1* (Pt 6), 563-570.
167. Thommes, M.; Kaneko, K.; Neimark, A. V.; Olivier, J. P.; Rodriguez-Reinoso, F.; Rouquerol, J.; Sing, K. S. W. *Pure Appl. Chem.* **2015,** *87* (9-10), 1051-1069.
168. Brunauer, S.; Emmett, P. H.; Teller, E. *J. Am. Chem. Soc.* **1938,** *60* (2), 309-319.
169. Langmuir, I. *J. Am. Chem. Soc.* **1918,** *40* (9), 1361-1403.
170. Olivier, J. P. *Carbon* **1998,** *36* (10), 1469-1472.
171. Kupgan, G.; Liyana-Arachchi, T. P.; Colina, C. M. *Langmuir* **2017,** *33* (42), 11138-11145.
172. Lázaro, I. A. *Eur. J. Inorg. Chem.* **2020,** *2020* (45), 4284-4294.
173. Vukotic, V. N.; Loeb, S. J. *Chem. Eur. J.* **2010,** *16* (46), 13630-13637.
174. Shaffner, T. J.; Veld, R. D. V. *J. Phys. E: Sci. Instrum.* **1971,** *4* (9), 633-637.
175. Wang, T. C.; Vermeulen, N. A.; Kim, I. S.; Martinson, A. B.; Stoddart, J. F.; Hupp, J. T.; Farha, O. K. *Nat. Protoc.* **2016,** *11* (1), 149-162.
176. Passos, M. L. C.; Sarraguça, M. C.; Saraiva, M. L. M. F. S.; Prasada Rao, T.; Biju, V. M., Spectrophotometry | Organic Compounds. In *Encyclopedia of Analytical Science (Third Edition)*, Worsfold, P.; Poole, C.; Townshend, A.; Miró, M., Eds. Academic Press: Oxford, 2019; pp 236-243.
177. Gika, H.; Kaklamanos, G.; Manesiotis, P.; Theodoridis, G., Chromatography: High-Performance Liquid Chromatography. In *Encyclopedia of Food and Health*, Caballero, B.; Finglas, P. M.; Toldrá, F., Eds. Academic Press: Oxford, 2016; pp 93-99.
178. Ellman, G. L. *Arch. Biochem. Biophys.* **1959,** *82* (1), 70-77.
179. Popov, A. *J. Ocul. Pharmacol. Ther.* **2020,** *36* (6), 366-375.
180. Kudelka, M. R.; Ju, T.; Heimburg-Molinaro, J.; Cummings, R. D. *Adv. Cancer Res.* **2015,** *126*, 53-135.
181. Boddupalli, B. M.; Mohammed, Z. N.; Nath, R. A.; Banji, D. *J. Adv. Pharm. Technol. Res.* **2010,** *1* (4), 381-7.
182. Bansil, R.; Turner, B. S. *Curr. Opin. Colloid Interface Sci.* **2006,** *11* (2), 164-170.
183. Hodges, R. R.; Dartt, D. A. *Exp. Eye Res.* **2013,** *117*, 62-78.
184. Mantle, M.; Allen, A. *Biochem. Soc. Trans.* **1978,** *6* (3), 607-609.

185. Kilcoyne, M.; Gerlach, J. Q.; Farrell, M. P.; Bhavanandan, V. P.; Joshi, L. *Anal. Biochem.* **2011,** *416* (1), 18-26.
186. Ouellette, M.; Masse, F.; Lefebvre-Demers, M.; Maestracci, Q.; Grenier, P.; Millar, R.; Bertrand, N.; Prieto, M.; Boisselier, E. *Sci. Rep.* **2018,** *8* (1), 14357.
187. Sheldon, R. A. *Chem. Soc. Rev.* **2012,** *41* (4), 1437-51.
188. Tortell, P. D. *Proc. Natl. Acad. Sci.* **2020,** *117* (16), 8683-8691.
189. Ma, S.; Zhou, H.-C. *J. Am. Chem. Soc.* **2006,** *128* (36), 11734-11735.
190. Ding, M.; Flaig, R. W.; Jiang, H. L.; Yaghi, O. M. *Chem. Soc. Rev.* **2019,** *48* (10), 2783-2828.
191. Lee, J.; Farha, O. K.; Roberts, J.; Scheidt, K. A.; Nguyen, S. T.; Hupp, J. T. *Chem. Soc. Rev.* **2009,** *38* (5), 1450-1459.
192. Titi, H. M.; Do, J.-L.; Howarth, A. J.; Nagapudi, K.; Friščić, T. *Chem. Sci.* **2020,** *11* (29), 7578-7584.
193. Ajoyan, Z.; Marino, P.; Howarth, A. J. *CrystEngComm* **2018,** *20* (39), 5899-5912.
194. Kumar, S.; Jain, S.; Nehra, M.; Dilbaghi, N.; Marrazza, G.; Kim, K.-H. *Coord. Chem. Rev.* **2020,** *420*, 213407.
195. Preventing Adverse Health Effects from Exposure to: Dimethylformamide (DMF), https://www.cdc.gov/niosh/docs/90-105/default.html, (accessed March 22, 2021).
196. Byrne, F. P.; Jin, S.; Paggiola, G.; Petchey, T. H. M.; Clark, J. H.; Farmer, T. J.; Hunt, A. J.; Robert McElroy, C.; Sherwood, J. *Sustainable Chemical Processes* **2016,** *4* (1), 1-24.
197. Sustainability, https://elevance.com/sustainability/, (accessed March 22, 2021).
198. Weissermel, K.; Arpe, H. Industrial Organic Chemistry: Important Raw Materials and Intermediates. Wiley-VCH Verlag GmbH & Co. KGaA: 2008.
199. Rouwenhorst, K. H. R.; Krzywda, P. M.; Benes, N. E.; Mul, G.; Lefferts, L., Chapter 4 - Ammonia Production Technologies. In *Techno-Economic Challenges of Green Ammonia as an Energy Vector*, Valera-Medina, A.; Banares-Alcantara, R., Eds. Academic Press: 2021; pp 41-83.
200. OECD, *Test No. 402: Acute Dermal Toxicity*. 2017.
201. OECD, *Test No. 301: Ready Biodegradability*. 1992.

202. Para, G.; Łuczyński, J.; Palus, J.; Jarek, E.; Wilk, K. A.; Warszyński, P. *J. Colloid Interface Sci.* **2016,** *465*, 174-182.
203. Burrows, A. D.; Cassar, K.; Friend, R. M. W.; Mahon, M. F.; Rigby, S. P.; Warren, J. E. *CrystEngComm* **2005,** *7* (89), 548-550.
204. McGuire, C. V.; Forgan, R. S. *Chem. Commun.* **2015,** *51* (25), 5199-5217.
205. Morelli Venturi, D.; Campana, F.; Marmottini, F.; Costantino, F.; Vaccaro, L. *ACS Sustain. Chem. Eng.* **2020,** *8* (46), 17154-17164.
206. Sheldrick, G. M. *Acta Crystallogr. A: Found Adv.* **2015,** *71* (Pt 1), 3-8.
207. Sheldrick, G. M. *Acta Crystallogr. C: Struct. Chem.* **2015,** *71* (Pt 1), 3-8.
208. Spek, A. L. *Acta Crystallogr. C: Struct. Chem.* **2015,** *71* (Pt 1), 9-18.
209. Furukawa, H.; Gandara, F.; Zhang, Y. B.; Jiang, J.; Queen, W. L.; Hudson, M. R.; Yaghi, O. M. *J. Am. Chem. Soc.* **2014,** *136* (11), 4369-81.
210. Karagiaridi, O.; Lalonde, M. B.; Bury, W.; Sarjeant, A. A.; Farha, O. K.; Hupp, J. T. *J. Am. Chem. Soc.* **2012,** *134* (45), 18790-6.
211. Chui, S. S. Y.; Lo, S. M. F.; Charmant, J. P. H.; Orpen, A. G.; Williams, I. D. *Science* **1999,** *283* (5405), 1148.
212. Park, K. S.; Ni, Z.; Côté, A. P.; Choi, J. Y.; Huang, R.; Uribe-Romo, F. J.; Chae, H. K.; O'Keeffe, M.; Yaghi, O. M. *Proceedings of the National Academy of Sciences* **2006,** *103* (27), 10186.
213. Liu, X.; Kirlikovali, K. O.; Chen, Z.; Ma, K.; Idrees, K. B.; Cao, R.; Zhang, X.; Islamoglu, T.; Liu, Y.; Farha, O. K. *Chem. Mater.* **2021,** *33* (4), 1444-1454.
214. Zhang, B.; Zhang, J.; Liu, C.; Sang, X.; Peng, L.; Ma, X.; Wu, T.; Han, B.; Yang, G. *RSC Adv.* **2015,** *5* (47), 37691-37696.
215. Muller, K.; Singh Malhi, J.; Wohlgemuth, J.; Fischer, R. A.; Woll, C.; Gliemann, H.; Heinke, L. *Dalton Trans* **2018,** *47* (46), 16474-16479.
216. Kida, K.; Okita, M.; Fujita, K.; Tanaka, S.; Miyake, Y. *CrystEngComm* **2013,** *15* (9).
217. Jian, M.; Liu, B.; Liu, R.; Qu, J.; Wang, H.; Zhang, X. *RSC Adv.* **2015,** *5* (60), 48433-48441.
218. Fidelli, A. M.; Karadeniz, B.; Howarth, A. J.; Huskić, I.; Germann, L. S.; Halasz, I.; Etter, M.; Moon, S.-Y.; Dinnebier, R. E.; Stilinović, V.; Farha, O. K.; Friščić, T.; Užarević, K. *Chem. Commun.* **2018,** *54* (51), 6999-7002.

219. Islamoglu, T.; Otake, K.-i.; Li, P.; Buru, C. T.; Peters, A. W.; Akpinar, I.; Garibay, S. J.; Farha, O. K. *CrystEngComm* **2018,** *20* (39), 5913-5918.
220. Methanol, Ethanol and Ethyl Acetate are listed as "preferred" solvents by Pfizer, whereas Toluene is listed as "usable" by Pfizer and "Substitution Advisable" by Sanofi. (Ref 196)
221. Barin, G.; Krungleviciute, V.; Gutov, O.; Hupp, J. T.; Yildirim, T.; Farha, O. K. *Inorg. Chem.* **2014,** *53* (13), 6914-6919.
222. Meeting the Eye Health and Vision Care Needs of Canadians: A Workforce Analysis, Canadian Association of Optometrists, https://opto.ca/sites/default/files/resources/documents/workforce_analysis_report_april_2018_en.pdf, (accessed September 16, 2021).
223. Cataract, American Optometric Association, https://www.aoa.org/healthy-eyes/eye-and-vision-conditions/cataract?sso=y, (accessed September 16, 2021).
224. Common Eye Disorders and Diseases, Centers for Disease Control and Prevention, https://www.cdc.gov/visionhealth/basics/ced/index.html, (accessed September 16, 2021).
225. Gupta, V. B.; Rajagopala, M.; Ravishankar, B. *Indian J. Ophthalmol.* **2014,** *62* (2), 103-110.
226. Navarro, R. *J. Optom.* **2009,** *2* (1), 3-18.
227. Ruan, X.; Liu, Z.; Luo, L.; Liu, Y. *BMJ Open Ophthalmol.* **2020,** *5* (1), e000459.
228. Your Eyes, KidsHealth, https://kidshealth.org/en/kids/eyes.html. (accessed November 25, 2021).
229. Cataract, AboutKidsHealth, https://www.aboutkidshealth.ca/article?contentid=837&language=english. (accessed November 25, 2021).
230. *Community Eye Health J.* **2000,** *13* (34), 17-19.
231. Matossian, C. *US Ophthalmic Rev.* **2020,** *13* (1), 18-22.
232. Ghate, D.; Edelhauser, H. F. *Expert Opin. Drug Deliv.* **2006,** *3* (2), 275-287.
233. Yavuz, B.; Bozdağ Pehlivan, S.; Ünlü, N. *Sci. World J.* **2013,** *2013*, 732340.
234. Lang, J. C. *Adv. Drug Deliv. Rev.* **1995,** *16* (1), 39-43.
235. Maurice, D. M. *Surv. Ophthalmol.* **2002,** *47 Suppl 1*, S41-52.
236. Joshi, A.; Maurice, D.; Paugh, J. R. *Invest. Ophthalmol. Vis. Sci.* **1996,** *37* (6), 1008-1016.

237. Kessler, C.; Bleckmann, H.; Kleintges, G. *Graefes Arch. Clin. Exp. Ophthalmol.* **1991,** *229* (5), 487-91.
238. Loftsson, T.; Jansook, P.; Stefánsson, E. *Acta Ophthalmol.* **2012,** *90* (7), 603-608.
239. An, J. A.; Kasner, O.; Samek, D. A.; Lévesque, V. *J. Cataract Refract. Surg.* **2014,** *40* (11), 1857-1861.
240. Vandenbroeck, S.; De Geest, S.; Dobbels, F.; Fieuws, S.; Stalmans, I.; Zeyen, T. *J. Glaucoma* **2011,** *20* (7).
241. Li, J.; Li, Z.; Liang, Z.; Han, L.; Feng, H.; Siyu, H.; Zhang, J. *Drug Deliv.* **2018,** *25*, 938-949.
242. Porter, C. J. H.; Trevaskis, N. L.; Charman, W. N. *Nat. Rev. Drug Discov.* **2007,** *6* (3), 231-248.
243. Li, J.; Mooney, D. J. *Nat. Rev. Mater.* **2016,** *1* (12), 16071.
244. Wadhwa, S.; Garg, V.; Gulati, M.; Kapoor, B.; Singh, S. K.; Mittal, N. *Methods Mol. Biol.* **2019,** *2000*, 1-17.
245. Zhao, X.; Li, W.; Luo, Q.; Zhang, X. *Eur. J. Drug Metab. Pharmacokinet.* **2014,** *39* (1), 61-7.
246. Liechty, W. B.; Kryscio, D. R.; Slaughter, B. V.; Peppas, N. A. *Annu. Rev. Chem. Biomol. Eng.* **2010,** *1*, 149-173.
247. Sung, Y. K.; Kim, S. W. *Biomater. Res.* **2020,** *24* (1), 12.
248. Horcajada, P.; Serre, C.; Vallet-Regí, M.; Sebban, M.; Taulelle, F.; Férey, G. *Angew. Chem. Int. Ed.* **2006,** *45* (36), 5974-5978.
249. Abuçafy, M. P.; Caetano, B. L.; Chiari-Andréo, B. G.; Fonseca-Santos, B.; do Santos, A. M.; Chorilli, M.; Chiavacci, L. A. *Eur. J. Pharm. Biopharm.* **2018,** *127*, 112-119.
250. Kim, S. N.; Park, C. G.; Huh, B. K.; Lee, S. H.; Min, C. H.; Lee, Y. Y.; Kim, Y. K.; Park, K. H.; Choy, Y. B. *Acta Biomater.* **2018,** *79*, 344-353.
251. Gandara-Loe, J.; Souza, B. E.; Missyul, A.; Giraldo, G.; Tan, J. C.; Silvestre-Albero, J. *ACS Appl. Mater. Interfaces* **2020,** *12* (27), 30189-30197.
252. Abánades Lázaro, I.; Forgan, R. S. *Coord. Chem. Rev.* **2019,** *380*, 230-259.
253. The What and Why of Dry Eye, Dresden Vision, https://dresden.vision/ca/eye-health/dry-eye#/. (accessed November 25, 2021).

254. Blazaki, S.; Tsika, C.; Tzatzarakis, M.; Naoumidi, E.; Tsatsakis, A.; Tsatsanis, C.; Tsilimbaris, M. K. *Graefes Arch. Clin. Exp. Ophthalmol.* **2017,** *255* (12), 2375-2380.

255. Kim, S. J.; Schoenberger, S. D.; Thorne, J. E.; Ehlers, J. P.; Yeh, S.; Bakri, S. J. *Ophthalmology* **2015,** *122* (11), 2159-2168.

256. Flurbiprofen Sodium Solution/Drops, National Institutes of Health, U.S. National Library of Medicine. https://dailymed.nlm.nih.gov/dailymed/drugInfo.cfm?setid=11db354f-caf9-4567-811e-6c9beb1330c7 (accessed November 25, 2021).

257. Abdel-Aziz, A. A. M.; Al-Badr, A. A.; Hafez, G. A., Chapter 4 - Flurbiprofen. In *Profiles of Drug Substances, Excipients and Related Methodology*, Brittain, H. G., Ed. Academic Press: 2012; Vol. 37, pp 113-181.

258. Morales, A. M.; Kivilcim, M.; Peyman, G. A.; Main, M.; Manzano, R. P. *Ophthalmic Surg. Lasers Imaging* **2009,** *40* (1), 38-42.

259. Vial, L.; Ludlow, R. F.; Leclaire, J.; Pérez-Fernández, R.; Otto, S. *J. Am. Chem. Soc.* **2006,** *128* (31), 10253-10257.

260. Gold Biotechnology, Ellman's Test Protocol. https://www.goldbio.com/documents/2359/Ellmans+Test+Protocol.pdf (accessed June 29, 2021).

261. Li, P.; Modica, J. A.; Howarth, A. J.; Vargas, L. E.; Moghadam, P. Z.; Snurr, R. Q.; Mrksich, M.; Hupp, J. T.; Farha, O. K. *Chem* **2016,** *1* (1), 154-169.

Appendix

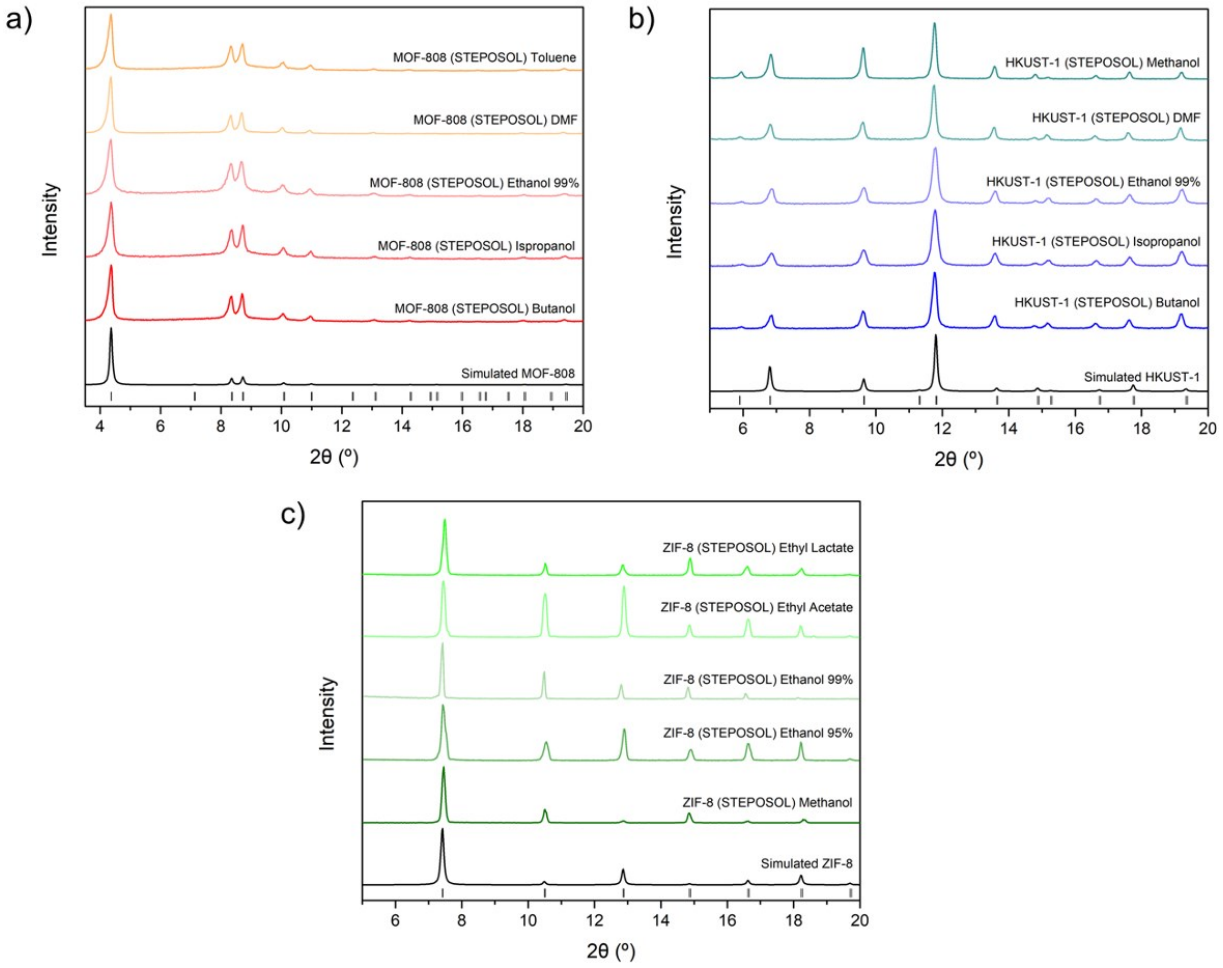

Figure A.1. PXRD patterns of (a) MOF-808 synthesized by STEPOSOL® MET-10U and washed with different organic solvents including butanol, isopropanol, ethanol 99%, DMF and toluene, (b) HKUST-1 synthesized by STEPOSOL® MET-10U and washed with different organic solvents including butanol, isopropanol, ethanol 99%, DMF and methanol, and (c) ZIF-8 synthesized by STEPOSOL® MET-10U and washed with different organic solvents including methanol, ethanol 95%, ethanol 99%, ethyl acetate and ethyl lactate.

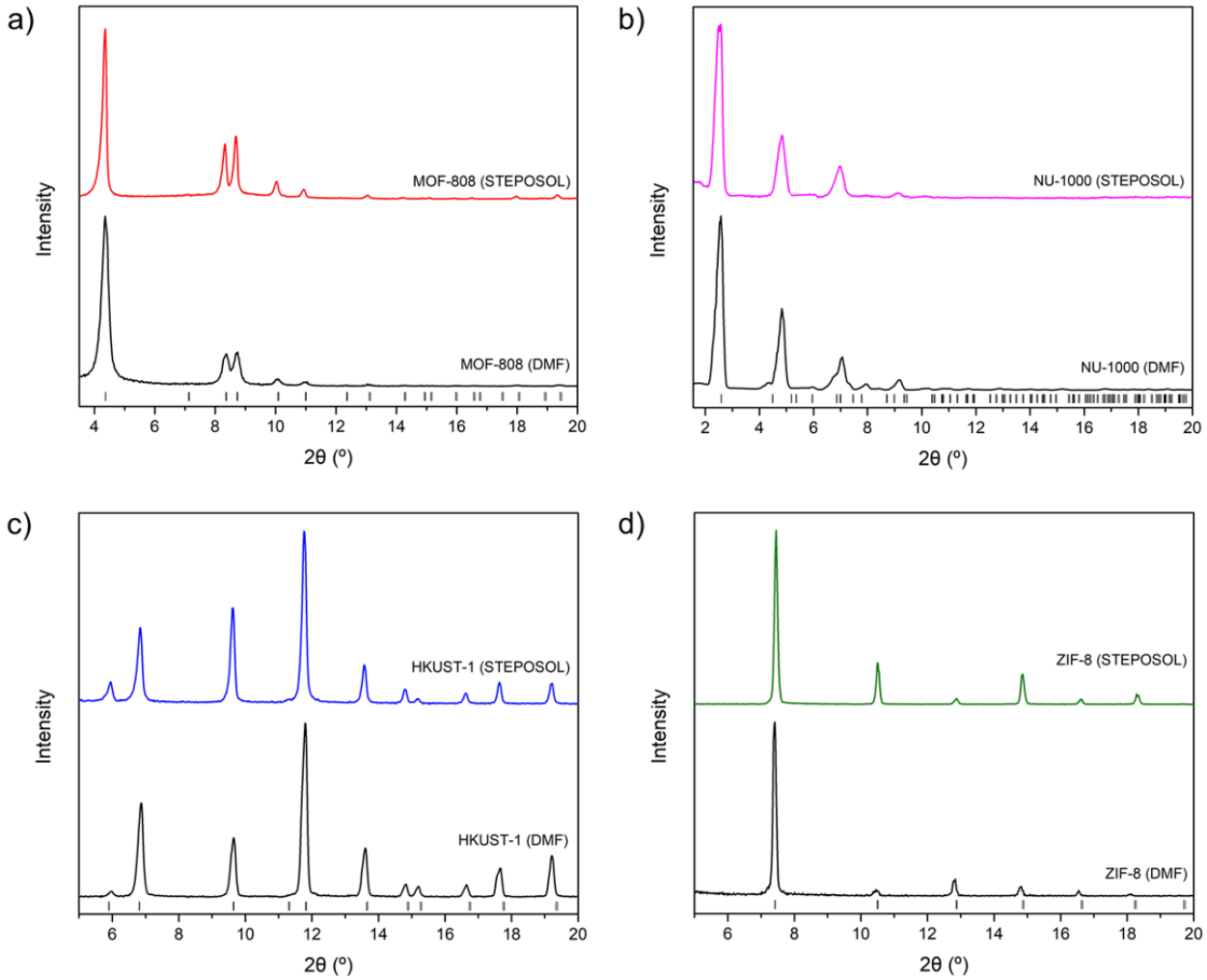

Figure A.2. PXRD patterns of (a) MOF-808 synthesized by STEPOSOL® MET-10U and by DMF, (b) NU-1000 synthesized by STEPOSOL® MET-10U and by DMF, (c) HKUST-1 synthesized by STEPOSOL® MET-10U and by DMF, and (d) ZIF-8 synthesized by STEPOSOL® MET-10U and by DMF.

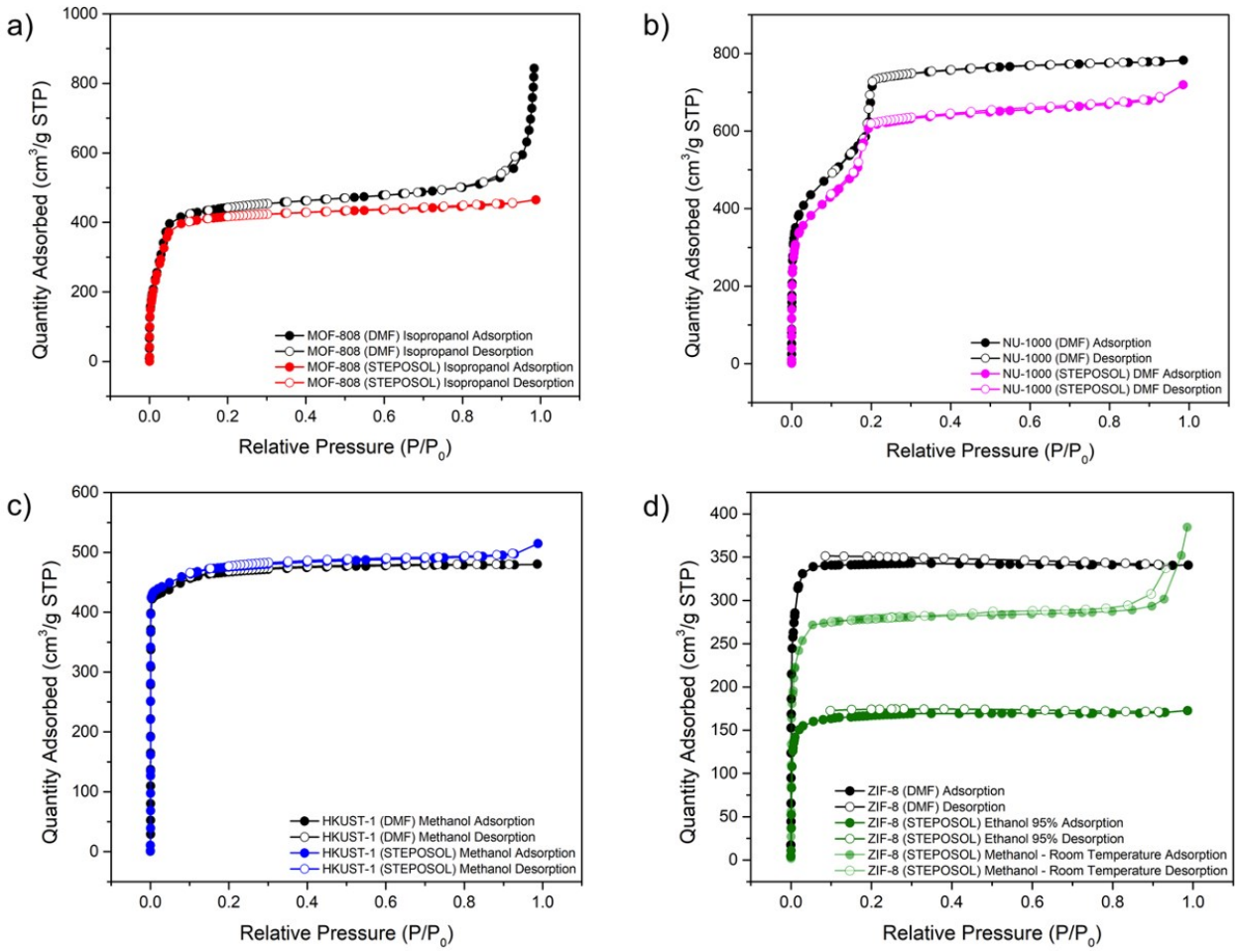

Figure A.3. N_2 adsorption-desorption isotherms and BET surface area values of (a) MOF-808 (Type I(b)) synthesized by STEPOSOL® MET-10U and washed with STEPOSOL® MET-10U and isopropanol (S_{BET} = 1720 m^2 g^{-1}) and by DMF and washed with DMF and isopropanol (S_{BET} = 1835 m^2 g^{-1}), (b) NU-1000 (Type IV(b)) synthesized by STEPOSOL® MET-10U and washed with DMF (S_{BET} = 1635 m^2 g^{-1}) and by DMF and washed with DMF (S_{BET} = 1865 m^2 g^{-1}), (c) HKUST-1 (Type I(a)) synthesized by STEPOSOL® MET-10U and washed with methanol (S_{BET} = 1860 m^2 g^{-1}) and by DMF and washed with methanol (S_{BET} = 1815 m^2 g^{-1}), and (d) ZIF-8 (Type I(a)) synthesized by STEPOSOL® MET-10U (solvothermal) and washed with ethanol 95% (S_{BET} = 670 m^2 g^{-1}), by DMF and washed with DMF (S_{BET} = 1435 m^2 g^{-1}) and by STEPOSOL® MET-10U (room temperature) and washed with methanol (S_{BET} = 1155 m^2 g^{-1}).

a)

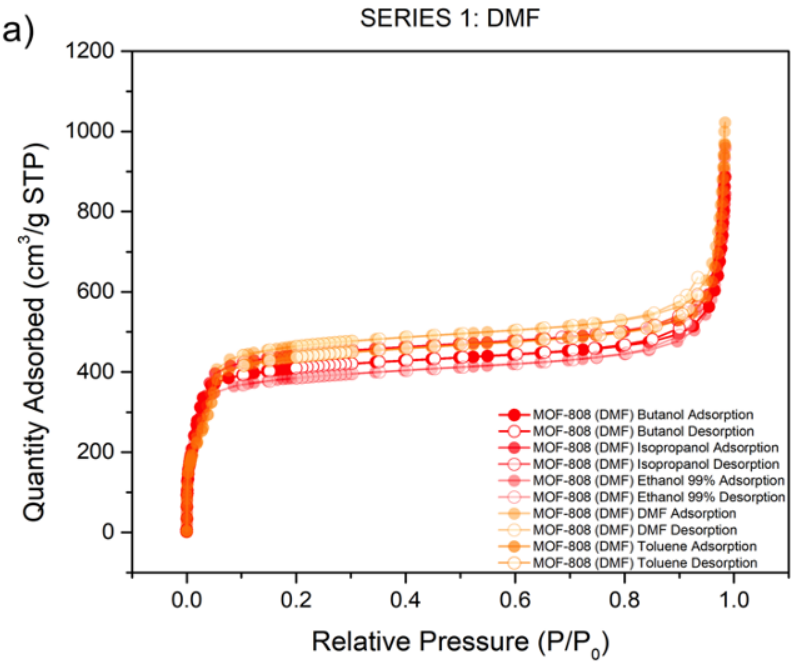

MOF-808 (DMF)	BET Surface Area ($m^2\ g^{-1}$)
Butanol	1790
Isopropanol	1835
Ethanol 99%	1660
DMF	1745
Toluene	1650

Samples were washed with DMF, then the solvent listed in the table above, and then acetone

b)

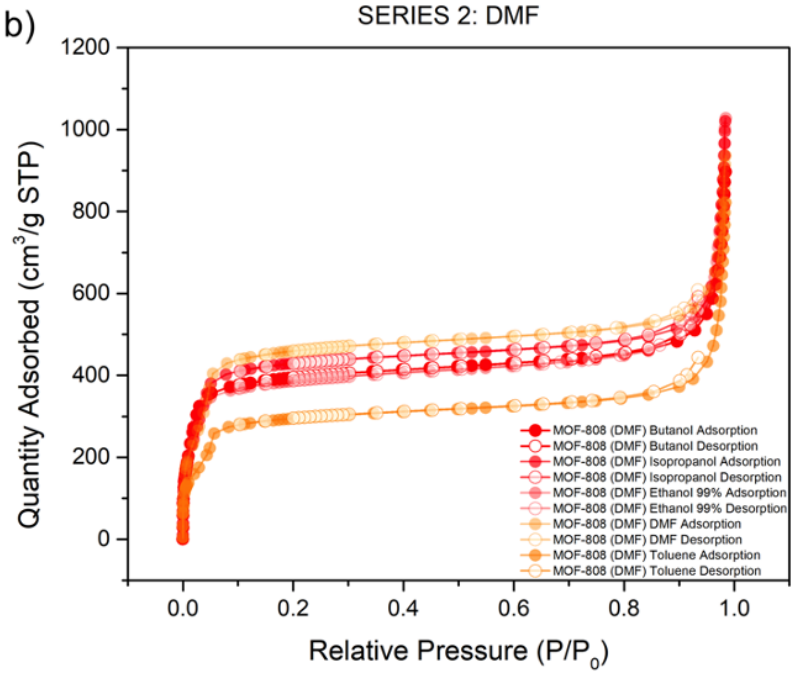

MOF-808 (DMF)	BET Surface Area ($m^2\ g^{-1}$)
Butanol	1710
Isopropanol	1740
Ethanol 99%	1645
DMF	1770
Toluene	1070

Samples were not washed with DMF, but first with the solvent listed in the table above, and then acetone

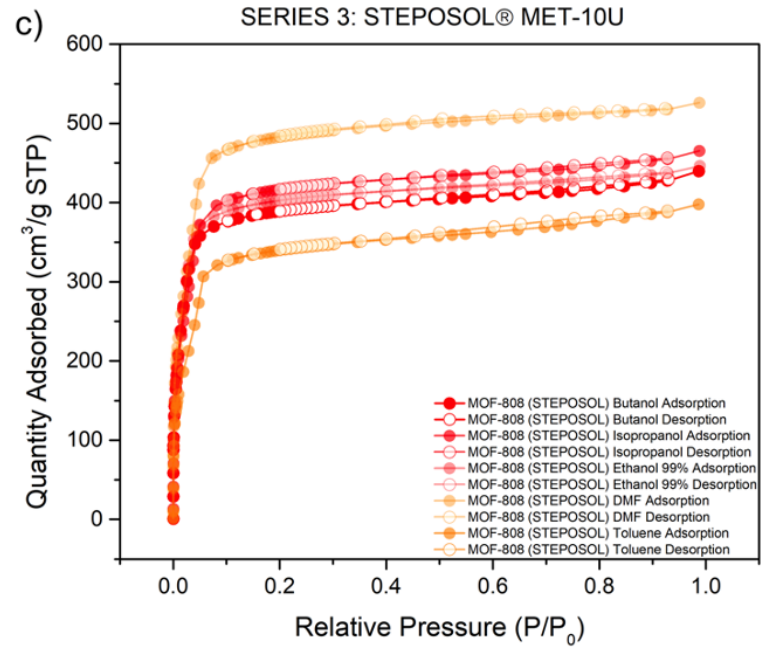

MOF-808 (STEPOSOL)	BET Surface Area (m^2 g^{-1})
Butanol	1700
Isopropanol	1720
Ethanol 99%	1760
DMF	1940
Toluene	1330

Samples were washed with STEPOSOL® MET-10U, then the solvent listed in the table above, and then acetone

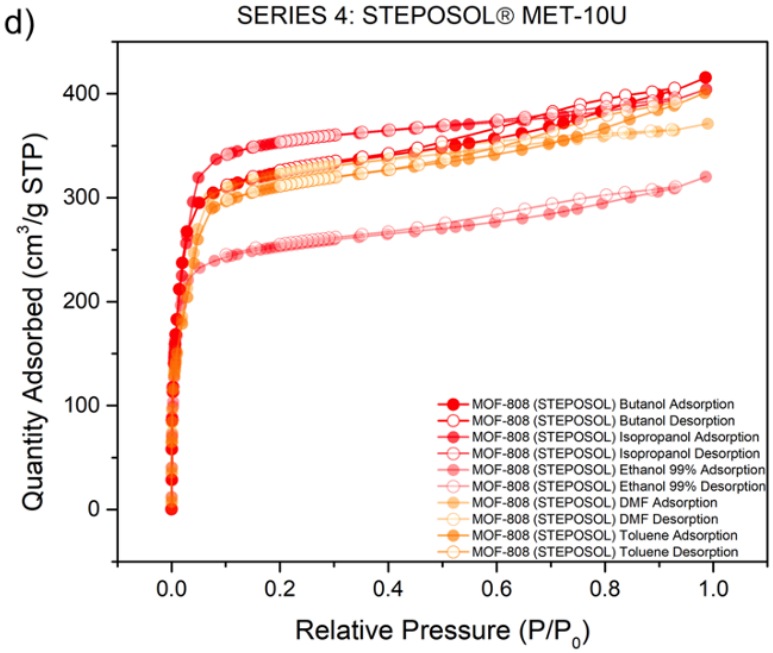

MOF-808 (STEPOSOL)	BET Surface Area (m^2 g^{-1})
Butanol	1370
Isopropanol	1455
Ethanol 99%	1045
DMF	1225
Toluene	1160

Samples were not washed with STEPOSOL® MET-10U, but first with the solvent listed in the table above, and then acetone

Figure A.4. N_2 adsorption-desorption isotherms and BET surface area values of MOF-808 (Type I(b)) (a) series 1 synthesized by DMF and washed with DMF and different organic solvents including butanol, isopropanol, ethanol 99%, DMF and toluene, (b) series 2 synthesized by DMF and washed directly with different organic solvents, (c) series 3 synthesized by STEPOSOL® MET-10U and washed with STEPOSOL® MET-10U and different organic solvents including butanol, isopropanol, ethanol 99%, DMF and toluene, and (d) series 4 synthesized by STEPOSOL® MET-10U and washed directly with different organic solvents.

a)

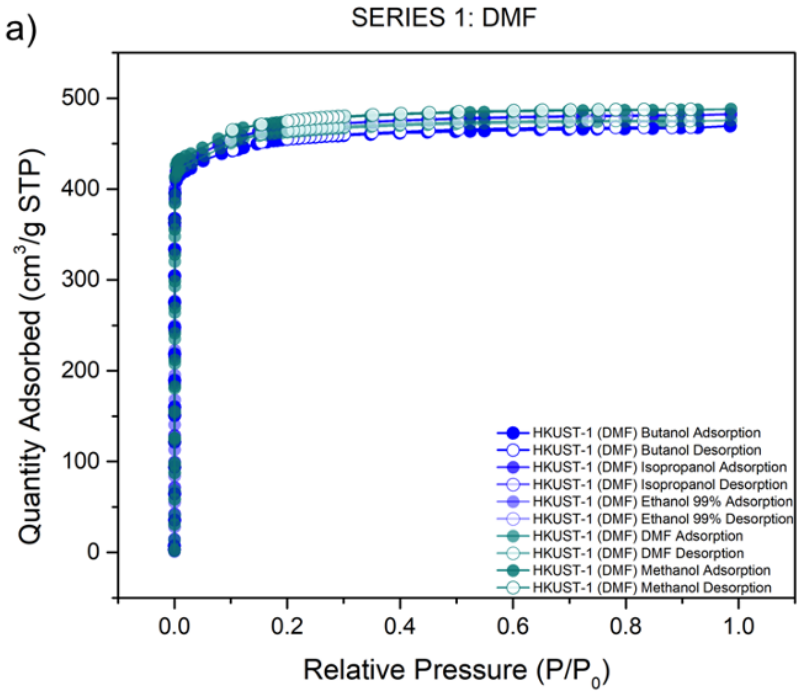

HKUST-1 (DMF)	BET Surface Area (m^2 g^{-1})
Butanol	1780
Isopropanol	1820
Ethanol 99%	1815
DMF	1795
Methanol	1840

Samples were washed with DMF, then the solvent listed in the table above, and then acetone

b)

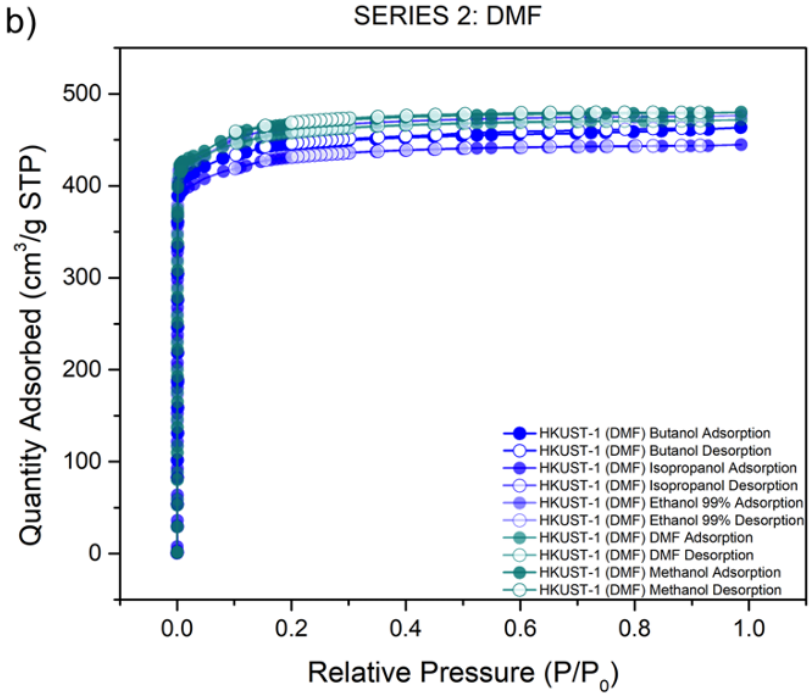

HKUST-1 (DMF)	BET Surface Area (m^2 g^{-1})
Butanol	1745
Isopropanol	1690
Ethanol 99%	1795
DMF	1790
Methanol	1815

Samples were not washed with DMF, but first with the solvent listed in the table above, and then acetone

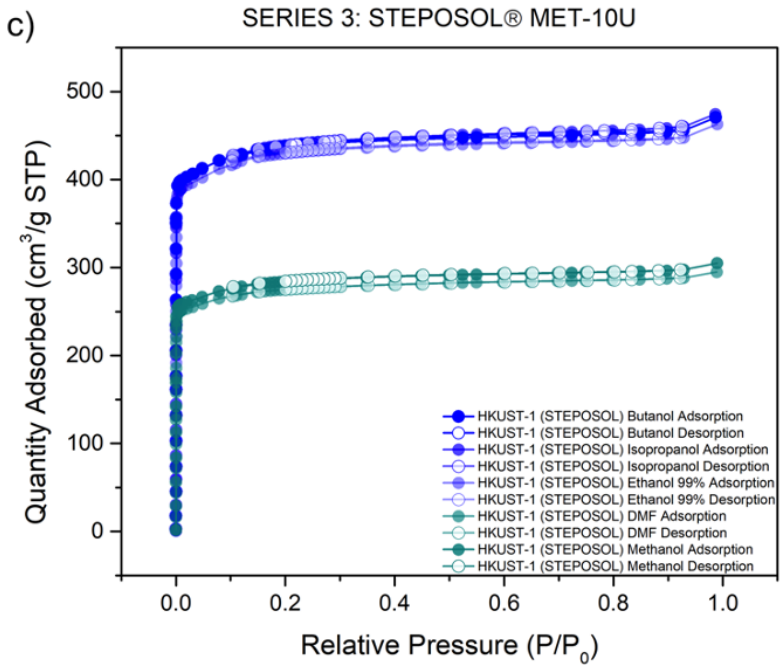

HKUST-1 (STEPOSOL)	BET Surface Area ($m^2 g^{-1}$)
Butanol	1710
Isopropanol	1705
Ethanol 99%	1670
DMF	1070
Methanol	1105

Samples were washed with STEPOSOL® MET-10U, then the solvent listed in the table above, and then acetone

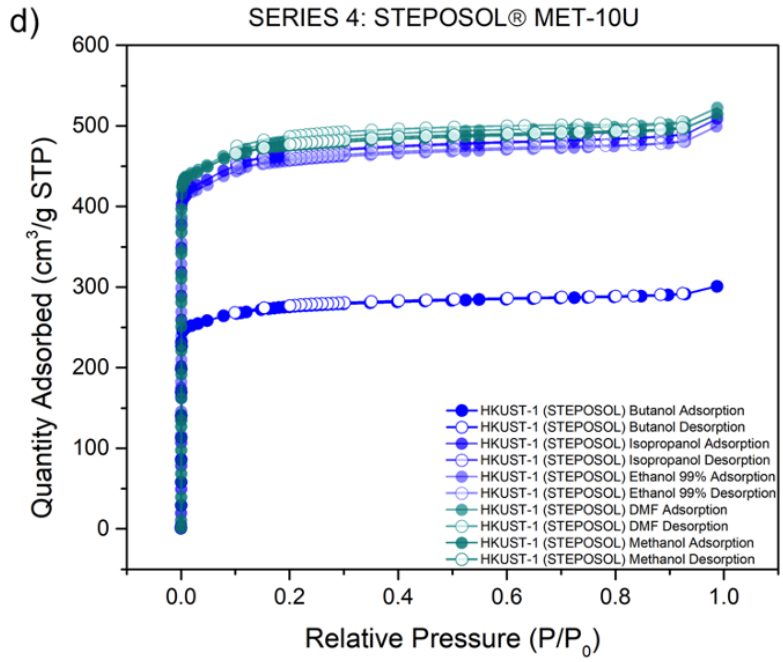

HKUST-1 (STEPOSOL)	BET Surface Area ($m^2 g^{-1}$)
Butanol	1070
Isopropanol	1795
Ethanol 99%	1765
DMF	1870
Methanol	1860

Samples were not washed with STEPOSOL® MET-10U, but first with the solvent listed in the table above, and then acetone

Figure A.5. N_2 adsorption-desorption isotherms and BET surface area values of HKUST-1 (Type I(a)) (a) series 1 synthesized by DMF and washed with DMF and different organic solvents including butanol, isopropanol, ethanol 99%, DMF and toluene, (b) series 2 synthesized by DMF and washed directly with different organic solvents, (c) series 3 synthesized by STEPOSOL® MET-10U and washed with STEPOSOL® MET-10U and different organic solvents including butanol, isopropanol, ethanol 99%, DMF and toluene, and (d) series 4 synthesized by STEPOSOL® MET-10U and washed directly with different organic solvents.

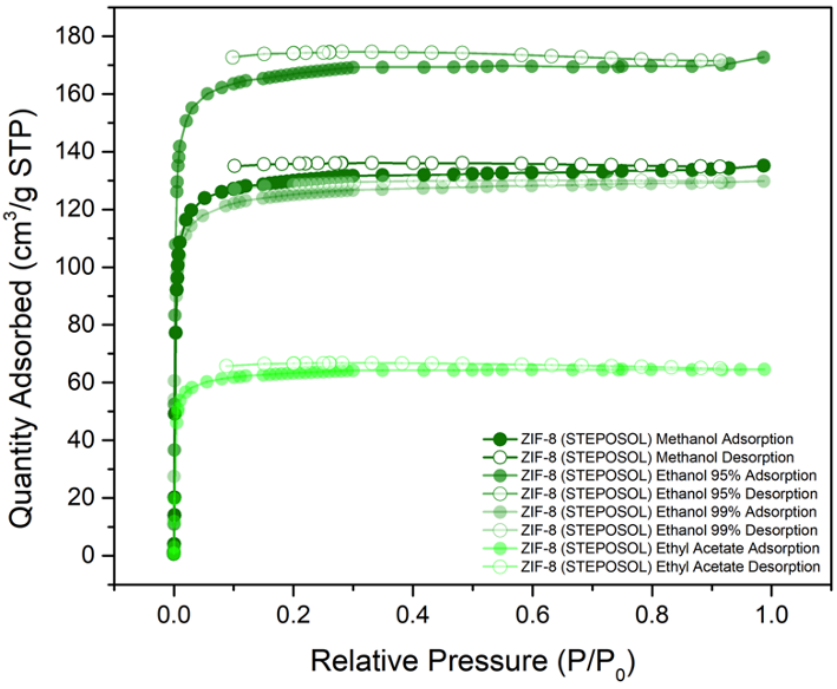

ZIF-8 (STEPOSOL)	BET Surface Area ($m^2\ g^{-1}$)
Methanol	590
Ethanol 95%	670
Ethanol 99%	485
Ethyl Acetate	255

Figure A.6. N_2 adsorption-desorption isotherms and BET surface area values of ZIF-8 (Type I(a)) synthesized by STEPOSOL® MET-10U and washed with different organic solvents including methanol, ethanol 95%, ethanol 99%, and ethyl acetate.

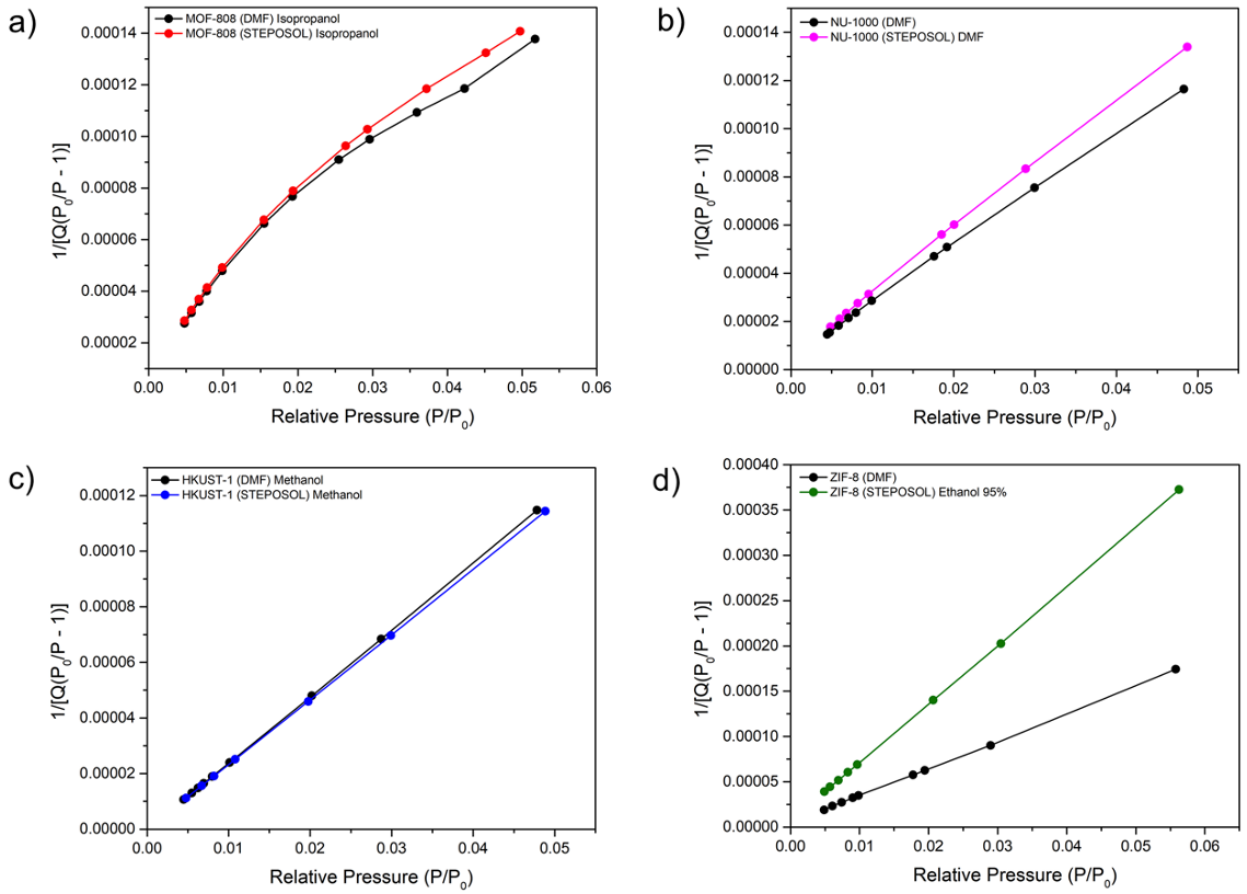

Figure A.7. BET linear surface area plot of (a) MOF-808 synthesized by STEPOSOL® MET-10U and washed with STEPOSOL® MET-10U and isopropanol (BET plot taken from P/P_0 = 0.0048−0.050) and by DMF and washed with DMF and isopropanol (BET plot taken from P/P_0 = 0.0048−0.052), (b) NU-1000 synthesized by STEPOSOL® MET-10U and washed with DMF (BET plot taken from P/P_0 = 0.0048−0.049) and by DMF and washed with DMF (BET plot taken from P/P_0 = 0.0045−0.048), (c) HKUST-1 synthesized by STEPOSOL® MET-10U and washed with methanol (BET plot taken from P/P_0 = 0.0048−0.049) and by DMF and washed with methanol (BET plot taken from P/P_0 = 0.0045−0.048), and (d) ZIF-8 synthesized by STEPOSOL® MET-10U and washed with ethanol 95% (BET plot taken from P/P_0 = 0.0049−0.056) and by DMF and washed with DMF (BET plot taken from P/P_0 = 0.0049−0.055).

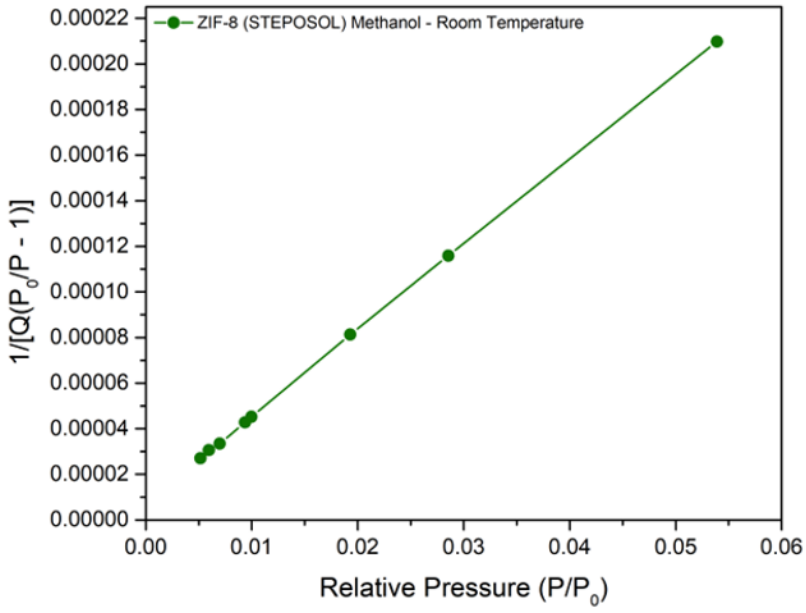

Figure A.8. BET linear surface area plot of ZIF-8 synthesized by STEPOSOL® MET-10U at room temperature and washed with methanol (BET plot taken from $P/P_0 = 0.0060-0.054$).

BET Consistency Criteria:

(i) the BET constant "C" must be positive

(ii) $n(1 - P/P_0)$ should increase monotonically with P/P_0

(iii) the monolayer capacity (n_m) should correspond to a pressure within the limits of the data

(iv) the calculated value for monolayer formation ($1/(\sqrt{C} + 1)$) should be approximately equal to P/P_0 at the monolayer capacity

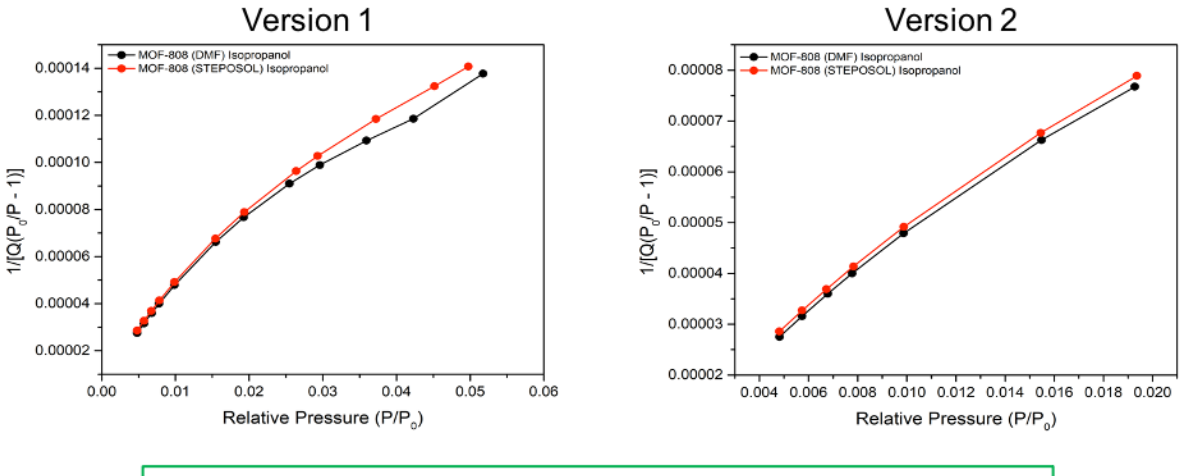

Rouquerol plot increases monotonically with P/P_0 for both versions

Version 1	MOF-808 (DMF)	MOF-808 (STEPOSOL)
BET Area	1835.0583 ± 89.9156 $m^2 g^{-1}$	1718.9862 ± 73.0252 $m^2 g^{-1}$
Slope	0.002348 ± 0.000116 g cm^{-3} STP	0.002509 ± 0.000108 g cm^{-3} STP
Y-Intercept	0.000024 ± 0.000003 g cm^{-3} STP	0.000023 ± 0.000003 g cm^{-3} STP
C	100.498698	108.614724
Q_m	421.6026 $cm^3 g^{-1}$ STP	394.9352 $cm^3 g^{-1}$ STP
R^2	0.9879816	0.9909391
$1/\sqrt{C} + 1$	0.091	0.058

Version 2	MOF-808 (DMF)	MOF-808 (STEPOSOL)
BET Area	1277.9699 ± 38.9871 $m^2 g^{-1}$	1258.2336 ± 36.0951 $m^2 g^{-1}$
Slope	0.003393 ± 0.000104 g cm^{-3} STP	0.003446 ± 0.000099 g cm^{-3} STP
Y-Intercept	0.000013 ± 0.000001 g cm^{-3} STP	0.000014 ± 0.000001 g cm^{-3} STP
C	266.740930	255.337272
Q_m	293.6122 $cm^3 g^{-1}$ STP	289.0778 $cm^3 g^{-1}$ STP
R^2	0.9976643	0.9979331
$1/\sqrt{C} + 1$	0.088	0.059

Figure A.9. BET analysis based on the BET consistency criteria for MOF-808 (DMF) and MOF-808 (STEPOSOL), showing the differences in selecting a larger range (less linear) and narrower range (more linear) of relative pressure points. Green box = criteria is met, red box = criteria is not met.

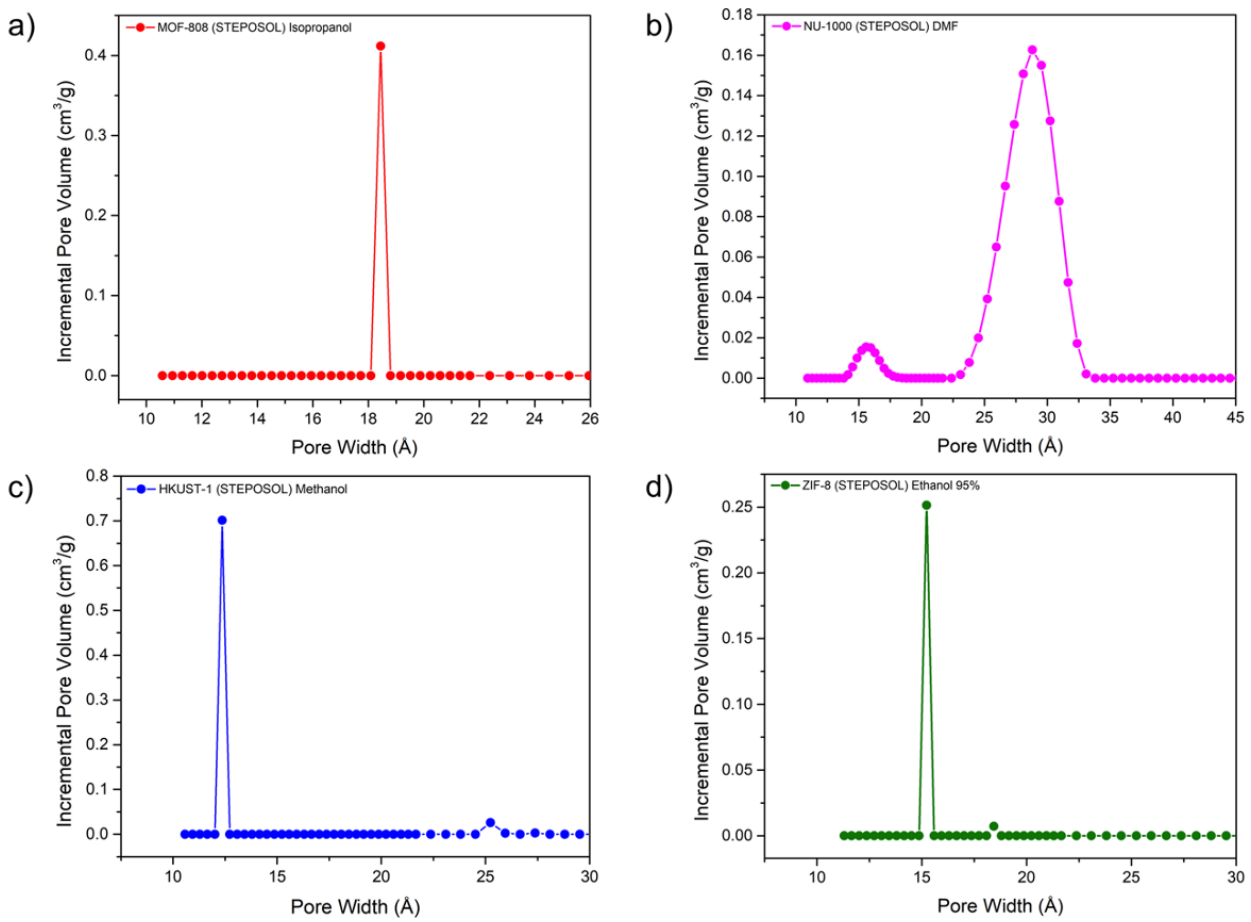

Figure A.10. Pore size distribution analysis performed by non-local density functional theory (NLDFT) of (a) MOF-808 synthesized by STEPOSOL® MET-10U and washed with STEPOSOL® MET-10U and isopropanol (pore diameter = 18.4 Å), (b) NU-1000 synthesized by STEPOSOL® MET-10U and washed with DMF (pore diameter = 29.5 Å), (c) HKUST-1 synthesized by STEPOSOL® MET-10U and washed with methanol (pore diameter = 12.4 Å), and (d) ZIF-8 synthesized by STEPOSOL® MET-10U and washed with ethanol 95% (pore diameter = 15.2 Å).

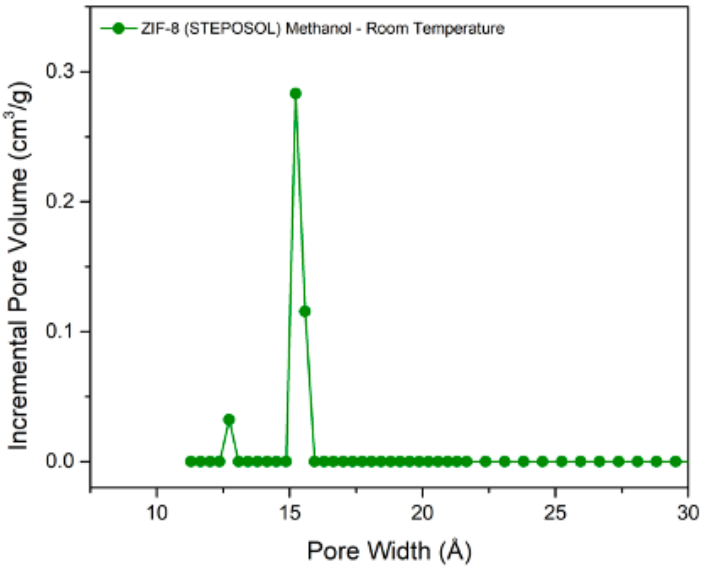

Figure A.11. Pore size distribution analysis performed by non-local density functional theory (NLDFT) of ZIF-8 synthesized by STEPOSOL® MET-10U at room temperature and washed with methanol (pore diameter = 15.2 Å).

Table A.1. Costs of the solvents used for the reactions and washings of various MOFs.

Solvent	DMF	STEPOSOL® MET-10U	Acetone	Ethanol	Isopropanol	Methanol
Cost (list price) ($CAD L^{-1})	107	36	55	25	37	49

Table A.2. Cost analysis of MOF-808 samples synthesized using DMF and STEPOSOL® MET-10U.

MOF-808	**DMF Sample**			**STEPOSOL® MET-10U Sample**		
	Solvent	**Quantity (mL)**	**Cost ($CAD)**	**Solvent**	**Quantity (mL)**	**Cost ($CAD)**
Reaction	DMF	10	1.07	STEPOSOL	10	0.36
Activation	DMF	60	6.42	STEPOSOL	60	2.16
Activation	Isopropanol	60	2.22	Isopropanol	60	2.22
Activation	Acetone	30	1.65	Acetone	30	1.65
Total Cost	N/A	N/A	11.36	N/A	N/A	6.39

Table A.3. Cost analysis of NU-1000 samples synthesized using DMF and STEPOSOL® MET-10U.

NU-1000	DMF Sample			STEPOSOL® MET-10U Sample		
	Solvent	**Quantity (mL)**	**Cost ($CAD)**	**Solvent**	**Quantity (mL)**	**Cost ($CAD)**
Reaction	DMF	8	0.86	STEPOSOL	8	0.29
Activation	DMF	30	3.21	DMF	30	3.21
Activation	Acetone	30	1.65	Acetone	30	1.65
Total Cost	N/A	N/A	5.72	N/A	N/A	5.15

Table A.4. Cost analysis of HKUST-1 samples synthesized using DMF and STEPOSOL® MET-10U.

HKUST-1	DMF Sample			STEPOSOL® MET-10U Sample		
	Solvent	**Quantity (mL)**	**Cost ($CAD)**	**Solvent**	**Quantity (mL)**	**Cost ($CAD)**
Reaction	DMF	2	0.21	STEPOSOL	2	0.07
Activation	Methanol	60	2.94	Methanol	60	2.94
Activation	Acetone	30	1.65	Acetone	30	1.65
Total Cost	N/A	N/A	4.80	N/A	N/A	4.66

Table A.5. Cost analysis of ZIF-8 samples synthesized using DMF and STEPOSOL® MET-10U.

ZIF-8	DMF Sample			STEPOSOL® MET-10U Sample		
	Solvent	**Quantity (mL)**	**Cost ($CAD)**	**Solvent**	**Quantity (mL)**	**Cost ($CAD)**
Reaction	DMF	15	1.61	STEPOSOL	15	0.54
Activation	Ethanol	60	1.50	Ethanol	60	1.50
Activation	Acetone	30	1.65	Acetone	30	1.65
Total Cost	N/A	N/A	4.76	N/A	N/A	3.69

ZIF-8	Room Temperature Sample		
	Solvent	**Quantity (mL)**	**Cost ($CAD)**
Reaction	STEPOSOL	17	0.61
Activation	Methanol	5	0.25
Total Cost	N/A	N/A	0.86

Single Crystal X-ray Diffraction (SCXRD) Analysis

Table A.6. Crystallographic data for two single crystals of ZIF-8 (STEPOSOL) and one single crystal of ZIF-8 (DMF).

	ZIF-8 (STEPOSOL)	**ZIF-8 (STEPOSOL)**	**ZIF-8 (DMF)**
Empirical formula	$C_8H_{10}N_4Zn$	$C_8H_{10}N_4Zn$	$C_8H_{10}N_4Zn$
Formula weight	227.57	227.57	227.57
Temperature/K	298(2)	298(2)	298(2)
Crystal system	Cubic	Cubic	Cubic
Space group	$I\bar{4}3m$	$I\bar{4}3m$	$I\bar{4}3m$
a/Å	17.0225(3)	17.0455(3)	17.0347(3)
b/Å	17.0225(3)	17.0455(3)	17.0347(3)
c/Å	17.0225(3)	17.0455(3)	17.0347(3)
α/°	90	90	90
β/°	90	90	90
γ/°	90	90	90
Volume/Å^3	4932.5(3)	4952.6(3)	4943.1(3)
Z	12	12	12
ρ_{calc}g/cm^3	0.919	0.916	0.917
μ/mm^{-1}	1.875	1.868	1.871
F(000)	1392.0	1392.0	1392.0
2*q* range for data collection/°	19.512 to 143.588	19.484 to 143.908	19.498 to 144.132
Reflections collected	13087	7564	9990
Independent reflections	922 [R_{int} = 0.0812, R_{sigma} = 0.0323]	921 [R_{int} = 0.0793, R_{sigma} = 0.0455]	908 [R_{int} = 0.0280, R_{sigma} = 0.0178]
Data/restraints/ parameters	922/0/34	921/0/35	908/0/34
Goodness-of-fit on F^2	1.047	1.068	1.119
Final R indexes [I>=2σ (I)]	R_1 = 0.0319, wR_2 = 0.0871	R_1 = 0.0419, wR_2 = 0.1162	R_1 = 0.0167, wR_2 = 0.0480
Final R indexes [all data]	R_1 = 0.0429, wR_2 = 0.0993	R_1 = 0.0475, wR_2 = 0.1237	R_1 = 0.0168, wR_2 = 0.0481
Largest diff. peak/hole / e Å^{-3}	0.19/-0.18	0.56/-0.27	0.10/-0.12

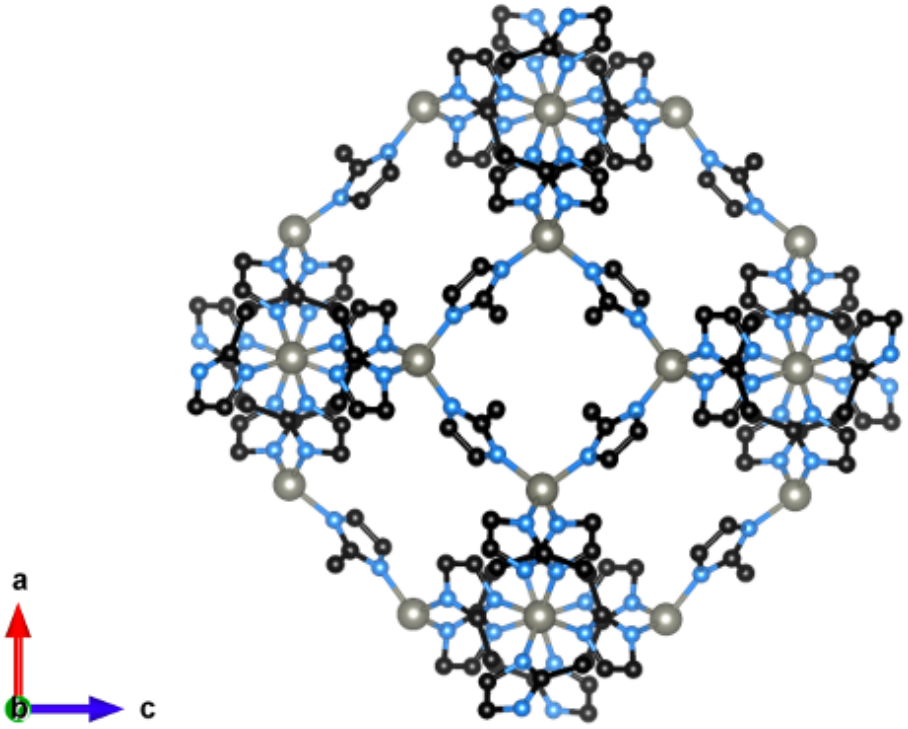

Figure A.12. Structure of ZIF-8 (STEPOSOL), showing one view of the MOF along the *b*-axis. Zn = grey, N = blue, C = black.

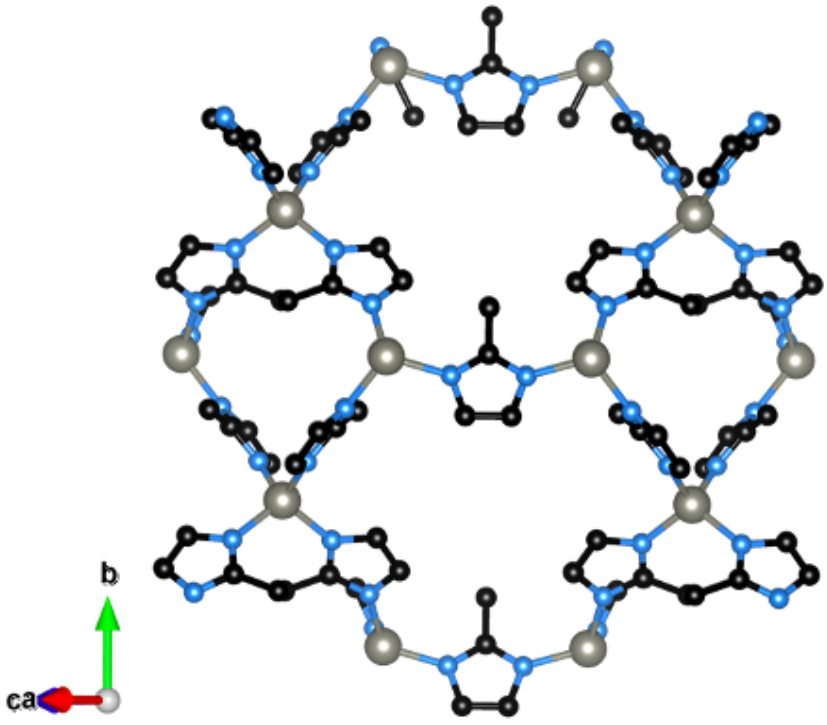

Figure A.13. Structure of ZIF-8 (STEPOSOL), showing another view of the MOF through the plane (101). Zn = grey, N = blue, C = black.

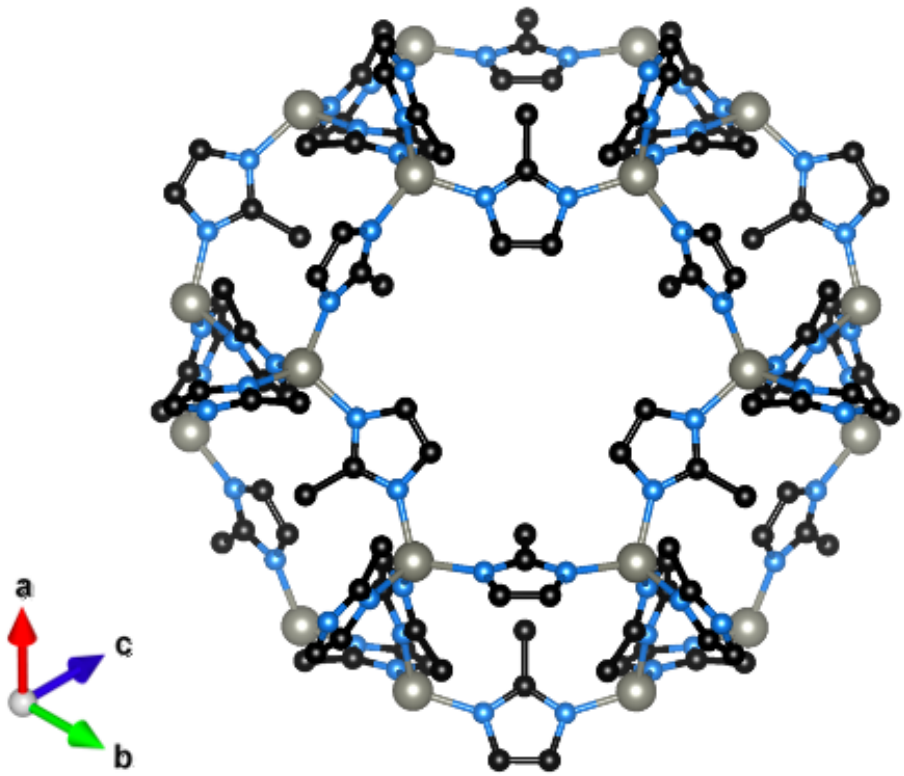

Figure A.14. Structure of ZIF-8 (DMF), showing an alternative view of the MOF. Zn = grey, N = blue, C = black.

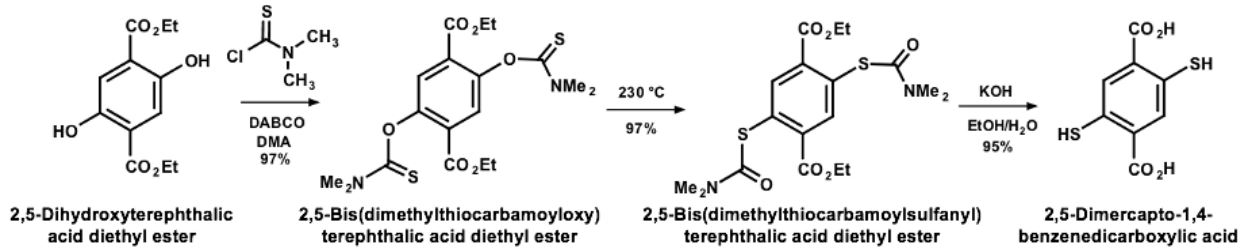

Figure A.15. Reaction scheme for the synthesis of 2,5-dimercapto-1,4-benzenedicarboxylic acid (H_2DMBD).

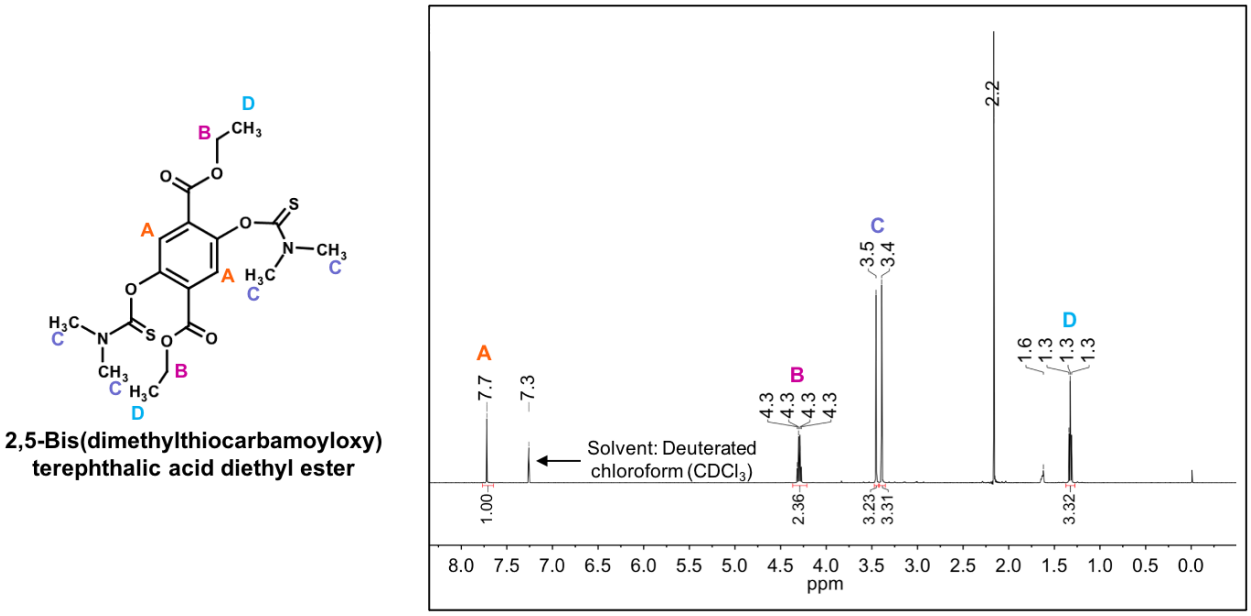

Figure A.16. ^{1}H-NMR spectrum of 2,5-bis(dimethylthiocarbamoyloxy)terephthalic acid diethyl ester.

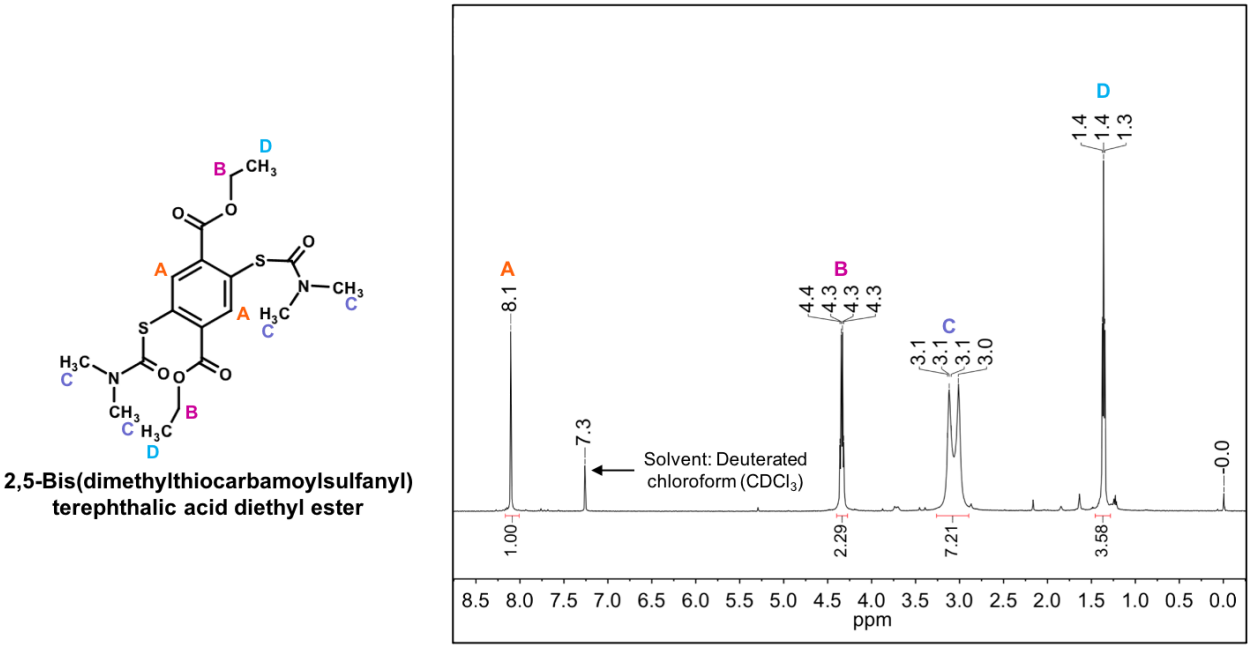

Figure A.17. ^{1}H-NMR spectrum of 2,5-bis(dimethylthiocarbamoylsulfanyl)terephthalic acid diethyl ester.

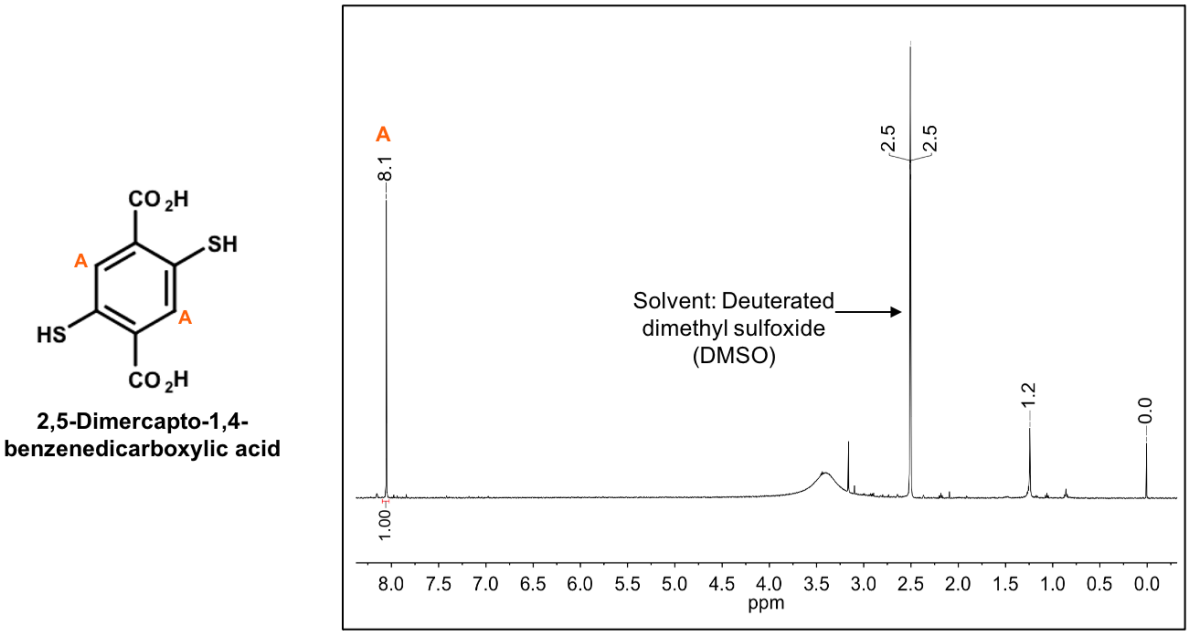

Figure A.18. ^{1}H-NMR spectrum of 2,5-dimercapto-1,4-benzenedicarboxylic acid (H_2DMBD).

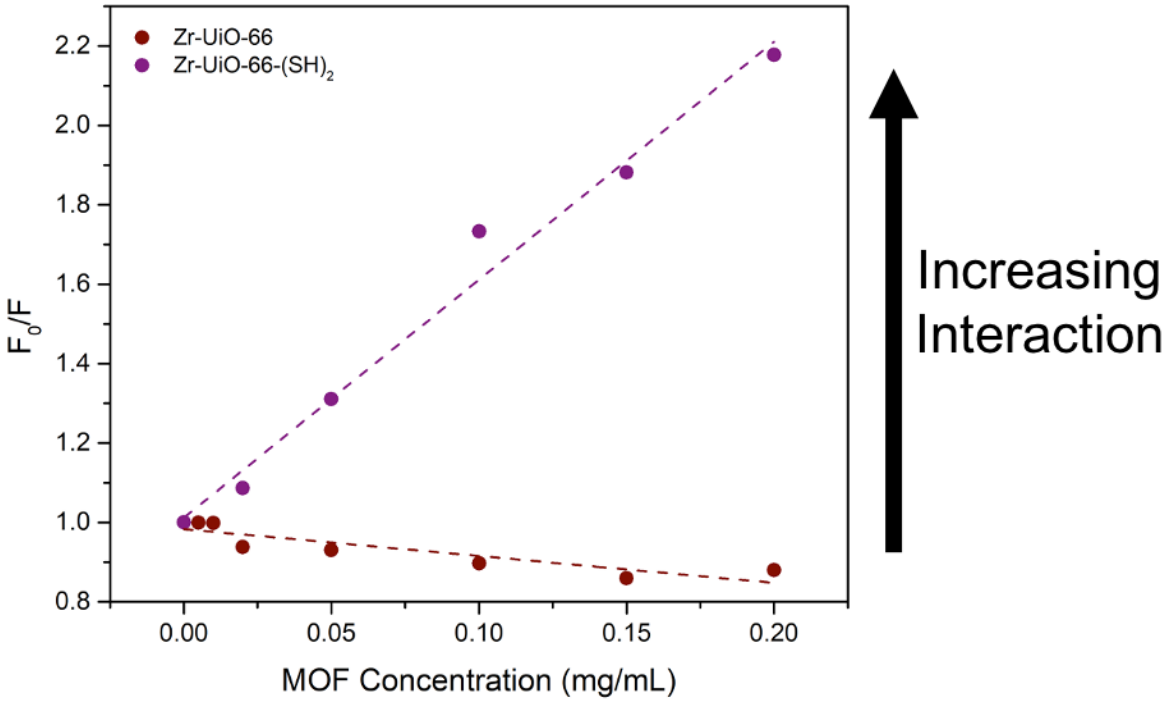

Figure A.19. Mucoadhesion of the thiolated and control Zr-UiO-66 assessed by fluorescence spectroscopy.

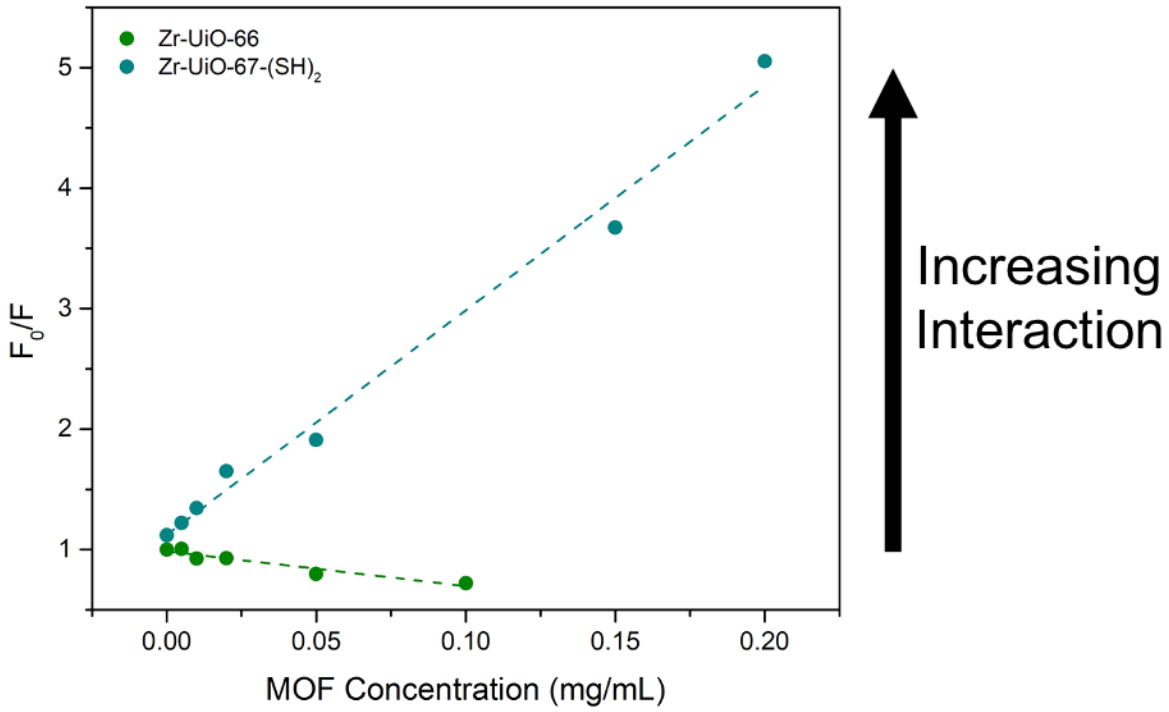

Figure A.20. Mucoadhesion of the thiolated and control Zr-UiO-67 assessed by fluorescence spectroscopy.

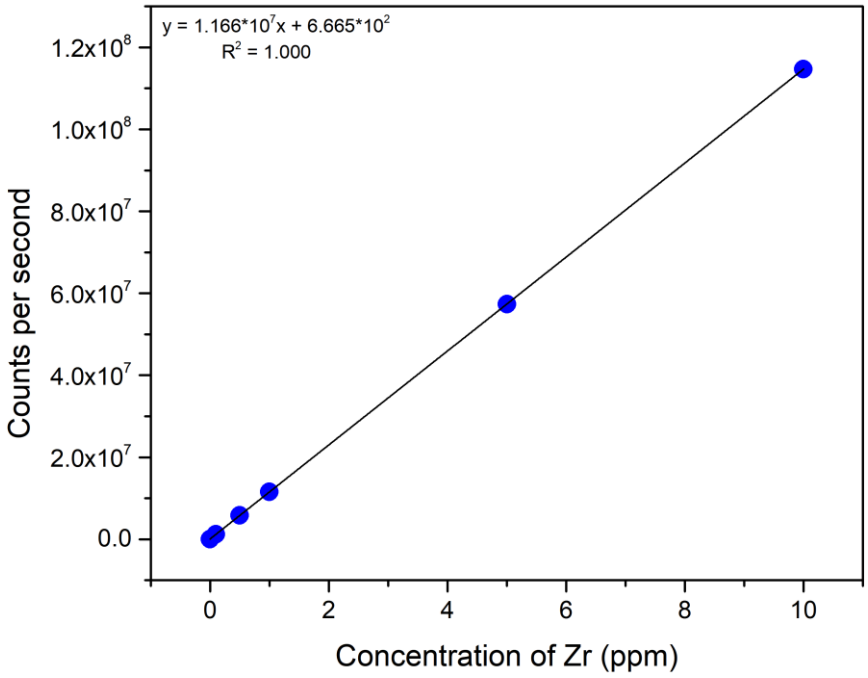

Figure A.21. ICP-MS calibration curve for the concentration of zirconium.

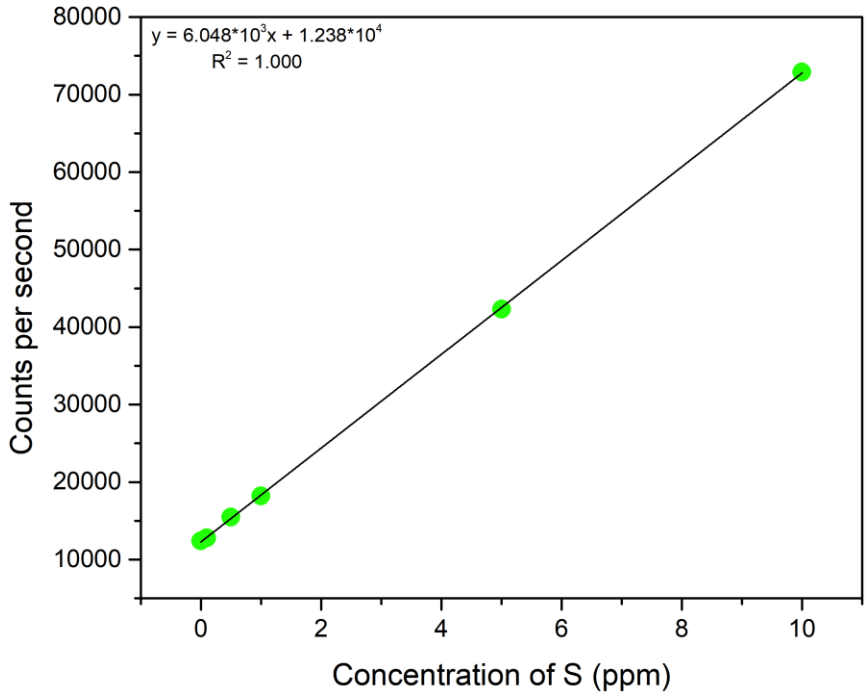

Figure A.22. ICP-MS calibration curve for the concentration of sulfur.

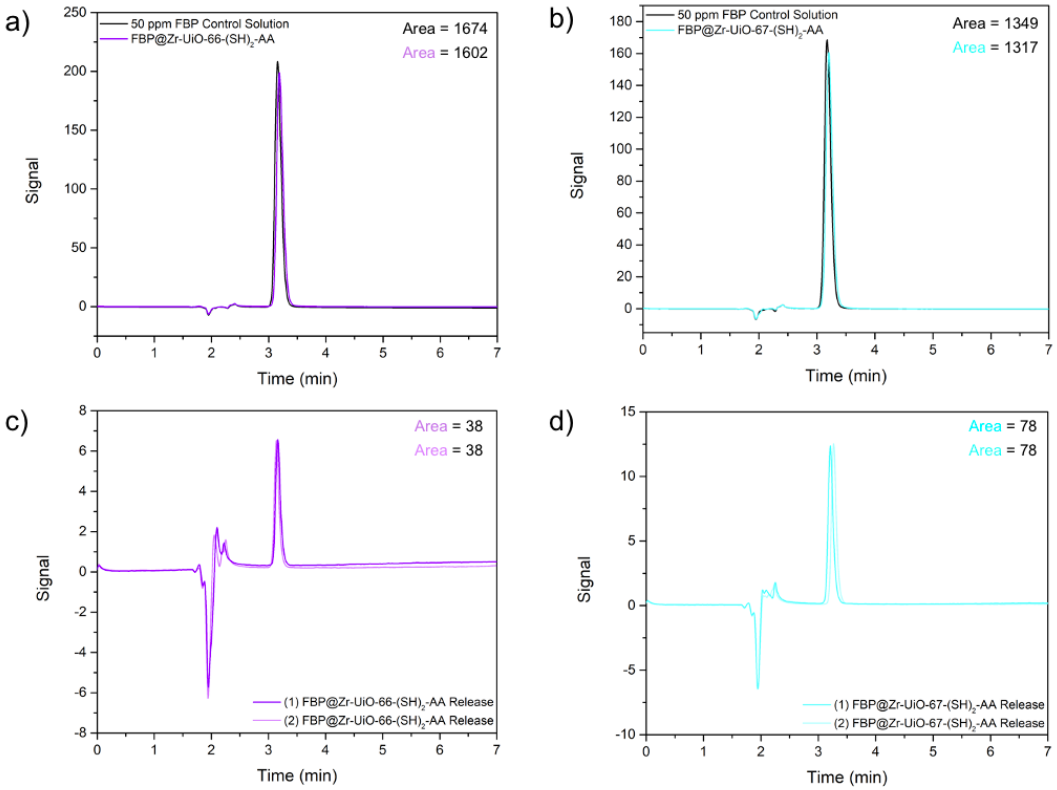

Figure A.23. HPLC chromatograms for flurbiprofen drug loading, (a) Zr-UiO-66-$(SH)_2$-AA, and (b) Zr-UiO-67-$(SH)_2$-AA, and release experiments, (c) Zr-UiO-66-$(SH)_2$-AA, and (d) Zr-UiO-67-$(SH)_2$-AA.

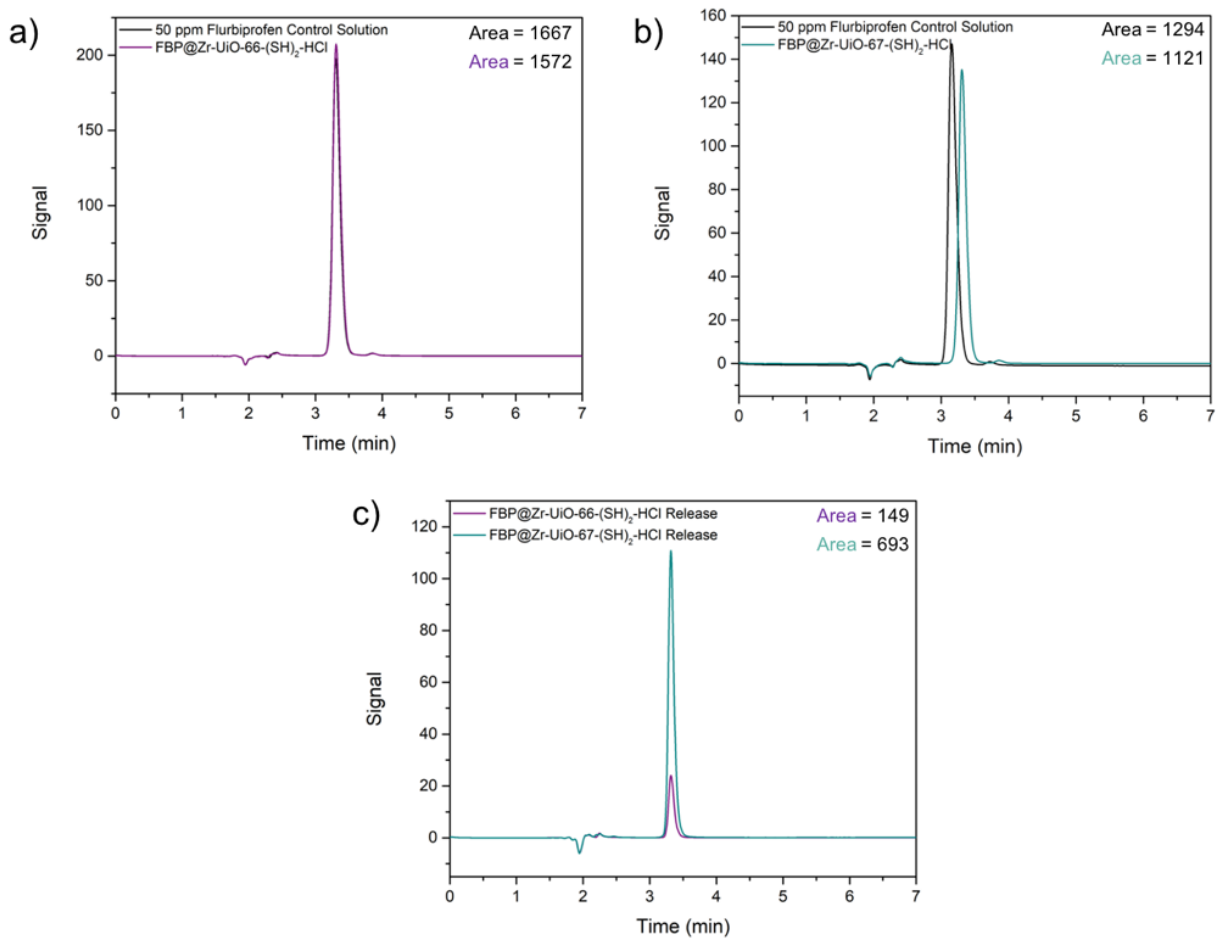

Figure A.24. HPLC chromatograms for flurbiprofen drug loading, (a) Zr-UiO-66-$(SH)_2$-HCl, and (b) Zr-UiO-67-$(SH)_2$-HCl, and release experiments, (c) Zr-UiO-66-$(SH)_2$-HCl and Zr-UiO-67-$(SH)_2$-HCl.

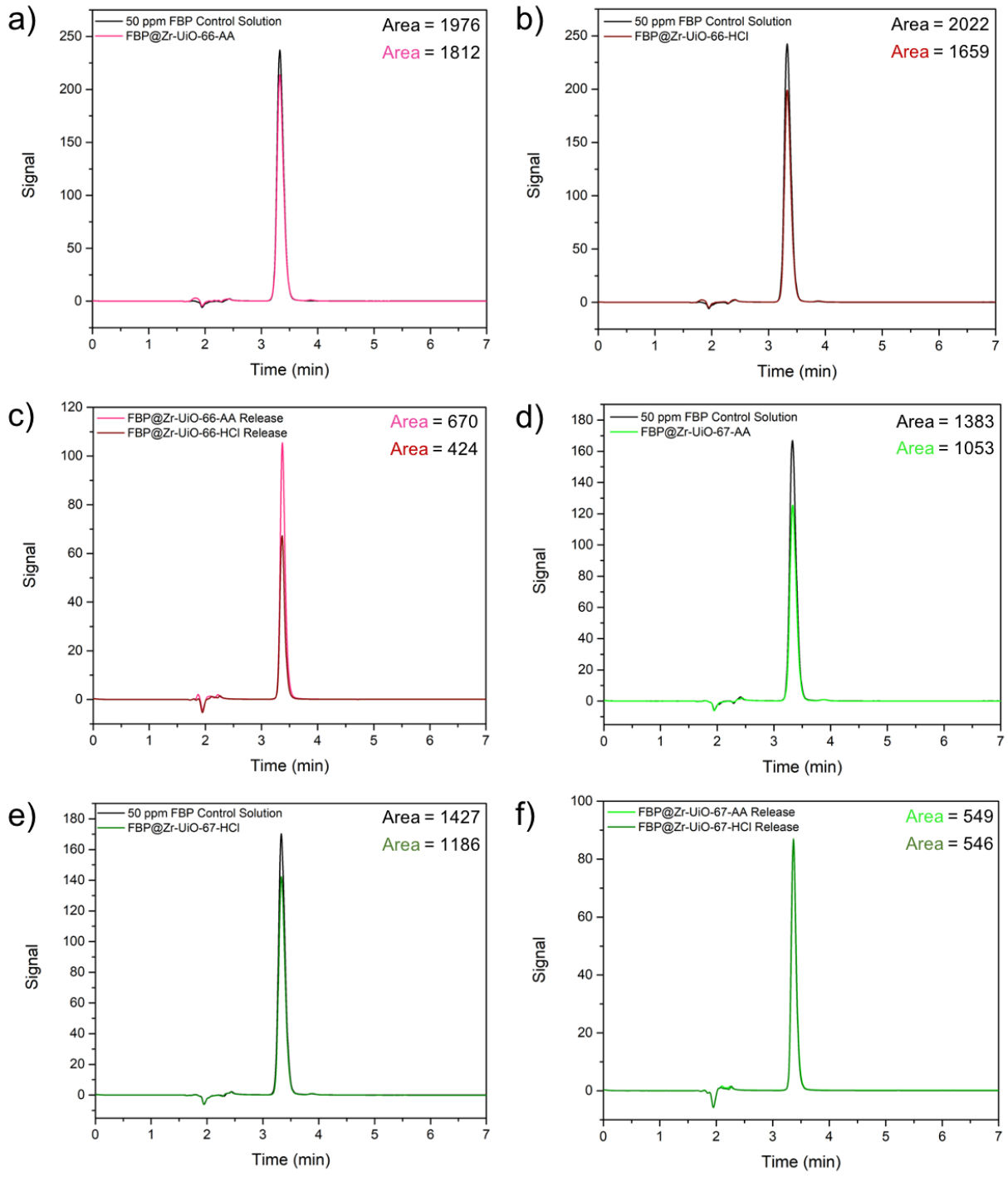

Figure A.25. HPLC chromatograms for flurbiprofen drug loading of (a) Zr-UiO-66-AA, and (b) Zr-UiO-66-HCl, and release experiments, (c) Zr-UiO-66-AA and Zr-UiO-66-HCl, and for drug loading of (d) Zr-UiO-67-AA, and (e) Zr-UiO-67-HCl, and release experiments, (f) Zr-UiO-67-AA and Zr-UiO-67-HCl.

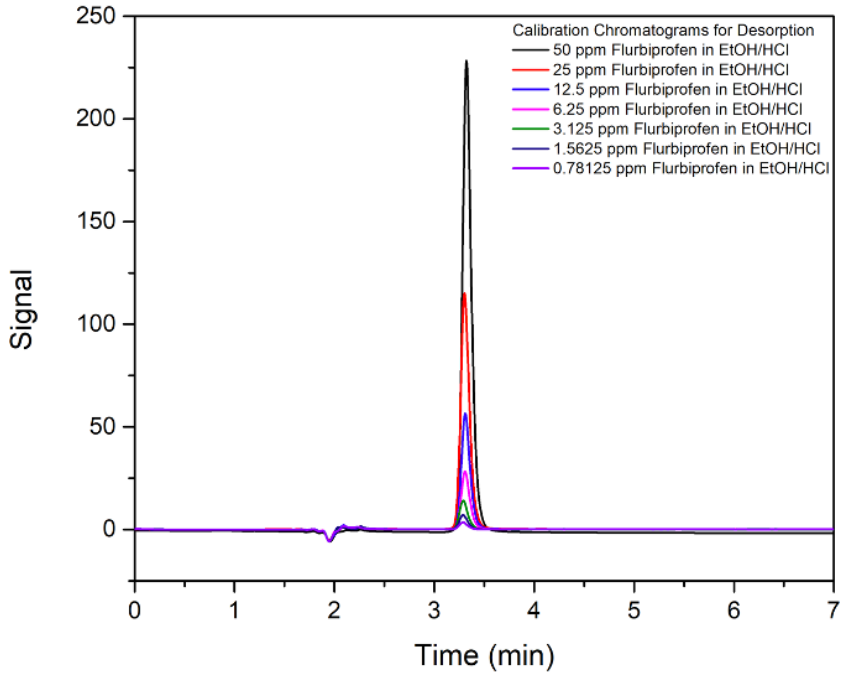

Figure A.26. HPLC chromatograms to generate a calibration curve for the release of flurbiprofen.

Table A.7. Concentrations of flurbiprofen and areas obtained by HPLC chromatograms.

Concentration of FBP in EtOH/HCl (ppm)	Area
50	1471
25	725
12.5	353
6.25	176
3.125	87
1.5625	43
0.78125	21